EPFL

Hyperpolarization of inorganic solids

Snaedis BJÖRGVINSDÓTTIR

École
polytechnique
fédérale
de Lausanne

2020

Abstract

Solid-state NMR can provide information about the atomic level structure and dynamics of materials. It directly probes symmetry and structure at nuclear sites, and is especially useful for investigation of disordered or amorphous solids that lack long range order. However, the application of solid-state NMR is sometimes limited by its relatively low sensitivity, caused by low concentrations and low gyromagnetic ratios of the magnetically active nuclei.

Dynamic nuclear polarization (DNP) can provide significant signal enhancements in magic-angle-spinning (MAS) NMR experiments. This is usually achieved by introducing stable organic radicals to the sample of interest, and transferring their large electron spin polarization to nearby nuclear spins via microwave irradiation near to the EPR frequency. Methods to hyperpolarize the bulk of solid materials containing protons are well established, whereas NMR of proton-free bulk materials remains challenging in many cases, especially when nuclear relaxation times are long, and if isotopic enrichment or paramagnetic doping to enhance relaxation rates are not feasible.

The overall objective of the work described in this thesis is to improve sensitivity in DNP enhanced solid-state NMR experiments, and to extend the application of DNP to systems that are currently difficult to access. In particular, this includes developing a strategy to hyperpolarize the bulk of proton-free inorganic materials.

In the first part, the classic flip-back method to recover bulk proton magnetization is combined with DNP of ^{1}H containing solids with characteristic build-up times spanning two orders of magnitude. Gains in sensitivity in the ^{13}C spectra of powdered crystalline theophylline, histidine and salicylic acid are reported, on top of the enhancements already provided by relayed DNP.

In the second part, a general strategy where the relayed DNP method is extended to proton-free inorganic materials is reported. The method uses a combination of impregnation DNP and slow spin diffusion between weakly magnetic nuclei such as ^{119}Sn and ^{31}P. Hyperpolarization is continuously generated at the surface either by direct DNP of the weakly magnetic nuclei, or by multiple bursts of cross polarization (CP) from protons in the wetting phase. Provided that bulk T_1 values are long, even slow spin diffusion can then transfer the surface-generated hyperpolarization to the bulk, resulting in spectra which exceed the sensitivity of conventional solid-state NMR. As an example, multiple contact CP can provide a factor 50 gain in overall sensitivity of the ^{119}Sn spectrum of SnO$_2$, allowing access to materials that were previously unfeasible to study. Overall in this thesis, hyperpolarization transport by spin diffusion is confirmed between ^{31}P nuclei in GaP and Sn$_2$P$_2$O$_7$, ^{119}Sn in SnO$_2$, ^{113}Cd in CdTe, ^{29}Si in SiO$_2$ (α-quartz) and ^{6}Li/^{7}Li in lithium titanates, and shown to improve sensitivity in their bulk NMR spectra. Strategies to optimize bulk hyperpolarization are shown, as well as two-dimensional spin diffusion experiments which provide insight into the process of polarization transfer from surface to bulk.

In the third part, DNP is explored at the highest field and spinning frequencies available for DNP to date. NMR signal enhancements of 200 are reported at 21.1 T, enabled by 65 kHz MAS at 100 K. The fast spinning frequencies also yield high resolution DNP enhanced ^{1}H-detected heteronuclear correlation spectra.

Keywords: solid-state NMR, dynamic nuclear polarization, spin diffusion, inorganic materials

Résumé

La RMN à l'état solide peut donner des informations sur la structure au niveau atomique et la dynamique des matériaux. Elle sonde directement la symétrie et la structure des sites atomiques et est particulièrement utile pour l'étude des solides désordonnés ou amorphes qui manquent d'ordre à longue distance. Cependant, l'application de la RMN à l'état solide est parfois limitée par sa sensibilité relativement faible, due aux par les faibles concentrations et bas rapports gyromagnétiques des noyaux magnétiquement actifs.

La polarisation nucléaire dynamique (DNP) peut fournir des gains significatifs du signal dans les expériences de RMN avec rotation à l'angle magique. Des procédés pour hyperpolariser le cœur des matériaux solides contenant des protons sont bien établis, cependant la RMN du cœur des matériaux sans d'hydrogène demeure difficile, en particulier lorsque les temps de relaxation nucléaire sont longs et si l'enrichissement isotopique ou le dopage paramagnétique pour améliorer les temps de relaxation ne sont pas réalisables.

L'objectif global des travaux décrits dans cette thèse est d'améliorer la sensibilité des expériences de RMN à l'état solide, et d'étendre le domaine d'application de la RMN DNP à des systèmes actuellement difficiles d'accès. En particulier, cela comprend le développement d'une stratégie pour hyperpolariser le cœur des matériaux inorganiques.

Dans une première partie, on propose de combiner la méthode classique *flip-back*, permettant de recycler l'aimantation des ^{1}H, avec l'hyperpolarisation par DNP. Cette méthode est démontrée sur des poudres organiques cristallines, dont les temps de relaxation T_1 s'étendent sur deux ordres de grandeur, et des gains de sensibilité importants dans les spectres ^{13}C ont été obtenus.

Dans une deuxième partie, j'introduis une stratégie générale où la méthode dite r*elayed DNP* est étendue aux matériaux inorganiques sans protons. Cette méthode combine la DNP par imprégnation à la diffusion lente de spin entre des noyaux faiblement magnétiques tels que ^{119}Sn et ^{31}P. L'hyperpolarisation est générée en continu à la surface soit par DNP direct des noyaux à la surface, soit par de multiples contacts de polarisation croisée (CP) à partir du solvant à la surface. À condition que les valeurs de T_1 soient longues, une diffusion de spin même lente peut transférer l'hyperpolarisation générée sur la surface vers l'intérieur, ce qui permet de dépasser la sensibilité de la RMN à l'état solide conventionnelle. Par exemple, la CP à contacts multiples fourni un gain d'un facteur 50 en sensibilité globale du spectre ^{119}Sn de SnO$_2$. On accède à l'analyse des matériaux auparavant irréalisables par RMN. Le transport de l'hyperpolarisation par diffusion de spin est confirmé entre les noyaux ^{31}P dans GaP, ^{119}Sn dans SnO$_2$ et Sn$_2$P$_2$O$_7$, ^{113}Cd dans CdTe, ^{29}Si dans SiO$_2$ (α-quartz) et ^{6}Li/^{7}Li dans les titanates de lithium. Plusieurs paramètres de notre méthodologie ont été étudiée permettant d'optimiser l'hyperpolarisation du *bulk* avec succès. Enfin, le processus de transfert de polarisation de la surface au *bulk* a été analysé à l'aide d'expériences de diffusion de spin 2D.

Dans une troisième partie, j'explore l'hyperpolarisation DNP à des champs magnétiques et des vitesses de rotation les plus élevées disponibles pour la DNP à ce jour. Des exaltations du signal RMN de 200 ont été ainsi mesurées à 21.1 T et rotation de l'échantillon à l'angle magique à 65 kHz MAS à 100 K.

Mots-clés : RMN à l'état solide, polarisation dynamique nucléaire, diffusion de spin, matériaux inorganiques

Contents

List of publications

The contents of this thesis are the result of my work, and this manuscript has not been previously submitted for consideration for any other degree. The work has resulted in the jointly authored publications listed below, and therefore this thesis includes the contributions of others where indicated. The thesis includes chapters based on the following publications:

1. S. Björgvinsdóttir, B.J. Walder, A.C. Pinon, J.R. Yarava, L. Emsley, "DNP enhanced NMR with flip-back recovery". *Journal of Magnetic Resonance* **2018,** 288, 69-75. (post-print)

2. S. Björgvinsdóttir, B.J. Walder, A.C. Pinon, L. Emsley, "Bulk nuclear hyperpolarization of inorganic solids by relay from the surface"*. Journal of the American Chemical Soc*iety **2018**, 140, 7946-7951. (post-print)

3. S. Björgvinsdóttir, B.J. Walder, N. Matthey, L. Emsley, "Maximizing hyperpolarization in pulse cooling under MAS". *Journal of Magnetic Resonance* **2019**, 300, 142-148. (post-print)

4. S. Björgvinsdóttir, P. Moutzouri, P. Berruyer, M.A. Hope, L. Emsley, "Sensitivity enhancement in lithium titanates by incipient wetness impregnation DNP NMR". *Journal of Physical Chemistry C* **2020**, 124, 30, 16524-16528. (post-print)

5. S. Björgvinsdóttir, P. Moutzouri, B.J. Walder, N. Matthey, L. Emsley, "Hyperpolarization transfer pathways in inorganic materials". *Submitted* **2020**. (pre-print)

6. P. Berruyer, S. Björgvinsdóttir, A. Bertarello, G. Stevanato, Y. Rao, G. Karthikeyan, G. Casano, O. Ouari, M. Lelli, C. Reiter, F. Engelke, L. Emsley, "Dynamic nuclear polarisation enhancement of 200 at 21.15 T enabled by 65 kHz magic angle spinning". *Journal of Physical Chemistry Letters* **2020**, 11, 19, 8386–8391. (post-print)

Chapter 1   Introduction

1.1   Solid-state NMR of materials

One of the most important aspects of chemistry and materials science is understanding how atomic-level structure affects the properties of materials. A number of experimental techniques exist for structural characterization, one of which is the focus of this thesis. High-resolution solid-state NMR can directly probe local atomic environments, and is especially useful for disordered or amorphous solids that lack long range order. In particular, it is element-specific and can give information about symmetry and structure at nuclear sites, as well as interatomic distances and the connectivity of atoms. Combining this information can yield full 3D structures. Furthermore, it is also sensitive to dynamics and can be used to study processes occurring at a range of timescales, from picoseconds to seconds. These qualities make solid-state NMR a method of choice to study the structure and dynamics of a range of disordered, amorphous and heterogeneous solids.[1-6]

1.1.1   The sensitivity problem

One of the main limitations of solid-state NMR is its low intrinsic sensitivity, which originates in essence in the small magnetic moments of nuclear spins. The magnetic moment is an intrinsic property of a nucleus which is determined by the gyromagnetic ratio, γ, and the spin quantum number, I. As an example, when a nucleus with $I = \frac{1}{2}$, which has two spin states, $+\frac{1}{2}$ and $-\frac{1}{2}$, is placed in a magnetic field, B_0, the two spin states will have different energies and their energy difference can be written as:

$$\Delta E = \gamma \hbar B_0 \qquad \text{(Eq. 1-1)}$$

where $\hbar$ is the reduced Planck's constant. The energy levels are populated following the Boltzmann distribution, and the nucleus has a net magnetic moment which is proportional to the population difference. The intensity of the measured NMR signal is directly related to the net magnetic moment, and the nuclear polarization which can be defined as:

$$P = \tanh\left(\frac{\gamma \hbar B_0}{2 k_B T}\right) \qquad \text{(Eq. 1-2)}$$

where k_B is the Boltzmann constant. Polarization is a dimensionless quantity and can take values between 0 and 1, where 0 represents equal population in both spin states and no net magnetic moment. From this equation, it is evident that increasing the magnetic field and lowering the temperature will lead to higher polarization, but these gains are currently limited by the available instrumentation. As an example, a proton in a magnetic field of 100 T and at a temperature of 1 K has polarization <0.02. This is far from unity, even though 100 T is higher than the highest available magnetic field today. The low sensitivity is especially prevalent in the case of nuclei with low γ and low natural abundance, as shown in Table 1-1, where the properties of several NMR active nuclei are listed and their sensitivities compared. When the sample of interest has a low volume of active spins, for example in the case of surfaces or other dilute species, the sensitivities are lowered even further.

Table 1-1. The spin quantum number, natural abundance, gyromagnetic ratio and receptivity of several NMR-active nuclei. The receptivity is defined as the product of the natural abundance and the NMR sensitivity, $R^x = NA \times [|\gamma^3| I(I + 1)]$. These specific nuclei were chosen because their spectra are shown later in this thesis.

nucleus	I (spin)	NA in %	γ in MHz/T	R^x rel. ^{13}C
^1H	$^1/_2$	99.99	42.6	5.87×10^3
^6Li	1	7.59	6.3	3.79
^7Li	$^3/_2$	92.41	16.5	1.59×10^3
^{13}C	$^1/_2$	1.07	10.7	1.00
^{29}Si	$^1/_2$	4.69	-8.5	2.16
^{31}P	$^1/_2$	100	17.2	3.91×10^3
^{113}Cd	$^1/_2$	12.22	-9.4	7.94
^{119}Sn	$^1/_2$	8.59	-15.9	2.66

The inherent insensitivity means that the signal acquired in NMR is accompanied by relatively large amounts of random electric noise. NMR generally uses signal averaging to get around this problem, where several experiments are added together to improve the signal-to-noise ratio (SNR). The signal increases linearly with each scan, but the random noise increases as the square root of the number of scans (ns), leading to the SNR increasing as $\sqrt{ns}$. As a result, NMR experiments can be very challenging for nuclei with low sensitivity, meaning that they are often restricted to 1D experiments which need a large number of scans for an acceptable SNR, if they are even feasible at all. Additionally, the perturbed spins need time between successive scans to return back to equilibrium. The length of this recovery period is determined by the characteristic longitudinal relaxation rate constant, T_1, and means that slow longitudinal relaxation can also lead to long experiments.[5, 7] (As a side note, the noise itself can be reduced to some extent by cooling down detection electronics in the probe to around 20 K.[8])

There are several methods which are routinely used to increase the sensitivity of solid-state NMR, not taking into account magic-angle-spinning (MAS)[9] and decoupling methods which improve resolution and consequently affect sensitivity.

Increasing the volume of magnetically active nuclei in the sample being studied is perhaps the most straightforward way of increasing sensitivity, as the signal-to-noise ratio is directly proportional to the quantity of sample. In solid-state NMR, this can for example be achieved by using a sample holder (rotor) with a larger diameter. Increasing the volume of the sample does however come with its own limitations when magic-angle-spinning is used to increase resolution. As an example, rotors with an outer diameter of 7 mm can hold relatively large amounts of sample, but their maximum spinning frequency is limited to 7 kHz at room temperature. Alternatively, the number of magnetically active nuclei in a given sample can be increased by isotopic labelling, either uniform or selective, which is especially common in biomolecular NMR.[10] Isotopic labelling is also sometimes used in NMR of materials, but it often requires synthetic modifications which are not always feasible.[1, 11]

Another approach to increase sensitivity is to reduce the apparent longitudinal relaxation rate, for example by adding low concentrations of paramagnetic impurities to the sample.[12] This shortens the overall experiment time, as the delay required between scans is reduced, as explained above. Longitudinal relaxation, or T_1 relaxation, is the return of perturbed magnetization to its equilibrium value (parallel to the external magnetic field, B_0, conventionally along the z-axis). For spin-½ nuclei, relaxation is mainly caused by fluctuating magnetic fields around the nuclear spins, which are induced by motion.[13] The recovery of longitudinal magnetization from zero can often usefully assumed to be mono-exponential:

$$M_z(t) = M_\infty \left[1 - e^{-\frac{t}{T_1}} \right]$$

(Eq. 1-3)

where M_z is the magnetization, M_∞ is the equilibrium magnetization and T_1 is the characteristic relaxation constant. The value of T_1 directly affects the sensitivity of NMR experiments, which is discussed in more detail in Chapter 2. Since the main source of relaxation is motion, lower temperatures tend to increase T_1. This means that even though lowering temperatures increases polarization, with an estimated gain in sensitivity of a factor 3 when going from 300 K to 100 K, or 300 if one goes to 1 K, it might not always translate into a gain in sensitivity over time since relaxation rates in experiments conducted at low temperatures can be very significantly longer than at room temperature.

Magnetization transfer methods represent yet another example of how sensitivity can be increased in solid-state NMR. Cross polarization (CP) is an example of this, it is widely used in solid-state NMR to enhance the sensitivity of nuclei with low gyromagnetic ratios.[14-15] The magnetization transfer is mediated through dipolar interactions, most commonly when two different nuclei are simultaneously spin-locked at the Hartmann-Hahn matching condition.[16] As an example, the sensitivity of ^{13}C nuclei in a given sample can theoretically be increased by a factor of four by transferring magnetization from more sensitive ^{1}H nuclei (corresponding to the ratio γ_{1H}/γ_{13C}). If the more sensitive nucleus has a shorter relaxation time than the less sensitive one, which is often the case, this can lead to additional enhancements, since more scans can be accumulated in a given time.

Figure 1-1 shows polarization as a function of temperature for ^{1}H and ^{13}C at two different magnetic fields, underlining that even though increasing the magnetic field or decreasing the temperature in an NMR experiment increases polarization, the gains are limited. Electrons, on the other hand, have a much higher spin polarization than nuclei, due to their higher gyromagnetic ratio. At temperatures that can be obtained experimentally, the electron polarization is in the high-temperature limit, which corresponds to the part of the graph where electron polarization is linear. In this limit, polarization increases with the inverse log of the temperature.
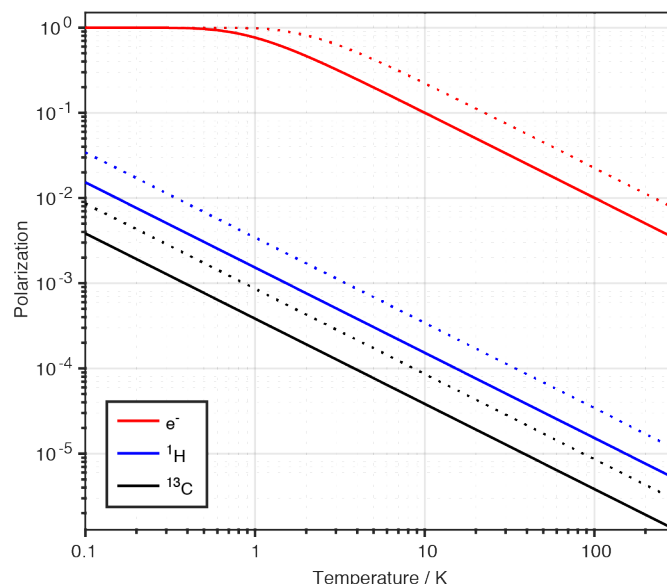
Figure 1-1. Polarization of electron, proton and carbon as a function of temperature, estimated with Eq. 1-2. The solid lines represent a magnetic field of 9.4 T and the dotted lines represent 21.1 T.

It was Albert Overhauser who first predicted, in 1953, that the high polarization of electrons could be transferred to NMR active nuclei through electron-nuclear interactions.[17] Later that same year Carver and Slichter reported the first DNP experiments, carried out on a sample of metallic lithium.[18] These contributions mark the beginning of dynamic nuclear polarization (DNP).

1.2 Dynamic nuclear polarization

In dynamic nuclear polarization, the polarization of unpaired electrons is transferred to coupled nuclei upon saturation of electron paramagnetic resonance (EPR) transitions, which is achieved by microwave irradiation at the EPR frequency. The transfer can take place through different mechanisms, and so far, three main polarization transfer mechanisms have been described for MAS DNP. These are the Overhauser effect,[17, 19] the solid effect[20-22] and the cross effect[23-26], but other mechanisms such as thermal mixing[27] and transfer by pulsed methods such as NOVEL[28] have also been described. The transfer mechanism is responsible for the initial transfer step from electrons to nuclei. The theoretical increase in nuclear polarization, or the maximum enhancement, is given by:

$$\varepsilon_{\text{max}} = \frac{P_{\text{e}}}{P_{\text{n}}} = \frac{\gamma_{\text{e}}}{\gamma_{\text{n}}}$$

(Eq. 1-4)

where P_{e} is the electron polarization and P_{n} is the polarization of a nucleus. This ratio corresponds to the ratio between the gyromagnetic ratios of the electron spin and the nuclear spin, as can be seen from Eq. 1-2. For protons, this factor corresponds to $\gamma_{\text{e}}/\gamma_{1\text{H}} \approx 660$, and for ^{13}C it is approximately 2600, but in practice the obtained enhancements are usually lower. After the initial transfer step to the coupled nuclei, the hyperpolarization needs to propagate to the nuclei of interest, which are often different than the directly coupled ones and can be further away from the electron spin. The hyperpolarization can be transferred to those nuclei by, for example, spontaneous spin diffusion (see Section 1.2.4) or cross-polarization. The observed DNP enhancement factor, ε, can be evaluated by comparing the NMR signal intensities with and without microwave irradiation, since the intensity of an NMR signal is directly related to the magnetic moment, and therefore the polarization of a given system:

$$\varepsilon = \frac{I_{\text{on}}}{I_{\text{off}}}$$

(Eq. 1-5)

where I_{on} and I_{off} are the signal intensities with and without microwave irradiation. This is a convenient way of evaluating DNP enhancements, although it does not always correspond to the overall sensitivity gains in practice. An example of a DNP enhanced NMR spectrum is shown in Figure 1-2. The enhancement factor ε is used throughout the thesis, along with more careful methods to evaluate gains in sensitivity, as discussed further in Section 1.2.3.

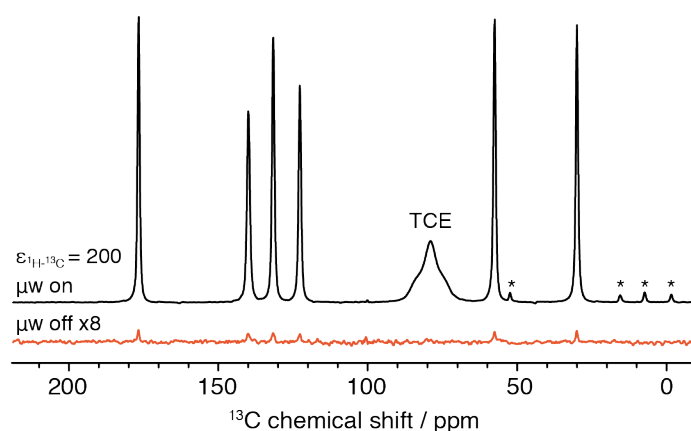Figure 1-2. DNP enhanced ^{1}H-^{13}C CP MAS spectrum of microcrystalline histidine impregnated with a 16 mM solution of TEKPol in TCE, compared to a spectrum of the same sample without microwave irradiation. The spectra were recorded at 100 K and 9.4 T, at a MAS rate of 12.5 kHz. A recycle delay of 60 s was used for both the microwave on and microwave off measurements. Spinning sidebands are marked with asterisks.

Since its discovery in the 1950's, DNP as a hyperpolarization method has grown over time to be compatible with solid-state NMR under MAS, and is therefore well suited for studying materials. High-field DNP has proven to be a powerful approach for the characterization of many different classes of materials, and the substantial increase in sensitivity has made it possible to access previously inaccessible parameters of structure and dynamics. It should however be noted that even though MAS DNP is the backbone of this thesis, other methods have also been used to increase nuclear polarization in NMR. These include dissolution DNP,[29] parahydrogen induced polarization (PHIP),[30] chemically induced DNP,[31-32] brute force methods using only field and temperature,[33-34] and optical pumping[35].

This section covers several aspects which are important in solid-state DNP NMR today, such as instrumentation, sample formulation and quantification of sensitivity gains.

1.2.1 Instrumentation for solid-state DNP NMR

Early DNP experiments were primarily carried out at relatively low magnetic fields, the main reason being the availability of appropriate microwave sources, since microwave sources for DNP need to output power at the EPR frequency corresponding to the field of the NMR magnet.[18, 36-38] High-field dynamic nuclear polarization in combination with MAS NMR became feasible in the 1990's when the Griffin group introduced the use of gyrotrons as sources of microwave radiation, which are compatible with higher magnetic fields.[39-40] Gyrotrons generate high-frequency electromagnetic radiation by cyclotron resonance of electrons in a magnetic field, and are able to deliver output powers at the sample of around 10 W or higher.

Current commercial MAS DNP instruments, shown schematically in Figure 1-3, consist of two main components: an NMR spectrometer and a microwave source. The superconducting NMR magnet is connected to a cooling unit which provides cryogenic gases for operating MAS at low temperatures, and it is equipped with an MAS probe that can go to temperatures of around 100 K. The microwave source, either a gyrotron or a klystron, generates continuous wave microwaves at a fixed EPR frequency corresponding to the frequency of NMR magnet. Since the microwave source has a fixed frequency, the NMR magnet often has a sweep coil with a range of several MHz, allowing it to match with the EPR absorption frequency of different radicals (see Section 1.2.2). A corrugated waveguide connects the microwave source to the stator of the NMR probe, delivering microwaves to the sample.[41-42] Recently, klystrons have been introduced as alternatives to gyrotrons.[43-44] These sources also create microwave emissions when energy is transferred from an electron beam to an electromagnetic wave, but their output power is lower (<5 W). Klystrons are significantly smaller than gyrotrons and can be placed closer to the NMR magnet, which reduces microwave transfer losses.
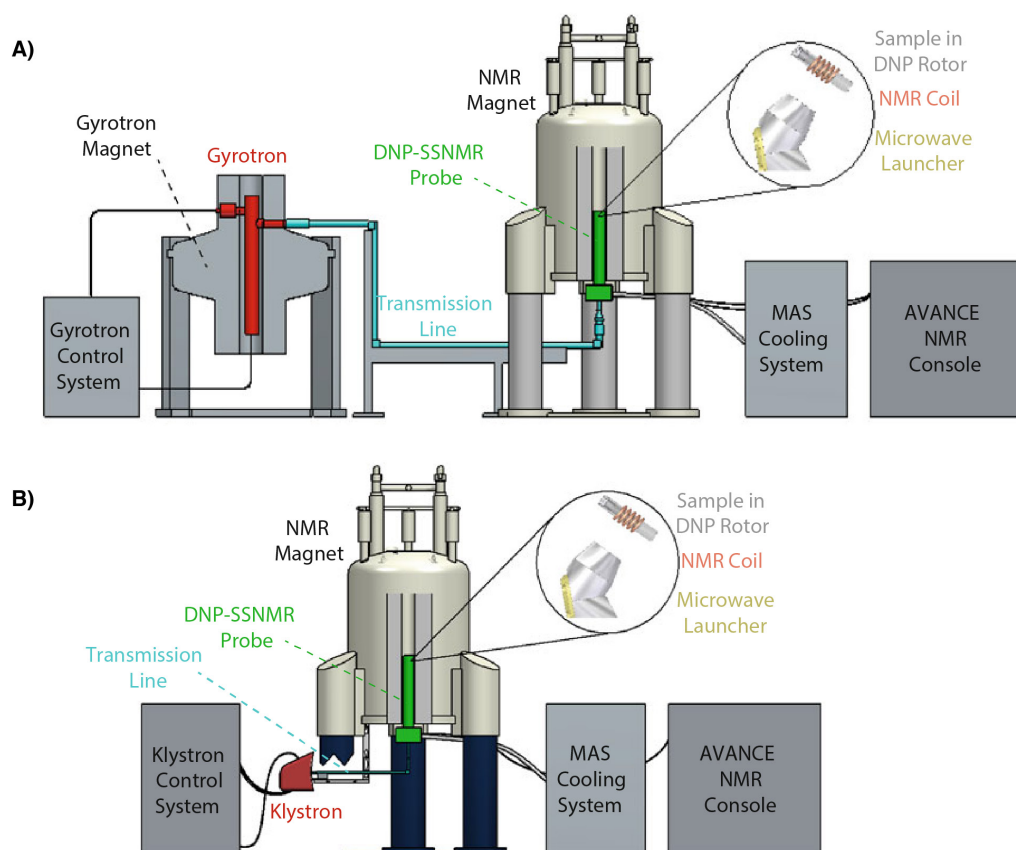
Figure 1-3. Schematic of two commercial solid-state DNP NMR systems with A) gyrotron and B) klystron microwave source. Figure adapted from reference[41] and reference[45].

To date, commercial DNP systems for 400 MHz, 600 MHz, 800 MHz and 900 MHz ^{1}H Larmor frequencies have been developed by Bruker, using gyrotrons with microwave frequencies of 263 GHz, 395 GHz, and 527 GHz and 593 GHz, respectively. Klystrons are currently available at 263 GHz. These two types of commercial DNP systems are described here because equivalent setups were used for the research presented in this thesis. Several other systems have been developed by academic research groups and companies, and a more complete description of MAS DNP instrumentation can be found elsewhere.[40-43, 46-50]

1.2.2   Sample preparation

The source of electron polarization in a DNP sample is usually an unpaired electron, either in the form of a free radical or a paramagnetic metal ion. These EPR active species, sometimes referred to as polarizing agents, and the way they are added to the sample, are important factors for the efficiency of DNP experiments. Following is a brief overview of DNP sample preparation.

Choice of DNP radical

Most commonly, polarizing agents are stable organic radicals that are added to the NMR sample as a part of a glassy matrix. As a general consideration, these radicals need to be soluble in a glass forming matrix, able to access the sample of interest, and have a large polarization transfer efficiency.[48, 51] The DNP transfer mechanism utilized by the radical depends on for example the homogeneous linewidth (δ, full width at half maximum) and the inhomogeneous breadth (Δ) of the EPR spectrum of the radical, the radical g-tensor anisotropy and the nuclear Larmor frequency of the NMR active species (ω_{0I}).[52-53] DNP radicals can be divided into two main categories, narrow line and broad line radicals, depending on their properties. The EPR lineshapes and magnetic field sweep

enhancement profiles (where enhancement is recorded as a function of magnetic field) of several radicals, both narrow line and broad line, are shown in Figure 1-4.

In narrow line radicals, the homogeneous linewidth and the breadth of the EPR spectrum are smaller than the Larmor frequency of the coupled nucleus ($\delta < \omega_{0I}$ and $\Delta < \omega_{0I}$) and DNP can be mediated by either the Overhauser effect[17, 19] or the solid effect[20-22]. Examples of narrow line radicals are the carbon-centered 1,3-bisphenylene-2-phenylallyl (BDPA) and trityl OX063, which have nearly isotropic g-tensors, as well as paramagnetic metal ions in symmetric environments such as Gd^{3+}-DOTA. Narrow line radicals are used less in MAS DNP than broad line radicals, but in some cases, they are a more appropriate choice. As an example, Gd(III) and Mn(II) complexes are biologically compatible and stable in reducing environments,[54-55] and BDPA utilizes the Overhauser effect which scales favorably with increase in magnetic field strength (which is discussed further in Chapter 4).
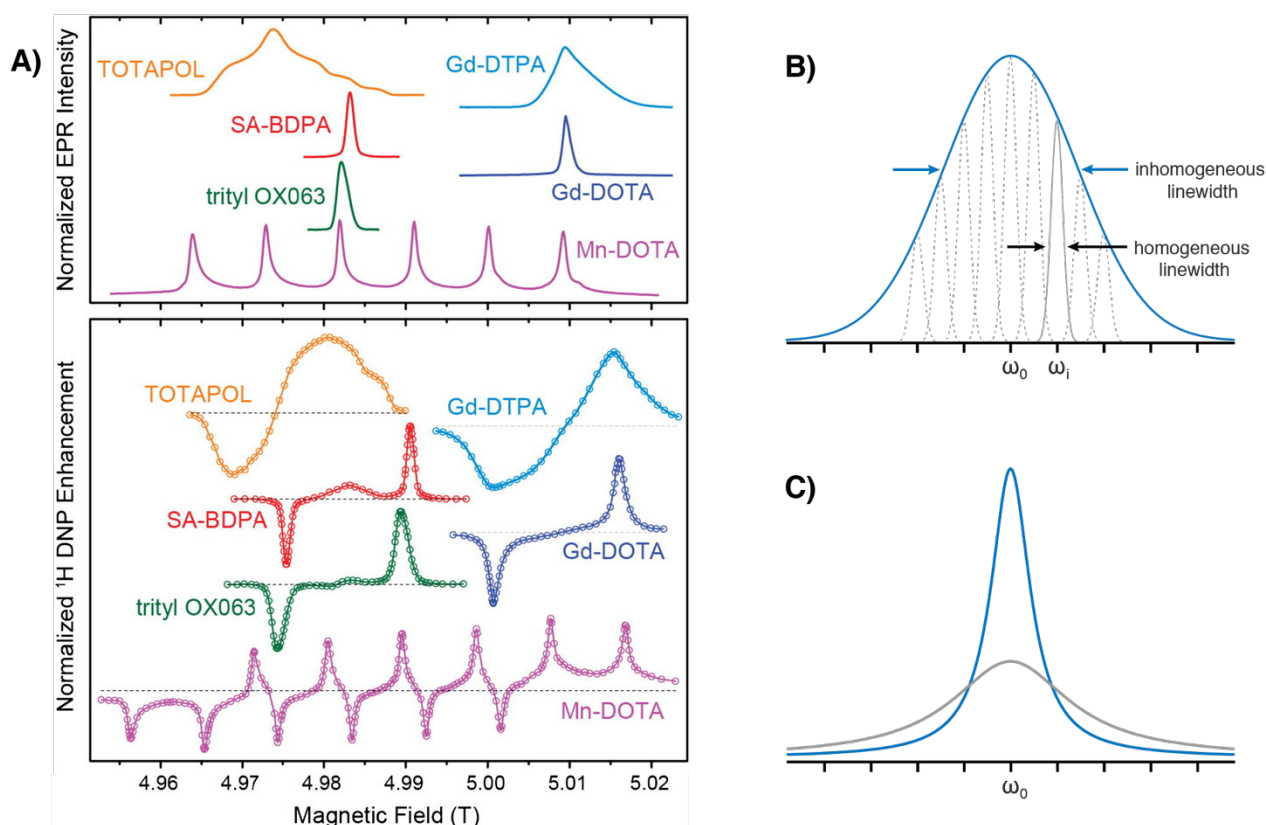

Figure 1-4. A) EPR lineshapes, as well as ^{1}H DNP enhancements as a function of magnetic field for different polarizing agents. Figure adapted from reference[54]. B) Schematic representation of an inhomogeneously broadened EPR line, where the total width of the line is determined by the sum of several narrow homogeneously broadened lines. Adapted from reference[56]. C) Schematic representation of two homogeneously broadened EPR lines, where the lineshapes are determined by different electron relaxation times.

Cross effect (CE) DNP is a three-spin mechanism where two coupled electron spins are required, separated by the Larmor frequency of the polarized nucleus. Broad line radicals, where the EPR line is inhomogenously broadened by the g-tensor anisotropy, can promote the CE mechanism if the condition $\delta < \omega_{0I} < \Delta$ is met.[52] Cross effect radicals are currently the most commonly used radical polarizing agents for high-field DNP. They are highly optimized for DNP enhanced CP experiments at 9.4 T, and are the result of extensive research of properties such as the electron-electron distance, the orientation between the nitroxide moieties, the electron relaxation properties and the radical surface interactions.[57-62] CE radicals typically consist of two nitroxide (2,2,6,6-tetramethylpiperidine-1-oxyl, TEMPO) radical moieties, which are covalently linked in order to strengthen electron-electron dipolar couplings for efficient CE. The structures of three commonly used biradical polarizing agents are shown in Figure 1-5. TOTAPOL[57] and AMUPol[59] are water-soluble and suitable for biological

applications, but for systems that are hydrophobic or not compatible with water, bTbK[60] and TEKPol[58] perform well. TEKPol is a derivative of bTbK, which has bulky substituents around the nitroxide moiety instead of methyl groups, giving rise to longer electron relaxation times (T_{1e} and T_{2e}) and higher enhancements.
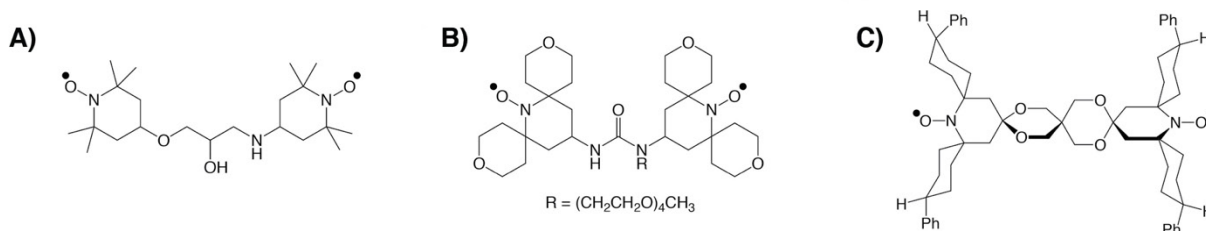

Figure 1-5. Three binitroxide radicals used in DNP enhanced solid-state NMR experiments. The structures of A) TOTAPOL B) AMUPol and C) TEKPol. Adapted from reference[63].

Increasing the magnetic field strength and the MAS frequency in solid-state NMR experiments results in increased sensitivity and resolution, which is often required for determining advanced atomic-level structural information. This will be discussed in more detail in Chapter 4. However, the performance of the nitroxide biradicals optimized for 9.4 T decreases significantly when the magnetic field is increased (as approximately $1/B_0$). As an example, the ^1H solvent enhancement of AMUPol in a glycerol/water solution decreases from ε = 250 at 9.4 T to 30 at 18.8 T and similarly the enhancement value for TEKPol in tetrachlororoethane goes from ε = 200 to at 9.4 T to around 15 at 18.8 T.[64] This decrease can be ascribed to a combination of factors, the main one being the increase of the width of the EPR signal at higher fields. (Note that depolarization and other quenching effects are not taken into account in these comparisons, but will be discussed in Section 1.2.3.)

A key finding in the development of CE radicals for higher fields was that they need to have larger electron-electron spin exchange interaction, which decreases the field dependence of the DNP enhancement factor. This can be achieved by tethering a narrow line radical and a broad EPR line radical,[65-66] based on the observation that mixtures of TEMPO and trityl radicals improve the efficiency of polarization transfer over that of monoradicals.[67] The structures of two heterobiradicals are shown in Figure 1-6. Trityl-nitroxides are soluble in water and intended for biological applications,[66] whereas BDPA-nitroxides are optimized for organic solvents.[64] Neither one of these heterobiradicals induces significant depolarization upon MAS. It should be noted that predicting the polarization transfer mechanism and the efficiency of radicals is still not straight forward and considerable effort has been put into assisting or guiding design by simulations.[68-70]
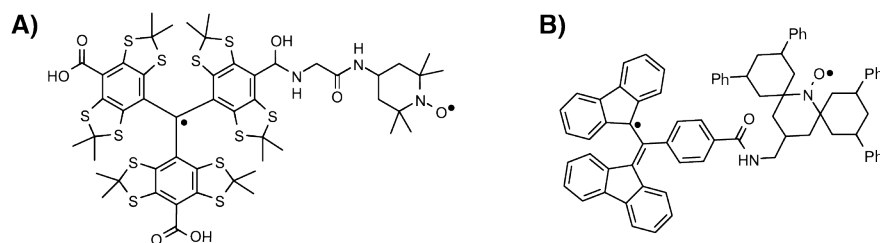
Figure 1-6. Heterobiradicals used in DNP enhanced solid-state NMR experiments. A) The structure of TEMtriPol-1, a water-soluble trityl-nitroxide biradical.[63] B) The structure of HyTEK2, a BDPA-nitroxide biradical.[64]

The above examples all describe polarizing agents which are added to the sample exogenously. Endogenous radicals can also be used for DNP, but the applicability depends strongly on the analyte of interest. Examples of endogenous radicals include high-spin transition metal ions incorporated as dopants into organic[71-72] or inorganic solids[73-74]. Alternatively, radicals can be created by gamma irradiation,[75] or by using electrical discharges.[76]

Choice of solvent system

Biradical polarizing agents are most efficient when they are dissolved and uniformly distributed in a glass forming solution, typically in concentrations of up to 20 mM. The radical-containing solution either dissolves the sample of interest or surrounds it, depending on the application. Several different sample preparations for DNP are shown schematically in Figure 1-7, and Section 1.2.4 will focus in more detail on the case where the radical-containing solution is selected so that it dissolves the radical but not the analyte. Some DNP sample formulations actually do not require the addition of a glass-forming solution, and those can be called matrix-free approaches. These include approaches where radicals are introduced to the bulk of the analyte by doping,[71-74] as well as approaches where a polarizing agent binds to the sample of interest, either covalently[77-80] or due to affinity to the surface[81-82].

Figure 1-7. Schematic depiction of different DNP sample preparations, showing the distribution of the analyte and the polarizing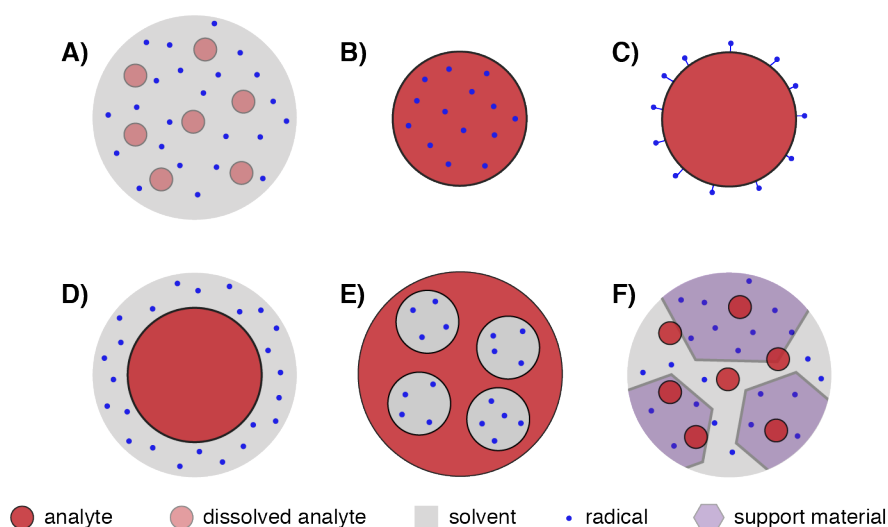 agent. A) Analyte and radical are dissolved and homogenously distributed in a glass forming solution. B) The bulk of the analyte is doped with radicals. C) radicals are covalently and selectively attached to the analyte surface. D) Analyte particle is coated with a radical containing solution that does not dissolve the analyte, restricting the radicals to the surface of the particle. E) Porous analyte which has been wetted with a radical containing solution that can enter the pores. F) Analyte is dispersed on a dielectric support material and the mixture is then wetted with a radical containing solution.

The most common DNP matrix for water-compatible samples is a mixture of H_2O and D_2O, with either glycerol or DMSO as a glass former. The glass former prevents the formation of ice crystals, since DNP experiments are typically carried out at around 100 K, where the electron relaxation times are longer and saturation easier. Without a good glass, aggregates of polarizing agents (phase separated from the molecule of interest) could form, and when radicals are too close to each other, strong electron-electron dipolar couplings shorten the electronic relaxation times and prevent efficient DNP. In addition, the glass former acts as a cryoprotection of the analyte upon freezing, which can be especially important for biomolecules that can undergo denaturation processes or phase transitions due to solvent crystallite formation.[83]

For MAS DNP of materials, 1,1,2,2-tetrachloroethane (TCE) was found to work well as a glass former.[84] Halogenated solvents give better DNP enhancements than fully protonated solvents, because of their lower proton content. The proton content of the glass forming solution can alternatively be optimized by partial deuteration, and water based matrices contain D_2O for this reason. The protons in the matrix are essential because spontaneous proton spin diffusion is the mechanism which carries the hyperpolarization from the radical source to the analyte (see Section 1.2.4). However, if the concentration of protons is too high, a relatively low concentration of radicals cannot efficiently hyperpolarize the matrix and the hyperpolarization is dispersed. Similarly, if the proton concentration is too low the transport of hyperpolarization is not efficient.[61, 85] An example

of a combination of radical and solvent that provides high enhancements in aqueous media is 12 mM AMUPol in a 60/30/10 (v/v/v) glycerol/H_2O/D_2O solution, which has a ${}^1H$ concentration of around 11 M.[59] In organic solvents, 16 mM TEKPol in TCE, where the ${}^1H$ concentration is 18 M, works well.[58] These combinations can be good starting points, although the optimal proton content in the matrix can sometimes be further optimized depending on the analyte.[61]

In some cases, for example when studying nanoparticulate compounds, the formation of aggregates needs to be prevented because they separate from the radical solution and decrease the DNP efficiency. This can be solved by dispersing the nanoparticles in mesoporous silica or in frozen acrylamide gels,[86-87] or by mixing them with dielectric support material, such as hexagonal boron nitride (h-BN).[88] Another possible problem is if the analyte reacts with the polarizing agent, which can either modify the material of interest, or decompose the radical and lower the DNP efficiency. In those cases, it is practical to spatially separate the radical and analyte, for example by putting the analyte inside a porous material and use a polarizing agent which is too bulky to enter the pores,[89] or by sterically hindering the radical from approaching the surface with the use of micelles or dendrimers.[90-91]

1.2.3 Enhancements and sensitivity

As explained earlier, the maximum theoretical enhancement that can be obtained with DNP corresponds to the ratio γ_e/γ_x, where γ_e and γ_x are the gyromagnetic ratios of the electron and polarized nucleus. This ratio is around 660 for ${}^1H$ (and even higher for nuclei with lower γ), but in practice ${}^1H$ enhancements of up to around 200 are routinely observed when using biradical polarizing agents at 9.4 T and 100 K.

The enhancement factor is a convenient measure of the efficiency of DNP, but it tells far from the full story. In reality additional factors such as depolarization and quenching, change in relaxation time constants, dilution and temperature effects need to be taken into account to compare the sensitivity of a DNP experiment to that of conventional MAS NMR on a dry sample. [77, 81, 92-93]

The build-up time of a radical containing DNP sample, T_B is accelerated compared to the longitudinal relaxation time, T_1, measured in an undoped sample due to the presence of paramagnetic species. The sample volume of the molecules of interest might also be decreased in DNP compared to conventional NMR in a rotor of the same size, due to addition of a radical containing glass-forming solution. The difference in Boltzmann polarization should also be taken into account when comparing DNP experiments at 100 K to a conventional NMR experiment at 298 K. Furthermore, addition of paramagnetic species can cause line broadening, as well as bleaching of nuclear spins in close proximity to electron spins (usually those within a radius of a few Å). The overall sensitivity enhancement can therefore be defined as:

$$\Sigma^{\dagger} = \varepsilon \times \theta \times \sqrt{\frac{T_1}{T_B}} \times \frac{298 \text{ K}}{100 \text{ K}}$$

(Eq. 1-6)

where θ is the quenching factor, calculated as the ratio of the signal intensity of a sample in contact with a radical containing solution and an analogous sample where the solution is without radicals (at 100 K, in the absence of microwaves).[92] Figure 1-8 shows ε, θ and $\Sigma^{\dagger}$ for a sample of mesoporous silica in TCE with different concentrations of the biradical bCTbK.[94] The figure shows significant signal quenching, which increases as the radical concentration is increased. This results in that, for a 16 mM radical concentration, as an example, the enhancements evaluated with ε are higher than the overall sensitivity enhancements Σ_{Si} (not taking Boltzmann polarization into account, red dots in Figure 1-8C). The figure also underlines why 12-16 mM biradical solutions are commonly used.
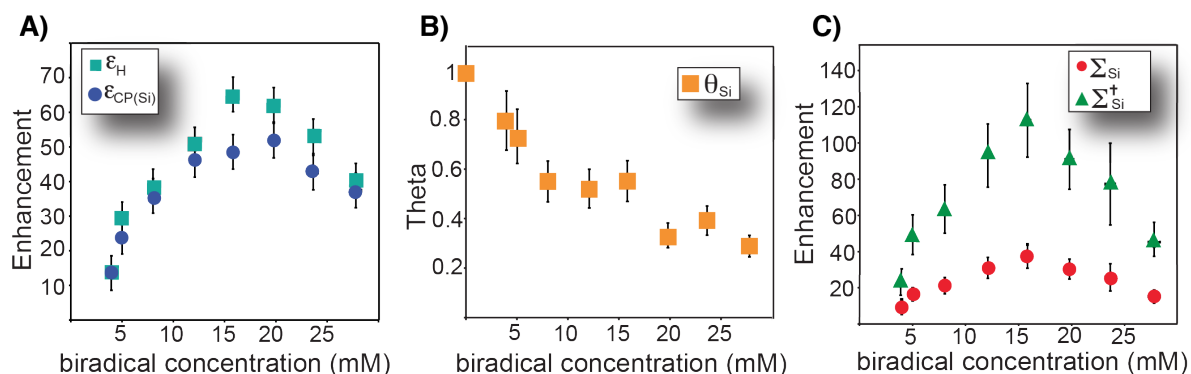
Figure 1-8. Enhancement properties of a sample of mesoporous silica polarized with a solution of bCTbK in TCE. A) ^{1}H enhancement (ε_H) and ^{1}H-^{29}Si CP enhancement ($\varepsilon_{CP(Si)}$). B) The quenching factor of ^{29}Si. C) Overall sensitivity enhancements of ^{29}Si, where $\Sigma^\dagger$ takes the difference in Boltzmann polarization into account whereas Σ does not. Adapted from reference[94].

One of the components included in θ is depolarization caused by MAS, which affects the sensitivity of CE DNP experiments.[95-96] This can be quantitatively evaluated with the depolarization factor, ε_{depo}, which is defined as the ratio between the signal intensity of a spinning DNP sample and the same sample under static conditions, in the absence of microwaves.[97] Taking AMUPol at 9.4 T as an example, the integrated signal intensity decreases compared to static conditions, showing that quenching is induced upon spinning. These depolarization effects depend on field and temperature, and on the properties of the radical polarizing agent.[98]

The bottom line is that sensitivity gains in DNP experiments cannot simply be evaluated by measuring ε. In this thesis, sensitivity ratios will be used to evaluate the gains in sensitivity attained by DNP NMR.[81, 93] Here, sensitivity is defined as signal-to-noise ratio per unit square root of time:

$$\text{sensitivity} = \frac{SNR}{m} \Big/ \sqrt{t} \qquad \text{(Eq. 1-7)}$$

where m is the mass of the sample. Sensitivity gains are then obtained by comparing the sensitivity under optimized DNP conditions with the sensitivity of an optimized standard solid-state NMR experiments. The sensitivity optimized reference experiment should be carried out on a sample without radicals, potentially using different temperatures or sample volumes, with the recycle delay scaled according to T_1 (as opposed to T_B in a DNP experiment). In this way, it is possible to quantify the overall gains in sensitivity provided by DNP, without going into detail about where they originate.

1.2.4 Application to microcrystalline solids

Application of MAS DNP initially focused on biomolecular solid-state NMR of frozen solutions,[83, 99-100] but since around 2010 organic and inorganic materials have become the main area of application of MAS DNP as a result of the introduction of the impregnation approach.[101] In this section, two different ways of polarizing microcrystalline solids will be described, as the bulk of the work presented in this thesis concerns this class of materials. These are surface enhanced DNP and relayed DNP.

Surface enhanced DNP

The characterization of surfaces at the molecular level is important so that the relationship between structure and activity can be understood. Knowing the structure can aid in rational design, where for example surface properties at active sites are tuned so that materials with specific functions can be produced. Probing the surface of materials with NMR spectroscopy is usually challenging because in most materials, the atoms on the surface make up a very small fraction of the total volume of the sample (see Figure 1-9). In addition, surface environments are often less

symmetric than bulk environments, leading to broader signals, since any variation in the local environment of a nucleus will result in changes to the NMR parameters, i.e. in the isotropic and anisotropic shielding, and the couplings between spins.[5, 85]
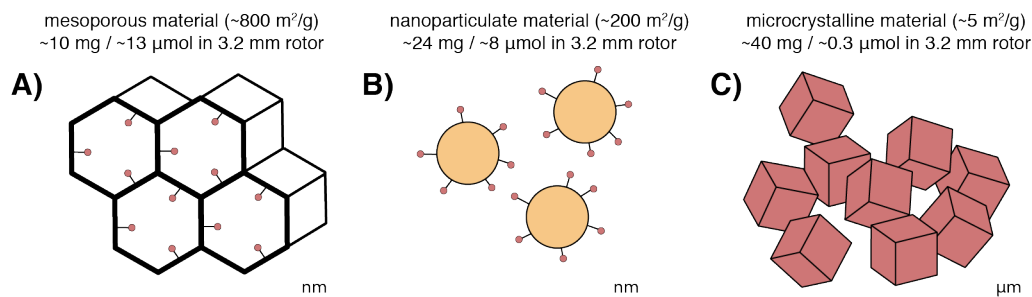

Figure 1-9. Specific surface areas of different materials, as well as the estimated number of nuclei of interest (in red) in a 3.2 mm diameter NMR rotor. A) Mesoporous material with a high surface area, which has a relatively low concentration of surface functionalities. B) Nanoparticulate material with functional groups on the surface. C) Microcrystalline solid with a specific surface area of around 5 m^2/g.

In surface enhanced NMR spectroscopy by DNP, or DNP SENS, the surface of a material is selectively hyperpolarized.[101-102] Sample preparation for surface enhanced DNP consist of wetting the dry samples with a solution containing the radical, using a method called incipient wetness impregnation. Since the surface of the material is being targeted, it is important that the glass forming solution is a non-solvent for the analyte.[101, 103] The radical-containing wetting phase can then be used to access the nearby surface, in one of two ways. The first method is through direct DNP from polarization agents located in the wetting phase near the surface of the materials to nuclei of the analyte located near the surface. The second approach is more common, it consists of hyperpolarization of protons in the wetting phase followed by polarization transfer to nuclei on the surface (sometimes called indirect DNP).[85, 101]

In a typical indirect DNP SENS experiment, depicted in Figure 1-10, the ^{1}H nuclei close to the polarizing agents get hyperpolarized by DNP upon microwave irradiation, and spontaneous ^{1}H spin diffusion distributes hyperpolarization throughout the wetting phase. Polarization transfer methods, such as cross-polarization, are then used to selectively hyperpolarize the surface of the material. The sensitivity gains provided by DNP SENS enable even very dilute surface sites to be observed by solid-state NMR.[104] A more complete description of DNP SENS, as well as examples of application, can be found in several review articles.[63, 85, 104]
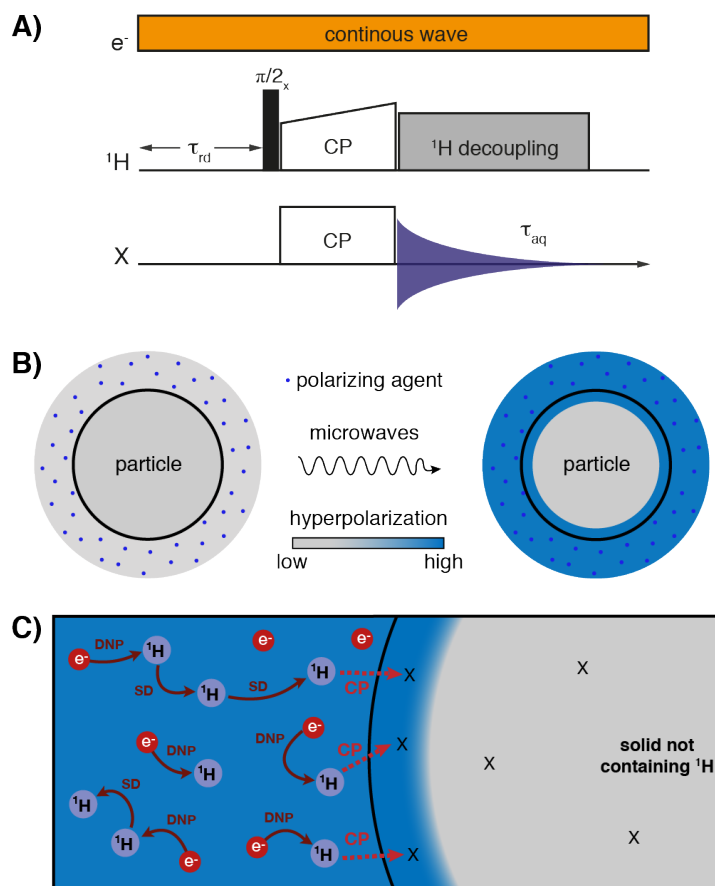
Figure 1-10. A) An example of a pulse sequence for DNP SENS. B) Schematic representation of a DNP SENS experiment, where a material is hyperpolarized using the incipient wetness impregnation method. C) The surface of a particle that is hyperpolarized by cross polarization in a DNP SENS experiment.

Relayed DNP

In relayed DNP, the inside of a particulate substrate is remotely polarized through spontaneous spin diffusion. The sample is usually prepared by coating particles with a small amount of a radical containing solution, in the same way as for DNP SENS. In a typical relay experiment, solvent protons close to the polarizing agents are hyperpolarized with DNP and the polarization then distributes around the wetting phase and to the surface of the target material, creating a polarization gradient at the surface. From there it travels across the solvent-solid interface and into the center of the target through a continuum of dipolar-coupled protons, aiming to reduce the polarization gradient at the surface and bringing the system back to equilibrium. The hyperpolarization can then be detected on protons, or transferred to heteronuclei with cross-polarization (CP) or other polarization transfer methods.[105-108] A schematic representation of relayed DNP is shown in Figure 1-11.

Relay is important when the polarizing agent cannot be brought in close proximity to the target nuclei. This is for example the case for microcrystalline solids and some porous materials, such as MOFs, zeolites, polymers, pharmaceuticals, and bulk inorganic solids. The enhancements obtained in the target location is usually lower than the enhancement on the surface, as some spin polarization is lost due to longitudinal relaxation during the relay from surface to bulk.[106, 109] Relayed DNP makes it possible to obtained natural abundance spectra, for example ^{13}C and ^{15}N spectra, with high signal-to-noise ratios in a fraction of the time it would otherwise take. In fact, the sensitivity is similar to that of conventional NMR of isotopically enriched samples. In addition, relayed DNP often leads to high-resolution spectra, since the material of interest is not dissolved and can therefore retain its crystalline nature if it has one.[110]
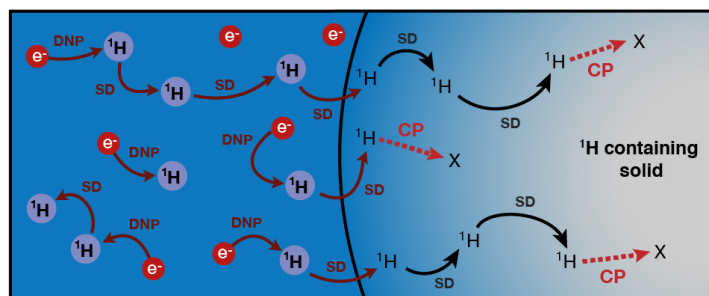
Figure 1-11. A) Schematic representation of relayed DNP where hyperpolarization is carried into the bulk of a particle, followed by cross polarization.

Spin diffusion is especially common in organic solids that have dense networks of protons, and is not specific to DNP.[111-112] It has over time had many applications in distance determination for structure determination of biomolecules,[113-114] polymers,[115-116] and small molecules[117-118]. Spin diffusion will be explained in more detail in the following section.

1.3 Spin diffusion

The concept of nuclear spin diffusion was first introduced by Bloembergen in 1949, to explain unexpected values of spin-lattice relaxation times in solids.[119] The term spin diffusion is used because the process describes the transfer of polarization through space, and can on a large scale be thought of as being analogous to diffusion. However, the entropy in a true diffusion process increases, whereas spin diffusion is a reversible process where entropy is conserved.[111] Spin diffusion is mediated through homonuclear dipole-dipole interactions, which under specific conditions allow energy conserving flip-flop transitions of neighboring nuclei so that the spin effectively hops, even though the nuclei themselves do not move and their Zeeman energy does not change. In this section, several concepts that are important in spin diffusion are discussed, including the interactions driving spin diffusion, the rate of spin diffusion and the effect of MAS, as well as the role of spin diffusion in DNP.

1.3.1 Dipolar interactions

Nuclear spins generate a local magnetic field according to the direction of the spin magnetic moment. A second nuclear spin will interact with the magnetic field of the first, and vice versa, in an interaction that is called dipole-dipole coupling. Dipolar couplings are through-space interactions, which can either be intramolecular or intermolecular. To put dipolar interactions into context, it can be useful to recall that for solid-state NMR, the Hamiltonian describing the spin system can be written as:

$$\mathcal{H} = \mathcal{H}_z + \mathcal{H}_Q + \mathcal{H}_D + \mathcal{H}_{cs} + \mathcal{H}_J \qquad \text{(Eq. 1-8)}$$

where $\mathcal{H}_z$ is the Zeeman Hamiltonian, $\mathcal{H}_{cs}$ is the chemical shift Hamiltonian, and $\mathcal{H}_Q$ is the quadrupolar Hamiltonian, which can be ignored for spin-½ nuclei. $\mathcal{H}_D$ and $\mathcal{H}_J$ are the dipolar and scalar coupling Hamiltonians, respectively. For high magnetic fields, this simplified form of the system Hamiltonian lists the most relevant terms in an order of decreasing magnitude. The nuclear precession frequencies measured in NMR are generally dominated by the Zeeman interaction, and the dipolar coupling term can be treated as a perturbation of the much larger $\mathcal{H}_z$. The secular part of the homonuclear dipole-dipole Hamiltonian for a rotating solid, which commutes with $\mathcal{H}_z$, can be written as:

$$\mathcal{H}_D = \frac{1}{2} d_{jk}(1 - 3\cos^2\theta_{jk})\big(3I_{jz}I_{kz} - \boldsymbol{I}_j \cdot \boldsymbol{I}_k\big) \qquad \text{(Eq. 1-9)}$$

where I_j and I_k are spin angular momentum operators and θ_{jk} is the angle between the internuclear vector and the external magnetic field.[13] The majority of the dipolar interactions can be removed by rotating the sample at the angle θ_{jk} = 54.7°, which will be discussed further below.[9, 120] The dipolar coupling constant, d_{jk}, gives the magnitude of the dipole-dipole interaction:

$$d_{jk} = \left(\frac{\mu_0}{4\pi}\right)\frac{\gamma_j\gamma_k\hbar}{r_{jk}^3} \qquad \text{(Eq. 1-10)}$$

Where μ_0 is the vacuum permeability, $\hbar$ is Planck's constant, γ is the gyromagnetic ratio of each nucleus, and r_{jk} is the distance between the two coupled spins. As seen in Equation 1-10, the strength of the dipolar coupling constant scales linearly with the gyromagnetic ratio of each spin, and it goes down as the inverse cube of the distance between the spins. Therefore, in the case of low abundance nuclei where the network of spins is sparse, this r^3 dependence significantly reduces the dipolar coupling strengths. This is shown graphically in Figure 1-12, where the homonuclear ^{1}H and ^{13}C dipolar coupling constants are plotted as a function of the distance between the spins. The ^{13}C dipolar couplings are a factor ~16 times weaker than the ^{1}H dipolar couplings, as indicated by the vertical separation of the two solid lines in the graph. In practice, the ^{13}C dipolar coupling is often much weaker,

as two ^{13}C atoms are on average much further apart than two protons, due to the significantly lower natural abundance of ^{13}C.
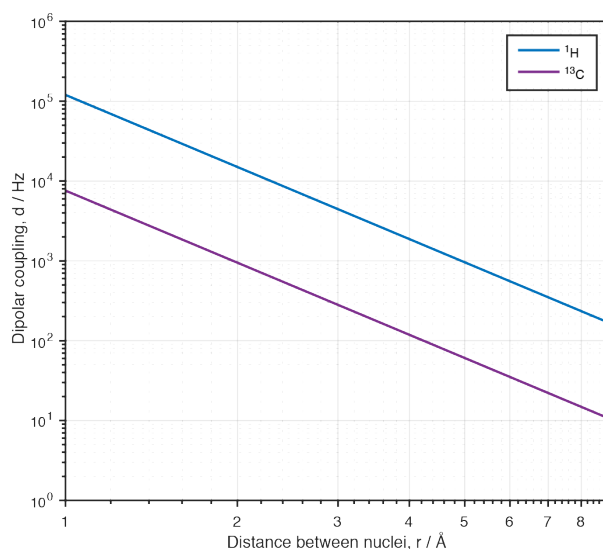

Figure 1-12. Homonuclear (^{1}H-^{1}H or ^{13}C-^{13}C) dipolar coupling strength as a function of the distance between two nuclei, plotted on a logarithmic scale.

Energy conserving zero-quantum (ZQ) flip-flop transitions between two dipolar coupled spins are responsible for spin diffusion, and spin diffusion in solids can be visualized in simple terms by looking at an energy level diagram of a system of two dipolar-coupled spins, j and k (Figure 1-13). When the two spin states are approximately equivalent in energy, i.e. when their dipolar coupling frequencies are higher than the chemical shift differences ($\omega_j - \omega_k < d_{jk}$), spin diffusion can occur spontaneously. This effect is especially prevalent in organic solids that have dense networks of protons. Most other nuclei have lower gyromagnetic ratios and longer distances between nuclei, which weakens the strength of the dipolar coupling constants and lowers the probability of an energy conserving flip-flop transition. In these systems, chemical shift differences are often greater than the dipolar couplings and spontaneous spin diffusion is less likely to happen. However, if there are other spins present in the system, dipolar couplings to them can broaden the energy levels of the homonuclear low-γ spin system. This leads to overlap of the energy levels, which compensates for the chemical shift difference, leading to a higher probability of an energy conserving ZQ flip-flop of the dipolar coupled spins. An example of this is proton-driven spin diffusion (Figure 1-13C).[121-122]
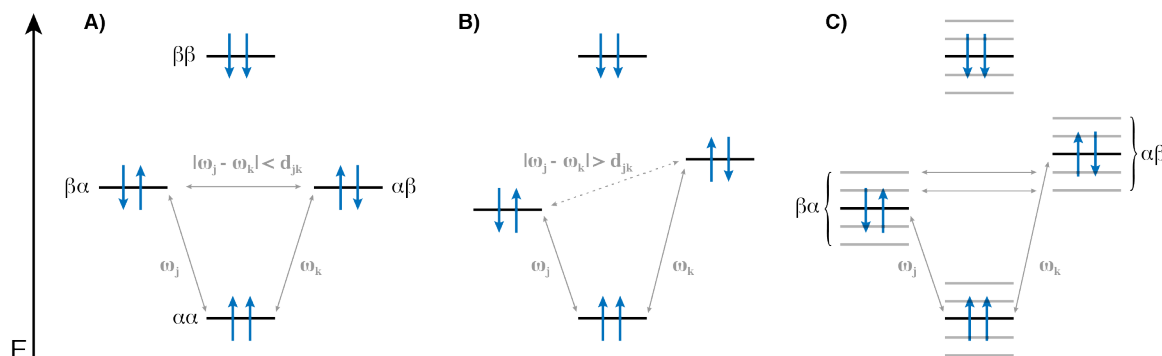
Figure 1-13. Energy level diagrams for a two-spin system. A) Energy conserving flip-flop transition of two equivalent spins, high probability of spin diffusion. B) The flip-flop transition of two spins that are not equivalent is not energy conserving, low probability of spin diffusion. C) The two inequivalent spins are coupled to many other spins, resulting in splitting (or broadening) of the energy levels of the two spin system. Energy conserving flip-flop transitions can occur between some of the levels $\alpha\beta$ and $\beta\alpha$. Figure adapted from reference[112].

It should be mentioned here that in non-viscous (isotropic) liquids, the dipolar couplings are essentially averaged to zero due to molecular motion. In solids, averaging of the dipolar interactions can be achieved by rotating the sample at the magic angle (θ_{jk} = 54.7°), which leads Equation 1-9 to go to zero.[9] It is important to note that the dipolar interactions are only averaged to zero at infinite spinning frequencies (ν_r), but in all other cases the averaging is incomplete. This can be justified by average Hamiltonian theory, where the time-dependent system Hamiltonian is expressed as a series of time-independent Hamiltonians:[123]

$$\bar{\mathcal{H}} = \overline{\mathcal{H}^{(1)}} + \overline{\mathcal{H}^{(2)}} + \overline{\mathcal{H}^{(3)}} + \cdots \tag{Eq. 1-11}$$

where the first three terms of the series expansion are given by:

$$\overline{\mathcal{H}^{(1)}} = \int_0^1 d\tau_1 \, \mathcal{H}(\tau_1) \tag{Eq. 1-12}$$

$$\overline{\mathcal{H}^{(2)}} = \frac{1}{\nu_r} \frac{-i}{2} \int_0^1 d\tau_2 \int_0^{\tau_2} d\tau_1 [\mathcal{H}(\tau_2), \mathcal{H}(\tau_1)] \tag{Eq. 1-13}$$

$$\overline{\mathcal{H}^{(3)}} = \frac{1}{\nu_r^2} \frac{-1}{6} \int_0^1 d\tau_3 \int_0^{\tau_3} d\tau_2 \int_0^{\tau_2} d\tau_1 \left[\mathcal{H}(\tau_3), [\mathcal{H}(\tau_2), \mathcal{H}(\tau_1)] \right] + \left[[\mathcal{H}(\tau_3), \mathcal{H}(\tau_2)], \mathcal{H}(\tau_1) \right]. \tag{Eq. 1-14}$$

In these equations, the rotor period is $\tau_r = 1/\nu_r$ and the normalized times τ_i correspond to t_i/τ_r. For the term $\overline{\mathcal{H}^{(1)}}$ only the isotropic contribution remains after integration over one rotor period (the dipolar Hamiltonian is 0 at the magic angle). To higher-order, $\overline{\mathcal{H}^{(2)}}$ and $\overline{\mathcal{H}^{(3)}}$, the dipolar terms do not vanish, but they do scale inversely with spinning frequency (as $1/\nu_r$ and $1/\nu_r^2$), becoming less and less important as the spinning frequency is increased. The second order term is usually the dominant contribution, and the residual dipolar couplings can be approximated to scale as $1/\nu_r$.[124-125]

The bottom line is that higher-order terms remain in the average Hamiltonian under MAS, and maintain the possibility of polarization exchange. If the broadening of states is large enough to cause an overlap between two resonances with different chemical shifts, then the flip-flop is energy conserving and spin diffusion can still occur. This is often the case for protons and spin diffusion can be observed even at $\nu_r \approx$ 100 kHz, because the residual dipolar couplings are still large enough and the chemical shift differences are relatively small.[125]

1.3.2 Rate of spin diffusion

Transfer of polarization by spin diffusion behaves very similarly to a thermal diffusion process, and the use of a diffusion equation is therefore a well-established way to describe polarization transfer.[119, 126] For a three-dimensional case, the diffusion of magnetization through space can be written as:

$$\frac{\partial M}{\partial t} = D\Delta M \tag{Eq. 1-15}$$

where D is the diffusion coefficient and ΔM is the Laplacian of the magnetization. The diffusion coefficient is a symmetrical second rank tensor, which depends on the angles between the principal axes of the tensor in the crystal and the external field. However, in cubic single crystals, D is reduced to a scalar (0th order tensor, a single number) and can be approximated as:

$$D \approx W r^2 \tag{Eq. 1-16}$$

where W is the probability of a flip-flop transition (per unit time) and r is the distance, as discussed before. This approximation also holds for polycrystalline samples or powders.[127] The diffusion coefficient gives information about how fast magnetization is transported through space, and will hereafter be given in units of $nm^2 s^{-1}$. Diffusion equations can be used to simulate polarization transfer, and this will be the subject of Section 1.3.5.

Going back to the energy conserving flip-flop transitions, the rate of spin diffusion depends on how likely it is that a transition happens. The probability of a transition between two nuclei, j and k, with effective Larmor frequencies ω_j and ω_k, can be given by:

$$W_{jk}(t) = \frac{1}{2}\pi f_{jk}(0)d_{jk}^2 t$$

(Eq. 1-17)

where d_{jk} is the dipolar coupling constant, and $f_{jk}(\omega)$ corresponds to normalized zero-quantum spectrum, centered at the difference in frequency between j and k $(\omega_j - \omega_k)$. These factors are important in determining the efficiency of spin diffusion. The equation is a result from perturbation theory, derived from Fermi's golden rule.[7, 128] In the case of spin diffusion, the time-independent perturbation is the dipolar coupling Hamiltonian which generates the magnetization transfer. W is then the probability that a transition has been made from the initial state to the final state at a time t. The zero-quantum lineshape is determined by couplings of the transitioning spin pair to other nuclei in the system. As an example, for a pair of ^{13}C nuclei in an organic solid, the ZQ lineshape is centered at the chemical shift difference of the two ^{13}C nuclei, and has a width corresponding to the average heteronuclear ^1H-^{13}C couplings (which are not mediating spin diffusion themselves). This describes proton-driven spin diffusion, which was briefly mentioned in the previous section. In the case of ^1H spin diffusion, a similar analogy can be found by splitting the homonuclear interactions into two categories: the interaction between the two spins that exchange magnetization through a flip-flop, and the dipolar interactions with all of the other spins with the two spins who flip. This allows the system to be treated with perturbation theory.[128]

Although the dipolar coupling, d_{jk}, is the interaction driving spin diffusion, the zero-quantum lineshape $f_{jk}(\omega)$ moderates the spin diffusion process. It is centered at the value of the chemical shift difference $(\omega_j - \omega_k)$, but the intensity relevant to spin diffusion is always the intensity at frequency 0 (Equation 1-17). This means that the lineshape needs to be relatively broad in order to have considerable intensity at 0. However, the area under the ZQ line is conserved, so when the breadth of the spectrum is increased, the intensity at 0 decreases. These conflicting requirements are shown schematically in Figure 1-14.[111]

Suter and Ernst calculated an approximate value for the zero-quantum relaxation time, which can be used to estimate the intensity of the normalized ZQ line.[121] Assuming a mono-exponential decay of the ZQ line, the intensity of the normalized Lorentzian ZQ line at frequency 0 can be calculated with:

$$f(0) = \frac{1}{\pi}\frac{1/T_2^{ZQ}}{\left(\omega_j - \omega_k\right)^2 - \left(1/T_2^{ZQ}\right)^2}$$

(Eq. 1-18)

where T_2^{ZQ} is the zero-quantum relaxation time. The probability of transition increases with increasing ZQ line width and $f(0)$ reaches its maximum value when the width of the ZQ line is equal to the chemical shift difference.[111] (Note that assuming a Lorentzian lineshape is an approximation.[129])
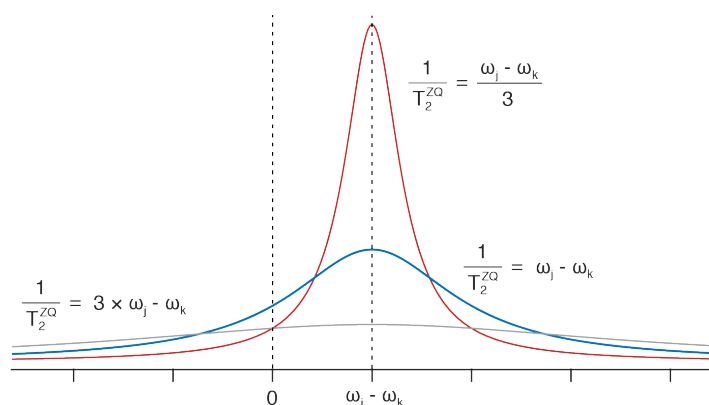
Figure 1-14. Normalized zero-quantum lineshapes of the spins j and k, for three different line widths. All the Lorentzian lines are centred at the difference in frequency, $\omega_j - \omega_k$. The efficiency of spin diffusion is determined by the intensity at 0. Figure adapted from reference[111].

Under magic-angle-spinning, the zero-quantum lineshape function is expected to scale inversely proportional to the spinning frequency, with the linewidth decreasing while the area stays constant.[124, 130] This behavior of the ZQ linewidth is expected to be the same as in the case of a single quantum line.[11] The overall scaling of W (and D) can therefore be expected to scale inversely with spinning frequency as $1/\nu_r$, leading to a slowing of spin diffusion with increased MAS frequencies.[131-133] It should be noted that other factors can also influence the rate of diffusion under MAS, including heteronuclear couplings,[121-122, 130, 134] and scalar couplings[130, 135]. While these interactions usually tend to further reduce the diffusion coefficient, they can also drive spin diffusion in some cases. Interactions that are time-dependent under MAS can interfere with the averaging of the homonuclear dipolar coupling, which may cease to be inhomogeneous even for a pair of like spins. The situation of rotor-driven spin diffusion[130, 136] by rotational resonance[137-138] is an example of this. Of note is the phenomenon of *n = 0* rotational resonance,[120, 139] where homonuclear spin diffusion between chemically equivalent sites, differing only with respect to the orientation of their shielding tensors, remains significant under MAS as the time-dependence of the instantaneous chemical shifts provides a mechanism of efficient spin exchange. In summary, the effect of MAS depends on many factors, and while it will often considerably reduce spin diffusion rates, in some cases, the overall rate of spin diffusion can be enhanced by MAS.[139-140]

1.3.3   Estimating spin diffusion coefficients

In some cases, it can be useful to relate the diffusion coefficient directly to internuclear distances or concentrations. Khutsishvili showed that for a pair of neighbouring spin-½ nuclei, j and k, separated by a distance r_{jk} in a cubic lattice, the probability per unit time of a mutual flip-flop transition is approximated as:[127]

$$W_{jk} = \frac{1}{8\sqrt{2}}\hbar^2\gamma^4 r_{jk}^{-6}(1 - 3\cos^2\theta_{jk})^2 T_2^{ZQ} \qquad \text{(Eq. 1-19)}$$

where T_2^{ZQ} is the zero-quantum relaxation rate as mentioned before and θ_{jk} is the angle between the internuclear vector and the external magnetic field. The transition rate W_{jk} depends inversely on the internuclear distance as r^6. It can be noted that this significant distance dependence means that the majority of flip-flop transitions occur between nearest neighbours, which justifies the use of diffusion equations. T_2^{ZQ} can be related to the distance between the two spins based on Van Vleck's theory of line widths in a rigid lattice. For a cubic crystal with a Gaussian lineshape, consisting of only identical spins:

$$T_2^{\text{ZQ}} = A \frac{r^3}{\hbar\gamma^2} \qquad \text{(Eq. 1-20)}$$

where A depends on the type of cubic lattice (A = 0.65 for primitive and A = 0.49 for body-centered or face-centered cubic lattices).[127] Making use of this approximation (and recalling that $D \approx Wr^2$) , we find that D scales with γ and r as:

$$D \propto r^{-1}\gamma^2 \qquad \text{(Eq. 1-21)}$$

The expression in Equation 1-20 can be used to relate the diffusion coefficient to the concentration of magnetically active nuclei in a given sample. The average distance between spins in a given volume can be approximated using the Wigner-Seitz radius, which is the radius of a sphere whose volume is equal to the mean volume per atom in a solid:[107]

$$r = 2 \times \sqrt[3]{\frac{3}{4\pi c N_A}} \qquad \text{(Eq. 1-22)}$$

where c is concentration and N_A is Avogadro's number. A modified Equation 1-21 can thus be written as:

$$D \propto \sqrt[3]{c}\gamma^2 \qquad \text{(Eq. 1-23)}$$

Using Equation 1-23 for scaling, the unknown diffusion coefficient in a compound of interest can be estimated from a measured value for a different nucleus. Figure 1-15 shows the estimated diffusion coefficients as a function of concentration, and dipolar couplings as a function of internuclear distance (in the same way as in Figure 1-12), for several different magnetically active nuclei. The diffusion coefficients are scaled from a measured value of ^{19}F diffusion in a static single crystal of CaF_2.[141] Furthermore, the graph shows the value of D for several inorganic compounds, which will be studied in Chapter 3.
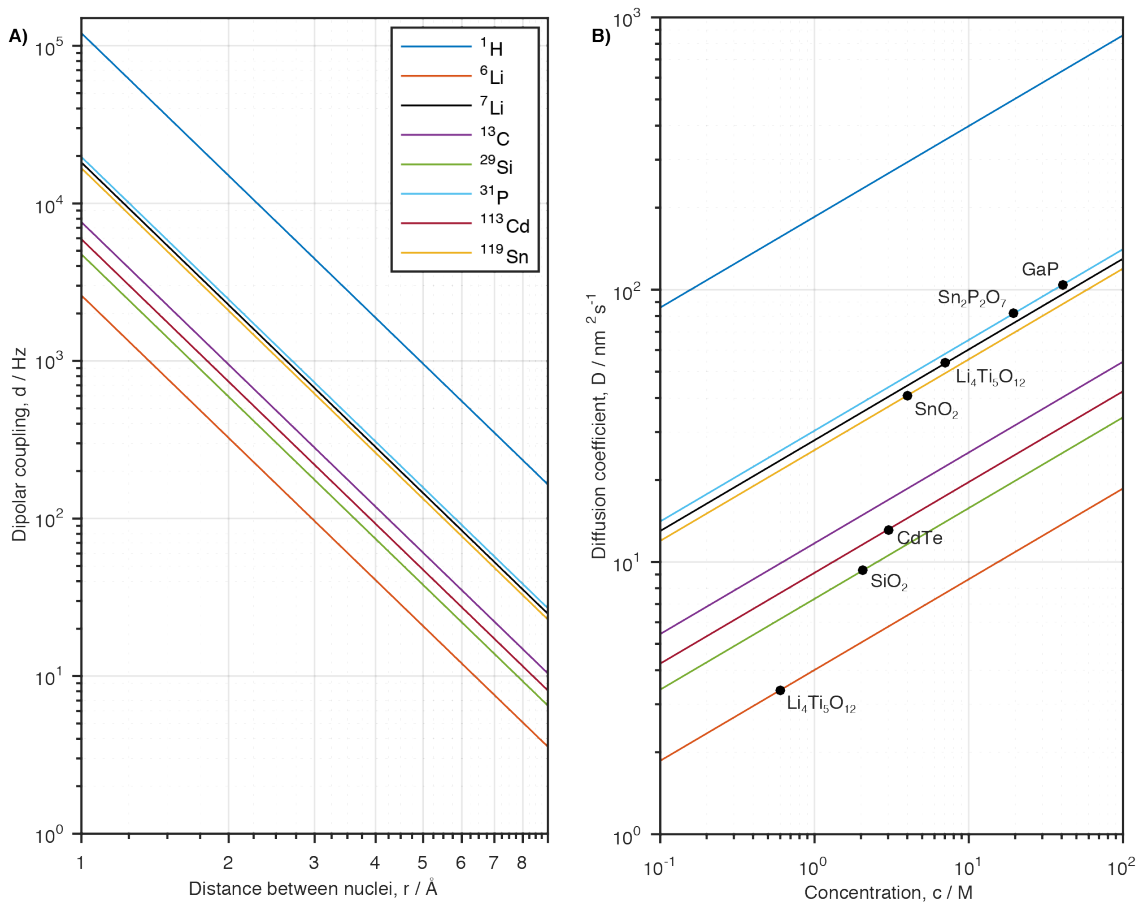
Figure 1-15. A) Dipolar coupling strength as a function of distance between two nuclei. B) Estimated diffusion coefficients as a function of concentration scaled from a measured value as explained in the text.

These estimates of D are approximations based on a diffusion coefficient measured in a non-spinning sample. As mentioned before, spin diffusion will slow down under MAS as approximately $1/\nu_r$.[122, 130, 133, 135] This is mainly due to the modulation of the dipolar couplings and the ZQ lineshape under MAS, as mentioned in the previous sections.

The spin diffusion coefficient provides information about the rate of magnetization transfer in a given system. In practice, the distance that the magnetization can travel depends on how much time is available for spin diffusion. The upper limit of that time period is related to the longitudinal relaxation time of the sample. It can therefore be useful to introduce the spin diffusion length for a three-dimensional object as $\sqrt{DT_1}$. Figure 1-16 shows how far magnetization can travel as a function of the time allowed for diffusion, and underlines the fact that even when spin diffusion coefficients are low, significant diffusion length can be reached if the relaxation rate of the sample is long enough.

Figure 1-16. Diffusion length as a function of time, plotted on A) linear and B) logarithmic scale.

1.3.4 Assisted spin diffusion

Spin diffusion is sometimes divided into two categories, spatial spin diffusion and spectral spin diffusion. Spatial spin diffusion was described in the previous section, as a process where a non-uniform spatial distribution of magnetization is introduced and then spin diffusion spontaneously equalizes it throughout the system. This process is energy conserving and the lattice does not participate. Spectral spin diffusion, on the other hand, is the flow of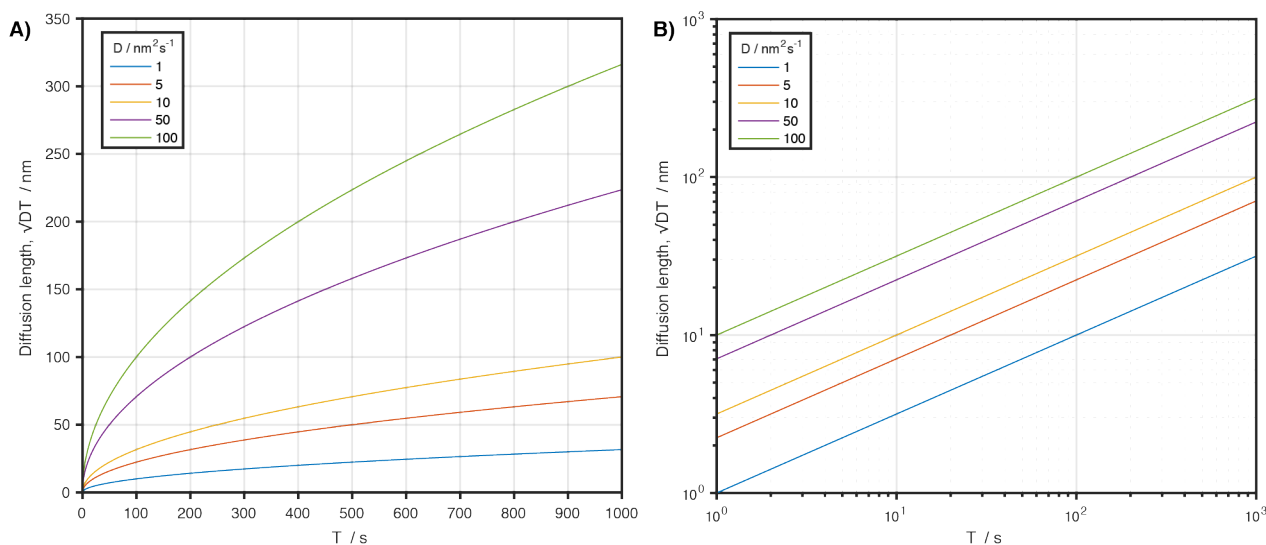 magnetization between nuclei that have different resonance frequencies. Spectral spin diffusion requires the participation of the lattice, as the elementary flip-flop transition itself is not energy conserving. In this case, energy can be added to the system in order to drive spin diffusion, and real systems can show aspects of both types of spin diffusion.[111, 121] Proton-driven spin diffusion (which was introduced in Section 1.3.1) is an example of this, where the energy for a flip-flop process is supplied by heteronuclear couplings to other nuclei. In other cases, energy can be added more explicitly to the system, and a brief overview of two such techniques is given below.

Radio-frequency (rf) driven spin diffusion is one way of supplying energy to the system in order to speed up spin diffusion. This is achieved by spin-locking the magnetization along the rf field, which removes chemical shift terms in the effective Hamiltonian, and makes flip-flop transitions more likely. If the chemical shift differences are small, a continuous wave rf field can be applied, but when the differences are larger multiple pulse schemes are used.[142] This resembles cross polarization (CP), where the dipolar couplings are exploited to transfer magnetization between heteronuclei. In rf driven spin diffusion of dilute spins, the spin-lock field scales the chemical shift differences of the coupled spins mediating polarization exchange to zero and decouples them from any abundant spins (such as ^{1}H). This leads to a significant increase in the rate of spin diffusion.

Another way of supplying energy for the flip-flop process is by mechanical rotation of the sample about the magic angle. This is called rotor driven spin diffusion, and only occurs when the frequency of rotation is an integer multiple of the difference of the isotropic chemical shifts of the two spins. Rotor driven spin diffusion is selective, as only the spins which satisfy this condition (with a chemical shift difference matching the MAS frequency) undergo polarization exchange, with the strongest recoupling observed for n = ±1 and ±2. [136-138]

1.3.5 Modelling spin diffusion

Spin diffusion models were originally developed to explain unexpected values of longitudinal relaxation in crystalline solids[119], but have since then been applied in other areas of solid-state NMR, for example to estimate

sizes of particles and domains.[115] This is usually done by selectively generating a non-equilibrium magnetization in a part of the sample, and observing its return back to equilibrium.

Spin diffusion is also important in dynamic nuclear polarization, as it is responsible for distributing hyperpolarization from nuclei in direct contact with the polarizing agent, to all other nuclei in the sample. This was introduced in Section 1.2.4, and can be especially important in systems where the radical polarizing agents are spatially separated from the nuclei of interest (and the hyperpolarization needs to cross an interface).[38] In general, ^{1}H spin diffusion is always present systems which contain protons, and even remote nuclei can be efficiently hyperpolarized by relay due to the relatively dense network of dipolar couplings.

Models of ^{1}H spin diffusion in DNP, both numerical and analytical, can help with the understanding of the different factors which modulate the obtained DNP enhancements in systems where there is hyperpolarization relay.[106-107, 109] For a DNP sample, such as a particle coated with a radical containing solution, high polarization is generated near the polarizing agents, and spin diffusion then acts to equalize polarization throughout the sample. This process can be described with a differential equation:[109]

$$\frac{\partial P(x,t)}{\partial t} = D(x) \cdot \Delta P - \frac{P(x,t) - P_0(x)}{T_1(x)}$$

(Eq. 1-24)

where x is the position relative to the interface between the radical solution and the particle and t is time. D is the rate of diffusion, and ΔP is the Laplacian of the polarization (which depends on symmetry). T_1 is the longitudinal relaxation time, P is the instantaneous polarization at the given position and time, and P_0 is the equilibrium polarization at position x, which corresponds to polarization in the absence of spin diffusion. Without DNP, P_0 has the same value everywhere in the sample, it corresponds to the Boltzmann polarization and is assigned a value of 1. DNP creates a non-uniform spatial distribution of equilibrium polarization, where the value of P_0 in the radical solution is high ($P_0 = \varepsilon_0$), while inside the analyte it still has a value of 1. Spin diffusion will then act to equalize the polarization in the sample.

An analytical expression for enhancements in relayed DNP was obtained by the Griffin group.[109] The expression assumes a one-dimensional symmetry under steady-state conditions, where $\partial P(x,t)/\partial t$ = 0 for long t:

$$\varepsilon = \varepsilon_0 \frac{2\sqrt{DT_1}}{w} \tanh\left(\frac{w}{2\sqrt{DT_1}}\right).$$

(Eq. 1-25)

In this equation, ε is the integrated DNP enhancement inside of the remotely polarized 1D region and w is the width of that region. ε_0 is the enhancement at the surface, corresponding to the enhancement in the radical solution, which is outside of the remotely polarized region. This equation can be used, for example, to predict the enhancement inside crystals that have different values of T_1. For constant values of D, w and ε_0, the model predicts that the enhancement inside the crystal, ε, increases with slower relaxation rates. Although this equation can be useful for estimating the magnitude of DNP enhancements, it assumes a 1D symmetry which might not always be applicable.

For a three dimensional spherical particle the diffusion equation does not have an analytical solution, but can be solved numerically to determine $P(x,t)$.[106] This method was first used to obtain information about enhancements, signal-build-up behaviour, and relaxation in microcrystalline solids coated with a radical-containing solution. Since DNP samples contain free organic radicals, recovery of longitudinal magnetization is not usually given by the intrinsic T_1 of the material.[143] The effective build-up time measured in a DNP sample is called T_B, and it is typically shorter than T_1, which in itself is an additional source of increased sensitivity for DNP enhanced solid-state NMR experiments (see Section 1.2.3). The nuclei that are at the surface of the microcrystals, in proximity to the

paramagnetic species, have a short T_B, due to paramagnetic relaxation. The T_B then increases as a function of distance from the surface, until it reaches an upper limit given by the intrinsic T_1 of the material. Solids that are surrounded by a radical-containing solution therefore exhibit a distribution of longitudinal relaxation rates, and their recovery back to equilibrium can be described as a stretched exponential:[144]

$$M_z(t) = M_\infty \left[1 - e^{-\left(\frac{t}{T_B}\right)^\beta} \right]$$

(Eq. 1-26)

where the stretching factor, β, takes a value between 0 and 1. A difference in the polarization build-up behaviour of the material with and without microwave irradiation can confirm the presence of ^{1}H spin diffusion in the system. This is shown schematically in Figure 1-17, where a neat sample without radicals exhibits mono-exponential build-up behaviour, whereas the DNP sample, wetted with a radical containing solution, has a shorter apparent relaxation rate, T_B. The difference between T_B with and without microwave irradiation can be explained by that when the P_0 at the particle surface is high (microwaves on) it accelerates the diffusion of polarization into the particles, and appears as if the T_B is shorter. This difference in build-up behaviour with and without microwaves leads to a difference in the DNP enhancement as a function of time, as seen in Figure 1-17B. This behaviour can be reproduced with the spin diffusion models introduced earlier.
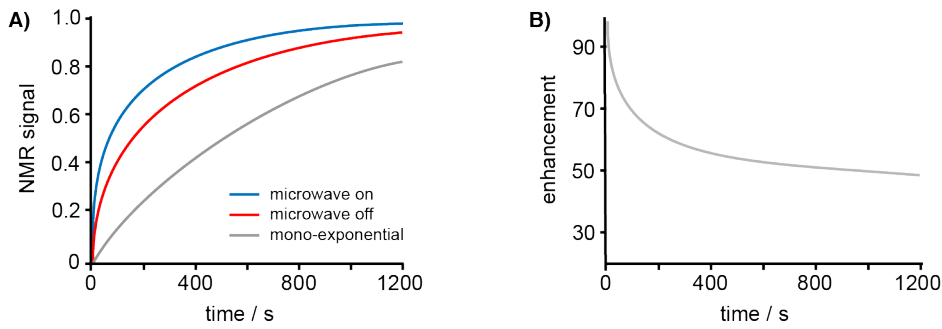

Figure 1-17. Predicted signal build-up rates for spherical particles, obtained by numerically solving the diffusion equation. A) Normalized NMR signal as a function of polarization time for intermediate size crystals (radius under 10 µm) with a T_1 of 700 s. The proton polarization at the crystal's surface was assigned values of $T_B = 1$ ms and $P_0 = \varepsilon_0 = 100$ under DNP. A mono-exponential signal build-up for $T_1 = 700$ s is shown for comparison. B) Calculated signal enhancement of the spherical particle as a function of polarization time. Adapted from reference[106].

The model predicts that polarization builds up faster in small particles than in larger ones, leading to higher enhancements.[106, 108] It should be noted that when the size of the polarized domain is small, spin diffusion is efficient enough to equalize the polarization of all the nuclei in the domain. This is for example the case for frozen radical-containing solutions, which usually have a mono-exponential build-up time which does not change upon microwave irradiation (in this case the solution is considered to be the target material). A phenomenological relationship between steady-state enhancement and the size of a spherically symmetric particle has been described:

$$\varepsilon_\infty = 1 + (\varepsilon_0 - 1) \frac{\sqrt[3]{DT_1}}{R} \left[\coth\left(\frac{R}{\sqrt{DT_1}}\right) - \frac{\sqrt{DT_1}}{R} \right]$$

(Eq. 1-27)

where R is the radius of the particle, ε_∞ is the DNP enhancement at steady-state, and ε_0 is the enhancement of the polarization source (the radical containing solution). Similarly, expressions for determining domain sizes in linear and cylindrical objects were also described.[107]

Spin diffusion models will be used throughout this thesis to support observations of spin diffusion.

1.4 Thesis outline

This chapter has provided a brief introduction to MAS DNP of materials and how sensitivity in solid-state NMR has improved significantly over the past years. It also introduced the basic principles of spin diffusion, and the role of spin diffusion in DNP experiments. Although DNP has proven to provide signal enhancements for a range of materials, there is still room for improvement. Notably, NMR of proton-free bulk materials remains challenging, especially when nuclear relaxation times are long (which can also be true for rigid organic solids). Consequently, many NMR studies of inorganic materials resort to isotopic enrichment to increase the number of magnetically active nuclei in the sample, or to doping with paramagnetic species to enhance nuclear relaxation rates.

The work presented in this thesis aims to improve sensitivity in DNP enhanced solid-state NMR experiments, and to extend the application of DNP to systems that are currently difficult to access. Specifically, the main goal was to develop a general method to hyperpolarize the bulk of inorganic materials.

Chapter 2 shows how sensitivity in relayed DNP of organic microcrystalline solids can be improved by revisiting an old trick which allows ^{1}H magnetization to be recycled more frequently. The classic flip-back method to recover bulk proton magnetization is combined with DNP and demonstrated to improve sensitivity in compounds with characteristic build-up times spanning two orders of magnitude: a bulk BDPA radical doped *o*-terphenyl glass and microcrystalline samples of theophylline, L-histidine monohydrochloride monohydrate, and salicylic acid, each impregnated by incipient wetness. For all of these systems, addition of flip-back is simple, improves the sensitivity beyond that provided by modern heteronuclear decoupling methods such as SPINAL-64, and provides optimal sensitivity at shorter recycle delays. The approach is especially efficient for solids that have long ^{1}H longitudinal relaxation rates. Overhauser effect DNP enhancements of over 70 at 21.1 T are also reported.

In Chapter 3, a method where dynamic nuclear polarization is used to hyperpolarize the bulk of proton-free solids is introduced. The hyperpolarization is generated in a wetting phase, transferred to nuclei near the surface and then relayed towards the bulk through homonuclear spin diffusion between weakly magnetic nuclei. This is achieved either through direct hyperpolarization or with a multiple contact cross-polarization method, where hyperpolarization is transferred from protons to heteronuclei at particle surfaces. The method is shown to increase the sensitivity in bulk spectra of powdered inorganic compounds, as an example providing a factor of 50 gain in overall sensitivity for the ^{119}Sn spectrum of powdered SnO$_2$. The method is also applied to ^{31}P spectra of GaP, ^{113}Cd spectra of CdTe, ^{29}Si spectra of α-quartz, and $^{6/7}$Li spectra of lithium titanates. The multiple contact cross polarization method is discussed in more detail in Section 3.2, and experimental optimization of the pulse parameters and delays is used to maximize its sensitivity on a sample of powdered SnO$_2$. In particular, an approach is introduced where the magic angle spinning rate is modulated during the experiment: the CP contacts are carried out at a slow spin rate to benefit from faster spin diffusion, and the spin rate is then accelerated before detection to improve line narrowing. The last part of the chapter, Section 3.4, shows how two-dimensional spin diffusion experiments can be used to gain insight into the pathways of spin diffusion from the surface of a material towards the bulk.

In Chapter 4, the role of higher fields and faster MAS rates in DNP are discussed and the very first DNP experiments using a 0.7 mm MAS probe are presented. At a magnetic field of 21.1 T, the polarizing agent HyTEK-2 provides DNP enhancements as high as 200 at a spinning rate of 65 kHz at 100 K, and BDPA yields an enhancement of 106 under the same conditions. Fast spinning rates also yield unprecedented ^{1}H resolution under DNP conditions, and resolved DNP enhanced ^{1}H detected ^{1}H-^{13}C and ^{1}H-^{15}N correlation spectra of microcrystalline histidine are presented.

Chapter 5 contains a summary of the presented results, as well as a general conclusion.

Chapter 2   Organic solids

2.1   DNP enhanced NMR with flip-back recovery

This chapter has been adapted with permission from: *"DNP enhanced NMR with flip-back recovery"*. S. Björgvinsdóttir, B.J. Walder, A.C. Pinon, J.R. Yarava, L. Emsley, *Journal of Magnetic Resonance* **2018,** 288, 69-75. (post-print)

2.1.1   Introduction

Cross-polarization magic angle spinning (CP MAS) NMR is the cornerstone experiment in solid-state NMR.[14-15] The sensitivity of conventional CP MAS experiments depends on the proton spin-lattice relaxation time, as it is the proton spin reservoir from which the rare nuclei draw their polarization. Many organic solids, however, have long proton spin-lattice relaxation times, which for rigid compounds can approach one hour. When combined with the low natural abundance and gyromagnetic ratio of important rare nuclei such as ^{13}C and ^{15}N this severely limits the sensitivity of CP MAS experiments, as mentioned in Section 1.1.1. The acquisition of one-dimensional spectra with usable signal-to-noise ratios is particularly difficult in such cases, and multi-dimensional experiments are usually precluded.

In the early days of CP, resolution of the rare spin spectrum was improved by decoupling using spin locking of the proton magnetization during acquisition with a high power "continuous wave" (cw) rf field.[14] After acquisition, a significant fraction of the original proton magnetization remained, dephasing only upon release of the spin locking field. Since the very inception of cross-polarization, it was recognized that the residual proton magnetization could be further utilized to improve the signal-to-noise ratio of the rare spin spectrum, and to this end strategies such as multiple contact/acquisition schemes were proposed.[14] The method of using a $\pi/2$ pulse to return the residual proton magnetization to the *z*-axis after acquisition to allow a shorter recovery period was introduced by Tegenfeldt and Haeberlen in 1979.[145] Owing to its facile implementation, use of this flip-back recovery method increased throughout the subsequent decades, with examples including work on zeolites[146], bacteriorhodopsin[147] and multidimensional ^{13}C tensor correlation experiments on saccharides.[148-149]

With the introduction of TPPM decoupling in 1995,[150] followed by other modern heteronuclear decoupling methods such as SPINAL-64[151] it became more difficult to lock the proton magnetization during decoupling,[152] and the flip-back experiment largely fell into disuse. However, the flip-back pulse element remains essential to schemes such as those used in quantitative cross-polarization methods,[153] RELOAD-CP,[154] dissolution DNP,[155] and the suppression of water signals in solution NMR.[156] Recently, classic flip-back has been shown to be useful in the context of fast MAS, where efficient heteronuclear decoupling at sample rotation rates >50 kHz can be provided by low power cw spin locking fields.[157-158]

Solid-state magic-angle-spinning dynamic nuclear polarization (DNP) can provide exquisite enhancements in overall sensitivity for a range of materials from frozen solutions to microcrystalline powders.[101, 105-106, 159] Most strategies involve the generation of hyperpolarization close to a radical source and transportation of this polarization to the target substrate by spontaneous proton spin diffusion (see Section 1.2.4).[39, 107] This is followed by conventional cross-polarization transfer of the enhanced proton polarization from the proton bath to the rare spins. For example, the use of incipient wetness impregnation DNP for microcrystalline systems can enhance the sensitivity of CP MAS experiments by factors of 100 or more at temperatures of 100 K.[106] However, since the

polarization must be transported, the overall sensitivity of relayed DNP experiments is throttled by the long build up times needed to optimize sensitivity.

Here we show that flip-back methods can significantly improve the overall sensitivity of MAS DNP experiments.

2.1.2   Experimental methods

Salicylic acid, L-histidine monohydrochloride monohydrate and theophylline were obtained from Sigma Aldrich. The samples were ground by hand with a mortar and pestle for 5 minutes and subsequently wetted with a 16 mM solution of TEKPol[58] in 1,1,2,2-tetrachloroethane (TCE),[84] which dissolves the radical but is a non-solvent for the powders.[101] The formulation ratio was 10 μL of radical solution to 40 mg of powdered solid. The wet powder was packed in a 3.2 mm sapphire rotor and centered with a polytetrafluoroethylene insert.

All experiments on microcrystalline samples were performed on a widebore 9.4 T Bruker Avance III solid-state NMR spectrometer coupled with a 263 GHz microwave source.[42] The samples were spun in a 3.2 mm low-temperature MAS probe at a rate of 12.5 kHz at temperatures near 90 K. To improve enhancements, the samples were deoxygenated with three thawing cycles by repeated ejection and insertion of the sample in the NMR probe.[160] Polarization enhancement factors of the TCE protons were estimated from comparing proton spectra at a 5 s recycle delay with and without microwave irradiation, indicating enhancements over 200 for L-histidine monohydrochloride monohydrate and salicylic acid. The enhancement of the theophylline system could not be estimated in this way because of substantial recovery of the theophylline protons due to their short intrinsic proton T_1. On the basis of CP spectra with and without microwave irradiation (Figure 2-8 in Appendix I), the TCE enhancement of the theophylline system is similar to that of the other two microcrystalline systems.

BDPA (α,γ-bisdiphenylene-β-phenylallyl) was obtained from Sigma Aldrich and dissolved in partly deuterated ortho-terphenyl (95:5 OTP-d$_{14}$:OTP). The resulting 75 mM solution was melted in a 3.2 mm rotor, topped with a polytetrafluoroethylene insert and rapidly inserted into a cold NMR probe.

Overhauser effect DNP experiments[19] on BDPA in OTP[161] were carried out at 21.14 T using a Bruker Avance Neo spectrometer. The frequency of the microwave beam could be lowered to reach the Overhauser effect condition from the optimum binitroxide cross effect condition by changing the temperature of the resonant cavity (Figure 2-10 in Appendix I). The OTP sample was spun at a rate of 12.5 kHz in a low-temperature MAS probe. The signal enhancement factor, ε_C, as indicated by the ratio of signal with and without microwave irradiation was 73 (Figure 2-9 in Appendix I).

Unless otherwise specified, a 93 kHz radio-frequency field amplitude was used for the heteronuclear decoupling fields. For XiX decoupling[162] the pulse widths used were 640 μs. CP contact time was 2 ms for the microcrystalline solids and 4 ms for the OTP glass. The ^{1}H rf field amplitude was ramped from 90% to 100% during CP for all compounds. The acquisition time for the microcrystals was 26 ms and 4 ms for the OTP system. In order to reach a steady state condition, a number of dummy scans, roughly equal to 10% of the scans used during data accumulation, were implemented for the flip-back experiments. The experiments were performed in order of high to low values of recycle delay, further minimizing the change in steady state condition between consecutive experiments.

For the INADEQUATE experiments, 20 complex t_1 points at an indirect sampling interval of Δt_1 = 0.16 ms were acquired at effective 512 scans each for a total experiment time of ~14 h. A 150 kHz radio-frequency field amplitude was used for decoupling.

We simulate the diffusion of polarization from the impregnating solution to the microcrystal using numerical simulations as described in detail elsewhere.[107] The resulting polarization is integrated over the microcrystal

volume. The polarization is then scaled by the retention factor and propagated again during the subsequent polarization period. This procedure is repeated for the number of experimental scans. The resulting accumulated signal is then scaled by the number of loops, and by the square root of time, to obtain a sensitivity curve as a function of the recycle delay. This procedure is repeated for all recycle delays, numbers of scans, and the only variable parameter between the "with flip-back" case and "without flip-back" case is the retention factor.

2.1.3   Results and discussion

The fundamentals of bulk proton magnetization recovery using a flip-back pulse and an excellent overview of the benefits of the sequence were given in the seminal work of Tegenfeldt and Haeberlen.[145] In a thermodynamic framework, the heat capacity of the abundant ^{1}H spin reservoir far exceeds that of the rare ^{13}C spin reservoir, particularly when the latter is present at natural abundance. As CP MAS NMR is usually practiced today, the proton magnetization is destroyed during acquisition by heteronuclear decoupling methods such as TPPM or SPINAL. Consequently, the magnetization must recover over a recycle delay τ_{rd} prior to the execution of the following scan. In a simple exponential model of recovery from zero intensity, the degree to which the magnetization is restored during τ_{rd} is given by

$$M_z(\tau_{rd}) = M_\infty \left[1 - e^{-\frac{\tau_{rd}}{T_B}} \right].$$

(Eq. 2-1)

We introduce the build-up time constant, T_B, in this expression to acknowledge that in DNP the magnetization does not usually recover according to the intrinsic spin-lattice relaxation time, T_1, of the substrate.[143] Only for conventional NMR of a pure solid analyzed in the absence of the exogenous source of polarization, is $T_B = T_1$. This is important, since in many DNP experiments $T_B < T_1$, and this is already a source of increased overall sensitivity for DNP enhanced solid-state NMR experiments.[25, 92, 163]

At temperatures around 100 K or below, where MAS DNP experiments are today most efficient, there is often a more or less pronounced loss in spectral resolution due to freezing out molecular motions.[164-165] The cw method of heteronuclear decoupling can thus often be used with only a modest loss of resolution (*vide infra*). In this case, proton magnetization can be locked during decoupling and is depleted primarily through $T_{1\rho}$ relaxation (and, to a lesser extent, direct polarization transfer to ^{13}C nuclei). Upon flip-back, the longitudinal component of the proton magnetization, M_z, resumes its build up toward M_∞, but at a significant nonzero initial amplitude. Under steady state conditions, this implies that

$$M_z(0) = f_0 \, M_z(\tau_{rd}).$$

(Eq. 2-2)

where f_0, the retention factor, is the ratio of bulk proton magnetization before and after the CP experiment. f_0 is an empirical parameter that depends on many factors in the experiment, including notably $T_{1\rho}$, the efficiency of the pulses, off resonance effects, and the decoupling sequence used. For decoupling methods such as TPPM, f_0 is usually zero, and the initial level of magnetization available for subsequent scans is also zero.

Assuming that the dynamics of CP transfer is independent of f_0 and τ_{rd}, the intensity of the ^{13}C NMR signals will be proportional to M_z. For a fixed experiment time, not only will the steady state value of M_z vary as a function of τ_{rd}, but the number of scans and hence the signal that is accumulated will be inversely proportional to τ_{rd}. The noise level of the final accumulated spectrum is inversely proportional to the *square root* of τ_{rd}. Thus, in consideration of these effects, we arrive at the following equation for expressing the experimental sensitivity for a monoexponential model of magnetization recovery:

$$S_{rel}(f_0, \tau_{rd}) = \frac{A}{\sqrt{\tau_{rd}}} \frac{1 - e^{-\frac{\tau_{rd}}{T_B}}}{1 - f_0 e^{-\frac{\tau_{rd}}{T_B}}},$$

(Eq. 2-3)

where A is a normalization factor such that $S_{rel}\left(0, \tau_{rd}^{(0)}\right) = 1$ with $\tau_{rd}^{(0)} \approx 1.256\, T_B$ which is the recycle delay where S_{rel} is maximized for the case $f_0 = 0$. This corresponds to the case of optimal sensitivity without flip-back. This function is plotted in Figure 2-1B as a function of recycle delay for selected values of f_0. For the case $f_0 = 0$, we see that $S_{rel} \leq 1$ for all values of τ_{rd}, as guaranteed by our choice of normalization. When $f_0 > 0$ sensitivity will be improved for all values of τ_{rd}. The degree of improvement, however, is modest until f_0 approaches unity, as illustrated by the fact that obtaining an 80% improvement in sensitivity over the reference experiment requires f_0 = 0.8, whereas a further improvement to almost 160% over the reference only requires an additional 12.5% increase in f_0 to 0.9. Retaining half the magnetization ($f_0 = 0.5$) only leads to a maximum improvement of 25%. High f_0 values are thus the key to obtaining high sensitivity increase with flip-back.
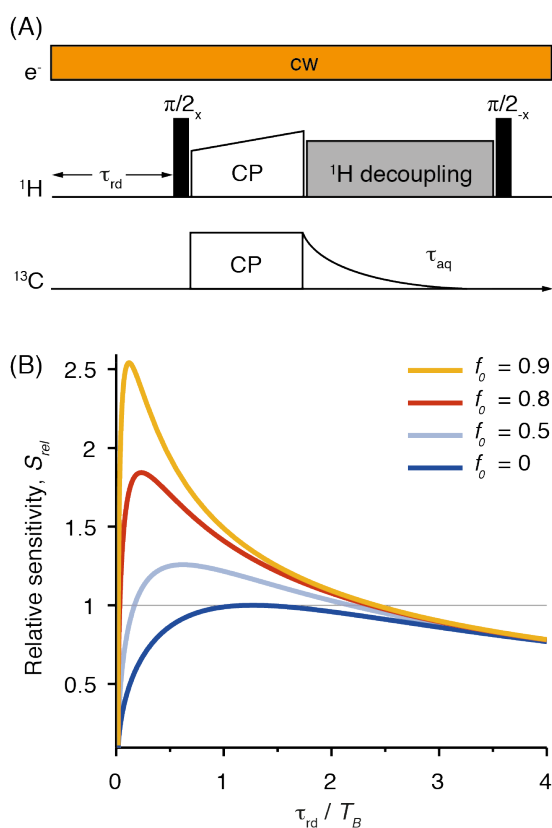
Figure 2-1. A) The ^{1}H-^{13}C CP pulse sequence with flip-back recovery. B) Calculated gain in sensitivity for different values of f$_0$ according to Eq. 2-3. The y-axis is normalized as defined in the text.

In addition to the improvement in sensitivity, another advantage of proton magnetization recovery is that the recycle delay required to optimize the experimental sensitivity, τ_{rd}^*, decreases with increasing f_0. We see from Figure 2-1B that when 90% of proton magnetization can be recovered, $\tau_{rd}^* \approx 0.1\, T_B$, yielding an order of magnitude reduction in optimum recycle time compared to $\tau_{rd}^{(0)}$ for the reference case.

To validate these features, we show results from CP MAS experiments of a frozen solution of BDPA in an OTP glass, enhanced by Overhauser effect (OE) DNP[19, 161] at 21.14 T (the highest field used in DNP to date). The ^{1}H DNP enhancement in this sample is $\varepsilon = 73$. Figure 2-2 shows the sensitivity gains obtained experimentally using cw decoupling and flip-back. The major features predicted theoretically from the simple model of single exponential recovery are all illustrated by the experimental data. The sensitivity is never impaired when the flip-back pulse is

included, no matter the recycle delay. The sensitivity maximum is found to occur at $\tau_{rd}^{*} \approx 0.6\tau_{rd}^{(0)}$ and the maximum sensitivity enhancement due to the recovery is roughly 25%, corresponding to an f_0 value of around 50%. Since the BDPA radical and OTP form a homogenous phase, $T_{1\rho}$ processes are enhanced by paramagnetic relaxation,[166] limiting the overall advantage due to the flip-back recovery. This could in principle be overcome by lowering the concentration of BDPA.
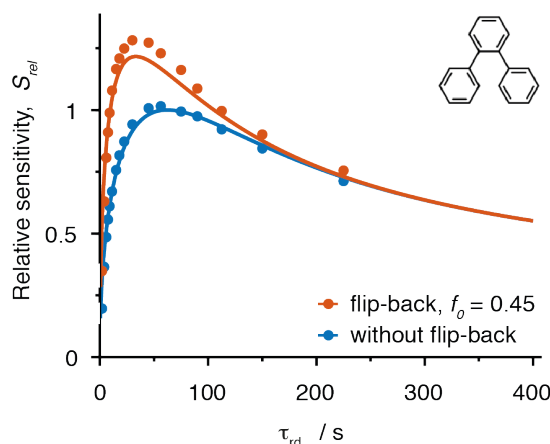

Figure 2-2.Measured sensitivity gains (filled circles) using DNP enhanced flip-back CP MAS on a sample of 95:5 OTP-d_{14}:OTP doped with 75 mM BDPA. Signal intensities from cw decoupled flip-back CP experiments (red dots) are compared to the same experiments without a flip-back pulse (blue dots). The rf field amplitude for decoupling was 100 kHz. The sensitivity is normalized to maximum sensitivity without a flip-back pulse. The curves are fit to the data with a monoexponential recovery model, as explained in the text.

Microcrystalline solids polarized by relay should not suffer from relaxation enhancement by the paramagnetic agent. We therefore investigated three microcrystalline solids enhanced by relayed DNP:[106-107] theophylline, L-histidine monohydrochloride monohydrate, and salicylic acid. The compounds exhibit characteristic build-up time constants ranging over two orders of magnitude from 15 s for theophylline to over 1000 s for salicylic acid. (Note that form II of theophylline used here does not convert under impregnation with TCE).[167] The measured values from a stretched exponential fit are given in Appendix I with the corresponding build up curves (Figure 2-11, Figure 2-12 and Figure 2-13).

The maximum achievable sensitivity is roughly doubled for the theophylline and L-histidine monohydrochloride monohydrate samples, and nearly tripled for salicylic acid (Figure 2-3).

Spin diffusion models have previously shown that the build-up time in impregnated samples depends on several parameters such as the size of the microcrystals, the intrinsic longitudinal relaxation time, or the spin diffusion coefficient. Here the retention of proton magnetization, f_0, depends on position since $T_{1\rho}$ is expected to be different in the impregnating radical solution and in the microcrystal. We have simulated the relayed DNP here with the retention of proton magnetization in the radical solution $f_{0,RS}$ assumed to be 0.5 for all the simulations, and the signal build-up time $T_{B,RS}$ was taken to be 2 s. The enhancement on the radical solution ε_{RS} was assumed to be 280 for each case. We assume the spin diffusion constant in the radical solution to be $D_{RS} = 1.7 \times 10^{-4}$ µm^{2}s^{-1}. The spin diffusion constant within the microcrystals, D_{MC}, is scaled according to the proton concentration, as shown in Table 2-1. Note that $f_{0,MC}$, the retention factor within the substrate, will have an influence on the build-up time of the signal from the microcrystals, and thus on the sensitivity.
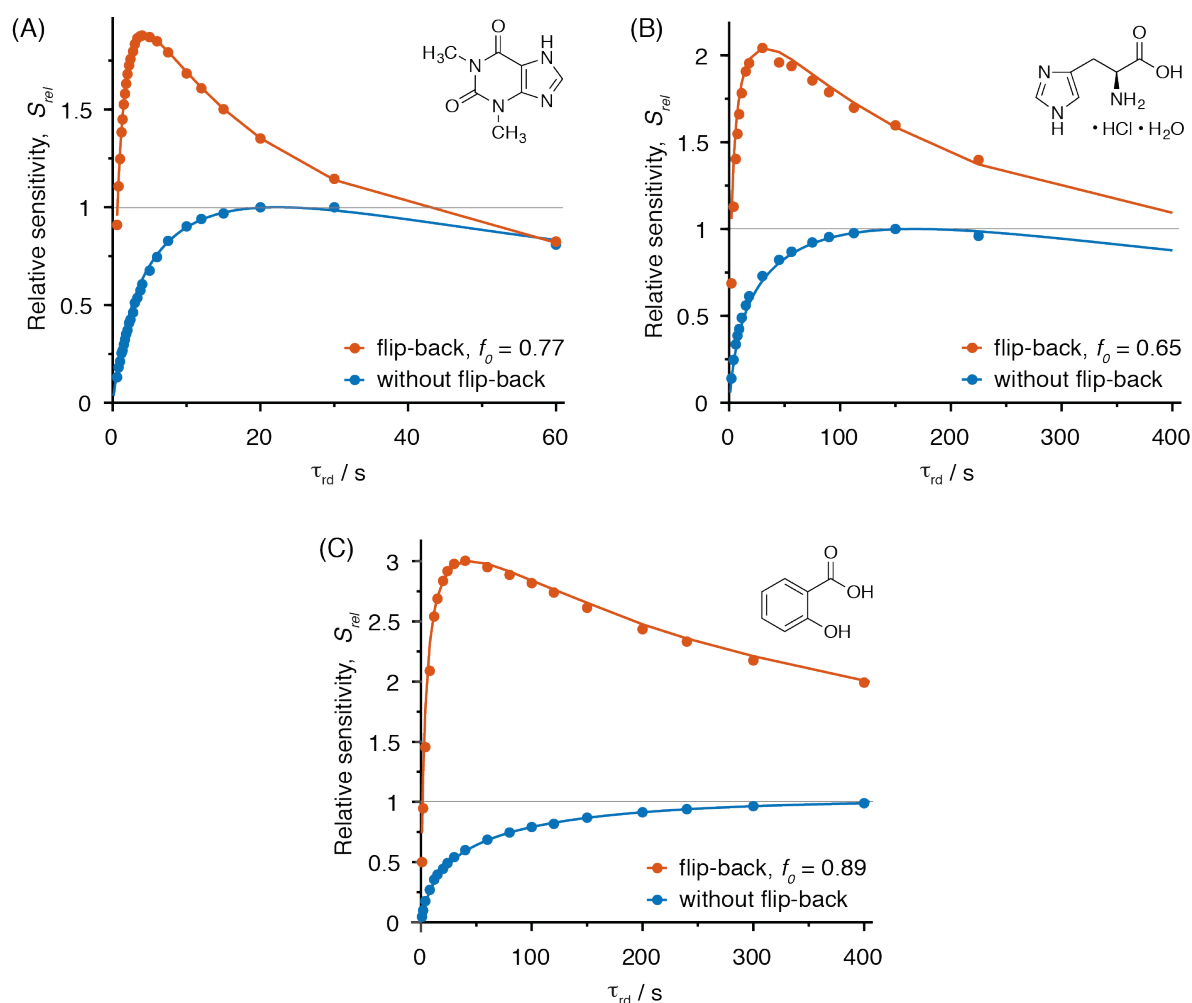
Figure 2-3. Measured sensitivity gains (filled circles) using DNP enhanced flip-back CP MAS on samples of A) theophylline, B) L-histidine monohydrochloride monohydrate, and C) salicylic acid, (using a carbonyl ^{13}C resonance in each spectrum). Data for decoupled CP MAS without flip-back recovery (blue) was acquired for each sample as a sensitivity benchmark. The number of scans were adjusted to preserve a constant total acquisition time between experiments. Dummy scans were used for the flip-back experiment in order to achieve a steady-state polarization prior to each experiment. The solid lines are predictions from numerical simulations for f_0 in the microcrystals according to a diffusion model of polarization transport.[107]

The data are well reproduced with the parameters given in Table 2-1, which lead to the curves shown in the Figures, where L corresponds to the diameter of the spherical particles, D_{MC} is the diffusion rate inside the particle, and $T_{1,MC}$ is the intrinsic longitudinal relaxation time. Note that fits to exponential and stretched exponential recovery models, failed to reproduce the data, as shown in Appendix I.

Table 2-1. Parameters used to reproduce the polarization dynamics shown in Figure 2-3 and Figure 2-5.

	L / μm	D_{MC} / (μm^{2}s^{-1})	$T_{1,MC}$ / s	$f_{0,MC}$
Theophylline	2.4	4.5×10^{-4}	10	0.77
Histidine (cw)	1.4	5.1×10^{-4}	1000	0.65
Histidine (XiX)	1.4	5.1×10^{-4}	1000	0.20
Salicylic acid	3.8	4.3×10^{-4}	80000	0.89

We note that these simulations suggest retention factors between 0.6 and 0.9 can be achieved with cw decoupling under DNP conditions. These retention factors are reasonable given that our estimated $T_{1\rho,MC}(^1H) > 100$ ms for the microcrystalline solids exceeds the ^{13}C acquisition time of 26 ms. If we consider from Figure 2-1 that relative sensitivity grows most rapidly between 0.9 and 1.0, this indicates that if the recovery factors could be increased further still by, for example, increasing the strength of the cw spin lock during signal acquisition on the ^{13}C channel, then the experiment may become even more efficient.

Increasing the cw decoupling power also leads to line narrowing in ^{13}C spectra by increasing the coherence lifetime during signal acquisition, T_2^*. Of course, the improvement in resolution is concomitant to an improvement of the signal-to-noise ratio and hence sensitivity. Since continuous wave decoupling has fallen out of favor in the era of modern CP MAS NMR because of the lackluster resolution provided by the method at practical rf field amplitudes, it is prudent to consider the effects of other decoupling methods on the sensitivity of flip-back experiments. Figure 2-4 shows the ^{13}C resonance of three of the carbons in the CP spectrum of L-histidine monohydrochloride monohydrate. In addition to cw, we consider decoupling by the XiX and SPINAL-64 schemes, and we give line widths measured at half height. This highlights an unsurprising general feature of the comparison; namely, that cw decoupling gives the poorest resolution and SPINAL-64 the best, with XiX in between.
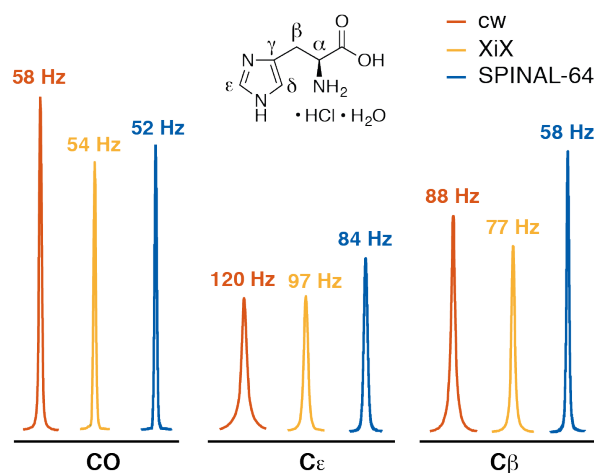

Figure 2-4. Selected peaks from DNP enhanced ^{13}C CP MAS spectra of L-histidine at a recycle delay of 150 s with 6 scans each. The spectra acquired with cw (with flip-back) and SPINAL-64 decoupling are respectively offset to the left and right of XiX decoupling (without flip-back) to facilitate comparison of the relative sensitivity of each ^{13}C resonance. Line widths displayed are measured at half peak height.

The XiX decoupling method preserves a well-defined spin locking axis and is, in principle, amenable to proton magnetization recovery. We therefore consider the use of flip-back recovery with the XiX decoupling scheme. This comparison is given in Figure 2-5 for ^{13}C L-histidine monohydrochloride monohydrate.

We see by this comparison a modest sensitivity improvement of about 10% is possible by using XiX decoupling instead of cw. Most of the sensitivity advantage of the XiX method comes from the narrower linewidth. The figure also shows the result from flip back with XiX, where there is an improvement with respect to ordinary XiX acquisition, but it is relatively low since the f_0 for this experiment is estimated to be around 0.2. This highlights that preservation of magnetization under more complex decoupling than cw is difficult. By far the best sensitivity is obtained with the cw flip-back experiment which here yields a factor 2 improvement. The price to pay in terms of resolution is relatively modest, going from 77 to 88 Hz for the C_β resonance as shown in Figure 2-4.
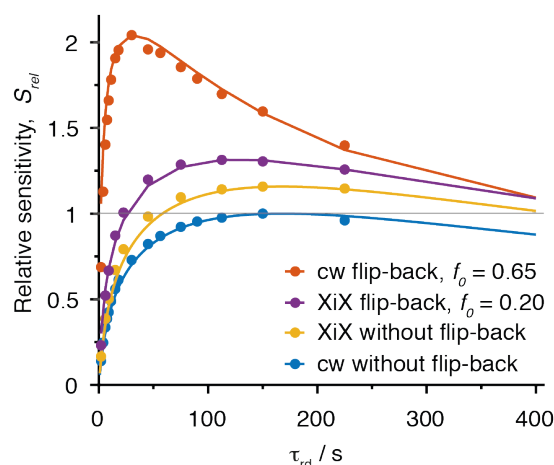
Figure 2-5. Relative sensitivity of DNP enhanced flip-back CP MAS experiments for cw and XiX decoupling as a function of recycle delay for the ^{13}C carbonyl resonance of L-histidine monohydrochloride monohydrate. Data for decoupled CP MAS without flip-back recovery (blue) was acquired as a sensitivity benchmark. In all cases the number of scans were adjusted to preserve a constant total acquisition time between experiments. Dummy scans were used to achieve a steady-state polarization prior to each experiment.

In Figure 2-6, three different sensitivity optimized ^{13}C CP MAS spectra of L-histidine monohydrochloride monohydrate are compared. The superior line narrowing capability of SPINAL-64 at the rf field amplitudes used here improves the sensitivity from between 20% and 100%, depending on the signal of interest. In particular, the sensitivity of the carbonyl signal, which experiences weaker proton couplings than the carbons with directly attached protons, is improved only marginally by the switch to SPINAL-64. In spite of this, the sensitivity of the flip-back experiment with cw exceeds that of SPINAL-64 for *each one* of the carbon signals, despite the slightly inferior resolution. Here again, the advantage is most striking for the carbonyl signal. All resonances are well resolved in all cases.
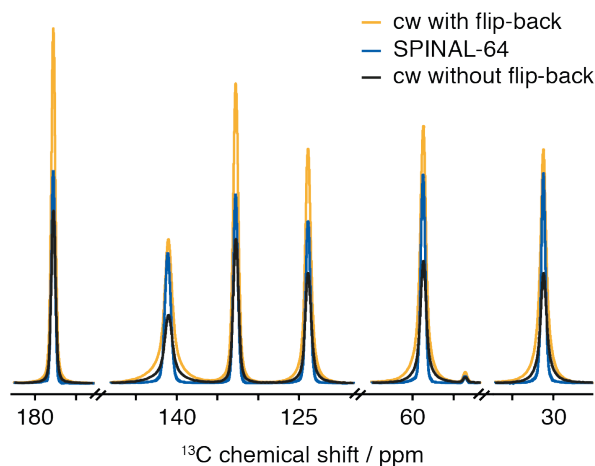
Figure 2-6. Sensitivity optimized DNP enhanced ^{13}C CP MAS spectra of L-histidine. A recycle delay of 150 s was used for the cw spectrum without flip-back and the spectrum implementing SPINAL-64 decoupling. A recycle delay of 30 s was used for the spectrum with a flip-back pulse. The number of scans were adjusted so the total experiment time was 15 minutes and each spectrum is displayed at the same level of noise. Consequently, the intensities correspond to the relative sensitivity of each ^{13}C resonance.

For relayed DNP systems, it is known that solids with intrinsically high proton T_1 values lead to higher polarization in the crystallites.[107] Further, in relayed DNP with long T_1, build-up times are limited by D, not T_1. The flip-back method compounds further advantages onto such systems by substantially and universally reducing the recycle delay required to reach a given level of sensitivity.

To demonstrate the power of the combined approach, Figure 2-7 shows the application of the 2D refocused scalar CP-INADEQUATE experiment[168] to the impregnated salicylic acid sample. When DNP enhancements are high (≥100) and polarization relay is efficient, INADEQUATE and similar ^{13}C-^{13}C correlation experiments on such samples become practical, but still generally require long periods of signal averaging.[106] In Figure 2-7 the flip-back INADEQUATE spectrum shows all the expected through-bond correlations, and the ^{13}C spectrum can be confidently assigned as shown. We observe that the quaternary carbon signals exhibit the greatest intensity. This is primarily attributed to more effective decoupling of these ^{13}C nuclei by the cw field, such that they possess longer coherence lifetimes T_2' than ^{13}C nuclei with attached protons and experience less dephasing during the mixing period.[168] To this result we compare the spectrum obtained with SPINAL-64 decoupling and no flip-back recovery. The sensitivity is significantly worse (as expected from the previous analysis), and only the two quaternary correlations are observed
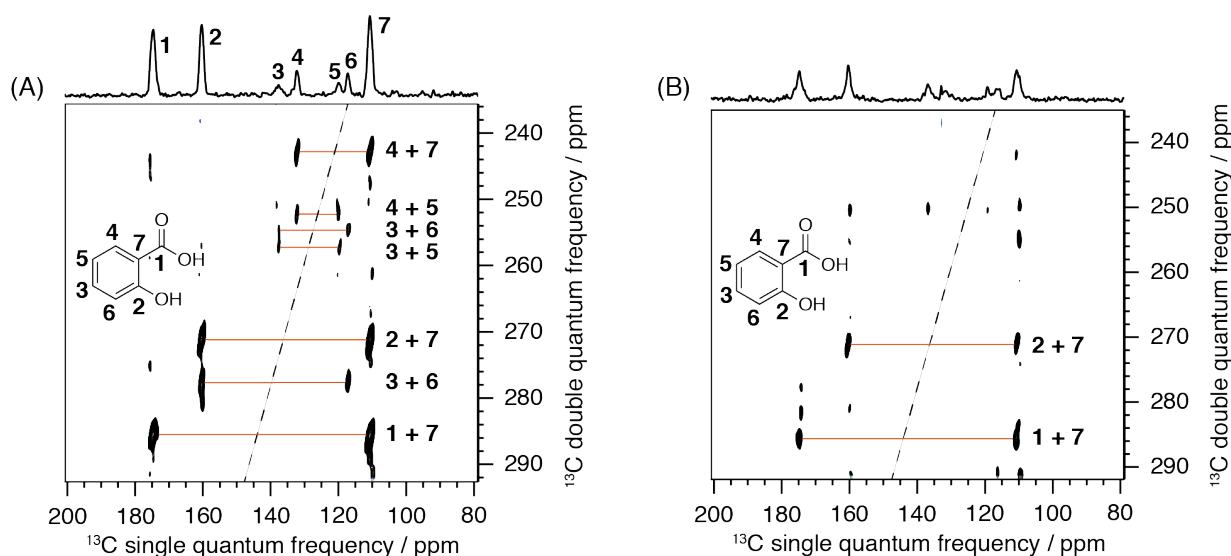

Figure 2-7. A) Two-dimensional DNP enhanced [^{13}C]^{13}C refocused CP-INADEQUATE correlation spectrum of salicylic acid with cw proton decoupling and flip-back recovery of magnetization. All through-bond correlations are observed. B) Comparable refocused CP-INADEQUATE spectrum without flip-back recovery using SPINAL-64 decoupling. Only two correlations are observed. The decoupling field amplitudes were $\nu_1(^1H)$ = 150 kHz. 64 dummy scans were used for the experiment implementing cw decoupling with flipback; presaturation was used instead for the SPINAL-64 implementation.

As Figure 2-2 and Figure 2-3 indicate, the sensitivity advantage of the flip-back recovery over the conventional cw experiment in the rapid recycling regime $\tau_{rd} \ll \tau_{rd}^* \approx 1$ min (assuming $f_0 \approx 0.9$), where τ_{rd}^* is the optimum recycle delay, can approach a factor of ten. This more than compensates the improvements in T_2^* and T_2' granted by SPINAL-64 decoupling and is the primary reason for the superior performance of the flip-back INADEQUATE experiment in our case. Note that in cases where large numbers of scans are required, for example with long phase cycles, and where sensitivity is not limiting, the number of scans becomes limiting for the total experimental time. In that case, with flip-back, more scans can be achieved per unit time since the optimal recycle delays are always shorter, thus reducing total experimental time.

2.1.4 Conclusion

The sensitivity of cross-polarization experiments on solids enhanced by relayed DNP can be further improved by recovering bulk proton magnetization with a flip-back pulse after an experiment using continuous wave decoupling during acquisition on ^{13}C. Using flip-back recovery always improves the sensitivity of such experiments and shifts the recycle delay which provides optimum sensitivity toward lower values. For practical rf field amplitudes, it is feasible to recover over 90% of the proton magnetization, which can triple the sensitivity over the

experiment without flip-back recovery for samples with long T_B, and reduce the optimum recycle delay by over a factor of ten. Use of continuous wave decoupling diminishes the sensitivity of the CP experiment by up to a factor of two compared to a state-of-the-art heteronuclear decoupling method such as SPINAL-64. Even so, the sensitivity of a flip-back optimized continuous wave decoupled experiment can easily exceed that of an experiment using SPINAL-64. When required, the combination of XiX decoupling and flip-back is representative of a compromise where sensitivity and resolution are improved over continuous wave while some level of enhancement using a flip-back pulse is retained. Despite relatively unfavorable effects on ^{13}C coherence lifetimes during the mixing period and acquisition, the sensitivity of a continuous wave decoupled flip-back 2D INADEQUATE experiment on an impregnated sample of salicylic acid acquired in a rapid recycling regime significantly exceeds that of one acquired with SPINAL-64.

2.1.5 Appendix I

DNP enhancements
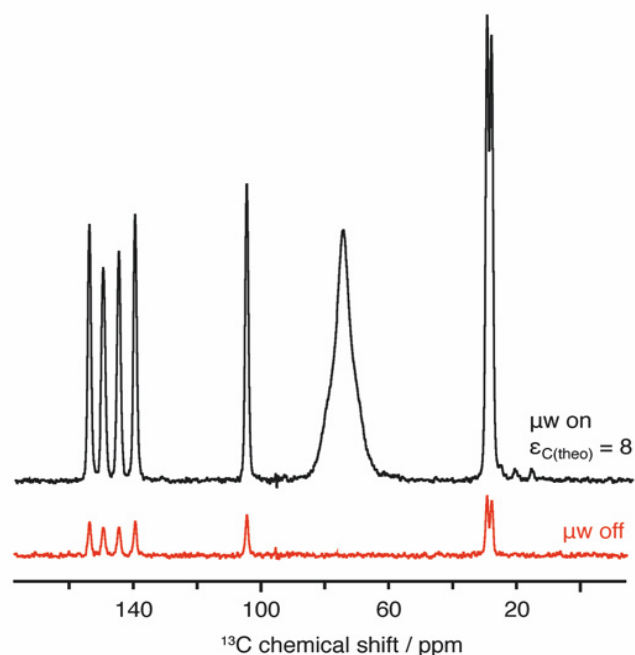
Figure 2-8. DNP enhanced ^{1}H-^{13}C CP MAS spectra of microcrystalline theophylline impregnated with a 16 mM solution of TEKPol in TCE. The spectra were recorded at 100 K and 9.4 T, at a MAS rate of 12.5 kHz. A recycle delay of 10 s was used for both the microwave on and microwave off measurements. The number of scans were the same in both cases.
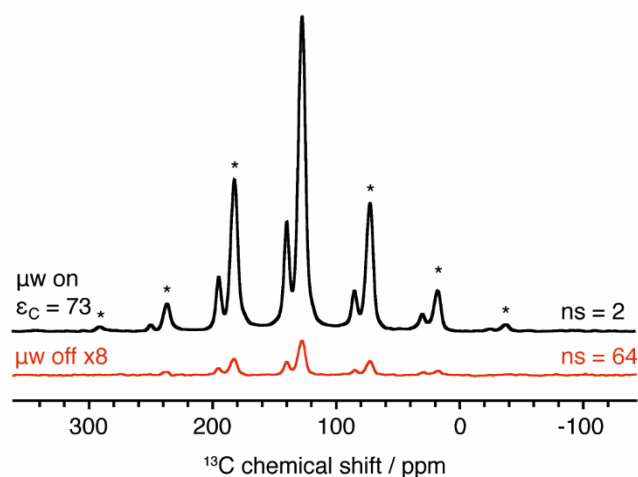
Figure 2-9. DNP enhanced ^{1}H-^{13}C CP MAS spectra of 75 mM BDPA in OTP (95:5 w:w OTP-d_{14}:OTP) at 100 K and 21.14 T. The temperature of the gyrotron resonant cavity was 33.0 °C. The cathode voltage and collector current were held constant at 18.70 kV and 190.0 mA. The MAS rate was 12.5 kHz. A recycle delay of 90 s, corresponding to roughly 1.8 times the build-up time, was used for both the microwave on and microwave off measurements. The total experimental time were 3 min and 96 min for the microwave on and off spectra, respectively. The sideband manifold is uniformly enhanced. An echo shift of one rotor period was introduced to eliminate receiver dead time. Spinning sidebands are marked with asterisks.

95%/5% dOTP/OTP DNP enhancement
75 mM BDPA
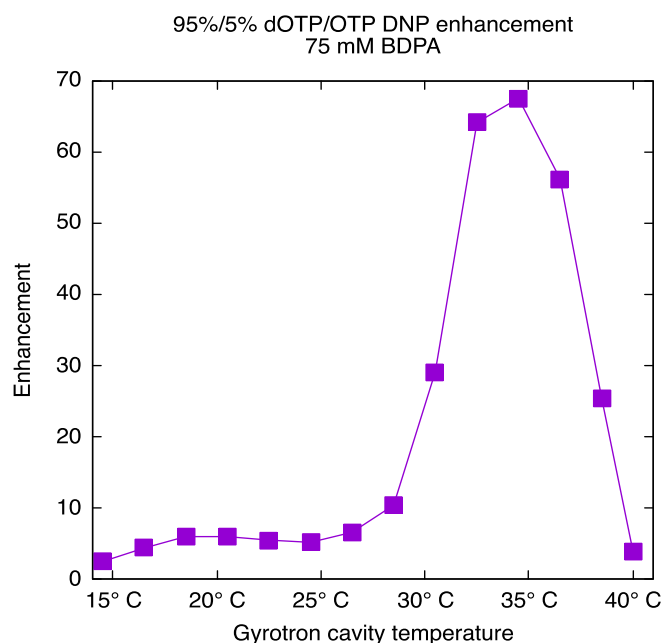
Figure 2-10. Dependence of the DNP enhancement at 21.141 T of ^{1}H-^{13}C CP MAS spectra of 75 mM BDPA in OTP (95:5 w:w OTP-d_{14}:OTP) on the temperature of the gyrotron cavity. The cathode voltage and collector current were held constant at 18.50 kV and 190.0 mA. The manufacturer indicated that the microwave frequency is modulated by the cavity temperature in a linear fashion with a proportionality constant of -9.8 MHz/K. Our results are in line with this expectation, and as a result, the profile resembles a small section of a conventional sweep field profile. The optimum binitroxide CE occurs near a 22 °C cavity temperature. As the microwave frequency moved lower the power output appeared to drop, and this was compensated to some degree by increasing the cathode voltage from 18.50 kV to 18.70 kV, leading to higher enhancements than those shown in the graph. Changing the cathode voltage also changes the microwave frequency slightly, but to a lesser extent. The MAS rate was 12.5 kHz. An echo shift of one rotor period was introduced to eliminate receiver dead time.

Saturation recovery curves
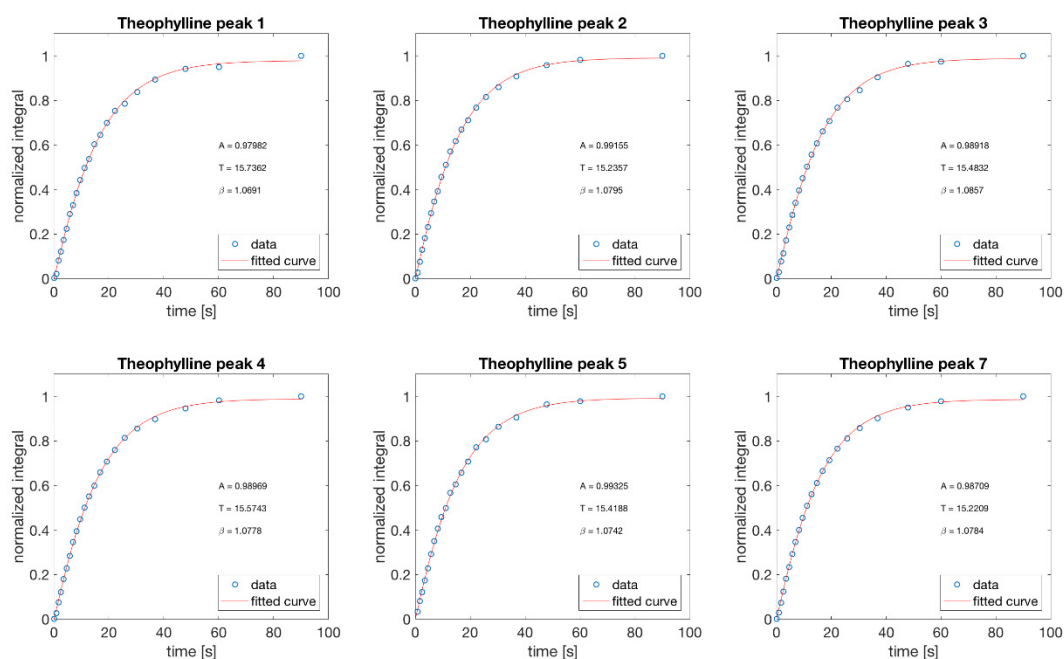
Figure 2-11. Saturation recovery curves for theophylline.
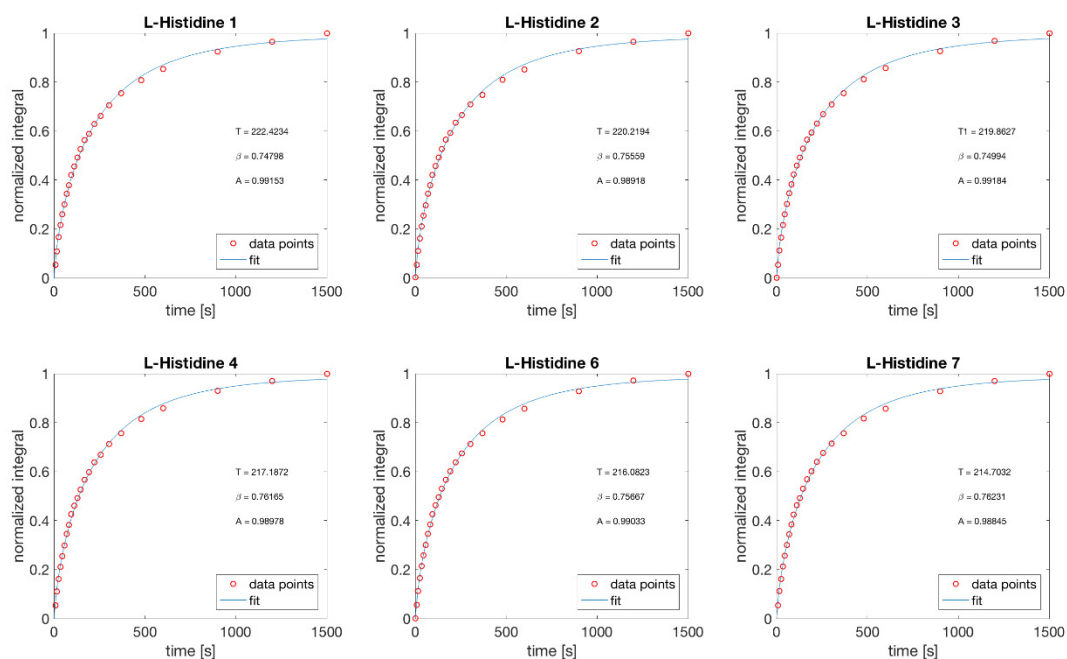
Figure 2-12. Saturation recovery curves for L-histidine monohydrochloride monohydrate.
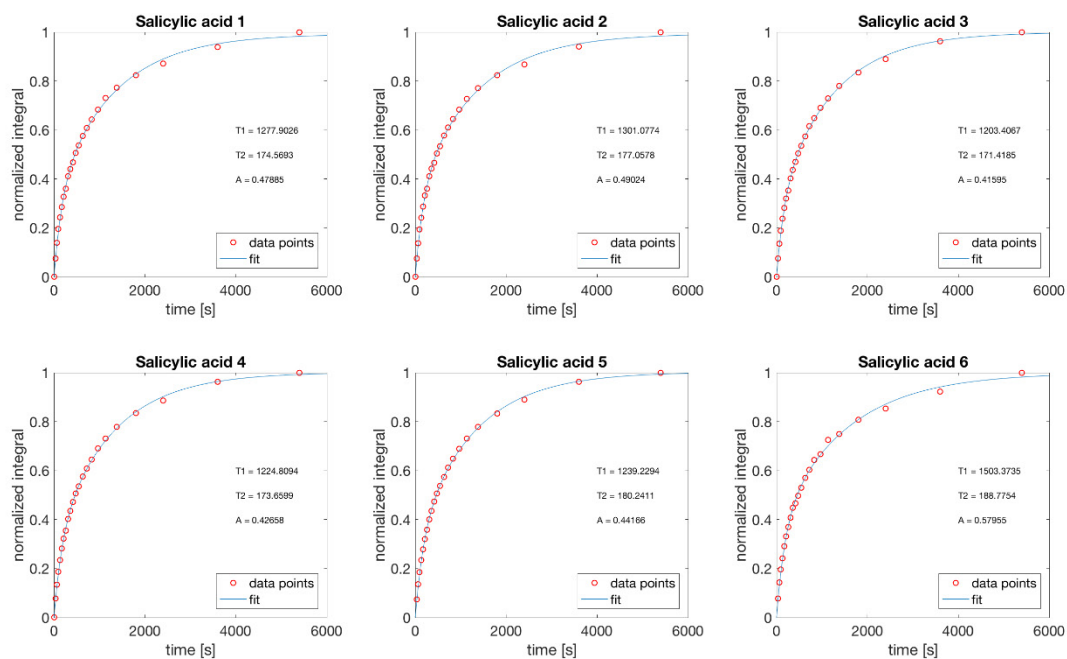
Figure 2-13. Saturation recovery curves for salicylic acid.

Fitting with a multi-exponential model

A multi-exponential model failed to fit the data presented in Figure 2-3. Using a multi-exponential model for magnetization recovery, the relative sensitivity without flip-back can be written as:

$$S_{rel} = \frac{A}{\sqrt{\tau_{rd}}} \left(1 - e^{-\left(\frac{\tau_{rd}}{T}\right)^{\beta}} \right)$$

(Eq. 2-4)

And the relative sensitivity with flipback as:

$$S_{rel} = \frac{A}{\sqrt{\tau_{rd}}} \left(1 - e^{-\left(\frac{\tau_{rd}}{T}\right)^{\beta}} \right) \sum_{n=0}^{\infty} f_0^n \, e^{-\left(\frac{n\tau_{rd}}{T}\right)^{\beta}}.$$

(Eq. 2-5)
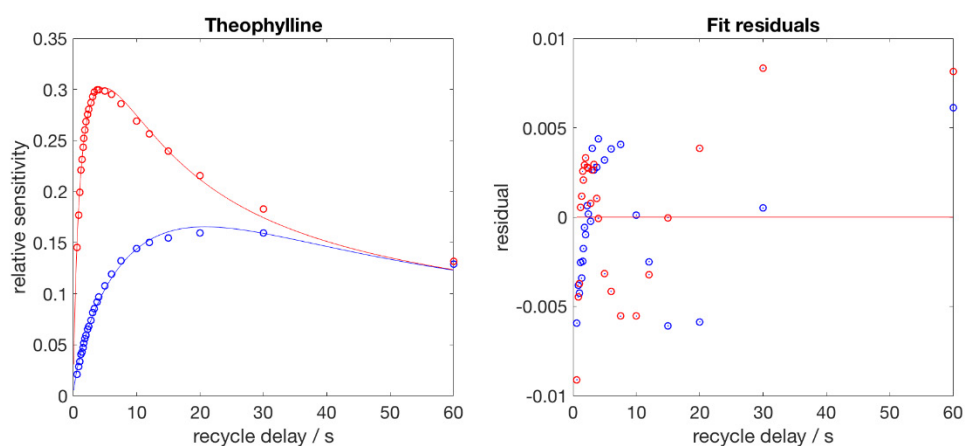
Figure 2-14. Measured sensitivity gains using DNP enhanced flip-back CP MAS on a sample of theophylline (same as the data in Figure 2-3). The solid lines are fits to the data using a multi-exponential model. The fit residuals show the limitations of the model.
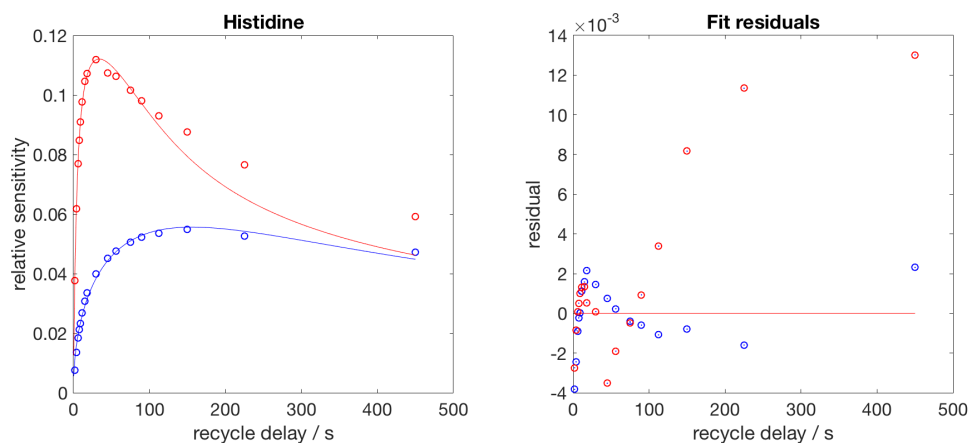
Figure 2-15. Measured sensitivity gains using DNP enhanced flip-back CP MAS on a sample of L-histidine·HCl·H$_2$O (same as the data in Figure 2-3). The solid lines are fits to the data using a multi-exponential model. The fit residuals show the limitations of the model.
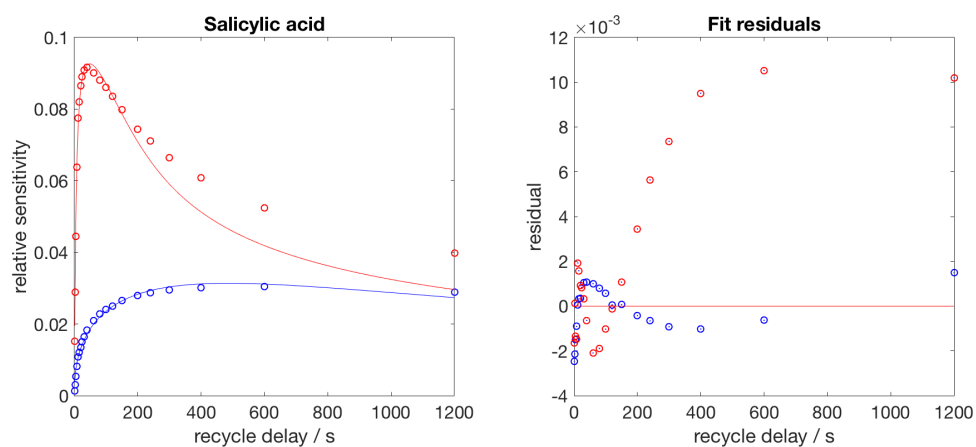
Figure 2-16. Measured sensitivity gains using DNP enhanced flip-back CP MAS on a sample of salicylic acid (same as the data in Figure 2-3). The solid lines are fits to the data using a multi-exponential model. The fit residuals show the limitations of the model.

Chapter 3   Inorganic solids

3.1   Hyperpolarization of inorganic bulk by relay from the surface

This chapter has been adapted with permission from: "*Bulk nuclear hyperpolarization of inorganic solids by relay from the surface*". S. Björgvinsdóttir, B.J. Walder, A.C. Pinon, L. Emsley, *Journal of the American Chemical Society* **2018**, 140, 7946-7951. (post-print)

3.1.1   Introduction

Inorganic solids such as silicates, phosphates, oxides, aluminates, ceramics or semi-conductors are at the heart of materials chemistry. The macroscopic properties of these materials are defined by their atomic level structures and morphologies. Single-crystal X-ray diffraction can provide atomic coordinates when suitable samples are available, but for microcrystalline powders or disordered structures, determination of atomic-level information is often difficult.

Solid-state NMR is a method of choice to determine structural and electronic features in inorganic materials, but its application can be limited by its low relative sensitivity. When the materials contain nuclei with low receptivity and/or low natural abundance, the use of multi-dimensional techniques is often precluded and acquisition of even one-dimensional NMR spectra can be difficult. This is especially true when relaxation times are long. As a result, many NMR studies of inorganic materials resort to isotopic enrichment or enhance nuclear relaxation rates by doping samples with paramagnetic species.

Dynamic nuclear polarization (DNP) has recently been developed to boost the sensitivity of magic-angle-spinning solid-state NMR[42, 169], and in particular it has been shown that incipient wetness impregnation can be used to obtain DNP surface enhanced NMR (SENS)[101-102], and this has led to a number of applications to the observation of the surfaces of various oxides and nanoparticles.[103, 170-178]

In this method, nuclear spin hyperpolarization of protons in the wetting phase is generated by an organic radical, transported to the surface by spontaneous spin diffusion[38, 102], and subsequently transferred to the nuclei of interest (^{29}Si, ^{13}C, ^{15}N, ^{31}P, ^{119}Sn, ^{113}Cd, ^{17}O) at the surface by cross polarization (CP).[14, 39] If the substrate contains protons, as would be the case for organic solids or strongly hydrated materials, then the polarization can continue to diffuse into the material and polarize the bulk sample, yielding overall sensitivity enhancement of the bulk sample by up to a factor 100.[105-107, 179-181]

However, in many of the most challenging cases for NMR, the material is proton-free. Examples include most inorganic oxides and semi-conductors. In these cases, impregnation DNP cannot be used to hyperpolarize the bulk of the materials *via* proton spin diffusion, though specific materials such as diamond, GaAs, InP, powdered silicon or coals have been polarized by DNP using either intrinsic paramagnetic defects or optical centers.[46, 182-184]

Here, we show how impregnation DNP can be combined with spin diffusion between low-γ, spin-½ nuclei to provide a general strategy to hyperpolarize proton-free inorganic solids. Two variants are presented, using both direct polarization of nuclei at the surface of the material, and a pulse cooling method that transfers hyperpolarization from protons. We demonstrate a factor 50 gain in overall sensitivity for the ^{119}Sn spectrum of

powdered SnO_2 using pulse cooling, corresponding to an acceleration of a factor 2500 in acquisition times. The method is also shown for ^{31}P spectra of GaP, for ^{113}Cd spectra of CdTe, and for ^{29}Si spectra of α-quartz.

3.1.2 Experimental methods

Sample preparation. SnO_2 (abcr GmbH) and SiO_2 (Sigma Aldrich) were crushed by hand with a mortar and pestle. GaP flakes (abcr GmbH) were milled in a mixer mill for 30 min (see SEM images in Figure 3-1). CdTe (Sigma Aldrich) was milled for 30 min in a mixer mill. The grinding medium was a stainless steel ball. The powdered samples were impregnated with a 16 mM solution of TEKPol[185] biradical in 1,1,2,2-tetrachloroethane (TCE). The TEKPol concentration was 12 mM in the case of SiO_2. The ratio of solvent to powder was approximately 10 μL of radical solution to 40 mg of SnO_2, 10 μL to 70 mg of CdTe and 10 μL to 50 mg of SiO_2. Powdered GaP was mixed with KBr, ca. 60 mg of 1:1 w:w GaP:KBr to 10 μL of radical solution. The impregnated powders were packed in 3.2 mm sapphire rotors and inserted rapidly into a cold NMR probe. Three thawing cycles were used to deoxygenate the SnO_2, CdTe and SiO_2 samples in order to improve DNP enhancements.[160]
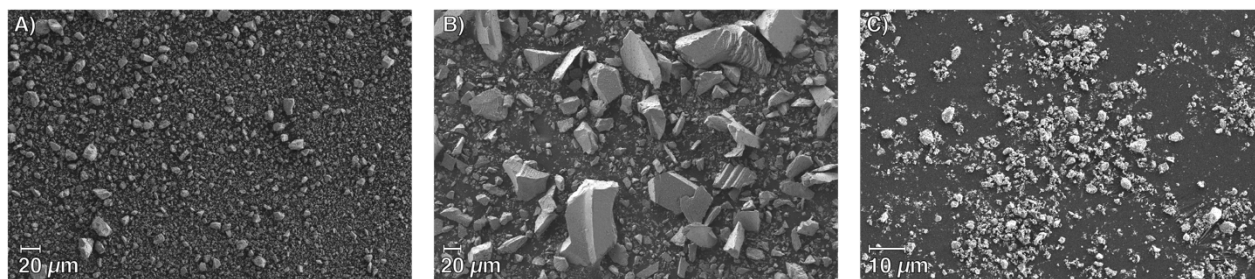
Figure 3-1. Scanning electron microscope (SEM) images of the compounds used for the NMR experiments. A) GaP milled in a mixer mill for 30 min. B) GaP ground by hand with a mortar and pestle for 5 min. C) SnO_2 ground by hand.

DNP enhanced NMR experiments. Solid-state NMR experiments were performed on a 9.4 T Bruker Avance III spectrometer, coupled with a 263 GHz gyrotron and equipped with a 3.2 mm low-temperature MAS probe.[42] The microwave beam power was optimized by changing the gyrotron collector current for each of the GaP, SnO_2, CdTe and SiO_2 impregnated formulations in order to maximize the ^1H solvent signal enhancement. The amplitude of the ^1H rf field was ramped from 90-100% during the cross polarization contact time to improve efficiency.[186] The CP contact power was adjusted to compensate changes in transfer efficiencies at different spin rates. Presaturation was used in all experiments. See Appendix II for more details.

3.1.3 Results and discussion

Although it has been observed previously, homonuclear spin diffusion between low-γ nuclei is often thought to be negligible in spinning samples.[187-188]

For example, in a static sample established models[119, 127] would predict ^{13}C spin diffusion rates in diamond at natural abundance to be ~50 times slower than proton spin diffusion rates in typical organic solids. However, we note here that relaxation times in inorganic materials can often be on the order of hours, or a factor 10^3 longer than in a typical organic solid. With this realization, we suggest that it might be possible to hyperpolarize inorganic solids by homonuclear spin diffusion between low-γ nuclei.

From the expressions for the steady state DNP enhancement obtainable inside a given particle,[107] being polarized by spontaneous spin diffusion (between either protons or low-γ nuclei), assuming the surface polarization gain (over Boltzmann) is maintained at P_{source} we can deduce an upper bound for the polarization gain in the bulk, P_{target}:

$$P_{\text{target}} = 1 + 3(P_{\text{source}} - 1)\frac{\sqrt{DT_1}}{R}\left[\coth\left(\frac{R}{\sqrt{DT_1}}\right) - \frac{\sqrt{DT_1}}{R}\right] \qquad \text{(Eq. 3-1)}$$

Here, D is the spin diffusion coefficient for the nuclei in the bulk, T_1 is their intrinsic spin-lattice relaxation time, and R is the particle radius. In the case where the diffusion length $\sqrt{DT_1} \ll R$ this simplifies to:

$$P_{\text{target}} = 1 + 3(P_{\text{source}} - 1)\frac{\sqrt{DT_1}}{R} \qquad \text{(Eq. 3-2)}$$

For nonspinning crystals in which all nuclei have identical chemical shifts, we estimate an upper bound for P_{target} by this model in the following way. First, we take D = 710 nm²/s, the experimentally measured diffusivity of ^{19}F polarization in a crystal of CaF_2 along the magnetic field aligned with the [001] direction,[141] and adjust it for target nuclide concentration n and gyromagnetic ratio γ_I assuming $D \propto n^{1/3}\gamma_I^2$.[127, 189] We note that this value of D and the measured ^{19}F T_1 = 115 s are similar to that found for protons in rigid organic solids, systems which are easily hyperpolarized by incipient wetness impregnation DNP under MAS.[106] Then, using reasonable estimates of T_1 we use Equation 3-1 to determine P_{target}. These values are given in Table 3-1 for various crystalline materials taking P_{source} = 100 and R = 0.5 μm. Perhaps surprisingly, the P_{target} values indicate that the steady-state bulk polarization in micrometer sized particles can approach the level of hyperpolarization being maintained at the surface, despite upper bounds for D in each case being one to two orders of magnitude lower than for protonated organic solids.

The potential bulk polarization gain realized for samples undergoing magic-angle spinning (MAS) is expected to be much less than this, and in fact may be thought of as negligible on the grounds that the homonuclear dipolar interaction between a pair of like spins is averaged to zero under MAS, removing internuclear couplings and quenching spin diffusion.[120] Nonetheless, it is important to realize that D is analytically zero only in the limit of infinite MAS rate. For a network of like spin I = ½ nuclei, the diffusion coefficient is predicted to drop off only in proportion to ν_r^{-1} when the MAS rate ν_r exceeds the dipolar line width.[133, 135, 190-191] This might typically lead to a reduction in D by a factor 10 when going from a static sample to around 10 kHz spinning.[191] Once again this should be considered as a guide for an upper bound. We note that in addition, there are many other factors that can modulate spin exchange in solids, including instantaneous chemical shift differences between coupled spins,[120-121, 192] heteronuclear couplings,[121-122, 130, 134] and scalar couplings[130, 135]. This was discussed in more detail in Section 1.3.2, with the conclusion that the effect of MAS is non-trivial. MAS often considerably reduces spin diffusion rates, but in some cases it can also enhance the overall rate of spin diffusion.[139]

Table 3-1. Estimated upper limits of the potential bulk polarization gain P_{target} for nuclei in six different materials without sample spinning, maintaining P_{source} = 100 and spherical particles having R = 0.5 μm, and with estimated T_1. The spin diffusion coefficients are scaled from a value determined by single crystal experiments on CaF_2 assuming the scaling law $D \propto n^{1/3}\gamma_I^2$ where n is the concentration of nuclei and γ_I is their gyromagnetic ratio.

Nucleus	n / M	D / nm²s⁻¹	T_1 / s	P_{target}
^{19}F in CaF_2 ∥ [001]	81.5	710†	115†	84
^{31}P in GaP	41.1	100	250	66
^{119}Sn in SnO_2	4.0	41	500	62
^{125}Te in CdTe	1.72	22	1800	74
^{13}C in diamond	3.25	17	10^5	99
^{113}Cd in CdTe	2.98	13	1800	64
^{29}Si in α-quartz	2.06	9.3	10^5	98

† measured, ref[141]

Therefore, we might consider that magnetization could be transported from the surface into the bulk by homonuclear spin diffusion between weakly magnetic nuclei under MAS, even if it occurs slowly. We turn to experiment for evidence that such a mechanism can indeed transport magnetization effectively.

Such evidence is given in Figure 3-2B, which shows DNP enhanced ^{1}H-^{119}Sn CP-MAS spectra of SnO_2 recorded at 9.4 T and 100 K using the pulse sequence shown in Figure 3-2A that allows for ^{119}Sn spin diffusion during the mixing time between cross polarization and detection. Under our DNP conditions, the CP step transfers the magnetization from hyperpolarized protons in the wetting phase to ^{119}Sn nuclei at the surface, leading to a gain in surface polarization estimated to be a factor of 350 greater than ^{119}Sn Boltzmann polarization. This sets up a large ^{119}Sn polarization gradient at the surface of the particle. In the spectra with τ_z = 0, peaks attributed to both surface (-590 ppm, -615 ppm) and bulk (-603 ppm) sites[193] are observed. As τ_z is increased, the surface signal diminishes while the bulk signal builds in such a way that the total signal integral *decreases* and at the same time the signal (height)-to-noise ratio of the spectrum *increases*. The intensity of the bulk signal reaches a maximum around τ_z = 60 s. *Thus, spin diffusion transferring magnetization from ^{119}Sn at the surface to ^{119}Sn in the bulk clearly occurs during τ_z, despite an MAS rate of 8 kHz that greatly exceeds the strength of the homonuclear ^{119}Sn dipolar couplings (expected to be 520 Hz at their strongest).*
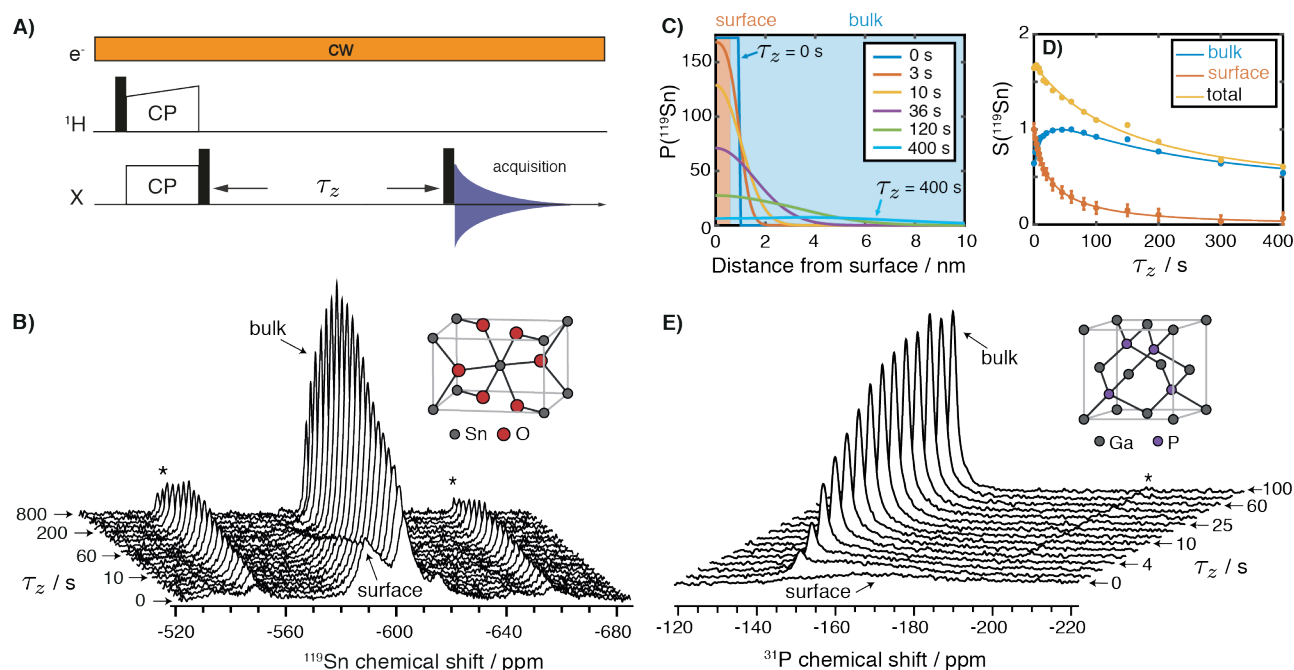
Figure 3-2. Spin diffusion in powdered materials impregnated with a 16 mM solution of TEKPol[185] in tetrachloroethane[84] spinning at 8 kHz. A) The *z*-filtered CP sequence. Spin diffusion occurs during the τ_z interval, when magnetization is stored longitudinally between polarization and signal acquisition. Black bars correspond to π/2 pulses. B) DNP enhanced ^{119}Sn CP MAS spectra acquired as a function of τ_z. Asterisks indicate spinning sidebands. C) Simulated ^{119}Sn polarization relay from the surface of the particle for different τ_z. D) Normalized ^{119}Sn bulk, surface and total signals as a function of τ_z. Experiment (dots) is compared to numerical simulations (solid lines) E) DNP enhanced ^{31}P CP MAS spectra acquired as a function of τ_z. Experimental and simulation details are given in Appendix II.

This behavior can be reproduced with numerical simulations of spin diffusion[107] as shown in Figure 3-2C and D. The diffusion model here uses a single spin diffusion coefficient for all ^{119}Sn nuclei in the sample, including those at the surface. In reality, the isotropic chemical shift differences that exist between surface and bulk species are expected to throttle the rate of spin diffusion, which may be a significant additional bottleneck for magnetization transport. On the other hand, SnO_2 possesses a rutile structure, in which neighbouring tin sites have isometric shielding tensors with different orientations. In addition to n = 0 rotational resonance enhancing the rate of bulk ^{119}Sn spin diffusion, it is likely that shielding anisotropy of the surface sites permits energy conserving spin exchange during some parts of the rotation cycle, preventing the isotropic shift differences from quenching

magnetization transport from the surface as they otherwise might. That said, to model the build-up of bulk signal in Figure 3-2B, we find a value of *D* of 0.035 nm^2/s, which is about two orders of magnitude slower than the upper bound we have estimated using the argumentation above.

This experiment was also performed for ^{31}P in powdered GaP in Figure 3-2E. This material possesses a zincblende structure and nuclear shielding anisotropy is absent from bulk sites (spinning sidebands in GaP result from significant bulk magnetic susceptibility effects), giving bulk ^{31}P signal at -148 ppm with a line width (FWHM) of about 3 ppm. From our analysis, bulk spin diffusion between ^{31}P should be relatively efficient. The surface sites are disordered and their isotropic shifts are distributed between -140 ppm and -200 ppm. From the τ_z = 0 s cross section, we see that CP polarizes surface sites exclusively. *Despite the large distribution of chemical shifts at the surface, we observe surface-to-bulk spectral diffusion in GaP.* We again conclude that isotropic shift differences between surface and bulk sites are not sufficient to fully eliminate spin diffusion, likely due to the presence of shielding anisotropy for the surface sites. Analysis of the ^{31}P lineshape for the surface resonances in Figure 3-2E as a function of τ_z might also suggest that polarization transfer among the surface sites occurs from low to high frequency across the lineshape, which might indicate that polarization hops between sites with nearly equivalent shifts in the first few seconds before finally moving into the bulk. More detailed analysis of the nature of surface to bulk spin diffusion will be the subject of further work (Section 3.4).

Given non-zero spin diffusion rates, if the T_1 is sufficiently long, then bulk hyperpolarization should be achievable by relay of hyperpolarization from radicals in a wetting phase at the surface, either by direct DNP to low-γ nuclei near the surface, as shown in Figure 3-3A, or by a multiple-contact cross-polarization scheme[14, 194] which we refer to as "pulse cooling", shown in Figure 3-3B. For the former, bulk spin diffusion spontaneously transports magnetization into the particle allowing repolarization of near-surface nuclei by the radicals. A single direct excitation pulse detects the signals resulting from hyperpolarization which accumulates in the bulk. The optimum recycle delay for this experiment will therefore be on the order of the intrinsic nuclear T_1.

In the pulse cooling scheme, the multiple CP contacts maintain a low spin temperature of surface heteronuclei during the polarization period, τ_P, by transfer of hyperpolarization from the protons in the impregnating phase. Interim periods of magnetization storage, τ_z, permit spontaneous homonuclear spin diffusion to propagate polarization into the bulk. During τ_z, ^{1}H hyperpolarization is rapidly replenished in the impregnating phase. Typically, τ_z should be longer than the ^{1}H build-up time in the solvent, whereas τ_P should be long enough to allow for the accumulation of polarization in the bulk by spin diffusion and is ultimately limited by the intrinsic nuclear T_1.

We note that due to the size of the particles, some of which are on the order of micrometers, we do not necessarily expect the center of the particles to be hyperpolarized. The distance the hyperpolarization can travel from its origin on the surface can be limited by the longitudinal relaxation rate of the particles, which would result in a hyperpolarized layer with a given thickness at steady state. As an example, the estimated maximum ^{119}Sn-^{119}Sn diffusion length in 500 s, for a non-spinning particle of SnO$_2$, is expected to be around 140 nm (and shorter for spinning samples, as suggested by the simulations in Figure 3-2C and Figure 3-3C). The thickness of this layer can be thought to be relatively independent of the particle size, meaning that for small particles the hyperpolarized volume represents a larger amount of the total particle volume than for big particles. The conclusion is that for a given surface enhancement, the bulk DNP enhancements will be larger for smaller particles. Also, the build-up of polarization is predicted to be faster for small particles.[106]
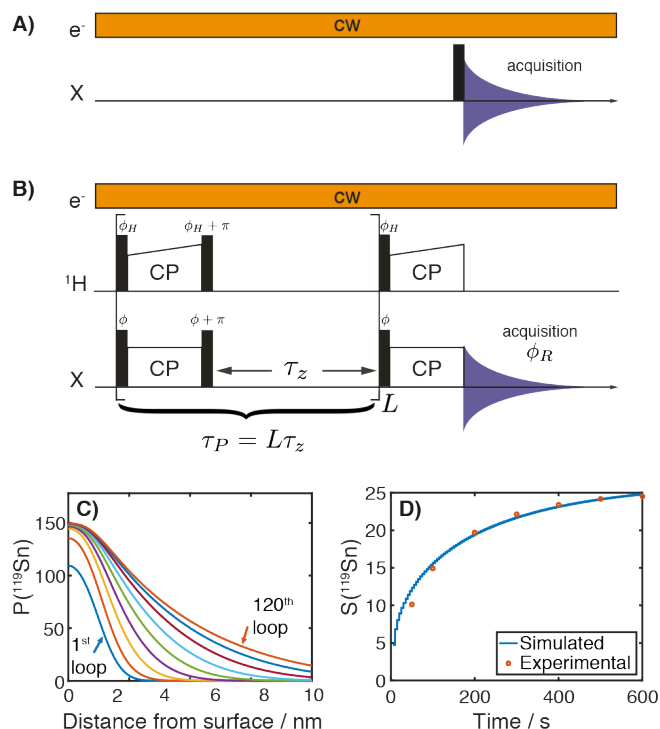
Figure 3-3. A) Pulse sequence used for bulk nuclear hyperpolarization by direct DNP. B) Pulse cooling sequence using multiple-contact CP. Holding the pulse phases ϕ and ϕ_H fixed while alternating ϕ_R over two steps excludes signals from the intrinsic polarization of the bulk (including direct DNP), while two-step alternation of all phases together includes them. C) Simulated ^{119}Sn polarization as a function of the distance from the surface of the particle after different numbers of loops, with τ_z = 5 s. D) Corresponding normalized ^{119}Sn signal as a function of τ_P. Pulse sequences and pulse cooling simulation parameters are given in Appendix II.

Figure 3-4 shows the results obtained for SnO_2 and GaP, using the two different acquisition methods. Direct excitation of ^{119}Sn and ^{31}P nuclei with a $\pi/2$-pulse was used to record NMR signals from neat SnO_2 and GaP samples and provide the reference sensitivity achievable without DNP. In Figure 3-4 these results are compared to those with the pulse cooling scheme of Figure 3-3B for DNP experiments on both GaP and SnO_2. For these experiments, τ_z and τ_P were both optimized, and phase cycling was chosen to include contributions from intrinsic heteronuclear polarization build-up. As an example, at 8 kHz the optimum recycle delay for the neat SnO2 sample is 502 s and the optimized delays for for the pulse cooling experiments are τ_P = 200 s and τ_z = 12.5 s. We find that longer τ_z generally requires a longer τ_P in order to optimize sensitivity; however, the actual value of the optimum sensitivity is roughly constant over a wide region of τ_z and τ_P values, and is always higher than the conventional experiments. (Experimental optimization of sensitivity in the pulse cooling experiment is the topic of Section 3.2.)

The normalized sensitivity, defined as signal-to-noise ratio divided by the mass of the bulk material in the rotor and the square root of the experiment time, of the neat samples decreases with the MAS rate due to an increased number of spinning sidebands. For the impregnated samples, this effect is countered by a corresponding increase in the rate of spin diffusion. In decreasing the MAS rate from 12.5 kHz to 8 kHz to 4 kHz, the sensitivity of the reference experiments on neat SnO_2 decreases by steps of 7% and 33%, whereas the sensitivity of the pulse cooling experiment *increases* by 30% before the proliferation of the spinning sidebands decreases the sensitivity by 6%. At higher spin rates, the signal originating from protons decreases relative to the intrinsic build-up of heteronuclear polarization. This is primarily due to lower spin diffusion rates permitting relatively larger contributions from both intrinsic longitudinal recovery of the bulk as well as direct DNP of bulk heteronuclei.
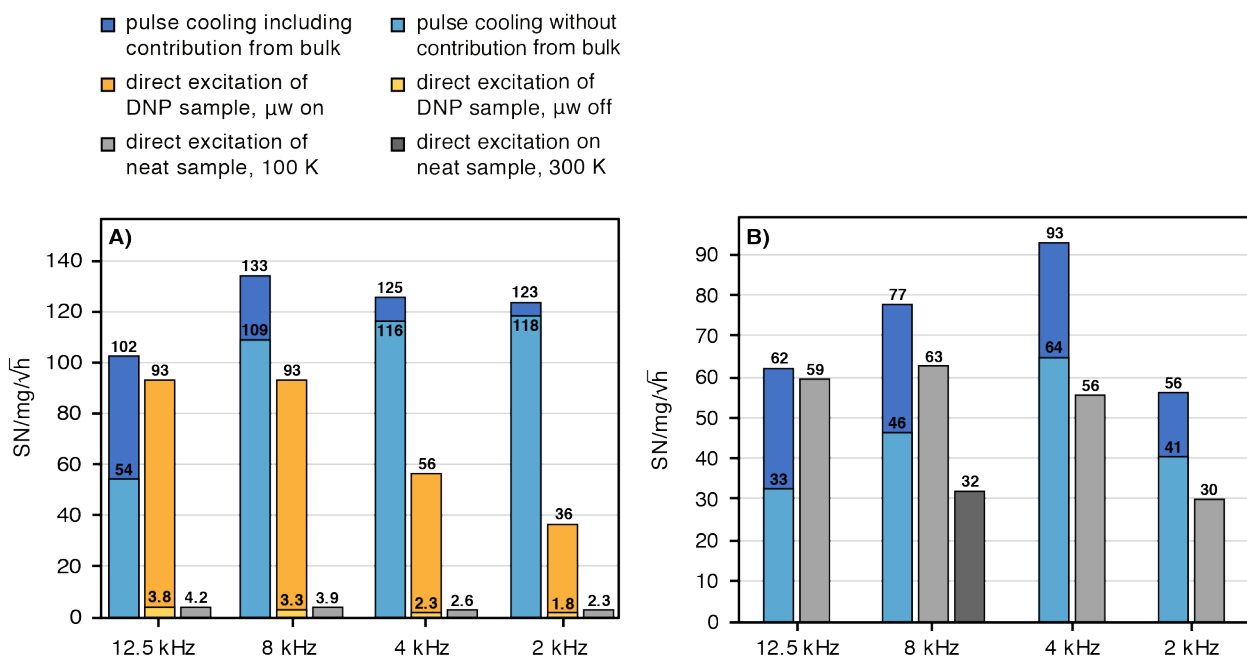
Figure 3-4. Comparisons of fully normalized NMR sensitivity between different experiments for A) SnO_2 and B) GaP formulations. Neat samples are compared to powders impregnated with a 16 mM solution of TEKPol in tetrachloroethane. The recycle delay for direct excitation of the neat samples and τ_z and τ_p for pulse cooling were optimized for each spin rate. Full details are given in Appendix II.

For SnO_2, direct [119]Sn DNP enhancements are substantial, around 25 with a 900 s polarization delay, but direct ^{31}P enhancements are essentially nonexistent for GaP. This parallels the trend in surface-based (^{1}H) polarization enhancement measured by cross-polarization, which was found to be 320 for SnO_2 and 20 for GaP. This is likely due to differences in how the TEKPol radical interacts with the surface of these materials,[61] and is the primary reason why pulse cooling yields higher sensitivity enhancements for SnO_2. Optimising high surface DNP enhancements is obviously crucial to this method.

Very long T_1 favors our approach. We have also obtained enhanced [113]Cd spectra from CdTe, and enhanced [29]Si spectra of α-quartz using pulse cooling. For both compounds, we once again clearly see evidence for spin diffusion between the surface and the bulk (Figure 3-5A and B). CdTe has a T_1 of 1 hour, and we obtain an enhancement of the bulk [113]Cd signal (395 ppm)[195] by nearly a factor of 5 in Figure 3-5C. Our sample of α-quartz is estimated to have a T_1 of at least 4 h, the longest out of the four compounds presented here. We show in Figure 3-5D a practical sensitivity enhancement of a factor of 85, using the pulse sequence in Figure 3-3 for direct DNP of [29]Si using long recycle delays. This level of enhancement was achieved without adjusting the static field to optimize cross-effect DNP for [29]Si, which should occur at much lower field value than we used here.
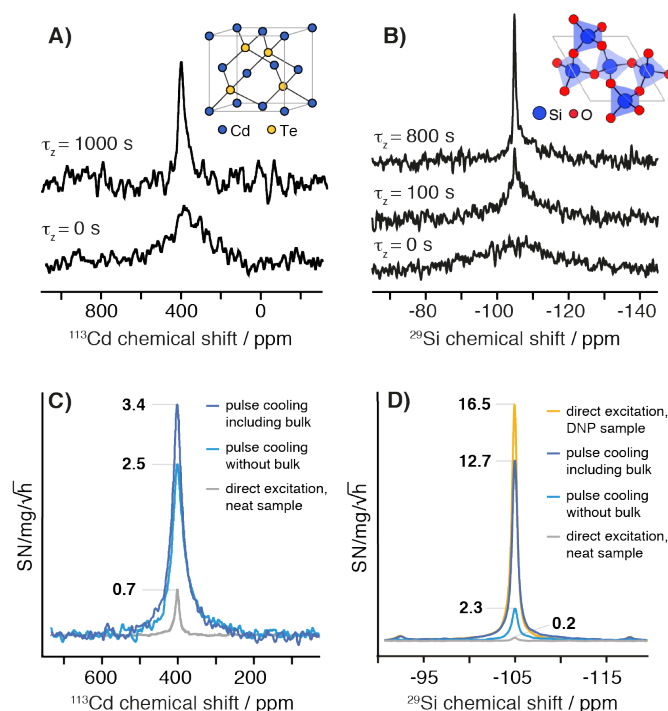
Figure 3-5. ^{113}Cd spectra of powdered zincblende CdTe and ^{29}Si spectra of α-quartz. A) Spin diffusion from hyperpolarized surface nuclei into the bulk for ^{113}Cd nuclei in a sample of CdTe impregnated with 16 mM TEKPol in tetrachloroethane, spinning at 2 kHz. B) Spin diffusion between ^{29}Si nuclei in powdered SiO$_2$ impregnated with 12 mM TEKPol in tetrachloroethane, spinning at 1 kHz. The spectra were observed using the pulse sequence in Figure 3-2. C) Pulse cooling spectra of impregnated CdTe at 1 kHz MAS compared to sensitivity optimized ordinary pulse-acquire spectra on a neat sample spinning at 8 kHz. D) DNP spectra of impregnated α-quartz at 1 kHz MAS compared to the spectrum of a neat sample. The intensities are scaled to match the fully normalized sensitivity of each experiment (the measurements were not constant time). Full experimental details are given in Appendix II.

3.1.4 Conclusion

We have shown that homonuclear spin diffusion between low-γ nuclei can be used as a mechanism for transferring surface-based hyperpolarization into the bulk for ^{31}P, ^{119}Sn, ^{113}Cd, and ^{29}Si nuclei. This is exploited to develop a general strategy for increasing the sensitivity of NMR signals originating from the bulk of proton-free inorganic solids, using either direct DNP or repetitive bursts of cross-polarization to maintain a high level of surface-based hyperpolarization. These approaches lead to gains of up to a factor 85 in sensitivity here.

3.1.5   Appendix II

Experimental parameters

Table 3-2. Experimental NMR parameters for the pulse cooling experiments. Asterisk denotes values used at 4 kHz.

	GaP:KBr	SnO_2	CdTe	SiO_2
Size of FID, real points	4096	2048	2048	16384
Acquisition time / ms	10.2	8.2	4.1	65.5
Spectral width / kHz	200	125	250	125
^1H rf field amplitude / kHz	100	100	100	60
X rf field amplitude / kHz	100	87	83	60
CP contact time / μs	1500	1500	4000	4500
CP contact power at 8 kHz MAS / kHz	89	87	87	60*
Gyrotron collector current / mA	27.5	30	40	45
^1H enhancement at 8 kHz MAS	108	245	350	305*

Figure 3-6. Magnetic field dependence of ^1H and ^{119}Sn DNP enhancements in a sample of SnO_2 impregnated with 16 mM TEKPol in TCE, spinning at 8 kHz. 30 mA microwave collector current was used.

Table 3-3. Experimental details for data presented in Figure 3-4A. Comparison between different experimental methods for acquiring bulk ^{119}Sn NMR signal of SnO_2. A) 43.32 mg SnO_2 impregnated with 10 μL 16 mM TEKPol/TCE at four different spi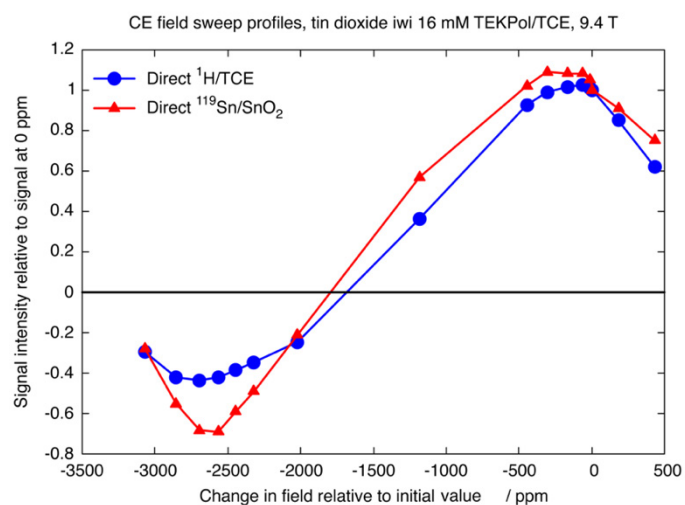n rates. Pulsecooling and maxcooling refer to the pulse cooling scheme of Figure 3-3B without and with switching the relative phase of the proton and heteronuclear CP flanking pulses between scans, which respectively excludes and includes the contribution of the intrinsic heteronuclear build-up to the signal. B) Direct acquisition of ^{119}Sn on a dry sample of SnO_2. The recycle delay d_1 corresponds to the optimum recycle delay, calculated from the relaxation rate of the sample at each spin rate. C) Direct acquisition of ^{119}Sn on an impregnated sample of SnO_2. Direct hyperpolarization of ^{119}Sn is observed by comparing the μw on and μw off spectra. The number of scans was two in all cases. Signal processing was performed with *RMN*.[196] The signals were processed after quadrupling the length of the FID by zero filling without exponential apodization. Signal-to-noise was analyzed by comparison with a spectrum of pure noise.

A	MAS rate / kHz	mass / mg	d_1 / s	τ_z / s	L	expt / h	S/N	SN/mg/√h
maxcooling	12.5	38.71	5	50	8	0.23	1880.8	102.43
pulsecooling							-	54.32
maxcooling	8			12.5	16	0.11	1743.6	133.47
pulsecooling							-	108.74
maxcooling	4			5	20	0.06	1168.6	124.99
pulsecooling							-	115.60
maxcooling	2			4.17	18	0.04	1003.7	122.99
pulsecooling							-	118.28

B	MAS rate / kHz	mass / mg	d_1 / s	expt / h	S/N	SN/mg/√h
zg	12.5	41.07	547	0.30	94.15	4.16
	8		502	0.28	84.80	3.91
	4		333	0.19	46.01	2.60
	2		269	0.15	37.13	2.34

C	MAS rate / kHz	mass / mg	d_1 / s	expt / h	μw	S/N	SN/mg/√h
zg	12.5	38.71	905	0.50	on	2546.7	92.78
					off	105.0	3.83
	8				on	2546.4	92.77
					off	89.20	3.25
	4		605	0.34	on	1267.124	56.46
					off	50.891	2.27
	2		405	0.23	on	661.2386	36.01
					off	33.025	1.80

Table 3-4 Experimental details for data presented in Figure 3-4B. Comparison between different experimental methods for acquiring bulk ^{31}P NMR signal of GaP. A) GaP:KBr (30.25 mg : 29.89 mg) impregnated with 10 μL 16 mM TEKPol/TCE at four different spin rates. Pulsecooling and maxcooling refer to the pulse cooling scheme of Figure 3-3B without and with switching the relative phase of the proton and heteronuclear CP flanking pulses between scans, which respectively excludes and includes the contribution of the intrinsic heteronuclear build-up to the signal. B) Direct acquisition of ^{31}P on a dry sample of GaP. The recycle delay d_1 corresponds to the optimum recycle delay, calculated from the relaxation rate of the sample at each spin rate. The number of scans was two in all cases. Signal processing was performed with *RMN*, MATLAB, and TopSpin 3. The signals were processed after quadrupling the length of the FID by zero filling without exponential apodization. Signal-to-noise was analyzed by comparison with a spectrum of pure noise.

A	MAS rate / kHz	mass / mg	d_1 / s	τ_z / s	L	expt / h	S/N	SN/mg/√h
maxcooling	12.5	23.28	6	6	42	0.14	546.19	61.73
pulsecooling							289.51	32.72
maxcooling	8		5	5	51	0.14	685.49	77.48
pulsecooling							410.77	46.43
maxcooling	4		3	3	39	0.07	556.25	92.54
pulsecooling							393.20	65.41
maxcooling	2		2	2	44	0.05	291.95	56.08
pulsecooling							211.28	40.59

B	MAS rate / kHz	mass / mg	d_1 / s	expt / h	S/N	SN/mg/√h
	12.5	28.81	550.80	0.31	946.85	59.43
zg	8		381.80	0.21	834.35	62.91
	4		209.50	0.12	545.65	55.52
	2		110.70	0.06	213.92	29.97

Table 3-5 Experimental details for data presented in Figure 3-5C. Comparison between different experimental methods for acquiring bulk ^{113}Cd NMR signal of CdTe. Pulsecooling and maxcooling refer to the pulse cooling scheme of Figure 3-3B without and with switching the relative phase of the proton and heteronuclear CP flanking pulses between scans, which respectively excludes and includes the contribution of the intrinsic heteronuclear build-up to the signal. Direct acquisition of ^{113}Cd on a dry sample of CdTe was used as comparison. The number of scans was two in all cases. Signal processing was performed with *RMN*. Exponential apodization corresponding to 500 Hz (FWHM) was applied when processing the data. Direct DNP enhancement of ^{113}Cd was around 6 at 300 s.

	MAS rate / kHz	mass / mg	d_1 / s	τ_z / s	L	expt / h	S/N	SN/mg/√h
maxcooling	1	54.7	5	12.5	20	0.14	69.28	3.38
pulsecooling							51.85	2.53
zg neat	8	75.9	4610	-	-	2.56	84.01	0.69

Table 3-6. Experimental details for data presented in Figure 3-5D. Comparison between different experimental methods for acquiring bulk ^{29}Si NMR signal of SiO_2 (α-quartz). Pulsecooling and maxcooling refer to the scheme of Figure 3-3B without and with switching the relative phase of the proton and heteronuclear CP flanking pulses between scans, which excludes and includes the contribution of the intrinsic heteronuclear build-up to the signal. The result of the direct DNP scheme of Figure 3-3A is given as "zg iwi". Direct acquisition of ^{29}Si on a dry sample of SiO_2 was used as comparison. The number of scans was two in all cases. Signal processing was performed with *RMN*. Exponential apodization corresponding to 30 Hz (FWHM) was applied when processing the data.

|	MAS rate / kHz	mass / mg	d_1 / s	τ_z / s	L	expt / h	S/N	SN/mg/√h
maxcooling							901.8	12.65
pulsecooling	1	34.9	5	750	10	4.17	166.6	2.34
zg iwi			14400	-	-	8	1629.2	16.50
zg neat	2	35	22180	-	-	12.3	24.5	0.20

Parameters used in numerical simulations

Table 3-7. Parameters used in numerical simulations presented in Figure 3-2 and Figure 3-3. L_t is the diameter of the SnO_2 particle and L_s is the thickness of the radical solution layer coating the particle. $T_{B,s}$ is the build-up time in the radical solution layer. $T_{1,t}$ is the intrinsic relaxation rate of bulk SnO_2 and $T_{1,s}$ is the relaxation rate of tin nuclei on the surface of SnO_2. C_s is the proton concentration in the radical solution and C_t is the concentration of ^{119}Sn in the particle. D_s is the spin diffusion coefficient of ^1H in the radical solution and D_t is the spin diffusion coefficient for ^{119}Sn. ε_0 is the polarization enhancement of ^{119}Sn. ν_r is the MAS rate used to estimate the spin diffusion coefficients. τ_z is a polarization delay and L is the number of CP contacts used (Figure 3-2 assumes one CP contact and variable τ_z). The retention factors, f, represents the percentage of signal retained across each CP contact in the radical solution (^1H), the tin dioxide core (^{119}Sn,core) and the tin dioxide layer (^{119}Sn,layer). P_L is thickness of tin dioxide layer effected by CP. R_L is thickness of tin dioxide layer relaxed by the radical in the solvent. CS_L is thickness of the layer that leads to the surface chemical shift.

parameter	L_t	L_s	$T_{B,s}$	$T_{1,t}$	$T_{1,s}$	C_s	C_t	D_s	D_t	ε_0	ν_r	τ_z	L
value	1	150	3.35	1400	200	18	3.98	8.1×10^{-5}	3.5×10^{-8}	356	8	5	120
unit	μm	nm	s	s	s	mol.L^{-1}	mol.L^{-1}	μm^{2}s^{-1}	μm^{2}s^{-1}		kHz	s	

parameter	f_{1H}	$f_{119Sn,core}$	$f_{119Sn,layer}$	P_L	R_L	CS_L
value	88	99	90	1	0.3	0.6
unit	%	%	%	nm	nm	nm

Saturation recovery curves for neat samples
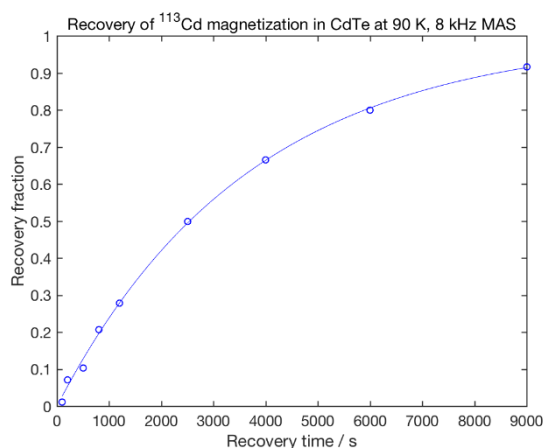
$$M_z(\tau_{rd}) = M_z \left(1 - e^{-\left(\frac{\tau_{rd}}{T_1}\right)} \right)$$

	T_1 / s
8 kHz, 90 K	3670

Figure 3-7. Saturation recovery curve for CdTe spinning 8 KHz and 90 K. The curve is fit to the data using a monoexponential model.
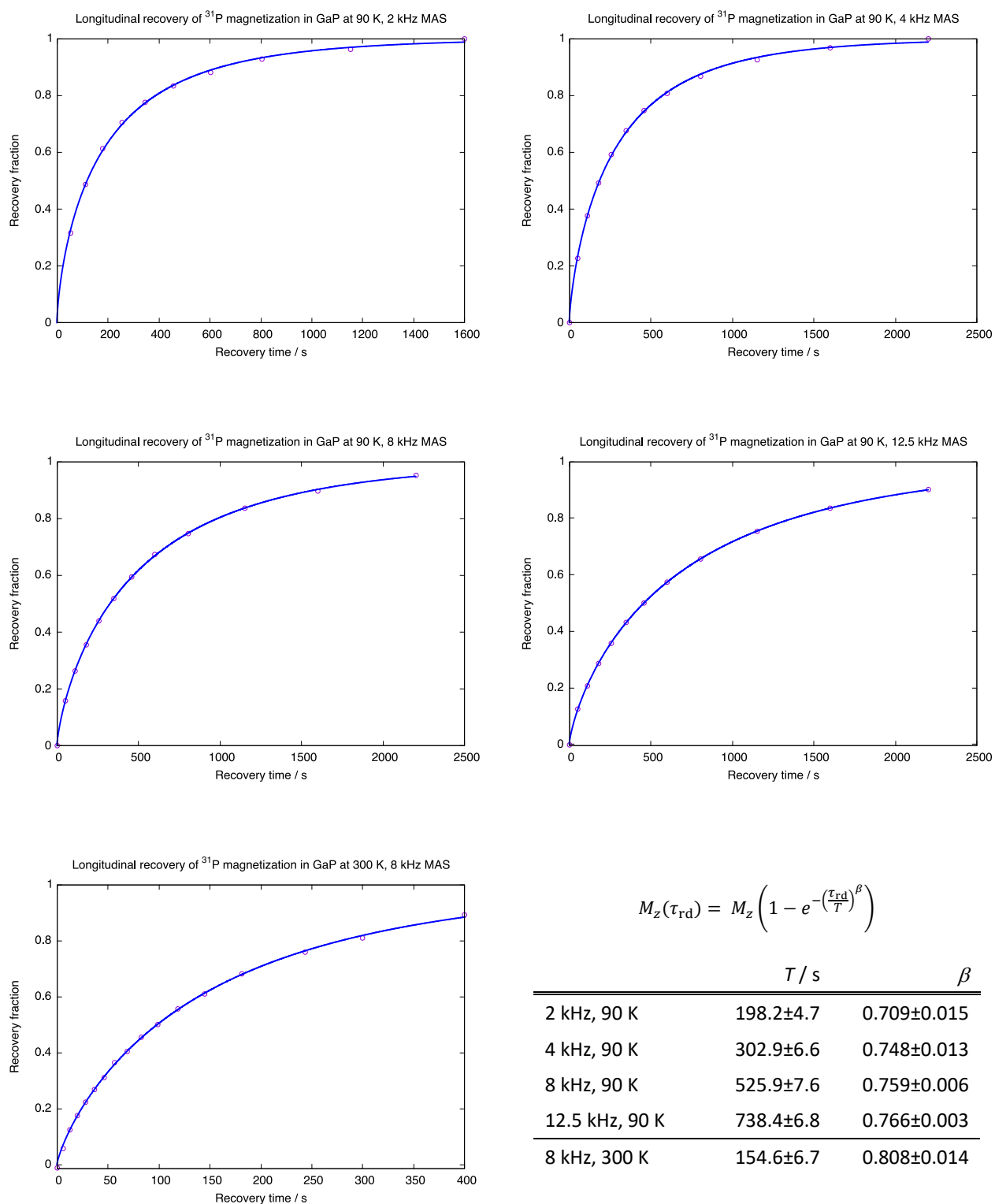
Figure 3-8. Saturation recovery curves for neat GaP spinning at four different spin rates at 90 K and at 8 KHz at 300 K. The curves are fit to the data using a stretched exponential model.

$$M_z(\tau_{\mathrm{rd}}) = M_z\left(1 - e^{-\left(\frac{\tau_{\mathrm{rd}}}{T}\right)^{\beta}}\right)$$

	T / s	β
2 kHz, 90 K	198.2±4.7	0.709±0.015
4 kHz, 90 K	302.9±6.6	0.748±0.013
8 kHz, 90 K	525.9±7.6	0.759±0.006
12.5 kHz, 90 K	738.4±6.8	0.766±0.003
8 kHz, 300 K	154.6±6.7	0.808±0.014
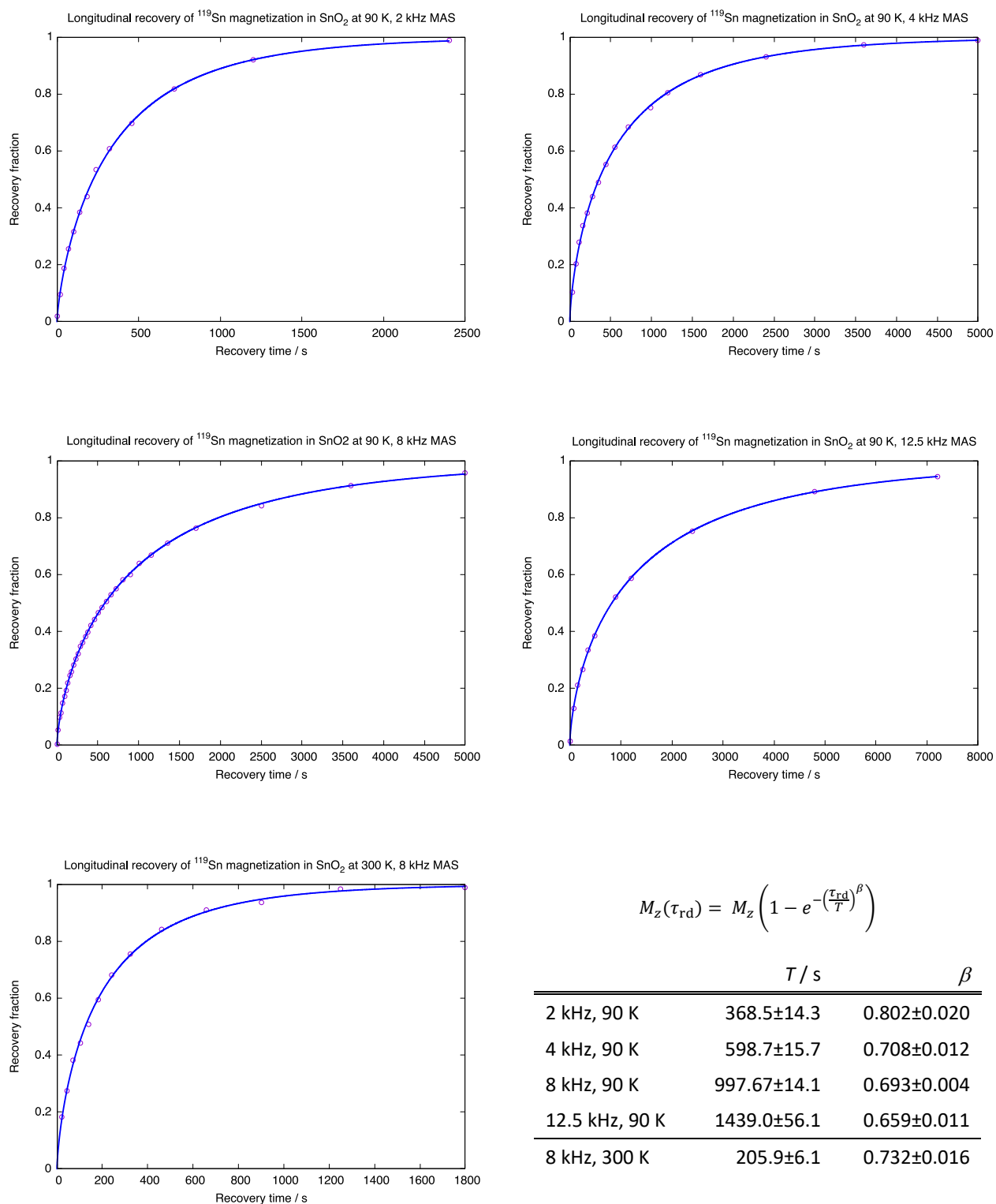
Figure 3-9. Saturation recovery curves for neat SnO2 spinning at four different spin rates at 90 K and at 8 KHz at 300 K. The curves are fit to the data using a stretched exponential model.

$$M_z(\tau_{\mathrm{rd}}) = M_z \left(1 - e^{-\left(\frac{\tau_{\mathrm{rd}}}{T}\right)^{\beta}} \right)$$

	T / s	β
2 kHz, 90 K	368.5±14.3	0.802±0.020
4 kHz, 90 K	598.7±15.7	0.708±0.012
8 kHz, 90 K	997.67±14.1	0.693±0.004
12.5 kHz, 90 K	1439.0±56.1	0.659±0.011
8 kHz, 300 K	205.9±6.1	0.732±0.016

3.2 Maximizing bulk hyperpolarization

This chapter has been adapted with permission from: "*Maximizing hyperpolarization in pulse cooling under MAS*". S. Björgvinsdóttir, B.J. Walder, N. Matthey, L. Emsley, *Journal of Magnetic resonance* **2019**, 300, 142-148. (post-print)

3.2.1 Introduction

The previous section (Section 3.1) showed how proton-free solids can be hyperpolarized using dynamic nuclear polarization (DNP) to provide significant signal enhancements in magic-angle-spinning (MAS) NMR experiments.[197] To give a brief overview, the method relies on (i) hyperpolarization of weakly magnetic nuclei at the surface of the substrate, and (ii) transport of hyperpolarization from the surface of the substrate to the bulk by spin diffusion among those weakly magnetic nuclei. To achieve this, we have previously described two approaches to implementation of the underlying concept, as shown in the schemes in Figure 3-10. The first is through direct DNP from polarization agents located in a wetting phase near the surface of the materials to nuclei of the substrate located near the surface. The second is a so-called "pulse cooling" strategy which uses a multiple-contact type cross-polarization sequence[14, 198] in which each successive CP step reestablishes thermal contact with the hyperpolarized protons in the wetting phase, and thus maintains a low surface spin temperature. In both cases the polarized spins of the substrate at the surface then undergo slow spontaneous spin diffusion to transport polarization into the bulk, hence also lowering the overall spin temperature. This process becomes especially efficient when the nuclear T_1 values in the substrate are comparatively long, and overall signal enhancements of up to a factor 50 were obtained for ^{119}Sn in SnO_2, and factors ranging from 2 to 85 for materials containing ^{31}P, ^{113}Cd, and ^{29}Si with T_1 values ranging from 200 to 10^5 seconds.

Multiple-contact CP sequences have been used to obtain quantitative ^{13}C MAS spectra,[153] to increase polarization transfer in non-spinning samples,[199] and to improve polarization transfer and enhancing signals of powders.[200]

The pulse cooling scheme used to polarize proton free solids is shown in Figure 3-10E and includes flip-forward, flip-back,[145] spin-locking, and spin diffusion elements. Each of these elements introduces parameters, as well as the number of CP contacts, that must be set properly in order to maximize sensitivity.

Here we experimentally investigate the relative importance of the various parameters in the pulse cooling sequence. We find that, in general, the sequence tolerates relatively large variations of most of the parameters without compromising sensitivity, and we find that the most critical parameters are the radio-frequency field amplitudes during the CP steps. In particular, in line with the expectation that polarization is relayed by spin diffusion between the weakly magnetic species,[197] we find that the best way to cool the bulk is to polarize the sample at a low spinning rate, where spin diffusion is relatively efficient, and then to accelerate the rate of sample spinning prior to detection, which improves line narrowing and thus sensitivity during detection. With this modulation of the rotation rate during the experiment, we improve upon the already impressive sensitivity of the pulse cooling experiment by an additional factor of over 3.5 for ^{119}Sn in SnO_2.
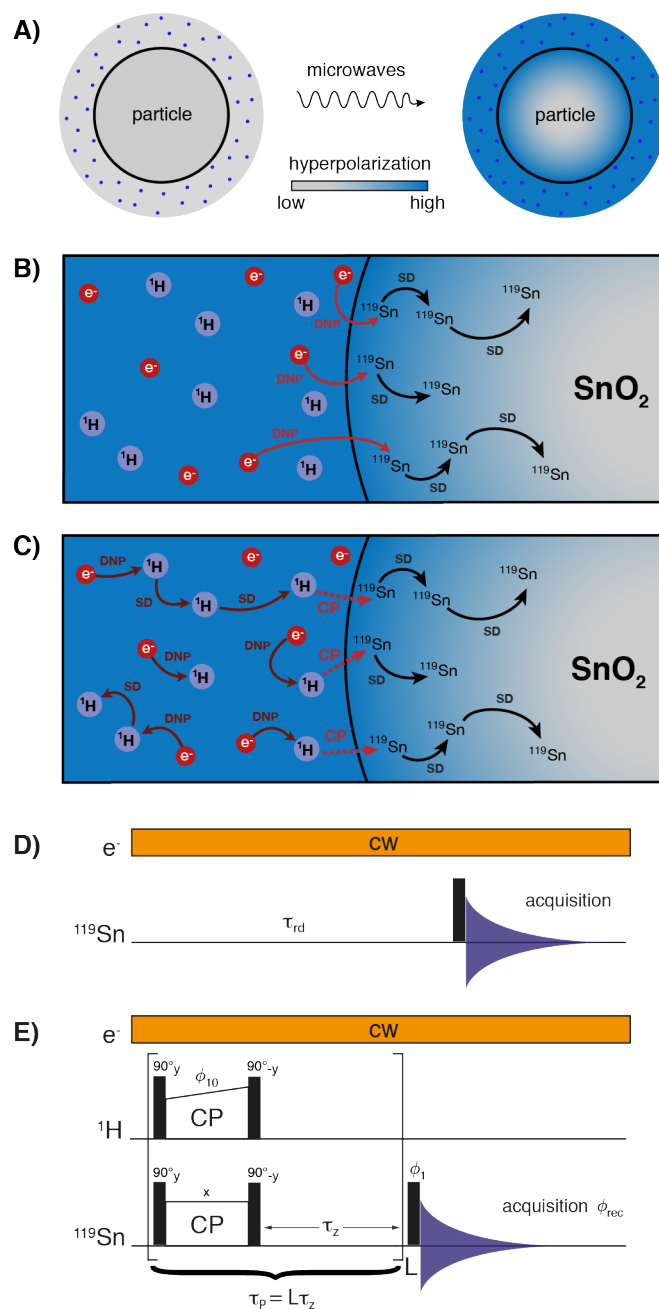
Figure 3-10. A) Schematic representation of hyperpolarization by relay from the surface. B) Direct polarization of ^{119}Sn near the surface, followed by spin diffusion. C) Hyperpolarization of surface ^{119}Sn by CP, followed by spin diffusion. D) Pulse sequence for direct DNP. E) Pulse cooling sequence using multiple-contact CP. Phase cycle φ_{10} = x, φ_1 and φ_{rec} = [y −y]. Phase cycling can be adjusted to select only ^{1}H sourced magnetization: φ_{10} = [x −x], φ_{rec} = [y −y] and φ_1 = y.

3.2.2   Experimental methods

The batch of SnO$_2$ (abcr GmbH) powder used to prepare DNP samples was described in our previous work.[197] The samples were made by impregnating[101-102] the SnO$_2$ powder (having particle sizes on the order of 1 μm) with a 16 mM solution of TEKPol[185] radical dissolved in 1,1,2,2-tetrachloroethane (TCE). The ratio in the formulations was approximately 10 μL radical solution to 40 mg of powder. The samples were deoxygenated with three thawing cycles to improve DNP enhancements.[160, 201]

Solid-state NMR experiments were carried out on a 9.4 T Bruker Avance III spectrometer coupled with a 263 GHz microwave source.[42] The samples were spun in a 3.2 mm low-temperature MAS DNP probe, at temperatures

around 90 K. The gyrotron collector current was adjusted to optimize the ^{1}H solvent signal enhancement. Radiofrequency field amplitudes of 100 kHz and a 2 ms contact time were used for cross-polarization, unless otherwise specified. The ^{1}H rf field amplitude was ramped from 90% to 100% during CP, to increase polarization transfer efficiency. Presaturation pulses were applied on both the ^{1}H and ^{119}Sn channels prior to the first polarization transfer. For the alternating spin rate version of pulse cooling, the spin rate the spin rate changes were controlled manually. More details and pulse programs are given in Appendix III.

3.2.3 Results and discussion

Efficiency in pulse cooling

In the pulse sequence of Figure 3-10E, multiple cross-polarization contacts repeatedly hyperpolarize the surface of the sample particles by DNP during the polarization period τ_P ($\tau_P = L\tau_z$). The CP blocks consist of a 90°$_y$ excitation pulse followed by spin-locks along x on both channels, followed by a 90°$_{-y}$ flip-back storage pulse that puts the magnetization back along the direction of the main magnetic field. Each block is then followed by a delay, τ_z, that allows protons in the wetting phase to repolarize under DNP while spin diffusion between the weakly magnetic nuclei transfers hyperpolarization from the surface of the sample particle towards the bulk.[197]

The overall efficiency of this method is governed by the DNP enhancements that can be obtained, either for ^{1}H nuclei close to the surface in the wetting medium for pulsed cooling or for the weakly magnetic nuclei at the surface of the sample particles for the direct DNP approach. These surface enhancements can vary significantly, depending on the substrate and the formulation. These effects are currently the subject of intense study.[61, 92, 202-204] Even here, where a single formulation is used throughout the study, we observed significant variability in DNP enhancements across experimental sessions, with the TCE ^{1}H enhancement at 8 kHz MAS ranging between 140 and 270. However, the surface DNP enhancement translates directly into the overall enhancement in a manner independent from the pulse sequence parameters, so we do not consider this further here, though it is important to keep in mind when establishing comparisons across different samples.

In a simplified model of the polarization build-up, approximating the most usual situation where the spin diffusion length is smaller than the characteristic length scale of the particles, we assume that each "flipforward-CP-flipback" cooling burst adds one unit of magnetization, with the ensuing interval of longitudinal storage τ_z chosen to be long enough such that this added magnetization is entirely transported into the bulk. During this interval, a fraction of the accumulated magnetization is lost due to relaxation. In the limit $\tau_z \ll T_1$, the amount of bulk magnetization that remains after τ_z is determined by multiplying the preexisting magnetization by the relaxation retention factor f_{relax}. In a similar fashion, we can assign a retention factor f_{burst} to each cooling burst to represent the amount of bulk magnetization that is retained across the burst of pulses, which is less than unity due to imperfections in the short pulse elements and $T_{1\rho}$ processes. Then the amplification of bulk polarization after L cycles during acquisition is given by

$$F_{\text{bulk}} = f_{\text{relax}} \frac{1 - (f_{\text{relax}} f_{\text{burst}})^L}{1 - f_{\text{relax}} f_{\text{burst}}},$$

(Eq. 3-3)

which becomes

$$F_{\text{bulk}} = \frac{f_{\text{relax}}}{1 - f_{\text{relax}} f_{\text{burst}}}$$

(Eq. 3-4)

at steady-state. Generally, between ten and twenty cooling bursts are used for pulse cooling and steady-state is approached. Using estimated values for the experimental parameters in Equation 3-4, we therefore see that small changes in the retention factors will lead to significant overall losses in the final signal intensity. For example, if

we take f_{relax} = 0.98 (such that τ_z/T_1 is about 2%), and assume that each cooling burst is 98% efficient (f_{burst} = 0.98), we find that F_{bulk} = 24.7. On the other hand, if each cooling burst is 2% less efficient in this scenario, (f_{burst} = 0.96), then F_{bulk} = 16.6, and another factor one-third of the potential magnetization build-up is lost.

In this light, it is imperative to understand the relative importance of the pulse cooling sequence parameters which influence retention of magnetization, in addition to those parameters which modulate spin diffusion. In the following sections, we look into the optimization of pulse parameters and delays in pulse cooling.

Effects of CP efficiency on pulse cooling

Figure 3-11A and B show the effect of different ^{119}Sn spin-locking rf field amplitudes and contact times on the signal-to-noise ratio of ^{119}Sn spectra in SnO$_2$. The normalized sensitivity, defined as the signal-to-noise ratio of the spectrum divided by the mass of the bulk material in the rotor and the square root of the experiment time, is increased by around 30% when going from amplitudes of 50 kHz to 125 kHz with a spin lock duration of τ_{CP} = 400 µs, with an even larger change observed when the contact time is longer. This is a striking improvement which can be rationalized by looking at the simplified model of polarization of the preceding section in greater physical detail. Changing the rf amplitude can affect the extent of polarization transfer to surface ^{119}Sn species by CP or the burst retention factor f_{burst}. A change in CP transfer efficiency is not sufficient to explain the factor of roughly one-third sensitivity gain with higher spin-locking fields, since the effect is maintained for contact times which deviate greatly from the optimum value of τ_{CP} = 2 ms, as shown in Figure 3-11A.

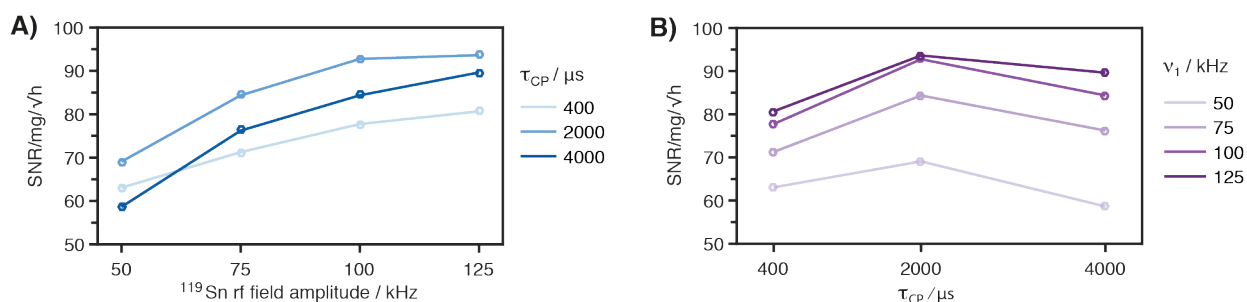Figure 3-11. Sensitivity (including intrinsic build-up of ^{119}Sn) as a function of A) spin-locking amplitude, ν_1, and B) as a function of spin lock duration, τ_{CP}. Pulse cooling parameters: τ_z = 10 s and τ_P = 120 s. The lines connecting the data points are a guide for the eye. For each of the different ^{119}Sn spin-locking fields, the amplitude of the ^{1}H spin-locking field was recalibrated using conventional (DNP enhanced) CP spectra to ensure the optimum matching conditions are fulfilled.

As is well-known, the rf amplitude has a strong influence on $T_{1\rho}$. A basic $\nu_1{}^2$ dependence might be expected for a network of like spin-½ nuclei in a rigid solid[205-206], like ^{119}Sn in SnO$_2$. This leads us to expect that $T_{1\rho}$ (^{119}Sn) at $\nu_1(^{119}$Sn) = 125 kHz is over six times larger than it is for $\nu_1(^{119}$Sn) = 50 kHz. If contributions to f_{burst} other than rotating frame relaxation are ignored, then $f_{burst} \approx 1 - \tau_{CP} / T_{1\rho}$, (assuming $\tau_{CP} \ll T_{1\rho}$), in which case f_{burst} draws substantially closer to unity when going from 50 kHz to 125 kHz (from 0.94 to 0.99). Considering that there are other sources that may contribute to loss of retention (for example fluctuating effective fields (such as those due to shielding anisotropy) leading to a less than expected gain in $T_{1\rho}$ (^{119}Sn), phase and amplitude transients, flanking pulse imperfections, etc.), any actual gain in the retention factor f_{burst} is likely to be much smaller. Nevertheless, as discussed in the previous section, small changes are still capable of producing large changes in the overall sensitivity, and we identify the $T_{1\rho}$ contribution to f_{burst} as the primary explanation of the large sensitivity gains when strong spin-locking fields are used in pulse cooling.

We also note that, in addition to the trend towards better pulse cooling sensitivity with increasing rf amplitude shown in Figure 3-11A, stronger spin-locking fields also attenuate the performance drop-off at contact times which

are longer than optimal, as shown in Figure 3-11B. This is consistent with the idea of a significant $T_{1\rho}$ (^{119}Sn) contribution to f_{burst}.

Regardless of details, higher spin locking fields should not, in general, inhibit efficient CP transfer, but they should allow for greater retention of magnetization (higher f_{burst} values) due to less efficient $T_{1\rho}$ relaxation. Thus, as a general rule, we conclude that one should use the highest spin-locking amplitudes that can be safely handled by the equipment.

Tolerance to misset and offset effects

The ^{119}Sn spectrum of SnO_2 only has one chemical shift, but its offset from the transmitter frequency can be used to simulate the effect on a system with more than one distinct chemical shift, where off-resonance irradiation is inevitable. Figure 3-12 shows how the signal intensity in the ^{119}Sn spectra of SnO_2 changes when the ^{119}Sn pulses are applied up to ±100 kHz off resonance and when the pulse and spin lock amplitudes are misset (by ±20 kHz from an ideal value of 100 kHz). As expected we see a gradual decline in intensity as a function of both offset and misset. For offset we note that >85% of the on-resonance intensity for a well calibrated 100 kHz 90° pulse is retained over a region of about 30 kHz. For misset of the pulse flip angle and the spin lock amplitude, at least 60% of the on-resonance intensity is retained for ±10% change in ^{119}Sn channel rf amplitude.
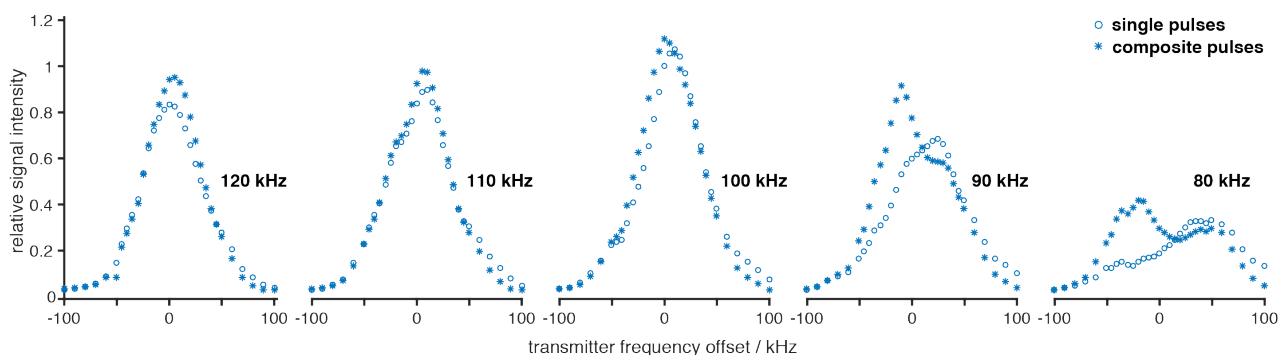

Figure 3-12. Effect of carrier frequency offset on the intensity of the ^{119}Sn signal in a pulsed cooling spectrum of impregnated SnO_2 spinning at 8 kHz, for ^{119}Sn rf frequency amplitudes ranging from 80-120 kHz, obtained with either single or composite pulses. The signal intensity is relative to that of a 100 kHz 90°pulse at 0 offset. Pulse cooling parameters: τ_z = 10 s and τ_P = 120 s.

An asymmetric appearance of the offset profiles about zero is notable, and particularly prominent for negative rf amplitude missets. In a conventional CP experiment, where the only pulse on the observe channel is the contact pulse, offset profiles are expected to be symmetric about zero. This is because the transverse component of magnetization is proportional to cos(ν_{off}/ ν_{eff}), which is an even function of the sign of the offset frequency ν_{off} (ν_{eff} refers to the effective field amplitude), and misset only affects the magnitude of the transfer. Multiple contact CP sequences such as pulse cooling, however, introduce the need to control the trajectory of magnetization across each CP burst. After each storage delay, the magnetization must be placed along the effective field axis, *and* returned to longitudinal storage after the transfer step is complete. Since the effective field direction depends on the sign of the offset, the performance of flip-forward and flip-back pulse elements, and the burst as a whole, also depends on the sign of the offset. For example, at severe negative rf amplitude missets, the single pulse elements have a flip-angle that is less than 90°, such that after excitation the magnetization is best aligned with a spin-locking field that possesses a positive offset. This leads to the "right-weighted" offset profile at 80 kHz rf amplitude shown in Figure 3-12.

Composite pulses can make pulse sequences more tolerant to resonance offset and misset pulse flip-angles.[207] Recently, Duan and Schmidt-Rohr developed a pair of composite pulses for excitation and storage in multiple

contact CP with composite pulses on the observe channel.[208] The excitation pulse becomes $90°_{270}180°_{45}$. Similarly, the storage pulse becomes $180°_{135}90°_{270}$. This pair of pulses are respectively designed to place the magnetization along and restore magnetization from the effective spin-locking field direction under conditions of offset and misset. In our experiments for pulse cooling, we find that these composite pulses (on the ^{119}Sn channel; composite pulses have not been tested on the ^{1}H channel) usually provide higher overall intensity. As might be expected, the improvement is most noticeable in cases where the rf field amplitude on the ^{119}Sn channel is lower than 100 kHz, where the spin-locking field is both less efficient and the nominal 90° pulse has a flip-angle that is too small. As an example, for 90 kHz ^{119}Sn amplitude and roughly -20 kHz transmitter offsets, the composite pulses can provide improvements up to a factor of 1.9 relative to the version implementing single pulses. We also note that these composite pulses tend to improve the symmetry of the offset profiles, particularly for the offset profile at 80 kHz rf amplitude. This is to be expected on the basis of their design principles.

Applying an amplitude ramp on one of the two B_1 fields during CP is known to increase the efficiency of polarization transfer.[16, 186, 209-210] The results presented here all have the ^{1}H rf field amplitude ramped from 90-100% during each spin-locking period. Adiabatic ^{1}H frequency sweeps[211] broaden the HH matching condition and might make the pulse cooling experiment even more tolerant to misset of the spin-locking fields. However, we have not found any significant improvement using frequency sweeps (see Figure 3-16 in Appendix III).

Choice of polarization and repetition times

In addition to pulse elements, the pulse cooling sequence also contains spin diffusion elements that need to be set properly in order to maximize polarization relay into the bulk of the material. The polarization gain is sensitive to the balance between the build-up rate of the compound, the rate of homonuclear spin diffusion, and the rate of T_1 relaxation. Therefore, selection of the polarization period, τ_P and the storage interval, τ_z, is important for efficient pulse cooling.

These parameters can be optimized experimentally for each spin rate as shown in Figure 3-13. The delay after each CP contact, τ_z, should in general be longer than the ^{1}H build-up time in the wetting phase, $T_{B,H}$. The polarization period τ_P ($\tau_P = L\tau_z$) should be long enough so that hyperpolarization transferred from the surface by spin diffusion can accumulate in the bulk, but shorter than the intrinsic T_1 of ^{119}Sn in SnO_2. We find that there is a correlation between parameters, the value of τ_z which leads to optimal sensitivity increases as τ_P increases. Nonetheless, taking 8 kHz MAS as an example, over 70% of the maximum sensitivity is retained over a range of τ_z = 5-50 s and τ_P = 100-500 s. The changes in sensitivity are observable, but not significant over a range of values of τ_P, τ_z and L, which shows that the method is fairly tolerant to imprecise setting of these values, at least when sensitivity enhancements are high. In general, setting the number of CP steps, L, to be 10-20 is a good rule of thumb. Exceptions might be when T_1 is comparable to the build-up time, in which case a smaller number of cycles will be preferred, or when the diffusion constant is very large, in which case shorter τ_z might be required with a larger number of repetitions.
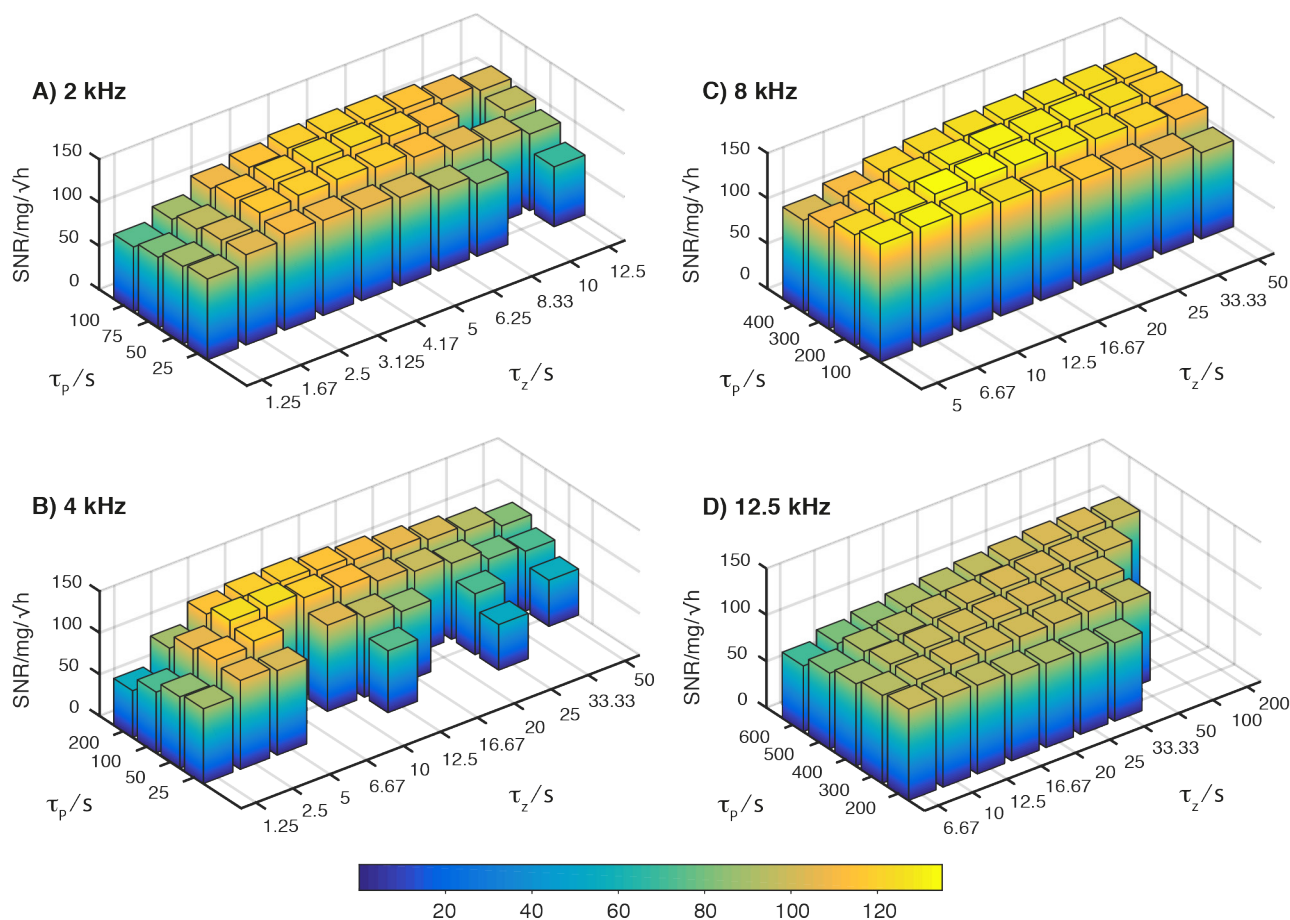
Figure 3-13. Optimization of the fully normalized sensitivity of the ^{1}H-^{119}Sn DNP enhanced spectra of SnO$_2$ impregnated with 16 mM TEKPol in TCE using the pulse cooling experiment for NMR signal acquisition. The fully normalized sensitivity is defined as signal-to-noise ratio divided by the mass of the bulk material in the rotor and the square root of the experiment time. The spectra were recorded at a MAS rate of A) 2 kHz, B) 4 kHz, C) 8 kHz and D) 12.5 kHz. The radio-frequency field amplitude during CP was adjusted to compensate for changes in transfer efficiency at each different spin rate.

The difference in the optimum τ_P and τ_z values for different spin rates can be explained by spinning induced changes in the intrinsic build-up of bulk ^{119}Sn polarization relative to the build-up rates of the surface protons. The intrinsic build-up of bulk ^{119}Sn is defined as the contribution from ^{119}Sn that does not arise by CP from hyperpolarized protons, i.e., it includes signal from hyperpolarized ^{119}Sn originating from direct DNP (with or without relay), or thermally polarized ^{119}Sn.

Figure 3-14 plots the normalized sensitivity values of the bulk ^{119}Sn signal in SnO$_2$ spinning at 8 kHz, obtained with different phase cycles that selectively included or excluded the intrinsic contribution to the bulk signal. The sensitivities are plotted as a function of τ_z for four different polarization delays, τ_P = 120 s, 240 s, 360 s, and 480 s. The build-up of proton polarization in the wetting phase by DNP is orders of magnitude faster than that of the build-up of thermal ^{119}Sn polarization, which is why the sensitivities are similar for values of τ_z up to the build-up rate of proton magnetization (here up to about 10 seconds). For longer τ_z the additional signal from polarization pathways including direct ^{119}Sn DNP becomes significant, and leads to significantly higher sensitivity than the ^{1}H sourced experiment.
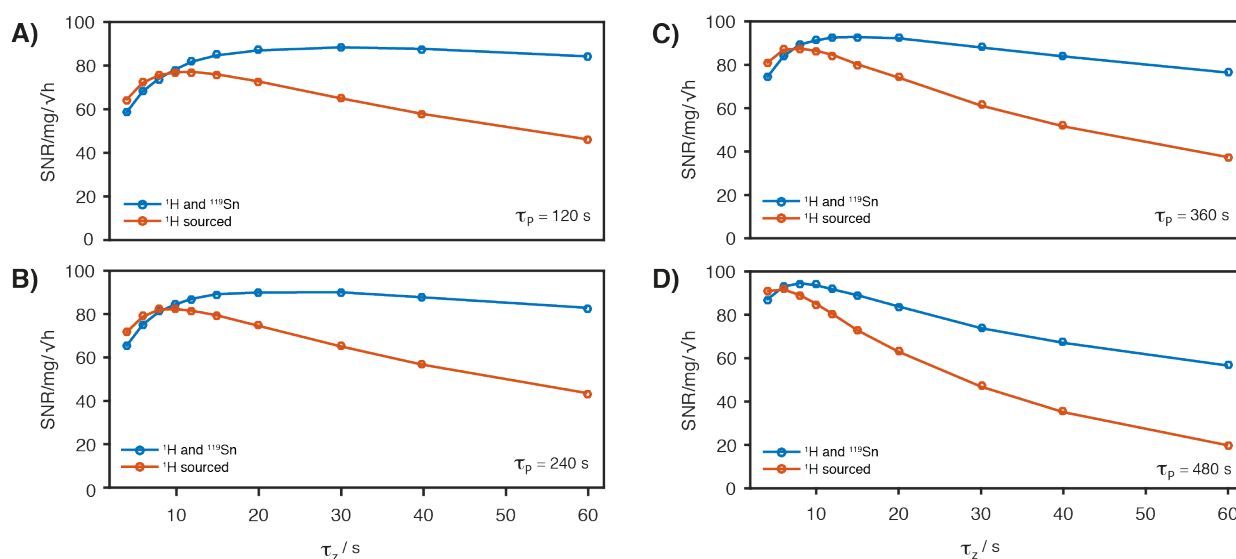
Figure 3-14. Comparison of the normalized sensitivity between pulse cooling experiments including intrinsic build-up of ^{119}Sn (^{1}H and ^{119}Sn, blue) and pulse cooling excluding intrinsic ^{119}Sn build-up (^{1}H sourced, red), at four different polarization delays, τ_P. The sample is SnO$_2$ impregnated with 16 mM TEKPol in TCE, spinning at 8 kHz MAS. The CP spin lock amplitude was ν_1 = 125 kHz and the contact time 2 ms. Solid lines are a guide for the eye. See Appendix III for different spin lock parameters.

Spin-up pulse cooling

The rate of spin diffusion slows down as the MAS rate is increased, when homonuclear dipolar interactions are averaged more efficiently.[120, 135, 190-191] However, sensitivity is lower at slow spin rates due to an increase in the number of spinning side bands in the presence of significant chemical shift anisotropy. In light of this, we present a version of pulse cooling (Figure 3-15A) where the multiple CP contacts are performed at a low MAS rate, ν_{pol}, to benefit from more efficient spin diffusion, while the FID is detected at a higher spin rate, ν_{aq}, to maximize sensitivity where the spinning side bands are reduced. The modified pulse sequence has two additional delays, τ_{up} and τ_{down}, which are used to change the MAS rate. We note that spin rate acceleration and deceleration during an experiment has been proposed previously for correlating static patterns to isotropic chemical shifts,[212] and for broadening CP matching conditions[213]. It has also been used in the context of DNP before (but in the opposite sense, polarizing with a spinning sample and detecting on a static sample for quadrupolar nuclei).[214]

Figure 3-15C shows the results obtained for a series of combinations of spinning rates. We see that a polarization spin rate, ν_{pol}, of 500 Hz results in the highest sensitivity for all acquisition spin rates, ν_{aq}. Polarizing at higher spin rates provides less of a gain, as the dipolar couplings are averaged out more efficiently, slowing down spin diffusion. When the MAS rate is higher than the strength of the dipolar couplings the rate of spin diffusion is usually inversely proportional to ν_r.[133, 135, 190-191] In this regime we find, for example, that if the spin rate is decreased from 8 kHz to 4 kHz during the polarization period, the sensitivity goes from 62 to 101, which is not far from the expected factor of 2, especially when the additional spinning sidebands at 4 kHz are considered. The pulse cooling parameters, τ_P and τ_z, used in each experiment are optimal for the spin rate used during the polarization period, ν_{pol}.
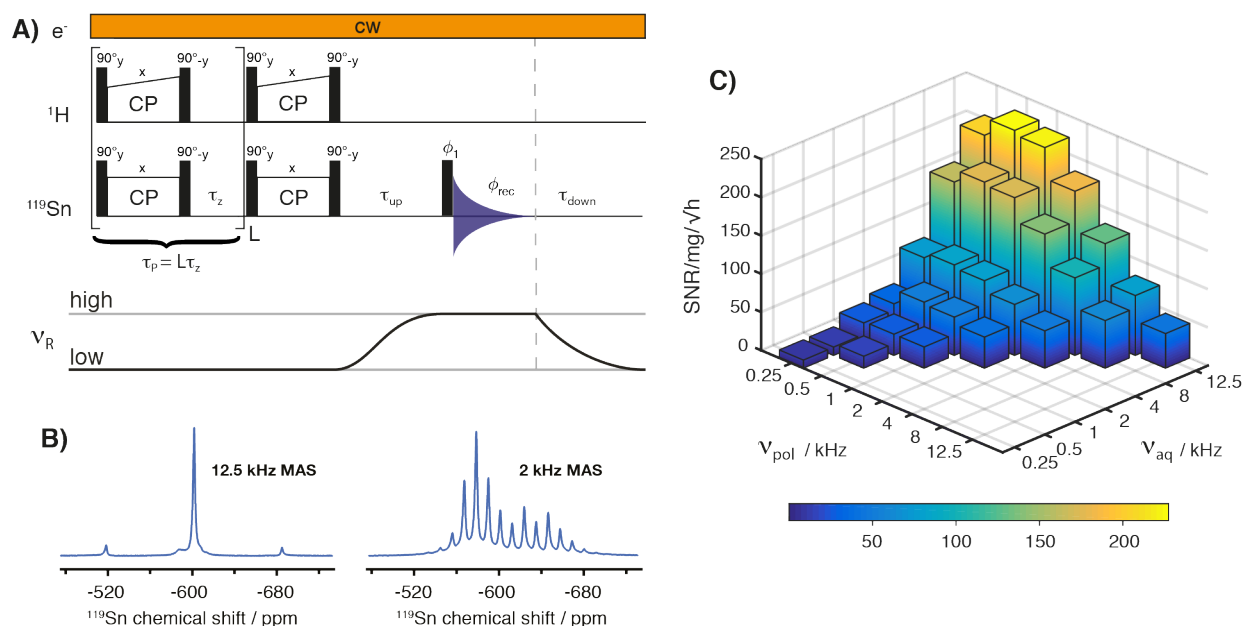
Figure 3-15. A) The pulse cooling sequence with MAS rate changes before and after acquisition. B) ^{1}H-^{119}Sn CP spectra of SnO$_2$ at two different spin rates. C) Sensitivity enhancements observed by using the pulse sequence in panel A. The numerical values which have been plotted are given in Table 3-9 in Appendix III. The pulse cooling parameters for each experiment are optimal for ν_{pol} and are given in Table 3-10.

We also note that polarizing at 250 Hz also results in lower sensitivity than at 500 Hz. This is possibly because 250 Hz is less than the strength of the estimated dipolar couplings in SnO$_2$, and hence spin diffusion is entering the quasi-static regime. It is known that slow spinning rates usually enhance spin diffusion rates as compared to the spin diffusion rate in a static sample.[139-140]

For a single spin rate, the balance between the rate of diffusion and the efficiency of CSA averaging is most favorable for SnO$_2$ at 8 kHz (it is the highest peak on the diagonal of Figure 3-15C).

The maximum length of the acceleration delay, τ_{up}, imposes a practical limitation on the difference between the high and low spin rate. If the delay is too long, part of the signal will be lost to relaxation effects. Here, all the acceleration and deceleration delays were 30 s which allows sufficient time to go from 250 Hz to 12500 Hz. We note that the spin rate modulation proposed here can in principle also be used in the direct DNP approach, by spinning up at the end of the relatively long recycle delay.

3.2.4   Conclusion

We have shown how parameters relating to specific elements in the pulse cooling method can be optimized experimentally. This is demonstrated on SnO$_2$, and we find that in general well calibrated pulses and high spin lock powers are beneficial for obtaining the best sensitivity. We also show how to select the delays and number of contacts in the pulse sequence in order to maximize polarization relay to the bulk. A variation of pulse cooling is presented where the rotation rate of the sample is modulated during the experiment, providing an additional gain in sensitivity of a factor of 3.5 for ^{119}Sn in SnO$_2$.

As a general guide for navigating the multidimensional parameter space presented in this work, we issue the following recommendations for setting up pulse cooling on an unknown sample:

i) use the highest spin locking power that can be safely tolerated by the instrument;

ii) ensure that the pulses which flank the CP bursts are calibrated well, using the composite pulses of Duan and Schmidt-Rohr[208] to further improve robustness toward misset and offset if needed;

iii) set the polarization delay τ_P to be on the order of the intrinsic nuclear T_1 of the species that is to be detected;

iv) set the number of CP contacts to between 10 and 20; and

v) spin the sample slowly, using the spin-up version of the experiment to improve resolution and sensitivity if necessary.

3.2.5   Appendix III

Additional experimental data and parameters
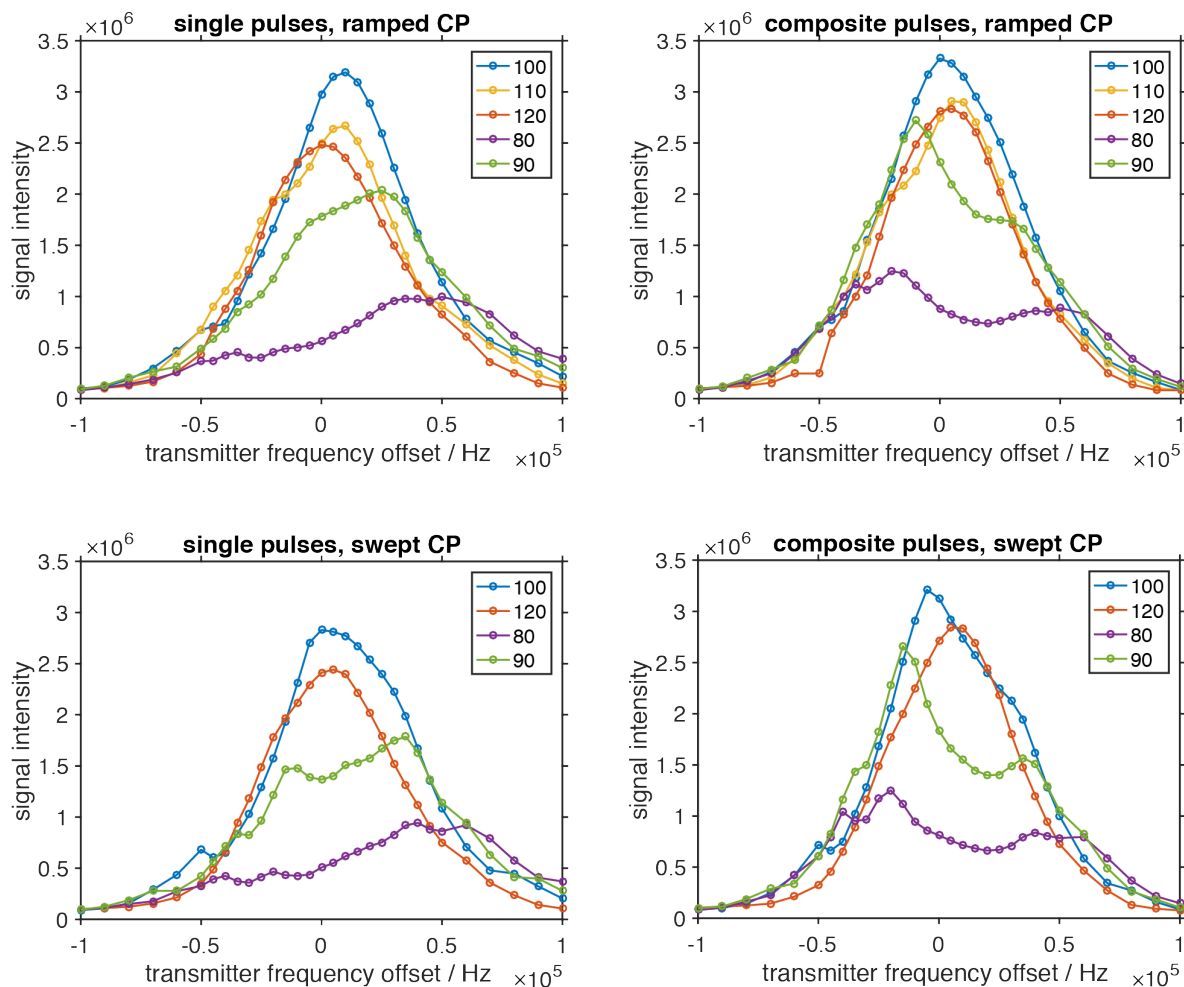
Figure 3-16. Signal intensities of DNP enhanced ^{119}Sn spectra of SnO_2 as a function of transmitter offset. The spectra were recorded at 90 K and 8 kHz MAS. The numbers in the legend correspond to the rf amplitude of the ^{119}Sn channel in kHz. The composite pulse pair is $90°_{270}180°_{45}$ for excitation and $180°_{135}90°_{270}$ for storage. The ^{1}H ramp during CP is a 90-100% ramp. Frequency sweeps on the ^{1}H channel during CP go from 0-75 kHz, starting from a 105 kHz rf amplitude. The lines connecting the data points are a guide for the eye. Each panel is plotted on the same arbitrary intensity scale.

Table 3-8. Experimental NMR parameters used to acquire the data presented in Section 3.2.3. The DNP enhancement, ε_H, of the bulk solvent at 8 kHz MAS ranged from 140-270. For example, in Figure 3-13, $\varepsilon_H = 245$.

	Figure 3-11 and Figure 3-14	Figure 3-12 and Figure 3-15	Figure 3-13
Size of FID / real points	2048	16384	2048
Acquisition time / ms	8.2	16.3	8.2
Spectral width / kHz	125	500	125
Number of scans	2	2	2
CP contact time / ms	0.4-4	2	1.5

Table 3-9. Data plotted in Figure 3-15. Normalized sensitivity, SNR/mg/√h, of ^{119}Sn spectra of SnO$_2$, acquired with the pulse cooling method. The uncertainty on the MAS rate was maximum ±50 Hz, when $\nu_{pol} \leq 500$ Hz and $\nu_{aq} = 12500$ Hz, and lower for other combinations of ν_{pol} and ν_{aq}.

		Polarization MAS rate ν_{pol} / Hz						
		250	500	1000	2000	4000	8000	12500
Acquisition MAS rate ν_{aq} / Hz	250	10.6	11.0	25.8	34.1	77.7	159.9	204.4
	500		15.6	27.8	52.9	84.9	176.5	227.4
	1000			27.7	50.0	81.0	172.8	221.7
	2000				40.6	66.6	141.9	181.3
	4000					48.8	101.3	129.4
	8000						62.2	78.3
	12500							45.2

Table 3-10. Optimized values of τ_z, τ_P and L used for the polarization period in pulse cooling with spin rate modulation, of an impregnated sample of SnO$_2$. The parameters are determined experimentally, as shown in Figure 3-13 in the main text.

ν_{pol}	τ_z / s	L	τ_P / s
250 Hz	2.5	12	30
500 Hz	2.5	12	30
1 kHz	3	15	45
2 kHz	4.17	18	75
4 kHz	5	20	100
8 kHz	12.5	16	200
12.5 kHz	50	8	400

Figure 3-17. Sensitivity in pulse cooling with a 50 kHz spin lock amplitude and different spin lock durations. Each bar chart shows the fully normalized sensitivity of ^{119}Sn spectra of a DNP sample of SnO_2, for different polarization and repetition times. The number of scans was 2 in all cases and the noise was estimated to be constant for all experiments (value of 478). The mass of SnO_2 in the rotor was 44 mg.
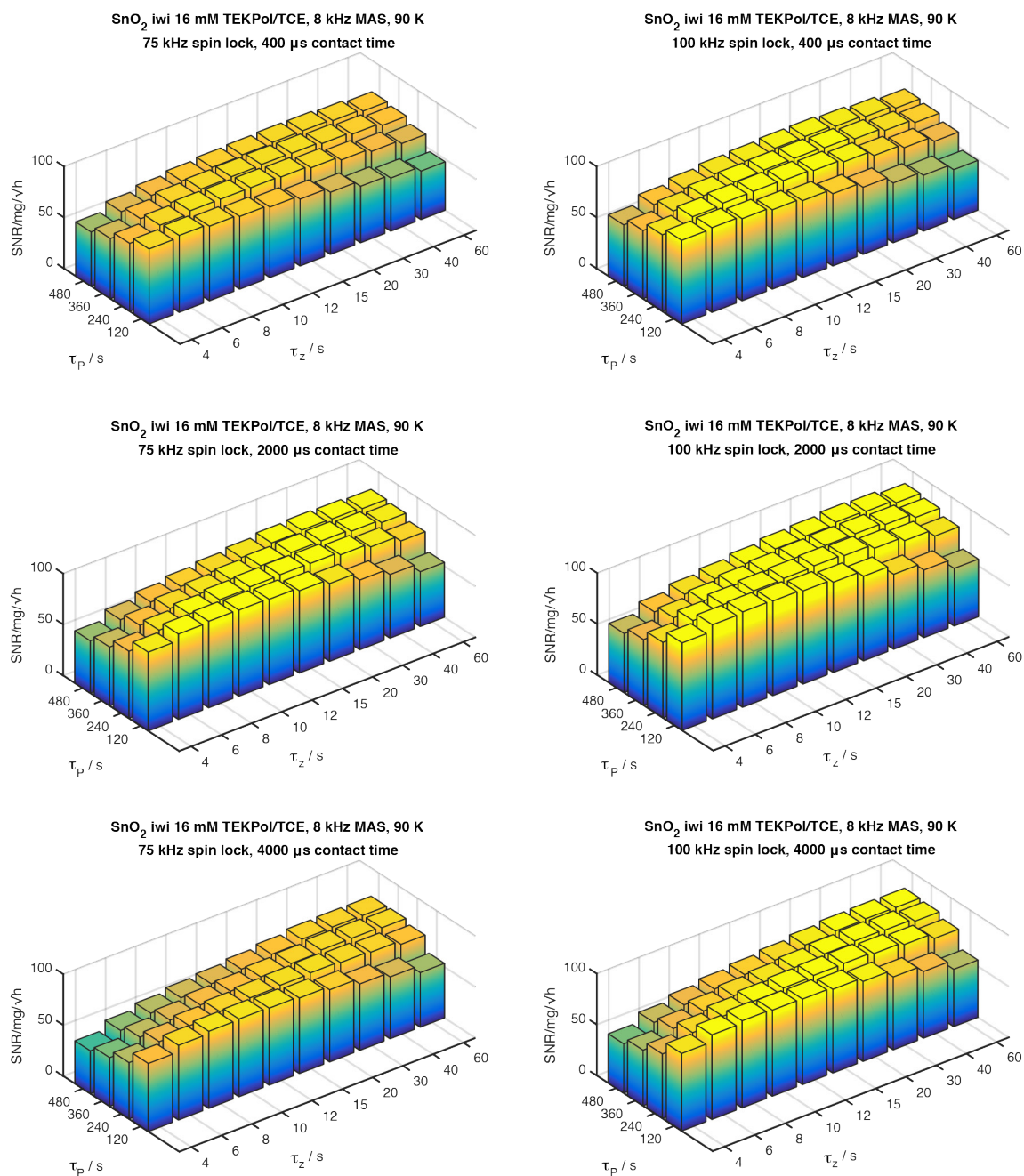
Figure 3-18. Sensitivity in pulse cooling with a 75 kHz spin lock amplitude and different spin lock durations. Each bar chart shows the fully normalized sensitivity of ^{119}Sn spectra of a DNP sample of SnO_2, for different polarization and repetition times. The number of scans was 2 in all cases and the noise was estimated to be constant for all experiments (value of 478). The mass of SnO_2 in the rotor was 44 mg.
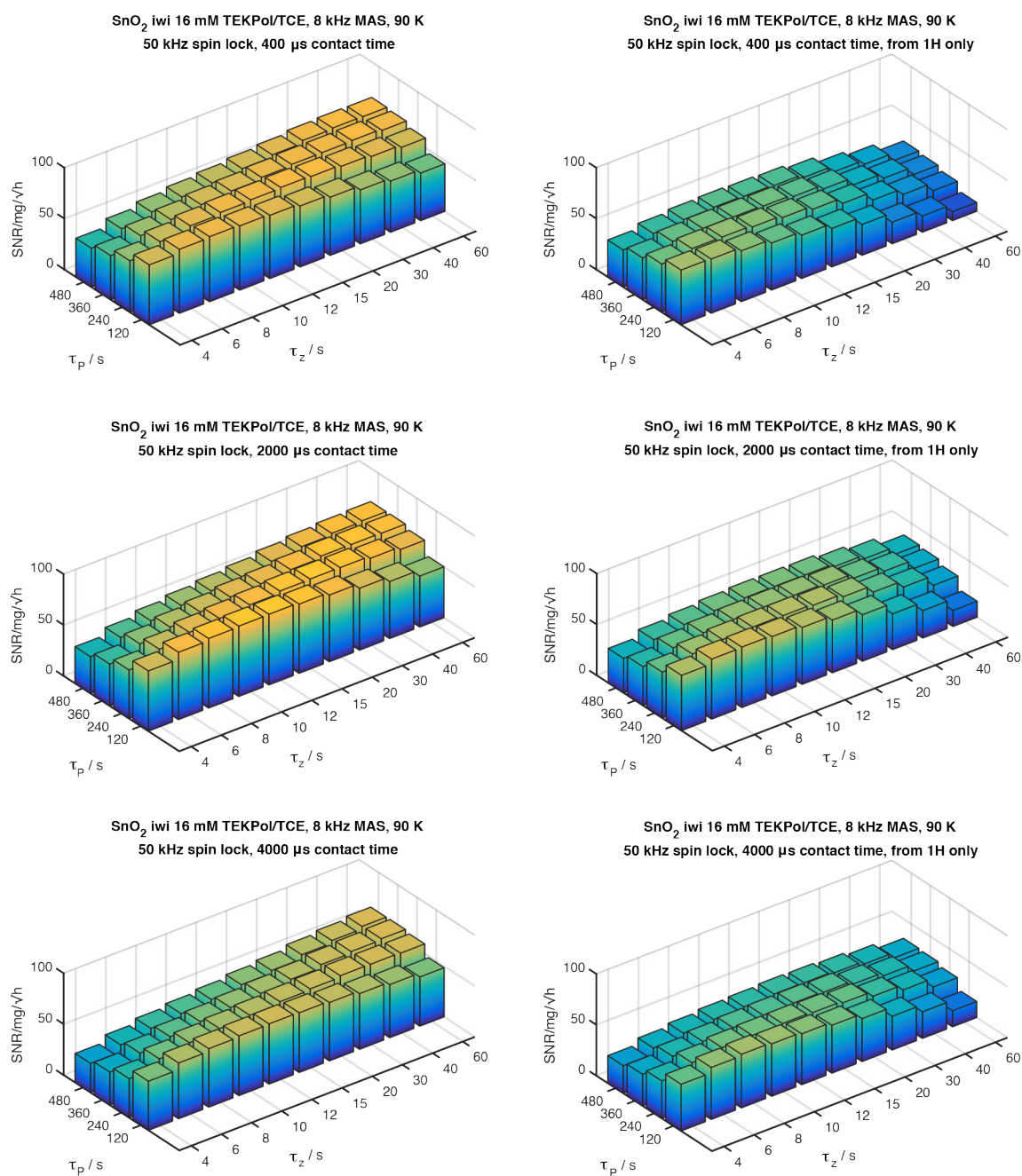
Figure 3-19. Sensitivity in pulse cooling with a 125 kHz spin lock amplitude and different spin lock durations. Each bar chart shows the fully normalized sensitivity of ^{119}Sn spectra of a DNP sample of SnO_2, for different polarization and repetition times. The number of scans was 2 in all cases and the noise was estimated to be constant for all experiments (value of 478). The mass of SnO_2 in the rotor was 44 mg.
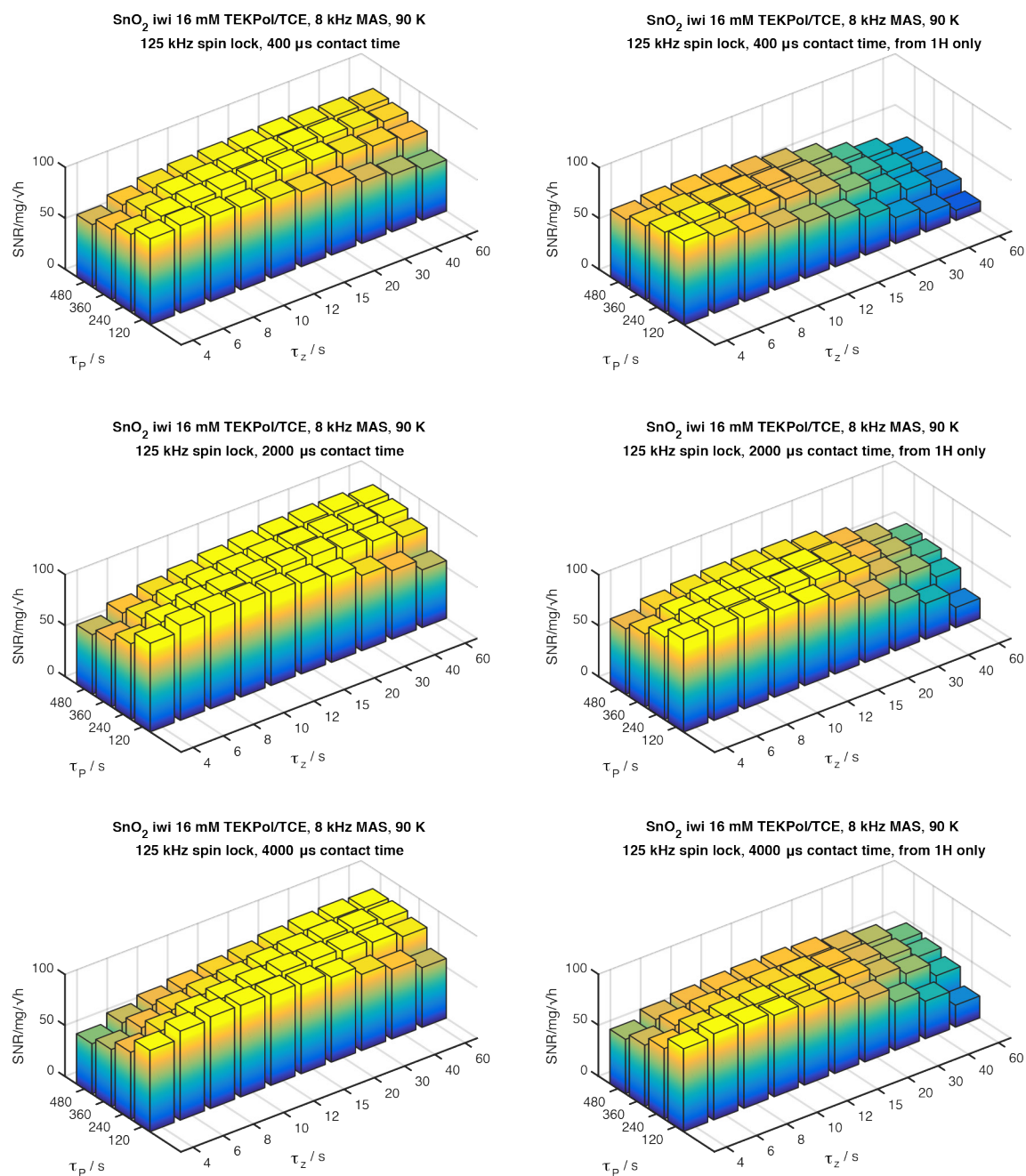
Pulse program

```
;$DIR=/opt/topspin3.5pl6/exp/stan/nmr/lists/pp/user/pulsecooling
;$CLASS=Solids
;$DIM=1D
;$TYPE=cross polarization
;$COMMENT=cross polarization with multiple cp contacts for hyperpolarization relay
;  See S. Bjoergvinsdottir, B. J. Walder, N. Matthey, L. Emsley, J. Magn. Reson. (2019)
;  OPTIONS: Presaturation, flanking composite pulse elements
;  Avance III, TopSpin 3.5.6 version
;
; WARNING: This pulse sequence is provided only as a guide for experienced users to
implement with all due care and attention.
; It may contain mistakes. Improper setting of any of the parameters may cause damage to
the spectrometer or the probes.
; ALL PROTECTIONS HAVE BEEN REMOVED !!
; The authors nor their employers accept any responsibility for loss or damage associated
with the use of this sequence.
; Any copy or modification of this sequence should also contain this entire header.


;ns 2-step phase cycle
;spnam0 1H contact pulse shape, e.g. square or ramp
;spnam17 excitation composite pulse
;spnam18 storage composite pulse
;p1 X pulse (pl1)
;p8 X flanking pulse (pl8)
;p9 1H flanking pulse (pl2)
;p15 contact time
;p31 1H decoupling pulse length
;pl1 final excitation 90 pulse
;pl2 1H pulse power
;pl8 X flanking pulse power
;pl10 1H contact power
;pl11 X contact power
;pl12 decoupling power level
;pcpd2 1H decoupling program pulse
;d1 recycle delay
;d15 longitudinal storage period
;l15 number of contact periods in loop
;cnst31 spin rate / Hz
;cpdprg2 cw, tppm, spinal (pl12)

;zgoptns -Dsat -Dcmp
;p17 length of excitation composite pulse (pl17)
;p18 length of storage composite pulse (pl18)
;pl17 excitation composite base power level
;pl18 storage composite base power level
;p20 X saturation pulse length
;p21 1H saturation pulse length
;pl20 X saturation pulse power
;pl21 1H saturation pulse power
;l20 saturation pulse loops
;d10 final z-filter delay
;d20 saturation delay

#include <Avance.incl>

"p30=p31-0.4u"

1  ze
2  10m
3  1u do:f2                          ;recycle delay, decoupler off

#ifdef sat
   3u pl20:f1 pl21:f2
20 d20
   p20:f1 ph20^
   1u
```

```
   p21:f2 ph21^
   lo to 20 times l20
#endif ;sat

   d1
4  1u

#ifndef cmp
   (ralign (p8 pl8 ph7):f1 (p9 pl2 ph9):f2)
   (p15 pl11 ph11):f1 (p15:spf0 pl10 ph10):f2        ;contact pulse with square or ramp
   (p8 pl8 ph8):f1 (p9 pl2 ph19):f2
#endif ;cmp
#ifdef cmp                                           ;composite flip-forward/flip-back
pulses by -Dcmp
   (ralign (p17:spf17 pl17 ph16):f1 (p9 pl2 ph9):f2)
   (p15 pl11 ph11):f1 (p15:spf0 pl10 ph10):f2        ;contact pulse with square or ramp
   (p18:spf18 pl18 ph16):f1 (p9 pl2 ph19):f2
#endif ;cmp

   d15                                               ;spin diffusion delay
   lo to 4 times l15
   (p1 ph1 pl1):f1                                   ;ordinary excitation pulse
   go=3 ph31
   1m do:f2
   10m mc #0 to 2 F0(zd)
exit

ph1=  1 3
ph7=  1
ph8=  3
ph9=  1
ph10= 0
ph11= 0
ph16= 0
ph19= 3
ph20= 0 1
ph21= 0 1
ph30= 0
ph31= 1 3

;for selecting only proton sourced hyperpolarization the phase cycle should be:
;ph1=  1
;ph7=  1
;ph8=  3
;ph9=  1
;ph10= 0 2
;ph11= 0
;ph16= 0
;ph19= 3
;ph20= 0 1
;ph21= 0 1
;ph30= 0
;ph31= 1 3
```

3.3 Surface and bulk hyperpolarization of lithium titanates

This chapter has been adapted with permission from: *"Sensitivity enhancement in lithium titanates by incipient wetness impregnation DNP NMR"*. S. Björgvinsdóttir, P. Moutzouri, P. Berruyer, M.A. Hope, L. Emsley, *Journal of Physical Chemistry C* **2020**, 124, 30, 16524-16528. (post-print)

3.3.1 Introduction

Lithium oxides are increasingly important in many areas of materials chemistry today, with lithium titanates being of particular interest as anode materials in solid-state batteries.[215-217] Understanding and then improving the performance of these materials depends crucially on experimentally determining the atomic-level structures and electronic environments of the materials. Solid-state NMR is a method of choice for these systems, as it can provide atomic-level information even in disordered materials, and such studies have been a primary source of structural data for developments in battery technology over the last decade or so.[6, 218]

However, the aforementioned intrinsically low sensitivity of NMR is a handicap to further development, and as a result there has been intense effort put into improving solid-state NMR sensitivity in lithiated materials, with recent examples using dynamic nuclear polarization (DNP) being particularly promising.[219-221] This has included endogenous DNP where battery materials are doped with paramagnetic ions to enhance bulk sensitivity,[73-74] lithium metal Overhauser DNP,[222] or ^{6}Li DNP combined with REDOR to measure Li-C distances in a frozen ionic liquid electrolyte.[223]

Here we use the method presented in Section 3.1, which is based on incipient wetness impregnation cross-effect (CE) DNP, to increase the sensitivity in the lithium NMR spectra of lithium titanates. This is demonstrated on two different lithium titanate materials, Li_2TiO_3 and $Li_4Ti_5O_{12}$, with high gains in sensitivity for both the surface and the bulk spectra of these compounds. We also show that polarization is relayed from the surface to the bulk for both ^{7}Li and ^{6}Li.

3.3.2 Experimental methods

Sample preparation. As received monoclinic Li_2TiO_3 (Sigma Aldrich, 80 mesh, 177 μm sieve opening) and spinel $Li_4Ti_5O_{12}$ (Sigma Aldrich, <200 nm particles) were ground by hand and impregnated with a 16 mM solution of the TEKPol[58] biradical dissolved in 1,1,2,2-tetrachloroethane (TCE), following previously described protocols.[101, 106] Scanning electron microscope (SEM) images of the powders after grinding show particles including agglomerates (Figure 3-20).

DNP enhanced NMR spectroscopy. Solid-state NMR spectra were acquired on a 9.4 T Bruker Avance III spectrometer equipped with a 264.6 GHz klystron microwave source. The sweep coil of the main magnetic field was set so that the microwave irradiation gave the maximum positive ^{1}H enhancement for a binitroxide radical. The formulated lithium titanate samples, in 3.2 mm sapphire rotors, were inserted into a pre-cooled DNP LTMAS probe and spun at temperatures of around 90 K. Both DNP samples were subjected to 3 freeze-thaw cycles before spinning, in order to improve solvent enhancements.[160] All spectra were collected at an MAS rate of 8 kHz, and their chemical shift was referenced to literature values.[74, 224] DNP enhancements, ε, were determined by the ratio of the intensities of the spectra acquired with and without microwaves ($\varepsilon = I_{on} / I_{off}$). Signal-to-noise ratios (SNR) were used to determine the sensitivity of the spectra. We define sensitivity as the SNR divided by the amount of lithium titanate in the rotor (in mg) and the square root of the experimental time in hours.

Direct Li spectra were acquired using a spin echo pulse sequence with a 3.125 μs pulse duration at a radiofrequency field amplitude of ν_1 = 80 kHz for ^{7}Li, and a 4.5 μs pulse at ν_1 = 55 kHz for ^{6}Li. We expect these pulses to be nonselective. The rf amplitudes at the Li frequency during CP were ν_1 = 80 kHz for ^{7}Li and 55 kHz for

[6]Li, and the CP contact time was 2.5-3.5 ms. The ^{1}H rf field amplitude during CP was ramped from 90-100% to improve polarization transfer efficiency.[186] The pulse parameters used in the multiple contact CP experiments were not optimized further. Longitudinal relaxation times, T_1, and polarization build-up times, T_B, were measured using a saturation recovery pulse sequence. Presaturation pulses were applied on all nuclei.

Numerical simulations. Simulations of hyperpolarization relay were carried out using numerical models based on diffusion.[107] See Table 3-15 in Appendix IV for further information.
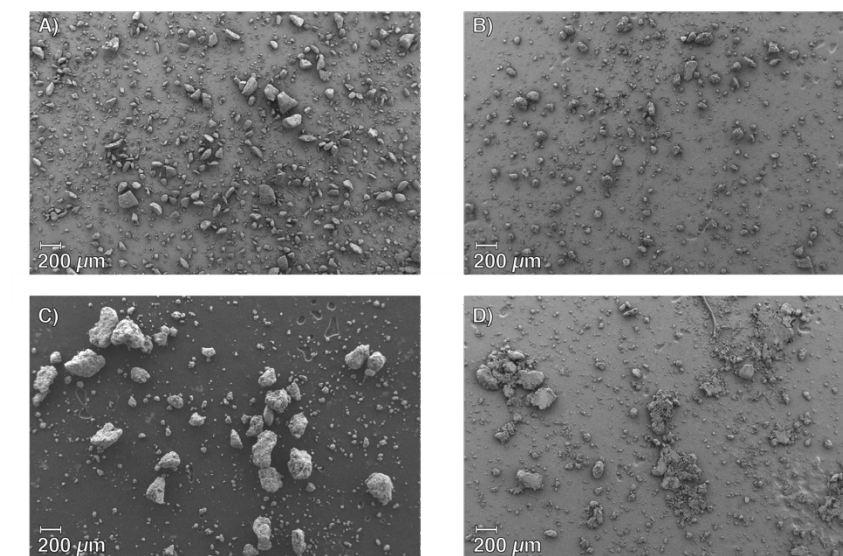

Figure 3-20. SEM images of the lithium titanate powders. a) Li_2TiO_3 as received. b) Li_2TiO_3 crushed by hand. c) $Li_4Ti_5O_{12}$ as received. d) $Li_4Ti_5O_{12}$ crushed by hand.

3.3.3 Results and discussion

In general, sensitivity is increased with DNP by inducing the transfer of the high polarization of unpaired electrons to nearby nuclei with microwave irradiation.[100, 169] It has been shown that the surfaces of diamagnetic materials can be very effectively enhanced at low temperature by incipient wetness impregnation of the sample with a radical containing solution, and then transfer of polarization from the radical source to the surface either directly or by cross polarization (CP).[101-103] More recently, it has been shown that this surface hyperpolarization can be efficiently relayed into the bulk of the material by spontaneous spin diffusion, even among weakly magnetic nuclei such as ^{119}Sn, ^{113}Cd or ^{29}Si at natural abundance.[197]

Here, applying this approach, two powdered lithium titanate materials were impregnated with a radical containing solution. At low temperatures (~100 K) the radical solution forms a glassy matrix where, upon microwave irradiation, nuclear spins close to the radicals are hyperpolarized.

Sensitivity enhancements, Li_2TiO_3

The DNP enhanced ^7Li and ^6Li spectra of Li_2TiO_3, recorded in this manner at 9.4 T and 90 K, are shown in Figure 3-21. A klystron with a microwave output power of around 5.2 W was used to transfer the high electron polarization of the radicals to protons in the TCE, yielding a ^1H DNP enhancement of around 400. CP was then used to transfer the hyperpolarization generated on protons to ^7Li and ^6Li nuclei close to the surface of the Li_2TiO_3 particles. This results in the DNP enhanced ^1H-$^{6,7}Li$ CP spectra, shown in Figure 3-21a and b, with $\varepsilon_{CP, 7Li} = 99 \pm 2$ and $\varepsilon_{CP, 6Li} = 184 \pm 26$. Since the material here is proton-free this method yields surface enhanced spectra of the compounds, as there is no proton spin diffusion possible to carry hyperpolarization into the bulk of the materials.

Indeed, we see a difference between the DNP enhanced surface spectrum recorded with ^{1}H-^{7}Li CP and the ordinary direct ^{7}Li spectrum acquired without DNP, which is dominated by signal from the bulk (Figure 3-21c). The surface-selective spectrum is broader, both in terms of linewidths and in terms of anisotropy, as seen by the more extended sideband pattern, corresponding to environments that are more anisotropic than the bulk environments.
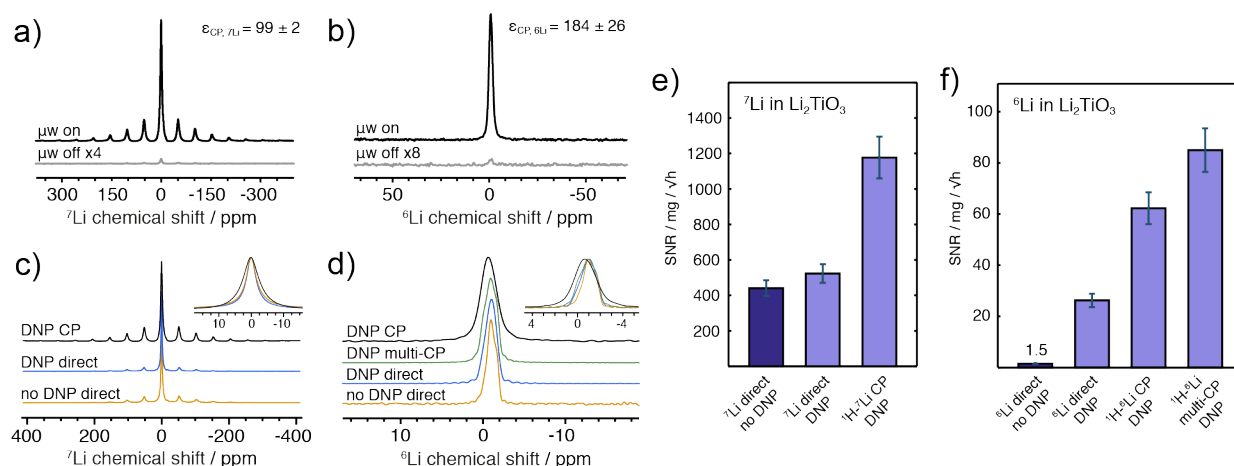

Figure 3-21. Spectra and sensitivity enhancements measured for Li$_2$TiO$_3$. a) DNP enhanced ^{1}H-^{7}Li CP MAS spectra and b) ^{1}H-^{6}Li CP MAS spectra. c) DNP enhanced ^{1}H-^{7}Li CP spectrum, and direct ^{7}Li spectra with and without DNP. d) ^{1}H-^{6}Li DNP enhanced CP and multi-CP spectra, and direct ^{6}Li spectra with and without DNP. The spectra are scaled to the same intensity. Sensitivity gains in the e) ^{7}Li and f) ^{6}Li spectra of Li$_2$TiO$_3$.

Figure 3-21e compares the sensitivity (SNR/mg/$\sqrt{h}$) of DNP enhanced ^{7}Li spectra to that of a conventional low temperature MAS spectrum of the undoped material.[92, 225] In all cases, the experiments were performed at a MAS rate of 8 kHz, and they are sensitivity optimized, i.e., the recovery delay is scaled according to the measured longitudinal relaxation times, T_1, or the DNP build-up times T_B. In the case of Li$_2$TiO$_3$, the relaxation times are $T_{1,7Li}$ = 70 s and $T_{B,1H}$ = 3.5 s. (See Appendix IV for further details). ^{7}Li is 92.3% abundant and has a relatively high gyromagnetic ratio, and as a result obtaining a spectrum with a high SNR is not usually a challenge. Nevertheless, a large gain in sensitivity is obtained using DNP enhanced ^{1}H-^{7}Li CP as seen in Figure 3-21e: the resulting sensitivity is over 2.5 times higher for the *surface-selective* DNP spectrum than for the conventional *bulk* spectrum of the neat sample. A more modest gain in sensitivity is achieved by direct polarization of the ^{7}Li nuclei. Furthermore, the lithium atoms initially hyperpolarized directly can be different from those initially polarized indirectly through protons, which might explain the difference. This has been seen previously for silicates, where direct hyperpolarization included atoms that were further away from the surface than in the case of CP.[170] That said, we note also that the main magnetic field was not adjusted for the optimum CE condition for direct ^{7}Li DNP.

Figure 3-21f shows how sensitivity for the ^{6}Li spectra of Li$_2$TiO$_3$ can be very significantly increased with impregnation DNP. Given the properties of the ^{6}Li nuclei, the sensitivity in the conventional spectrum is, unsurprisingly, low. Direct DNP of ^{6}Li shows an already sizeable sensitivity gain of around factor of 15. An even higher gain is generated by ^{1}H-^{6}Li CP, to yield a factor of ~40. This can be improved even further by the use of a multiple contact "pulsed-cooling" CP strategy, which here provides a sensitivity gain of almost a factor of 60. In this latter method, the particle surface is repeatedly hyperpolarized by CP, while simultaneously polarization is relayed towards the bulk by homonuclear spin diffusion between ^{6}Li nuclei. This method has been shown to enhance sensitivity in the bulk of proton-free materials, provided that the nuclear T_1 relaxation rate is long enough to accommodate for the slow spin diffusion.[197, 226] The increase in sensitivity here, exceeding that of regular CP, indicates that ^{6}Li hyperpolarization is relayed in Li$_2$TiO$_3$, which will be discussed in more detail later.

As for ^{7}Li, we also see a difference between the DNP enhanced surface-selective spectrum recorded with ^{1}H-^{6}Li CP, as compared to the ordinary direct ^{6}Li spectrum acquired without DNP, which is dominated by signal from the bulk (Figure 3-21d). The surface-selective spectrum is slightly broader and is clearly shifted by about 0.4 ppm, made visible by the higher intrinsic resolution of ^{6}Li. Here we also see that the pulsed cooling spectrum has the same shape as the bulk spectrum, which again confirms that polarization has been relayed from the surface into the bulk.

Sensitivity enhancements, Li$_4$Ti$_5$O$_{12}$

The second material we used here is Li$_4$Ti$_5$O$_{12}$, which is a promising high-rate anode material for lithium-ion batteries.[216, 227] This compound has significantly longer ^{6,7}Li longitudinal relaxation rates than Li$_2$TiO$_3$, with $T_{1,^7Li}$ = 940 s and $T_{1,^6Li}$ > 10000 s at 90 K (see Figure 3-26 in Appendix IV). Using the impregnation DNP method as above, the solvent protons are hyperpolarized efficiently, with ε_{1H} = 345, and the DNP enhanced ^{1}H-^{6,7}Li CP spectra are displayed in Figure 3-22a and b. (Note that the reason for the difference observed in the enhancement of ^{7}Li and ^{6}Li through protons is not fully understood, but tentatively we attribute it to the different concentrations and different spin dynamics of the two lithium isotopes.)

The spectra, which are shown in Figure 3-22c and d, share the same essential characteristics as for Li$_2$TiO$_3$ with the same differences observed between surface-selective and bulk spectra.
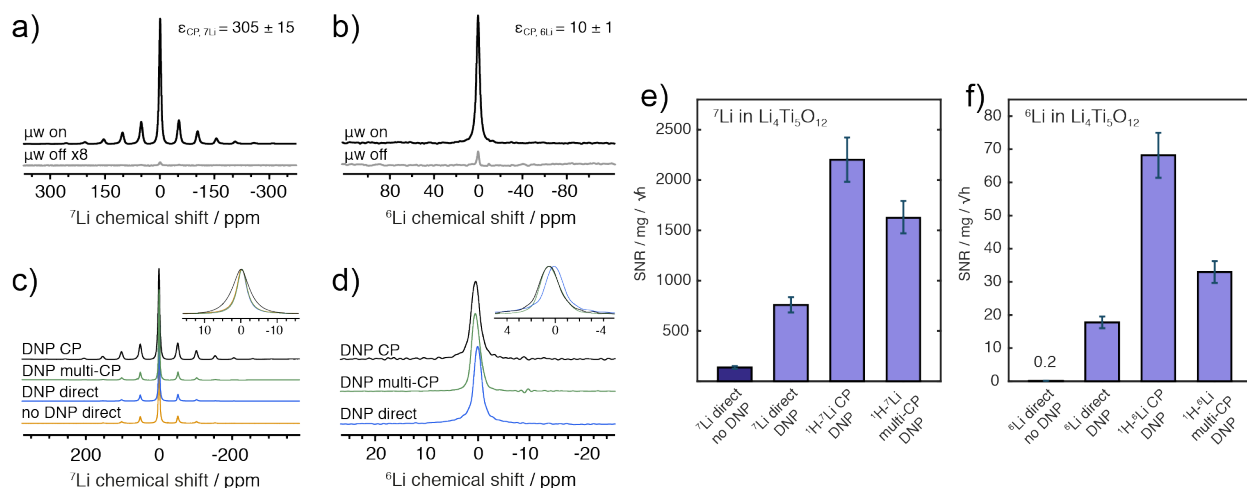

Figure 3-22. Spectra and sensitivity enhancements measured for Li$_4$Ti$_5$O$_{12}$. a) DNP enhanced ^{1}H-^{7}Li CP MAS spectra and b) ^{1}H-^{6}Li CP MAS spectra. c) DNP enhanced ^{1}H-^{7}Li CP and multi-CP (pulse cooling) spectra, and direct ^{7}Li spectra with and without DNP. d) ^{1}H-^{6}Li CP and multi-CP spectra, and direct ^{6}Li spectra with DNP. The spectra are scaled to the same intensity. Sensitivity gains in the e) ^{7}Li and f) ^{6}Li spectra of Li$_4$Ti$_5$O$_{12}$.

The sensitivity gains can be analyzed in the same way as previously. The sensitivity of ^{7}Li in Li$_4$Ti$_5$O$_{12}$ can be improved with direct DNP of the lithium nuclei, but a larger gain is produced by using ^{1}H-^{7}Li CP, for a factor of 15 (Figure 3-22e). In this case, the multiple contact CP yields a lower sensitivity than the regular CP, which could for example be ascribed to differences in pulse parameters,[226] or by relatively fast relaxation of surface Li atoms compared to the rate of spin diffusion, given that a long z-filter is used at the end of the pulse sequence to suppress the contribution from the surface. The spectrum obtained, however, corresponds to the ^{7}Li bulk spectrum of Li$_4$Ti$_5$O$_{12}$ (see Figure 3-22c), indicating that surface generated ^{7}Li hyperpolarization has been relayed to bulk environments.

Without DNP, the sensitivity of ^{6}Li is low and directly hyperpolarizing the ^{6}Li nuclei with DNP already improves sensitivity by a factor of ~90. Using ^{1}H-^{6}Li CP provides a sensitivity gain of 350, the highest obtained for this sample,

again despite being surface selective. The multiple contact CP method was also applied for ^{6}Li here, but in contrast to the case for Li_2TiO_3 discussed above, the ^{6}Li spectrum shown in Figure 3-22d matches that of the surface selective CP experiment. This indicates that for ^{6}Li in this compound, spin diffusion is not efficient enough to transfer significant polarization to the bulk, at least not under the experimental conditions used here. In addition, spin diffusion is expected to be slower in $Li_4Ti_5O_{12}$ than in Li_2TiO_3, by a factor of roughly 1.5, as the lithium atoms are spaced further apart in the structure, which decreases the strength of the dipolar couplings mediating spin diffusion.

^{7}Li—^{7}Li and ^{6}Li—^{6}Li spin diffusion

The results from the multiple-contact CP method indicate the presence of spin diffusion in these systems. In order to have a better understanding of polarization relay from the surface to the bulk, we recorded direct lithium DNP enhancements as a function of the polarization time (Figure 3-23). The ^{7}Li enhancement in $Li_4Ti_5O_{12}$ is first observed to increase to almost $\varepsilon_{7Li} = 100$, and then decrease as the polarization delay increases (Figure 3-23a, see Appendix IV for short delays). This change in enhancement as a function of time has been established previously as a clear signature of relay,[106-107] meaning that the highly polarized nuclei at the surface of the lithium titanate relay polarization towards the bulk of the material. For ^{6}Li in Li_2TiO_3 the enhancement is observed to increase with polarization delay, up to around 14 at a delay of 1000 s, again providing an unambiguous signature of relay from the surface to the bulk. Note that although the curves in Figure 3-23a and b have apparently different shapes, since the intrinsic T_1 of ^{6}Li in Li_2TiO_3 is >10000 s, the enhancement has not reached steady state at 1000 s and the enhancement curve is still only in the rising phase in Figure 3-23b.[107] In contrast, in Figure 3-23a the maximum is reached already at 100 s.

This behaviour can be reproduced quantitatively with numerical simulations using a diffusion model (first developed to measure domain sizes in hyperpolarized organic materials), as illustrated in Figure 3-23.[106-107, 109] Here we consider a thin layer at the surface of the lithium titanate particles to be the source of lithium hyperpolarization and model the relay into the bulk.
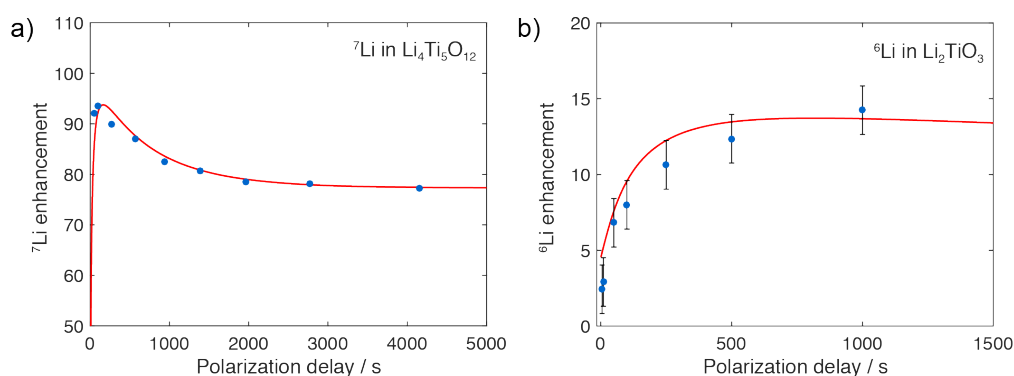

Figure 3-23. DNP enhancements of a) ^{7}Li in $Li_4Ti_5O_{12}$ and b) ^{6}Li in Li_2TiO_3 as a function of polarization delay. The solid lines are the fitted numerical simulations of polarization relay. Error estimations are explained in Appendix IV, the error bars for ^{7}Li are smaller than the data points.

We note that the case of lithium is different from most nuclei in this context, since Li atoms can themselves diffuse in these materials. Polarization transfer could potentially therefore either be achieved by physical diffusion of the lithium atoms or by spin diffusion between atoms induced by homonuclear Li–Li dipolar couplings. Lithium dynamics in lithium titanates have been studied with solid-state NMR and in these two materials the lithium dynamics have been found to be relatively slow, with estimates of Li diffusion coefficients at room temperature of 0.003 nm^2/s for Li_2TiO_3 and 0.18 nm^2/s for $Li_4Ti_5O_{12}$.[228-229] These rates are further reduced at low temperature. As a comparison, the ^{7}Li–^{7}Li dipolar driven spin diffusion rate in a static sample is predicted to be around 80 nm^2/s

in Li_2TiO_3 and the ^6Li–^6Li rate is estimated to be around 5 nm^2/s (see Table 3-11). We do not expect the spin diffusion rates to change significantly with temperature.

Table 3-11. Estimated upper bounds of the dipolar couplings d and the static spin diffusion coefficients D for ^6Li and ^7Li in Li_2TiO_3 and $Li_4Ti_5O_{12}$. The dipolar couplings are using $d = (\mu_0 h \gamma^2)/(4\pi r^3)$, where μ_0 and h are constants, γ is the gyromagnetic ratio (16.555 MHz/T for ^7Li and 6.27 MHz/T for ^6Li) and r is the shortest Li-Li distance in the known crystal structures[230-231]. The spin diffusion coefficients are scaled from the measured D for ^{19}F in a static single-crystal of CaF_2 ($D = 710$ nm^2 s^{-1}),[141] using the scaling law $D \propto \sqrt[3]{c}\, \gamma_I^2$ where c is the concentration of nuclei and γ_I is the gyromagnetic ratio.[127] The diffusion length $\sqrt{DT_1}$ reported is an upper limit, which is an approximation where the estimated diffusion coefficient for a static sample is used with the longitudinal relaxation, T_1 at 90 K and 8 kHz MAS rate. This is an overestimate, as D scales approximately $1/\nu_R$ with MAS[191] as and in addition many other factors affect the rate of spin diffusion.[197] (See Section 1.3.3)

	r (Å)	d (Hz)	c (M)	D (nm^2 s^{-1})	T_1 (s)	$\sqrt{DT_1}$ (nm)
^7Li in Li_2TiO_3	2.8	862	28.9	85.8	70	77.5
^6Li in Li_2TiO_3	2.8	124	2.3	5.3	4382	152
^7Li in $Li_4Ti_5O_{12}$	3.6	389	7.1	53.7	942	225
^6Li in $Li_4Ti_5O_{12}$	3.6	56	0.6	3.3	13100	208

The estimated dipolar driven spin diffusion coefficient of ^7Li in a static sample of $Li_4Ti_5O_{12}$ is around 10 times faster than the estimate for ^6Li in Li_2TiO_3. The diffusion coefficients for ^6Li and ^7Li spin diffusion extracted from the simulations in Figure 3-23 agree with this ratio and the expected diffusion coefficients under MAS (although some of the parameter estimations are only semi-quantitative). See Table 3-15 in Appendix IV for details of the fitting procedure and parameter estimations.

The diffusion length in the last column of Table 3-11 can be considered as a rough estimate of the upper limit of the thickness of the layer hyperpolarized by spin diffusion from the surface (and since it depends on D it is also expected to decrease upon sample spinning). We note that based on information from the supplier, the as-received $Li_4Ti_5O_{12}$ particles are expected to be smaller than the Li_2TiO_3 particles. Nevertheless, even for Li_2TiO_3, where the hyperpolarized layer is not expected to account for a large part of the total particle volume, the gains in overall sensitivity are still significant.

3.3.4   Conclusion

In conclusion, we have shown that incipient wetness impregnation DNP can be used to efficiently hyperpolarize both the surface and the bulk of unmodified diamagnetic lithium containing inorganic materials. We observe clear differences between surface and bulk spectra of both nuclei. The method yields a factor ~60 gain in spectral sensitivity for the bulk spectrum in the challenging case of ^6Li in pure Li_2TiO_3, corresponding to a factor >3600 acceleration in the time needed to acquire a spectrum. We obtain even higher enhancements, of up to a factor 350, for surface selective DNP SENS spectra of these materials. In principle, the method can be directly applied to obtain high-sensitivity surface and bulk spectra of other inorganic lithium containing oxides.

3.3.5 Appendix IV

Enhancements

Table 3-12. Enhancement values for Li_2TiO_3 and $Li_4Ti_5O_{12}$ impregnated with a 16 mM solution of TEKPol in TCE, spinning at 8 kHz MAS and at sample temperature of ~100 K. The spectra were processed with a 100 Hz line broadening. The enhancements are evaluated as $\varepsilon = I_{on} / I_{off}$, where I is signal intensity.

Li_2TiO_3	Recycle delay / s	ε	$\Delta\varepsilon$
^1H echo	4.375	415	5
CP ^1H-^7Li	4.375	99	2
echo ^7Li	81.25	1.6	0
CP ^1H-^6Li	4.375	184	26
echo ^6Li	1000	12	0.2

$Li_4Ti_5O_{12}$	Recycle delay / s	ε	$\Delta\varepsilon$
^1H echo	5	343	5
CP ^1H-^7Li	5	305	15
echo ^7Li	60	86	0.5
CP ^1H-^6Li	5	10	1

The estimation of errors reported on the enhancements in Figure 3-21 and Figure 3-22 (and Table 3-12), as well as on the enhancement curves in Figure 3-23, was done based on noise level.

$$\Delta\varepsilon = \varepsilon \sqrt{\left(\frac{\Delta I_{on}}{I_{on}}\right)^2 + \left(\frac{\Delta I_{off}}{I_{off}}\right)^2}$$

(Eq. 3-5)

Here, ε is enhancement based on signal integrals, I is the signal intensity with or without microwave irradiation, and ΔI is the noise value. Each curve in Figure 3-23 has a fixed error value, the highest absolute error among the points on the curve, which overestimates the errors of some of the single points.[161] The error bars for ^7Li are smaller than the data points.
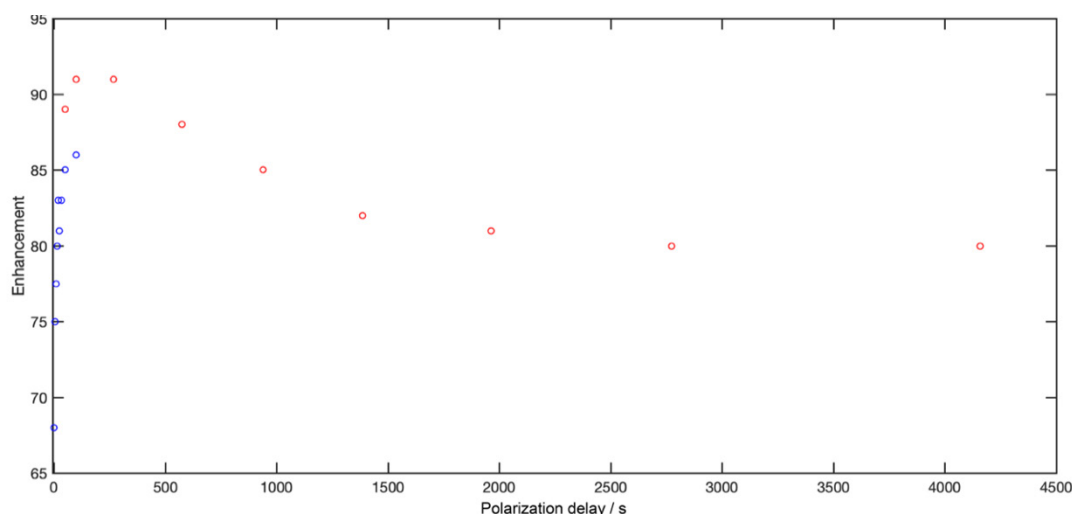

Figure 3-24. ^7Li enhancements as a function of polarization delay in $Li_4Ti_5O_{12}$ impregnated with a 16 mM solution of TEKPol in TCE, spinning at 8 kHz. The red and the blue dots probe different areas of the recovery curve, but since they are recorded on two different days there are slight differences in the enhancements for the overlapping delays of 50 and 100 s.
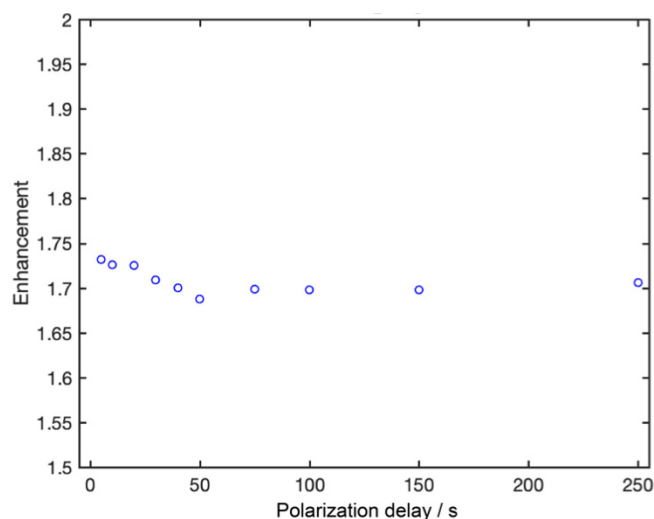
Figure 3-25. [7]Li enhancements as a function of polarization delay in Li_2TiO_3 impregnated with a 16 mM solution of TEKPol in TCE, spinning at 8 kHz. The T_1 of the neat sample is around 70 s.

Sensitivities

For the sensitivity values reported in Figure 3-21 and Figure 3-22, the signal-to-noise ratios of the spectra were measured in Topspin, where the noise value varies depending on the selected noise region. This can be due to baseline imperfections, correlated noise, residual signal from background or instrumental imperfections. We estimate this variability to be around 10% of the signal-to-noise ratio, and therefore add 10% error bars to each calculated sensitivity value, even if this is likely to overestimate the error for some of the sensitivities.

Table 3-13. Sensitivity values for Li_2TiO_3, which are displayed in the bar chart in Figure 3-21. The Li_2TiO_3 powders, either neat or impregnated with a 16 mM solution of TEKPol in TCE, were spun at 8 kHz MAS and at sample temperature of ~100 K. When measuring signal-to-noise ratios a 200 Hz exponential weighting function was applied before Fourier transform to all the data. The signal-to-noise ratios reported are the mean of two 500 ppm regions on either side of the lithium signal.

nucleus	experiment	Mass / mg	Recycle delay / s	Number of scans	Exp. time / h	SNR	Sensitivity SNR/mg/√h
7Li	neat direct	52.9	81.25	2	0.0451	4951	440.5
	DNP direct	36.3	81.25	2	0.0451	4035	523.2
	DNP CP	36.3	4.375	8	0.0097	4214	1177.4
6Li	neat direct	52.9	4000	2	2.2222	120	1.5
	DNP direct	36.3	2300	2	1.2778	1078	26.3
	DNP CP	36.3	4.375	8	0.0097	223	62.3
	pulse cooling	36.3	600	2	0.3333	1780	85

Table 3-14. Sensitivity values for $Li_4Ti_5O_{12}$, which are displayed in the bar chart in Figure 3-22. The $Li_4Ti_5O_{12}$ powders, either neat or impregnated with a 16 mM solution of TEKPol in TCE, were spun at 8 kHz MAS and at sample temperature of ~100 K. When measuring signal-to-noise ratios a 200 Hz exponential weighting function was applied before Fourier transform to all the data. The signal-to-noise ratios reported are the mean of two 500 ppm regions on either side of the lithium signal.

| nucleus	experiment	Mass / mg	Recycle delay / s	Number of scans	Exp. time / h	SNR	Sensitivity SNR/mg/√h
7Li	neat direct	43.8	1067	2	0.5928	4630	137.3
	DNP direct	30.2	587.5	2	0.3264	13090	758.7
	DNP CP	30.2	5	8	0.0111	7010	2202.1
	pulse cooling	30.2	300	2	0.1667	10048*	1630.0
6Li	neat direct	43.9	15000	2	8.3333	19	0.15
	DNP direct	30.2	4159	2	2.3106	816	17.8
	DNP CP	30.2	5	4	0.0056	154	68.2
	pulse cooling	30.2	300	2	0.1667	406	33.0

*A noise area of 100 ppm on each side of the signal was used due to baseline imperfections

Numerical simulations

Table 3-15. Parameters used for the simulations shown in Figure 3-23. The length of the target represents the size of the particles, which was assumed to be 200 nm (based on information from the supplier). The length of the source is the layer of lithium titanate that is directly polarized by DNP, assumed to be much smaller than the whole target. The build-up time of the source was estimated to be short, as it is close to the radical source. The intrinsic T_1 of the target is a measured value (see Figure 3-26). The parameters that were varied to fit the curves, shown in bold, are the spin diffusion rate, the source enhancement and the slope of the hyperbolic tangent function describing the change in parameters at the interface of the source and the target. The percentage of quenched signal in the source, as well as the depolarization, were kept constant. The MATLAB code used for the simulations is from ref[107].

parameter	^7Li in $Li_4Ti_5O_{12}$	^6Li in Li_2TiO_3
Length of target	0.2 μm	0.2 μm
Length of source	0.005 μm	0.005 μm
Source build-up time	0.1 s	0.1 s
T_1 of target	940 s	4400 s
Spin diffusion rate	**1 x 10^-6 μm²s⁻¹**	**1 x 10^-7 μm²s⁻¹**
Source enhancement	**450**	**80**
Slope of tanh function	**400**	**400**
Quenched signal in source	0	0
Depolarization in source	0.6	0.6

Saturation recovery relaxation measurements
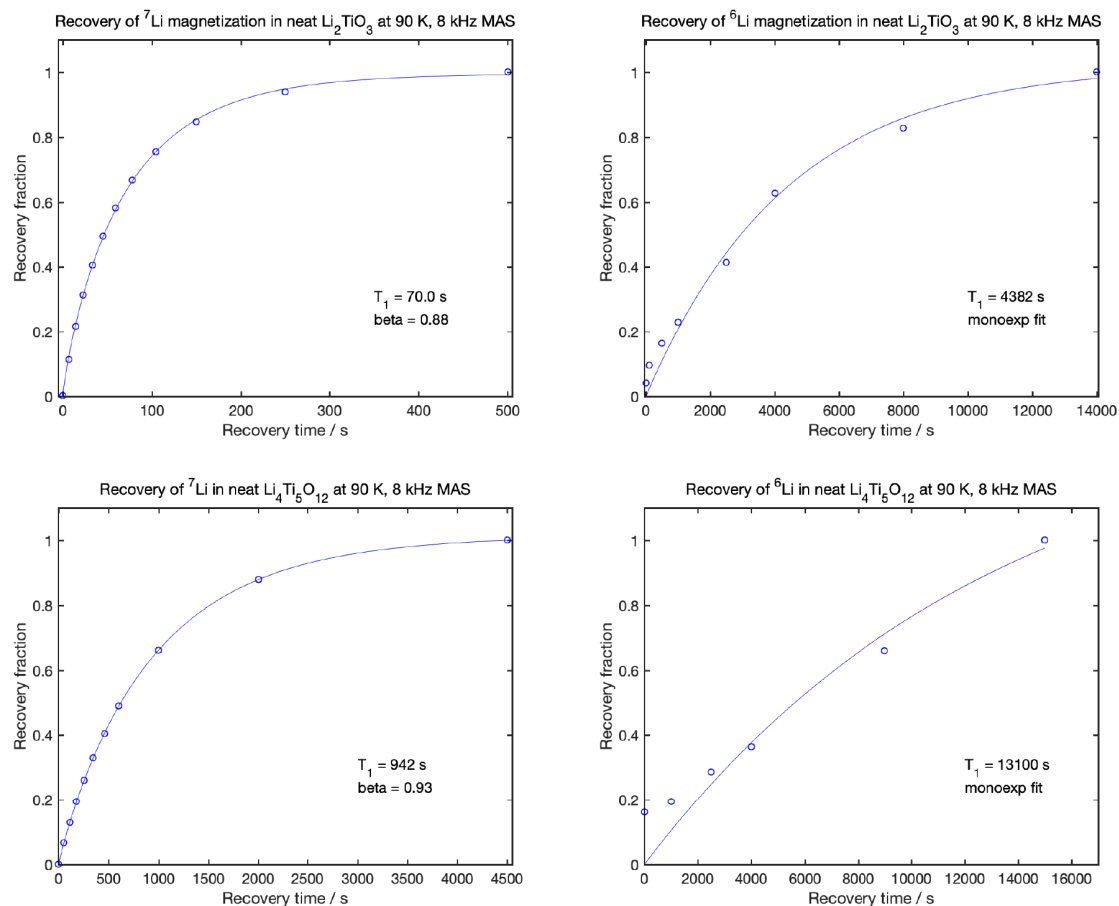
Figure 3-26. Recovery curves for ^{6}Li and ^{7}Li in non-impregnated samples of Li_2TiO_3 and $Li_4Ti_5O_{12}$ spinning at 8 kHz MAS and 90 K.

Longitudinal relaxation times, T_1, and polarization build-up times, T_B, were measured using a saturation recovery pulse sequence. The data points were fit to a multi-exponential model in the case of ^{7}Li and to a mono-exponential recovery model in the case of ^{6}Li. Even though impregnation is expected to modify the build-up behavior (specifically, it is expected to deviate from mono-exponential behavior in the case of ^{6}Li) we have not taken that into account here to avoid over fitting, since the recovery curves for ^{6}Li have not reached steady state. The parameters extracted from the fits were used qualitatively in order to set the optimum recycle delay for the sensitivity measurements. They were also used as parameters in the numerical simulations.

Table 3-16. Measured build-up times for ^{6}Li and ^{7}Li in impregnated samples of Li_2TiO_3 and $Li_4Ti_5O_{12}$ spinning at 8 kHz MAS and 90 K.

	T_B of ^{7}Li $$I(\tau_{rd}) = I_\infty \left[1 - \exp\left(-\frac{\tau_{rd}}{T_B}\right)^\beta \right]$$		T_B of ^{6}Li $$I(\tau_{rd}) = I_\infty \left[1 - \exp\left(-\frac{\tau_{rd}}{T_B}\right) \right]$$	
	μw off	μw on	μw off	μw on
Li_2TiO_3	69 s, β = 0.93	70 s, β = 0.92	1643 s	2076 s
$Li_4Ti_5O_{12}$	607 s, β = 0.92	488 s, β = 0.91	Not measured	6464 s

3.4   Hyperpolarization transfer pathways

This chapter has been adapted with permission from: "*Hyperpolarization transfer pathways in inorganic materials*". S. Björgvinsdóttir, P. Moutzouri, B.J. Walder, N. Matthey, L. Emsley, *submitted* **2020**. (pre-print)

3.4.1   Introduction

A method to hyperpolarize the bulk of proton-free inorganic materials using DNP was introduced in Sections 3.1 and 3.2, resulting in considerable sensitivity enhancements in solid-state MAS NMR spectra of inorganic bulk.[197, 226] This was demonstrated for [119]Sn spectra of SnO_2, ^{31}P spectra of GaP, [113]Cd spectra of CdTe and [29]Si spectra of SiO_2 (α-quartz). These materials, however, all have only a single isotropic chemical shift in the bulk. As such, the question remains of how hyperpolarization may be relayed through distinct surface and bulk species: is the transport of hyperpolarization into the bulk carried across different bulk species on distinct *hyperpolarization transfer pathways*, and is the net accumulation of polarization site dependent?

Figure 3-27 shows a schematic representation of four different transfer paths. The dominance of specific hyperpolarization transfer pathways and polarization ratios of bulk sites that differ from unity might be anticipated due to numerous site-specific factors which modulate the rate of spin diffusion. Large chemical shift differences are expected to slow down spin diffusion, roughly as the inverse square of the difference between the isotropic chemical shifts but with significant additional modulation by homonuclear *J*-coupling, chemical shift anisotropy, the relative orientation of anisotropic principal axis systems (including those of nuclei to which the site is coupled), all further complicated by rotational resonance effects introduced by MAS.[121, 130] The analysis is entirely nontrivial and differences in accumulated polarization can be readily envisaged.
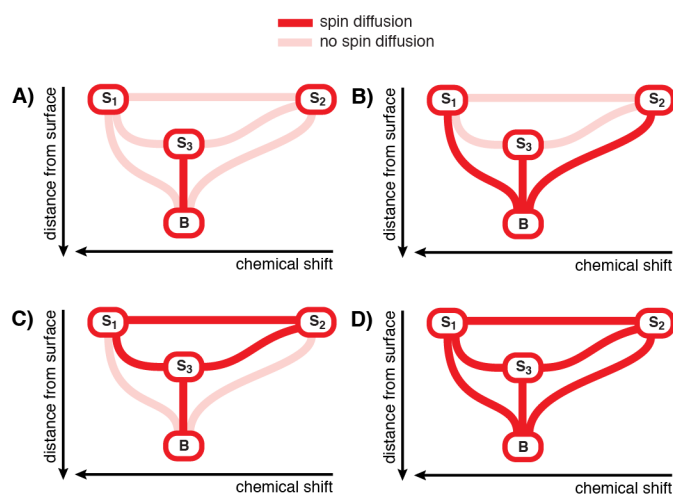

Figure 3-27. Schematic representation of possible hyperpolarization transfer pathways from three surface sites (S_1, S_2 and S_3) to bulk (B). S_3 has the same chemical shift as the bulk. A) Only transfer from S_3 to B. B) Transfer from all three surface sites to bulk. C) Exchange between all three surface sites, and transfer from S_3 to B. D) Transfer between all sites in the system.

Here we extend the method of hyperpolarization by relay from the surface to compounds that have more than one isotropic chemical shift in the bulk. We make use of two-dimensional experiments to probe hyperpolarization transfer pathways into the bulk beginning at the surface for the [119]Sn nuclei of SnO_2 and the ^{31}P nuclei of GaP, $Sn_2P_2O_7$ and $K_4P_2O_7$. We find that hyperpolarization can be efficiently relayed from surface sites to multiple sites in the bulk simultaneously, even when chemical shift differences are relatively large. We also see that polarization of the bulk sites exchanges rapidly between themselves and polarization from multiple surface sites can be relayed

simultaneously into bulk. In addition, we show evidence that disordered surface sites can exchange polarization between themselves.

3.4.2 Experimental methods

Solid-state NMR spectra were collected on a 9.4 T Bruker Avance III spectrometer coupled with a 263 GHz gyrotron microwave source.[42] The spectra were collected at a MAS rate of 8 kHz and a temperature of around 100 K using 3.2 mm sapphire rotors and a low-temperature MAS-DNP probe. For efficient spin locking during cross-polarization, a 100 kHz rf field amplitude was applied on the X channel unless otherwise specified. The ^{1}H rf field amplitude was ramped up from 90% during CP to improve polarization transfer efficiency. Presaturation pulses were used on both ^{1}H and X channels in all experiments. See Appendix V for further experimental details. DMFIT was used for spectral deconvolution.[232]

$Sn_2P_2O_7$ (abcr), SnO_2 (abcr) and $K_4P_2O_7$ (Sigma Aldrich) were ground by hand and GaP flakes (abcr) were crushed in a mixer mill with a stainless-steel ball. The resulting micrometer sized particles (see SEM images in Figure 3-28) were impregnated with a 16 mM solution of TEKPol[185] in 1,1,2,2-tetrachloroethane (TCE).[84, 101] The formulation ratio was 30-55 mg of powdered solid to 10 µL of radical solution, depending on the solid. Tin pyrophosphate was heated at 250°C overnight before impregnating. To improve DNP enhancements, the packed samples were deoxygenated by rapid freezing and subsequent thawing by three insert-eject cycles.[160, 201]
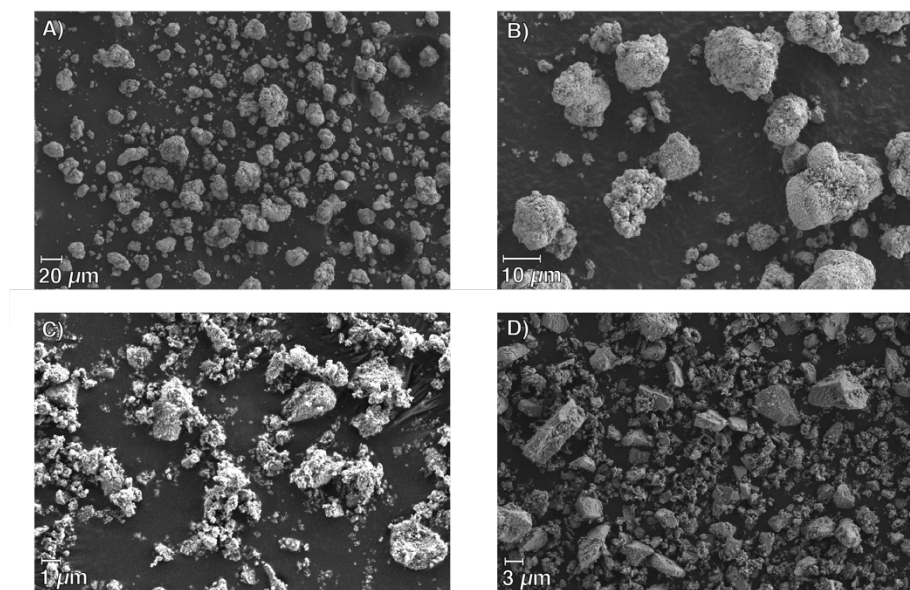

Figure 3-28. SEM images. A and B) Tin pyrophosphate ground by hand and kept in oven overnight at 250°C. Two different magnifications. C) SnO_2 ground by hand. D) GaP ground in a mixer mill.

3.4.3 Results and discussion

Part I - Hyperpolarization relay from the surface

^{31}P spin diffusion in tin pyrophosphate

We begin our investigation of relay into multiple bulk sites by considering tin pyrophosphate, $Sn_2P_2O_7$. The material has a triclinic crystal structure with two distinct bulk phosphorous sites,[233] leading to a ^{31}P MAS spectrum showing two distinct signals, at -11.6 ppm and -15.4 ppm, occurring in a 1:1 ratio.[234] To monitor the transport of ^{31}P magnetization, the powdered solid is impregnated with a radical containing solution and hyperpolarization is

generated on protons in the wetting phase by continuous microwave irradiation. Hyperpolarization is then transferred to ^{31}P nuclei near the surface of the tin pyrophosphate particle with cross-polarization. After CP, a flip-back storage pulse puts the ^{31}P magnetization along the z direction, where spontaneous ^{31}P homonuclear spin diffusion may transport magnetization between different phosphorous species during a delay τ_m. A final 90° pulse then puts the magnetization back in the transverse plane before acquisition.[197]. Figure 3-29A shows such DNP enhanced ^{1}H-^{31}P CP spectra of $Sn_2P_2O_7$, acquired at 8 kHz MAS and 100 K, collected for different values of τ_m. We see that for $\tau_m = 0$ only the surface is polarized, yielding a broad spectrum extending from 10 ppm to about 30 ppm. There is almost no signal from the bulk, as can be seen in the comparison shown in Figure 3-29B, where the ^{1}H-^{31}P CP surface spectrum is compared to the direct ^{31}P bulk spectrum of $Sn_2P_2O_7$. In line with previous observations on materials with only one bulk species, we then see that when τ_m is increased, the bulk signal intensity increases, while surface signals concomitantly diminish. Figure 3-29C shows the integrals of the surface and bulk sites, from which we see the total signal volume diminishes in a way consistent with longitudinal relaxation, implying the bulk sites have picked up enhanced polarization from the surface sites. This result unambiguously demonstrates that the transfer of polarization from the surface to the two bulk sites occurs spontaneously, and that they are polarized on the same timescale. However, this experiment does not provide sufficient information to infer many details about the relevant polarization transfer pathways.
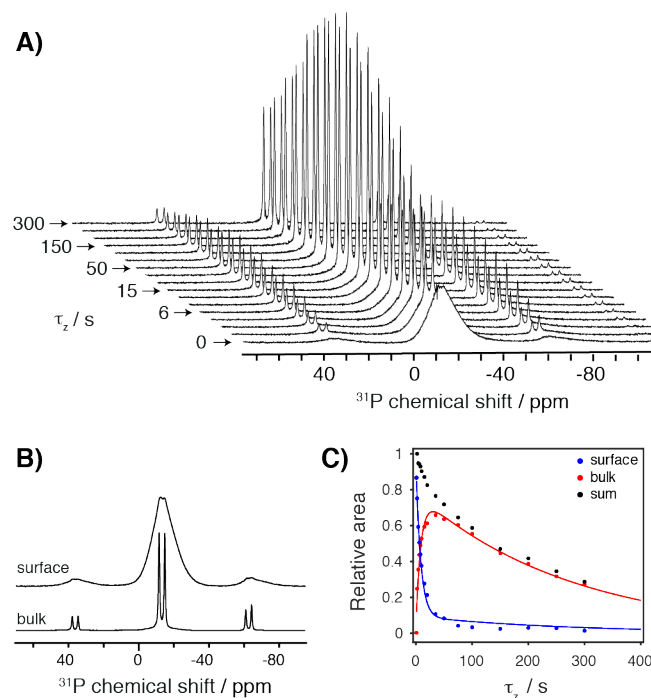

Figure 3-29. A) DNP enhanced ^{31}P CP spectra of $Sn_2P_2O_7$ acquired as a function of τ_m. B) ^{1}H-^{31}P CP surface spectrum, and direct ^{31}P bulk spectrum of $Sn_2P_2O_7$. C) ^{31}P peak areas for the surface and bulk sites as a function of time. The solid lines are fits to the data based on an exchange model as described in the text.

This kind of hyperpolarization relay has been simulated previously using numerical models based on diffusion.[107, 197] The diffusion model assumes that the transfer of polarization behaves like a thermal diffusion process, and it contains spatially juxtaposed components: typically, a hyperpolarization source, and a target which gets hyperpolarized by relay. These models are very powerful tools to determine the spatial arrangement of different components.[235-237]

However, in many inorganic solids, not only can there be a separation on the spin diffusion length scale between surface sites and the bulk, but there is often also frequency separation in the spectra between magnetically inequivalent sites that are neighbors on the atomic scale. In these cases, setting up a full spatial model of the

system is not straightforward, and is not necessarily required if the objective is to characterize the overall rates of flow of magnetization between the different chemical shifts. To address this problem here, we use a simplified kinetic model to approximate the dynamics.

In a simplified model, where a surface and bulk peak are in exchange, the peak volumes can be fit to the modified Bloch equations for a two-site exchange:[238-239]

$$S \text{ (surface)} \underset{k_{BS}}{\overset{k_{SB}}{\longleftrightarrow}} B \text{ (bulk)}$$
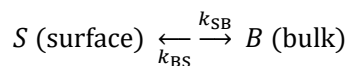
$$\frac{dV_S}{dt} = \frac{V_S^{eq} - V_S(t)}{T_{1,S}} - k_{SB}V_S(t) + k_{BS}V_B(t) \qquad \text{(Eq. 3-6)}$$

$$\frac{dV_S}{dt} = \frac{V_S^{eq} - V_S(t)}{T_{1,S}} - k_{SB}V_S(t) + k_{BS}V_B(t) \qquad \text{(Eq. 3-7)}$$

where t is time; V_S and V_B are the instantaneous volume magnetizations of the ^{31}P nuclei at the surface and in the bulk, which are proportional to the integrated signal intensities; k_{SB} and k_{BS} are the observed exchange rate constants; T_1 are the spin lattice relaxation rates; and V^{eq} are the equilibrium volume magnetizations (at $t = \infty$) of the surface and bulk. In the CP experiment used here, phase cycling is such that the magnetization decays to 0, $V^{eq} = 0$.

We use this model to fit the curves shown in Figure 3-29C, assuming that the two bulk sites are one site (since they have the same growth). The observed rate constants obtained from the fits are $k_{SB} = 0.09$ s^{-1} and $k_{BS} = 0.01$ s^{-1} (see Appendix V for details). While the microscopic interpretation of the observed rate constants in terms of spin flip-flops is not straightforward, they do provide a convenient way to quantify the overall flow of hyperpolarization from surface to bulk and the polarization exchange between the different sites in the spectra, which is the question addressed here. The observed rates do not directly correspond to spin diffusion rates between the different regions of the sample, which can only be extracted (in principle) using constitutive models taking into account the detailed geometry of the samples.[235]

The ^{31}P hyperpolarization transfer pathways from surface to bulk can alternatively be probed in with a two-dimensional experiment in the manner of classic exchange spectroscopy[240-242]. In the DNP enhanced 2D CP EXSY experiment, shown in Figure 3-30A, the effect of spin diffusion during the mixing period, τ_m, is to create off-diagonal intensities when magnetization is transferred to ^{31}P sites with chemical shifts that differ from the original species. An unusual aspect of this application of exchange spectroscopy is that the initial condition is very far from equilibrium, since the surface is hyperpolarized. Therefore, the flow of polarization will not be equal in both directions, and the 2D experiment primarily contains information about the forward (i.e. surface to bulk) direction of magnetization transfer, and leads to 2D spectra that are highly asymmetric.
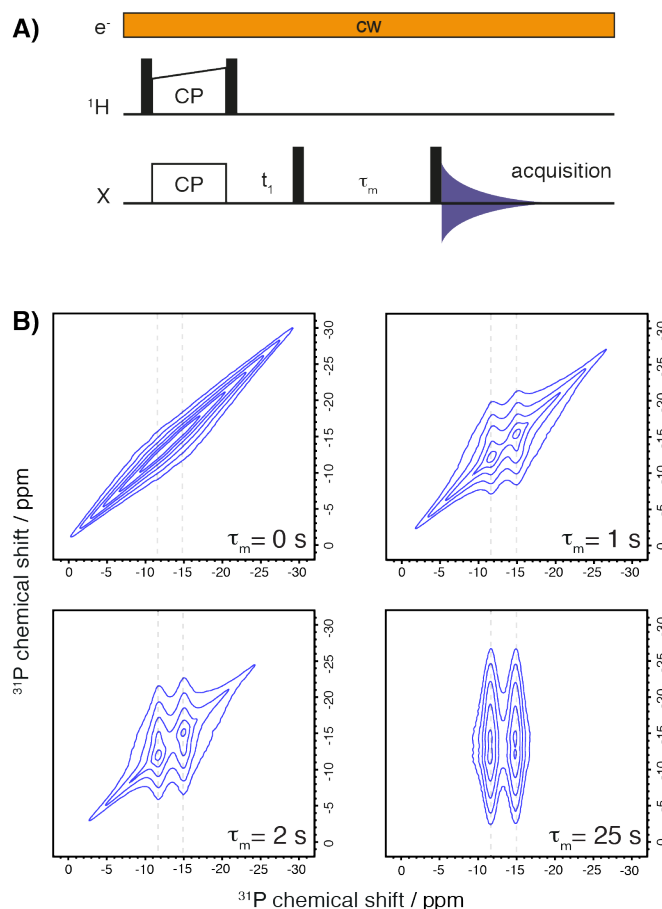
Figure 3-30. A) DNP enhanced 2D SD CP-EXSY pulse sequence used to monitor spin diffusion from surface to bulk. B) Contour plots of DNP enhanced 2D ^{31}P CP spin diffusion spectra of $Sn_2P_2O_7$ showing only the region of the centerband. They grey dashed lines are at the chemical shift of the two bulk peaks.

The ^{31}P 2D exchange spectra for tin pyrophosphate are shown Figure 3-30B. As expected, when the mixing time is 0 s, all the spectral intensity lies along the diagonal. For a 1 s mixing time, the polarization that was generated on the surface is now flowing into the bulk sites, resulting in significant off-diagonal intensities. In agreement with Figure 3-29C, the spectra indicate that the relatively broad range of surface shifts exchange with both of the bulk peaks on similar timescales. The spectrum with the longest mixing time shows how after a spin diffusion period of τ_m = 25 s, all of the polarization that was on the surface has now diffused into the bulk.

In addition, the off-diagonal intensities between the surface resonances close to the bulk resonances in the spectrum appear faster than the off-diagonal intensities between the bulk and the surface resonances furthest away from bulk (-5 and -25 ppm). This is shown in Figure 3-31 and suggests either that the rate of transfer to bulk is slower as the chemical shift difference increases, or that there is a relay step through surface sites having resonances closer to the bulk.

We note that only a handful of homonuclear surface to bulk correlations in inorganic materials have been reported previously, for example in the context of nanoparticles or battery materials.[88, 243]

τ_m / s	surface	bulk	ratio
0	1	0	-
1	0.46	0.13	3.54
2	0.34	0.19	1.79
25	0.06	0.47	0.13

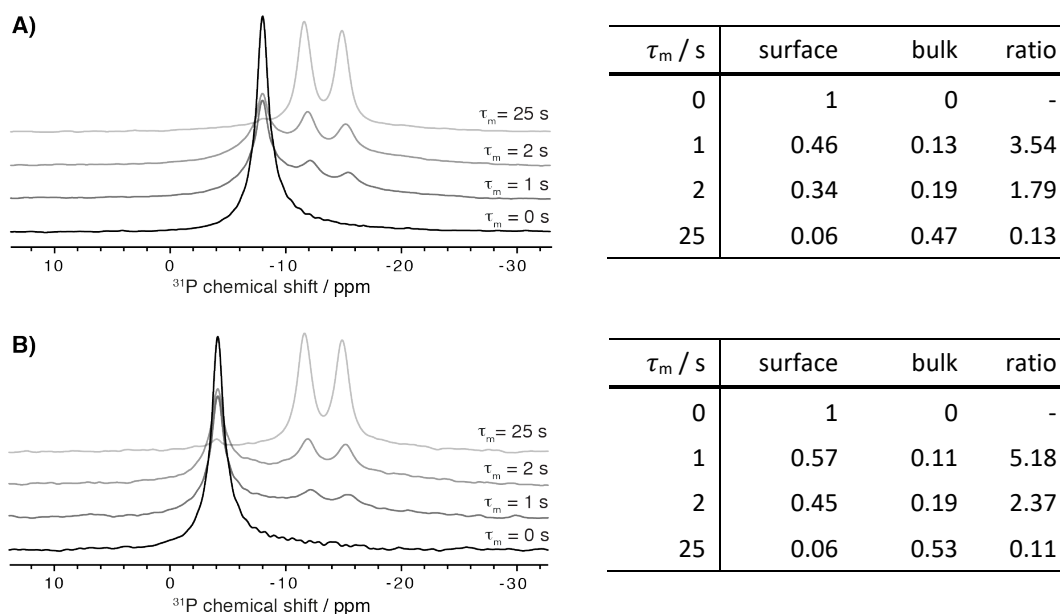| τ_m / s	surface	bulk	ratio
0	1	0	-
1	0.57	0.11	5.18
2	0.45	0.19	2.37
25	0.06	0.53	0.11

Figure 3-31. Horizontal cross-sections from the DNP enhanced ^{31}P 2D spin diffusion spectra of tin pyrophosphate (Figure 3-30B), taken at A) -8 ppm and B) -4 ppm. The tables show the relative intensities of the surface and the right bulk peak, normalized to surface before exchange. The surface-to-bulk ratios show that transfer from surface to bulk is faster for sites closer to the bulk resonances.

^{119}Sn spin diffusion in tin dioxide

Efficient hyperpolarization of the bulk ^{119}Sn atoms in SnO_2 was shown previously.[197, 226] Here we look into the mechanism of relay from surface to bulk in the same way as for tin pyrophosphate above. The DNP enhanced ^{119}Sn surface spectrum of SnO_2 is shown in Figure 3-32A. The surface spectrum of SnO_2 is characterized by three notable peaks corresponding to different sites. These signals can be observed in hydroxylated SnO_2 nanosheets and have been assigned to different atomic layers.[193] The bulk-like ^{119}Sn is at -604 ppm (*B*) and the first and second atomic layer, respectively, were assigned chemical shifts of -585 ppm (*S$_1$*) and -618 ppm (*S$_2$*). We note that the samples under consideration here are micrometer sized particles.

The ^{119}Sn 2D spectra of SnO_2 with a mixing time of 0 s do not have any cross peaks, as expected (see Figure 3-38 in Appendix V). With a τ_m = 1 s, the presence of off-diagonal intensity shows that spontaneous ^{119}Sn-^{119}Sn spin diffusion is present. Compared to spin diffusion between ^{31}P nuclei, ^{119}Sn-^{119}Sn spin diffusion is considerably slower (notably because the natural abundance of ^{119}Sn is 8.6%), and it takes longer for all of the surface hyperpolarization in SnO_2 to transfer to site *B*, corresponding to the bulk of the material.

As each of the surface sites in SnO_2 has a relatively well defined chemical shift range, it is possible to look at how the different sites exchange with the bulk. As an example, the region corresponding to transfer from surface site *S$_1$* to bulk is more intense than the peak for bulk to surface *S$_1$* transfer. This expected due to the predominantly forward transfer of surface hyperpolarization into the bulk of the SnO_2 particles due to the strong non-Boltzmann polarization gradient established near the particle surface.
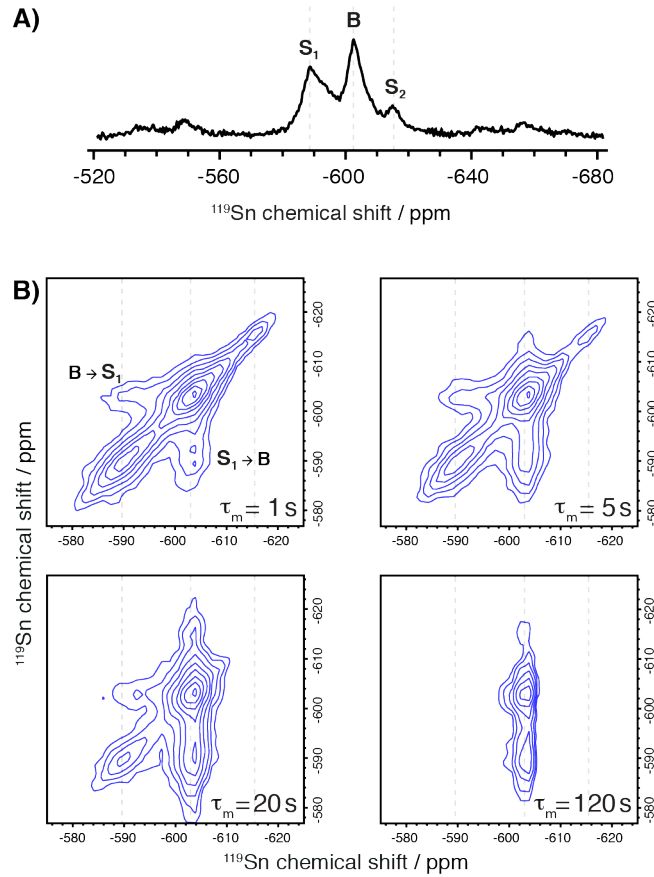
Figure 3-32. ^{119}Sn spectra of SnO_2 recorded at 9.4 T and 100 K. A) DNP surface enhanced CP-MAS ^{119}Sn spectrum of SnO_2. B) Contour plots of DNP enhanced ^{119}Sn spin exchange spectra of SnO_2 with different mixing times. They grey dashed lines are at the chemical shifts of the bulk and the two surface sites.

This can be analyzed in more detail with the kinetic model introduced above, this time with three sites, as shown in Figure 3-33A. The model considers reversible exchange between all three sites, represented by six rate constants, k. Additionally, the model takes into account three relaxation rates, R (where $R = 1/T_1$), one for each site. The total kinetic rate matrix can be written as

$$\mathbf{L} = \begin{bmatrix} -(k_{12}+k_{13})-R_{S2} & k_{21} & k_{31} \\ k_{12} & -(k_{21}+k_{23})-R_B & k_{32} \\ k_{13} & k_{23} & -(k_{31}+k_{32})-R_{S1} \end{bmatrix} \qquad \text{(Eq. 3-8)}$$

To find the rate constants representing the observed transfer between the different sites, the integrated areas, $\mathbf{I}$, from the two-dimensional spin diffusion spectra can be fitted to the following matrix equation

$$\mathbf{I}(t_m) = \mathbf{V_0} e^{L\tau_m} \qquad \text{(Eq. 3-9)}$$

where $\mathbf{V_0}$ is proportional to the volume magnetization before exchange.[242, 244]

The graphs in Figure 3-33 show the volume integral as a function of mixing time for each of the peaks in the 2D ^{119}Sn-^{119}Sn spectra (see Figure 3-38 in Appendix V for spectra). In general, the intensity of the observed cross peaks first increases as a function of mixing time and then decreases at longer τ_m due to spin-lattice relaxation. The diagonal peaks start off at the initial state of the magnetization, before spin diffusion, and they decrease as a function of mixing time as magnetization diffuses away from the site on which it originated.
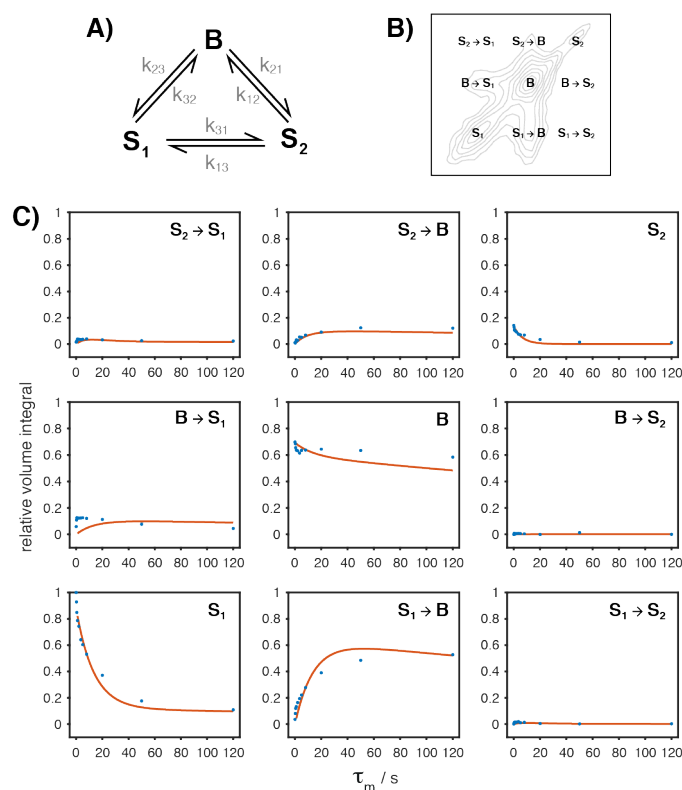
Figure 3-33. A) The three-site exchange model used to describe exchange between one bulk site and two surface sites. B) 2D spectrum marked with the first-order pathway of relay for each peak. C) Volume integrals of the diagonal and cross peaks from the 2D ^{119}Sn spectra of SnO_2 as a function of mixing time, τ_m. The solid lines are the results of the best fit of the data to the multisite exchange model described in the text.

The observed rate constants of transfer from surface to bulk extracted by fitting the peak volumes to the kinetic model ($k_{12} = 0.08$ s^{-1} and $k_{32} = 0.05$ s^{-1}, see Appendix V) are higher than the observed rate constant of back-transfer to the surface from the bulk ($k_{21} = 0.0001$ s^{-1} and $k_{23} = 0.01$ s^{-1}). The cross peaks between surface site S_1 and surface site S_2 are of low intensity, but the curves do show the expected characteristic behavior, and we find observed k_{13} = 0.06 s^{-1} and k_{31} = 0.003 s^{-1} (see Appendix V for details). This suggests that direct communication between the two surface sites occurs on a similar timescale as transfer to the bulk.

The apparent asymmetry in the observed rate constants (i.e. $k_{12} \neq k_{21}$) can be rationalized by the difference in the volume of the surface (lower volume) and bulk (higher volume). The microscopic forward and reverse spin exchange steps should have the same probability in both surface and bulk, but in the low volume of the surface part, a given transfer step is much more likely to lead to transfer to bulk than the reverse process. We note that the asymmetry in the spectra observed here require a difference in the forward and backward rate constants to be explained. This is not the same as asymmetry induced purely by non-equilibrium starting conditions.[245-246]

The spin-lattice relaxation rates extracted from the model are $R_{S1} \simeq R_{S2} \simeq 0.01$ s^{-1} and $R_B \simeq 0$ s^{-1} is not surprising considering that the longest mixing time is 120 s, and the build-up time of the bulk has been measured to be over 600 s at 8 kHz MAS rate. We also note that there are some systematic errors in the fit (notably for diagonal peak B and cross-peak $B{\rightarrow}S_1$) which might slightly affect the accuracy of the determination but which will not alter the overall conclusions.

^{31}P spin diffusion in gallium phosphide

We previously also showed how hyperpolarization from a broad range of surface shifts around the single ^{31}P bulk resonance of gallium phosphide, GaP, was transferred into the bulk by relay.[197]

Figure 3-34B shows contour plots of DNP enhanced 2D ^{31}P spin diffusion spectra of GaP with different mixing times. These spectra indicate two different surface sites (Figure 3-34A) transferring hyperpolarization into the bulk, which has a chemical shift of -148 ppm, on a timescale of around 10 s. The off-diagonal intensities representing surface transferring to bulk are observable within one second, and all of the surface polarization has been relayed from both surface sites to the bulk GaP after τ_m = 10 s. No cross peaks corresponding to bulk going back to surface are observed in these spectra.
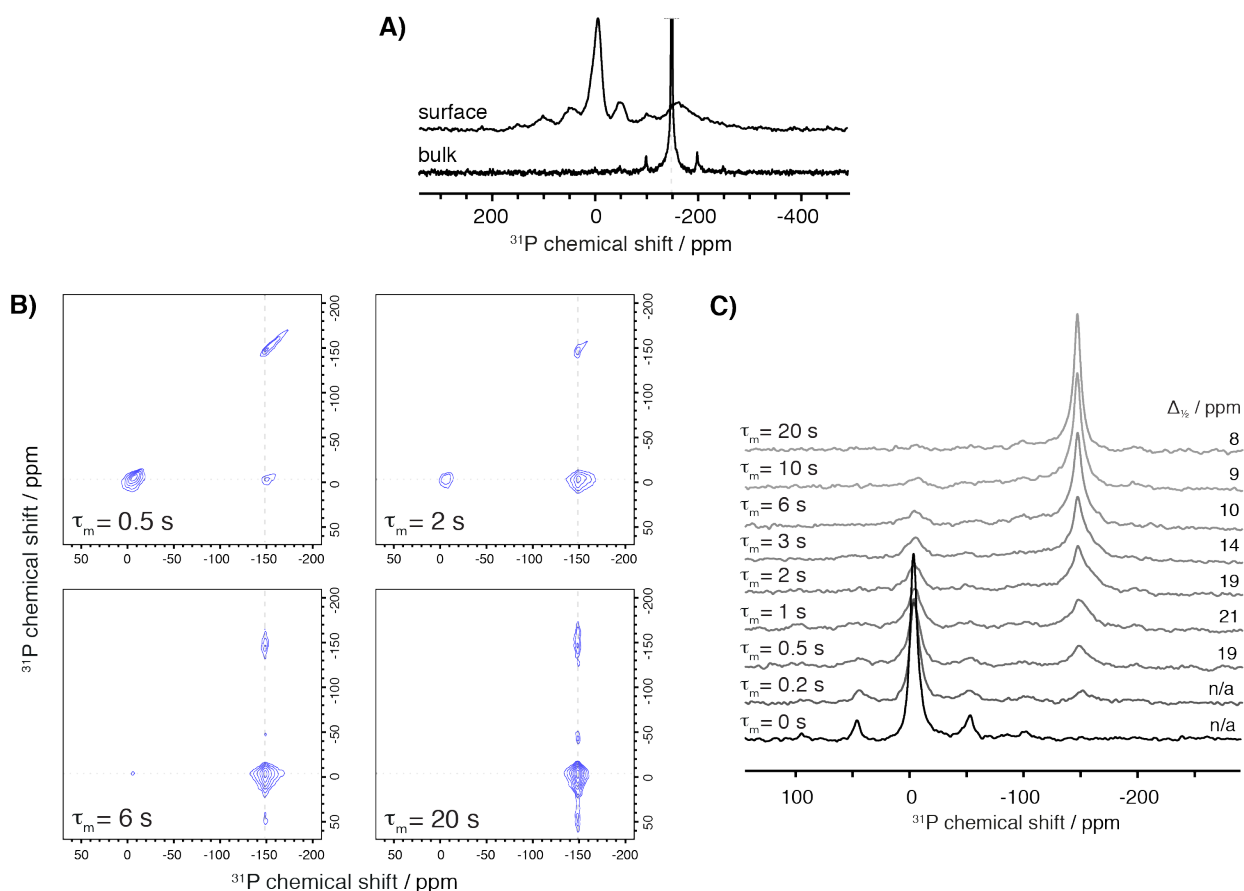

Figure 3-34. DNP enhanced ^{31}P spectra of GaP. A) Surface (^{1}H-^{31}P CP) and bulk ^{31}P spectra of GaP. B) Contour plots of DNP enhanced ^{31}P spin exchange spectra of GaP with different mixing times. The vertical dashed line is at the chemical shift of the bulk. C) Cross-sections taken along the dotted line in (b) parallel to ω_1 from the ^{31}P spin exchange spectra of GaP at different mixing times (see Figure 3-37 Appendix V). The full width at half height $\Delta_{\frac{1}{2}}$ of the cross peak located around -148 ppm is reported on the right.

Figure 3-34C shows cross-sections from the 2D spectra, taken parallel to ω_1. Each cross section contains a diagonal peak centered on the surface resonance at around -5 ppm. It decays monotonically as the mixing time is increased, as polarization is transferred to a region centered at -148 ppm. However, most interestingly, the linewidth of the cross peak at -148 ppm changes significantly with the length of the spin diffusion period, going from over 20 ppm when τ_m = 1 s to less than 8 ppm at τ_m = 20 s. This unambiguously indicates that some of the surface polarization that starts at -5 ppm is first transferred to other surface sites in the range -130 to -170 ppm, before then being further transferred to the bulk at -148 ppm. Figure 3-35 offers additional insight.
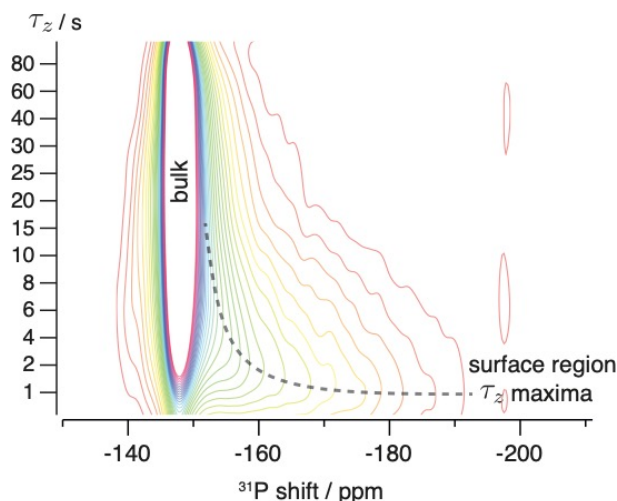
Figure 3-35. DNP enhanced ^{31}P CP spectra of GaP acquired as a function of τ_z. Complementary to Figure 3-34C, this series of 1D spectra suggests surface polarization from sites with the smallest chemical shifts moves through surface sites with progressively larger chemical shifts before making the jump into bulk.

Part II - Exchange between bulk sites

After looking into the relay process from surface to bulk, we shift the attention to polarization exchange between two or more different bulk sites in the same compound. The approach for studying this is well established and has been used before in the context of spin diffusion,[121] the main difference here being that the initial condition for the 2D experiment is prepared with the pulse cooling[197] method. This DNP enhanced variant of the conventional EXSY pulse sequence is shown in Figure 3-36A. Bursts of cross-polarization repeatedly hyperpolarize the surface of the particle, and the polarization moves towards the bulk during a spin diffusion delay τ_z, building up with the number of CP contacts. The advantage of using this strategy rather than direct excitation of the X nucleus is that it can provide higher signal-to-noise ratio for the bulk. Following the preparation of the initial condition, the pulse sequence continues as shown in Figure 3-36A with a 2D exchange experiment as described previously for the surface to bulk transfer. After the mixing period, τ_m, the absence or presence of an off-diagonal intensity will determine whether there is exchange/spin diffusion between the two bulk peaks.

[31]P spin diffusion in tin pyrophosphate

Figure 3-36B shows that polarization transfer between the two bulk sites in tin pyrophosphate happens on the order of a few seconds. In this case, the two-site exchange model where we assume $k_{AB} = k_{BA}$ can be used to determine the observed rate of transfer:

$$\frac{I_{AA}}{I_{AB}} = \frac{1 + \exp(-2kt_m)}{1 - \exp(-2kt_m)}$$

(Eq. 3-10)

The ratio of intensities for the diagonal peaks, I_{AA}, and cross-peaks, I_{AB}, are 1.98 and 1.94, giving an observed exchange rate constant of around $k = 0.11$ s^{-1}. In this case, there is no observable back-transfer to the surface.

[31]P spin diffusion in potassium pyrophosphate

Another example of this is shown for the ^{31}P spectrum of potassium pyrophosphate, $K_4P_2O_7$ (Figure 3-36C), which has five isotropic chemical shifts over a range of around 5 ppm.[247] This compound has a ^{31}P longitudinal relaxation rate of >400 s and, as before, the pulse cooling strategy is used before the mixing period, in order to increase sensitivity.

Cross peaks between the bulk sites in the DNP enhanced 2D bulk exchange spectrum in Figure 3-36C are apparent between all the bulk sites (one of the cross peaks is not shown in the contour plot as it is too close to the noise), as well as with the prominent slow-relaxing surface peak at around -1.5 ppm. This indicates that even if the surface hyperpolarization were only channeled into one of the bulk resonances, the rest of the bulk sites would also become hyperpolarized by relay, as the bulk resonances exchange with each other on a timescale that is shorter than the relaxation time of the compound.
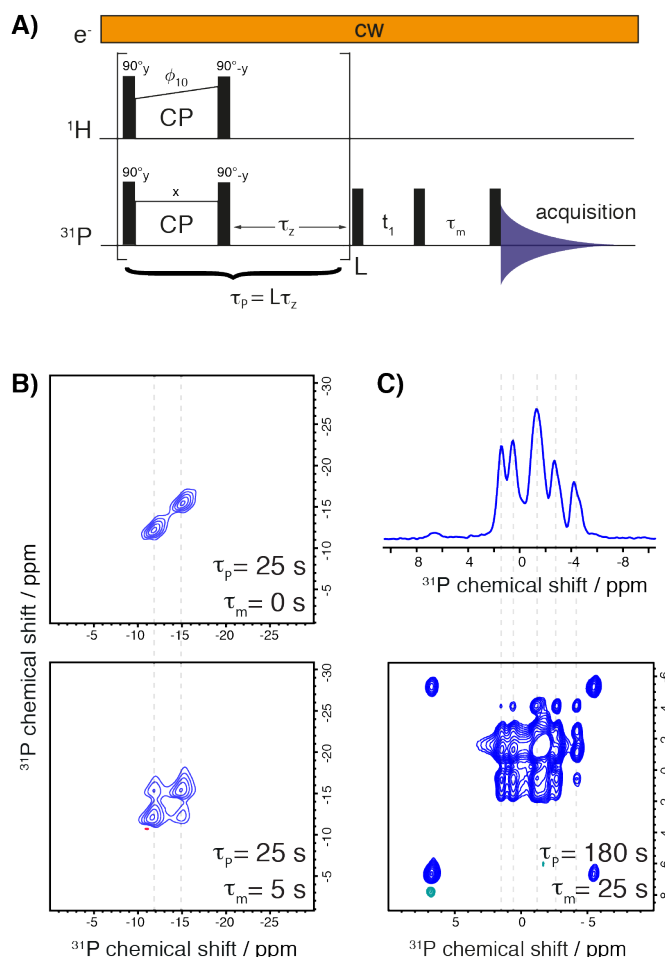
Figure 3-36. A) Pulse sequence used in the bulk-bulk 2D spin diffusion experiment. B) Contour plots of the DNP enhanced ^{31}P CP spectra of $Sn_2P_2O_7$ showing bulk exchange. C) ^{31}P spectrum of neat (not impregnated) $K_4P_2O_7$ above the DNP enhanced ^{31}P CP two-dimensional spectrum of $K_4P_2O_7$ showing bulk exchange.

3.4.4 Conclusion

We have shown how two-dimensional spin diffusion experiments can be used to study the pathways of polarization exchange between weakly magnetic nuclei in inorganic materials. In particular, we focus on magnetization transfer from surface sites to bulk under MAS, even in the presence of significant chemical differences. We show this with the ^{31}P spectra of $Sn_2P_2O_7$, GaP and $K_4P_2O_7$, and the ^{119}Sn spectra of SnO_2. We found that polarization can be transferred from a range of surface sites with different chemical shifts to other surface sites, and to one or more bulk sites on the same time scale.

3.4.5 Appendix V

NMR acquisition parameters and additional spectra

Table 3-17. NMR parameters used for the acquisition of the 2D spin diffusion spectra (Figure 3-30 to Figure 3-36).

	$Sn_2P_2O_7$	SnO_2	GaP	$K_4P_2O_7$
MAS rate / Hz	8000	8000	8000	8000
DNP solvent enhancement, $\varepsilon(^1H)$	255	80	92	75
Number of insert/eject cycles	4	3	3	3
Number of scans	6	48[a]	8	2
X rf field amplitude during CP / kHz	100	100	100	83
CP contact time / µs	2500	3000	2000	3500
Line broadening / Hz	100[b]	100	400	0

[a] For all τ_m except 50 s and 120 s, where the number of scans was 12

[b] The line broadening applied in Figure 3-30 was 100 Hz for f3 and 0.3 Hz for f2
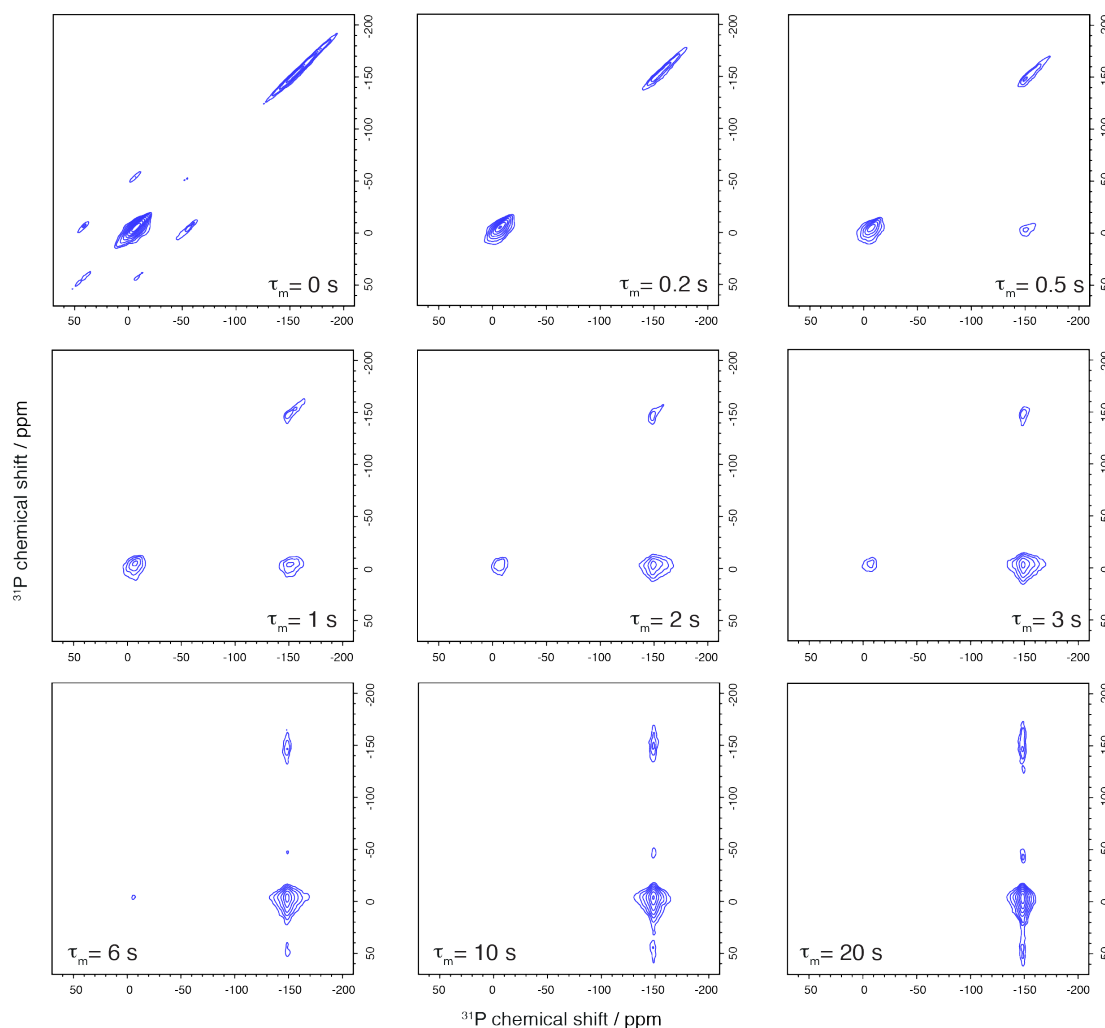
Figure 3-37. DNP enhanced ^{31}P 2D spin diffusion spectra of GaP with different mixing times. The spectra were recorded at 9.4 T and 100 K, at an MAS rate of 8 kHz. The GaP powder (42.3 mg, ground in a mixer mill) was impregnated with 7.5 µL of 16 mM solution of TEKPol in TCE. The ^1H enhancement of the solvent was 92 and the phosphorus enhancement through CP, ε_{1H-31P}, was 27. A recycle delay of 2.5 s and 8 scans were used, and the t1 increments were 140. The spectra were processed with a line broadening of 200 Hz in both dimensions. The phasing and the contours are the same for all spectra.
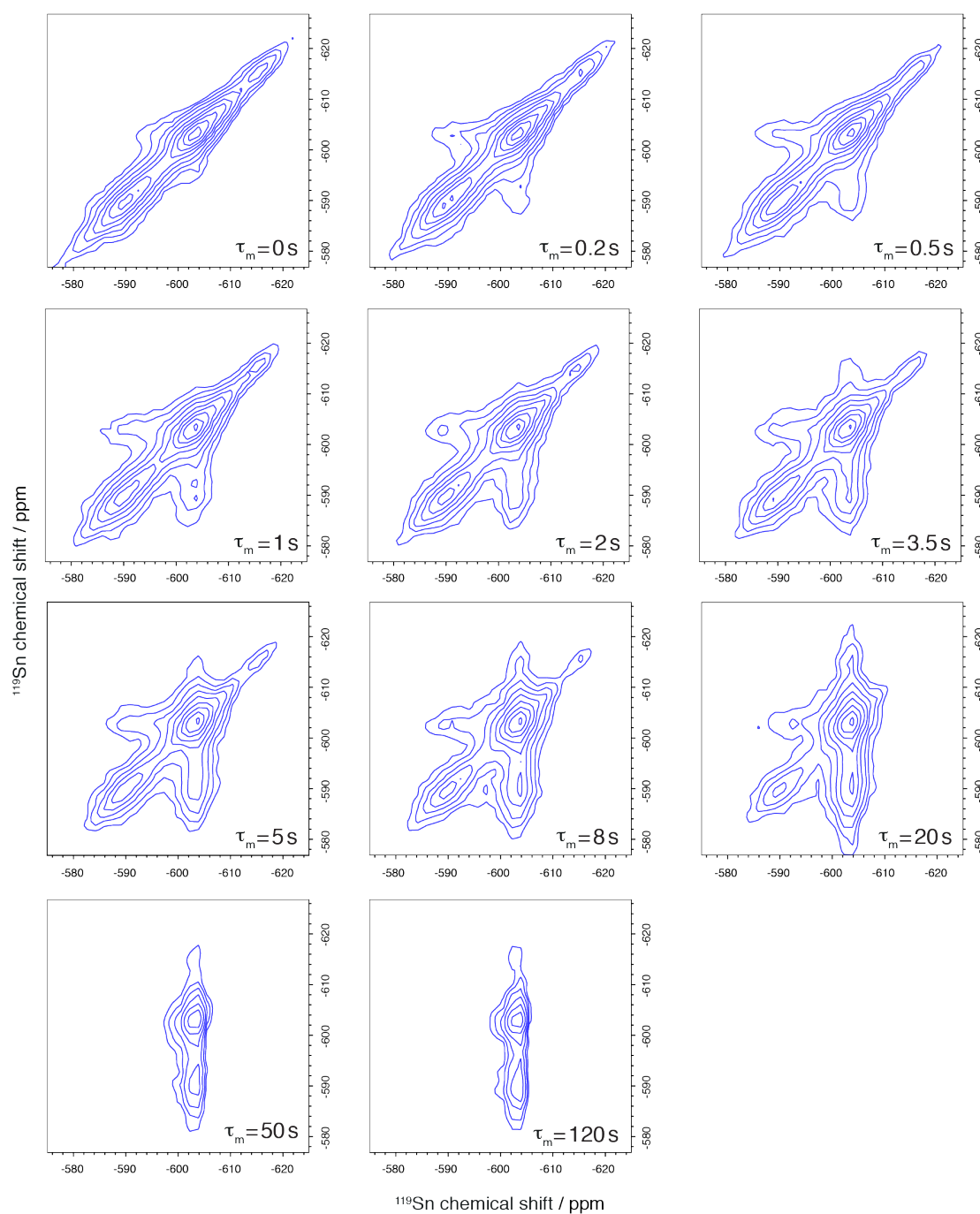
Figure 3-38. DNP enhanced ^{119}Sn 2D spin diffusion spectra of SnO$_2$ with different mixing times. The spectra were recorded at 9.4 T and 100 K, at an MAS rate of 8 kHz. The SnO$_2$ powder (41.5 mg, ground by hand) was impregnated with 10 μL of 16 mM solution of TEKPol in TCE. The ^{1}H enhancement of the solvent was 80 and the tin enhancement through CP, ε$_{1H-119Sn}$, was 75. A recycle delay of 2 s and 48 scans were used, except for the two longest mixing times, where 12 scans were used. The t1 increments were 32. The spectra were processed with a line broadening of 100 Hz in both dimensions. The phasing and the contours are the same for all spectra.

Fitting to kinetic models: two-site exchange

To evaluate the quality of the models used to fit the data in Figure 3-29, the fit parameters obtained from the experimental data were used to create a set of "perfect data". Random Gaussian noise, where $3\sigma = \pm 0.1$ relative area, was then added 200 times to those data points to create 200 new sets of data which were subsequently fit to the same exchange rate model as was used to fit the experimental data.

parameter	Fit result
k_{SB} (s^{-1})	0.089
k_{BS} (s^{-1})	0.012
$R_{1,S}$ (s^{-1})	0.017
$R_{1,B}$ (s^{-1})	0.002
V_S	0.942
V_B	0.041

Figure 3-39. ^{31}P peak areas for the surface and bulk sites in Sn$_2$P$_2$O$_7$ as a function of time. The solid lines are fits to the data based on the exchange model explained in the main text and the dotted lines show the region of 1.5σ of the noise that was added to the data. The table shows the parameters obtained from fitting the experimental Sn$_2$P$_2$O$_7$ data in Figure 3-29 to the two-site exchange model described in the main text.
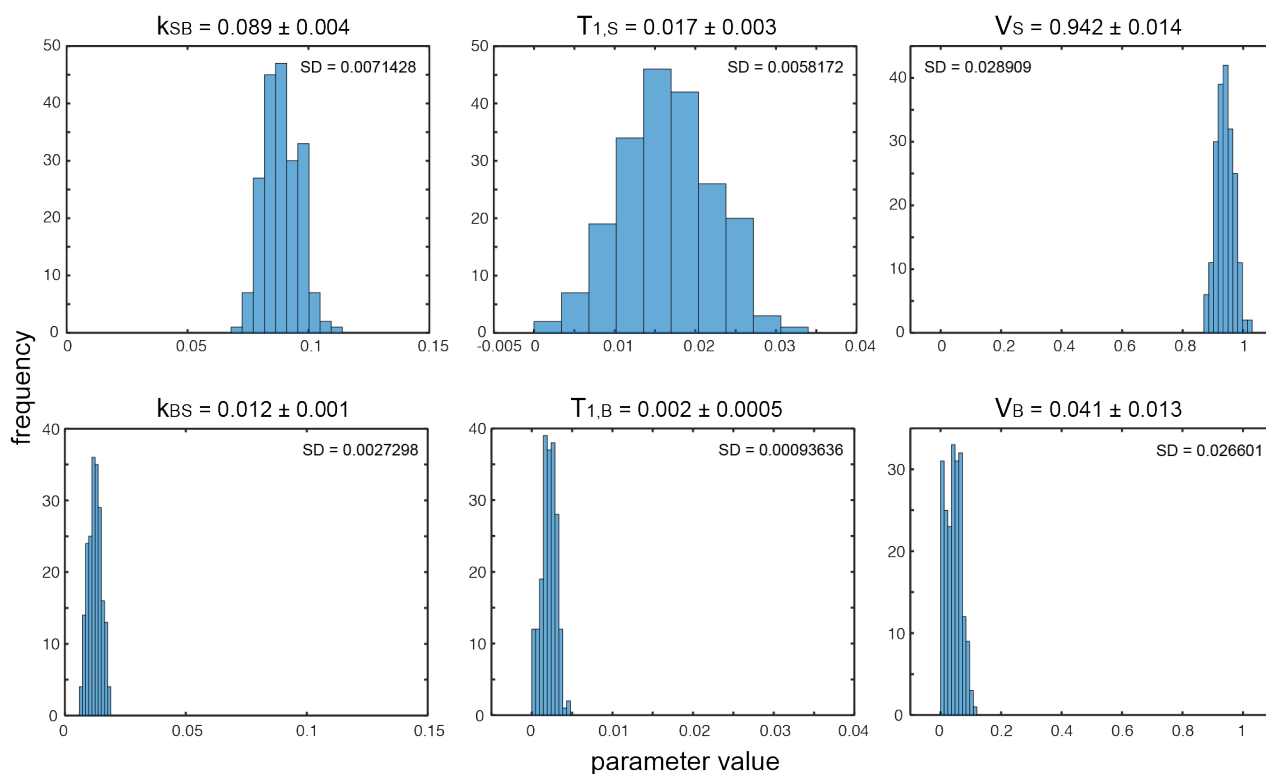
Figure 3-40. Histograms obtained from cross validation of fitting the data from the spin diffusion spectra of Sn$_2$P$_2$O$_7$ data to the two-site exchange model. The data was fit 200 times and the parameters are reported with their standard deviation. Each set of parameters, k_{SB} and k_{BS}, $T_{1,S}$ and $T_{1,B}$, V_S and V_B, is plotted on the same x-axes.

Fitting to kinetic models: three-site exchange

Table 3-18. Parameters obtained from fitting the experimental SnO_2 data to the three-site exchange model described in the main text.

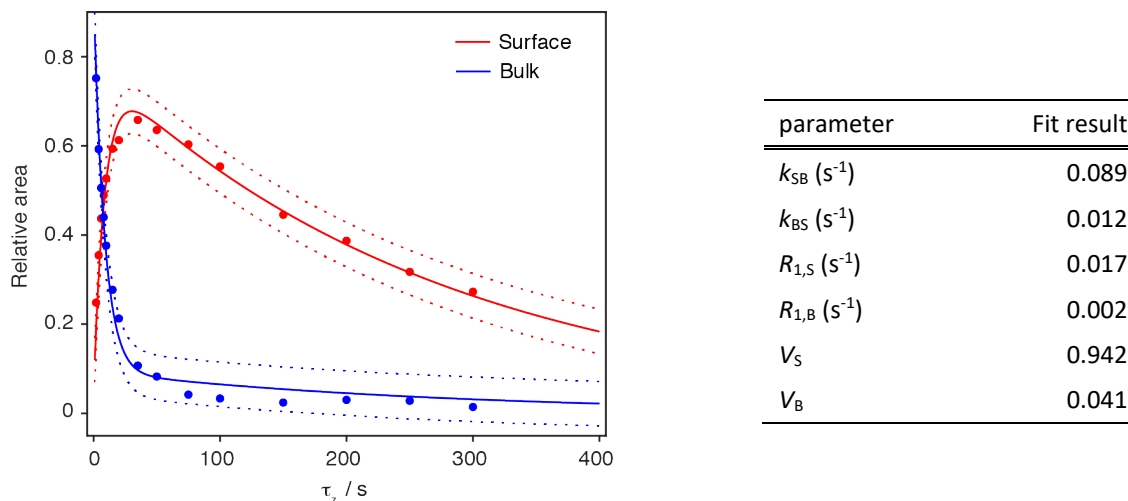| parameter	Fit result	parameter	Fit result
k_{12} (s^{-1})	0.0843	R_{S2} (s^{-1})	0.0058
k_{21} (s^{-1})	0.0001	R_B (s^{-1})	1×10^{-6}
k_{23} (s^{-1})	0.0116	R_{S1} (s^{-1})	0.0111
k_{32} (s^{-1})	0.0517	V_{S2}	0.1359
k_{13} (s^{-1})	0.0641	V_B	0.6912
k_{31} (s^{-1})	0.0029	V_{S1}	0.8778
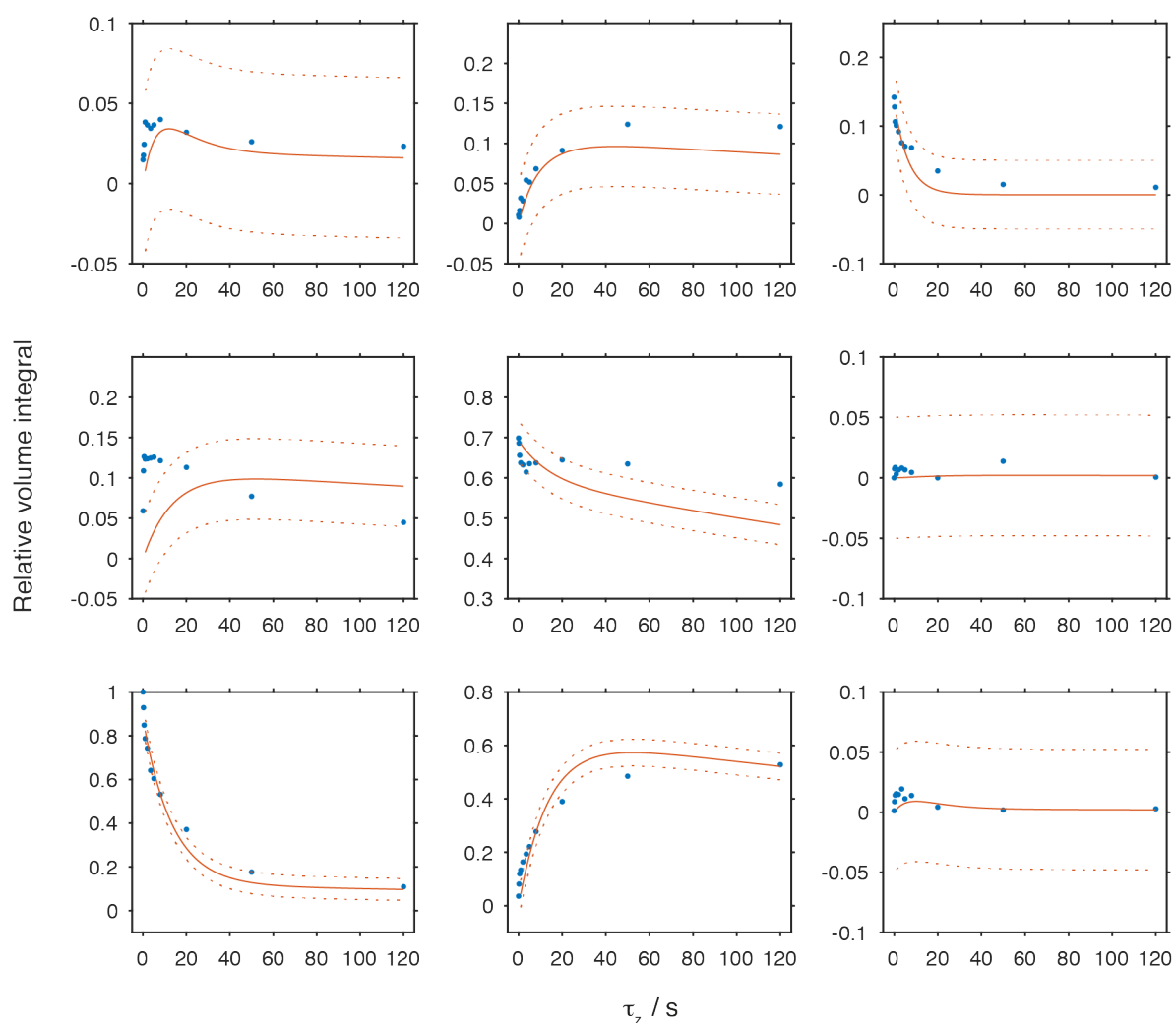
Figure 3-41. ^{119}Sn peak areas for the surface and bulk sites in SnO_2 as a function of time. The solid lines are fits to the data based on the three-site exchange model explained in the main text (same as Figure 3-33, but not with constant y-axes) and the dotted lines show the region of 1.5σ of the noise that was added to the data.
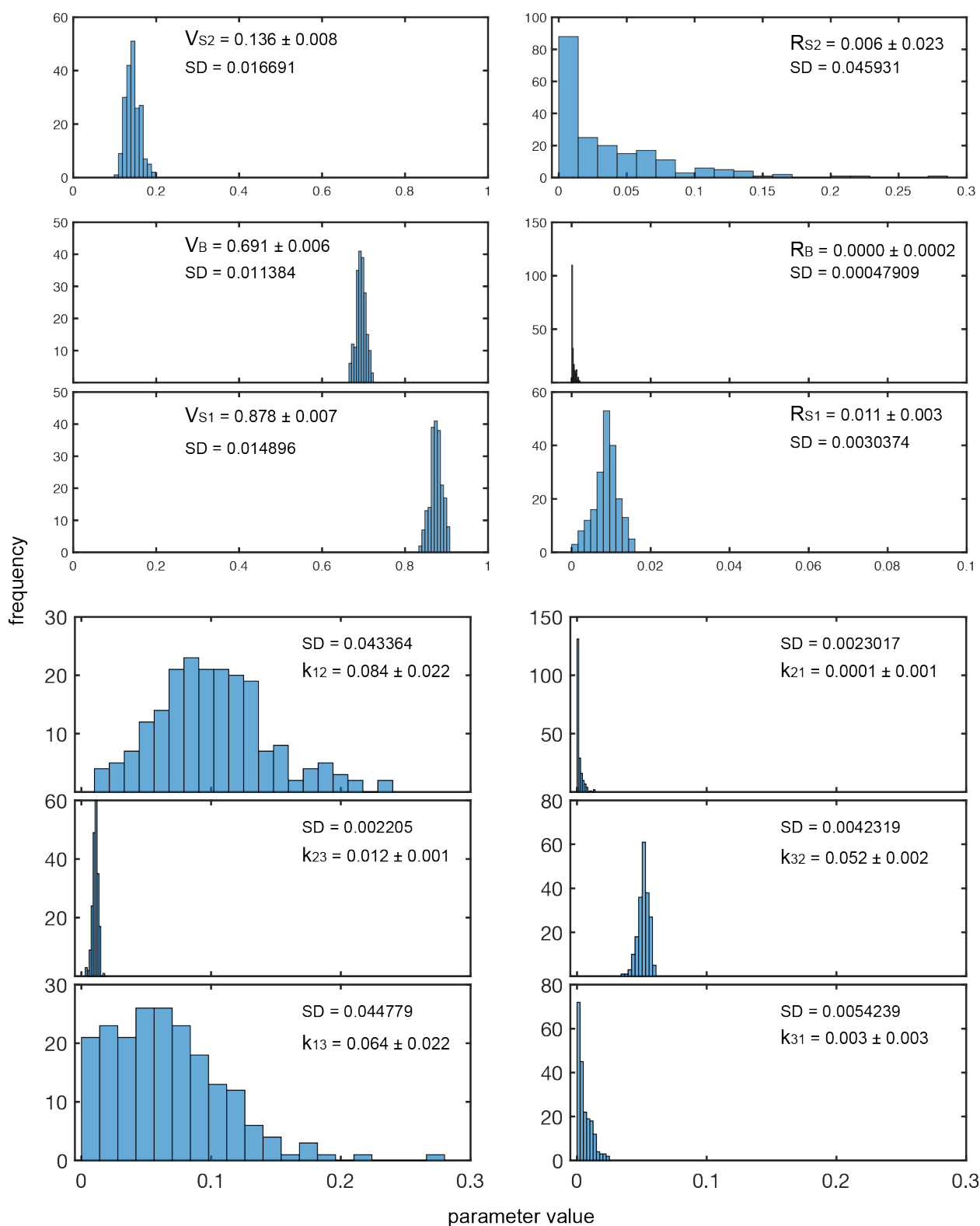
Figure 3-42. Histograms for the parameters obtained from cross validation of fitting the data from the 2D spin diffusion spectra of SnO_2 to a three-site exchange model. The data was fit 200 times, and the standard deviations are given. Parameters were constrained to not go below 0.

Chapter 4   DNP at fast MAS

4.1   The limits of MAS DNP

In solid-state NMR, the combination of high magnetic fields and fast magic-angle spinning (MAS) is often a requirement to allow the study of complex systems and to implement sophisticated multi-dimensional experiments. State-of-the-art commercial NMR instrumentation uses magnetic fields of up to 28 T (1.2 GHz) and MAS probes able to spin samples to 111 kHz at room temperature using 0.7 mm diameter rotors. Such spinning regimes significantly improve resolution in samples from small crystalline pharmaceuticals to fully protonated protein assembles,[248-250] and there is therefore tremendous interest in combining these approaches with DNP.

Up to now, the majority of MAS DNP development has been carried out at moderate magnetic fields (<14 T), with samples spinning at frequencies up to 15 kHz, at around 100 K. This chapter will give a brief overview of DNP outside these regimes,[251] before presenting the first ever results of MAS DNP at 65 kHz.

4.1.1   Higher magnetic fields

In a conventional solid-state NMR experiment, higher magnetic fields can provide improved resolution, with an increase in spectral resolution proportional to B_0 for spin-½ nuclei. It should be noted that in some instances higher fields are not as beneficial, an example being disorder where linewidths are dominated by a distribution of isotropic chemical shifts.[252] High magnetic fields also increase thermal polarization of nuclei, which generally improves the sensitivity in NMR experiments, as mentioned in Section 1.1.1. However, several other factors can also influence the SNR at higher fields, for example increased chemical shift anisotropy, as well as factors related to the probe and the receiver.[253-254]

Dynamic nuclear polarization at high fields is technologically more demanding than conventional solid-state NMR, as cryogenic temperatures (~100 K) are usually required. Another hurdle is that, as mentioned in Section 1.2.2, the efficiency of many polarizing agents commonly used at 9.4 T decreases with increase in magnetic field, as the cross-effect polarization transfer mechanism scales negatively with field. Thus, for efficient DNP at higher magnetic fields, the existing approaches need to be modified.

One approach is to utilize a different polarization transfer mechanism. In 2014, Can *et al.* used the carbon centred radical BDPA in a polystyrene matrix, to obtain significant proton DNP enhancements (ε_H) using either Overhauser effect (OE) or Solid-Effect (SE).[19] They found that the Overhauser effect scales favourably with field as seen in Figure 4-1, going from ε_H = 14 at 9.4 T to ε_H = 20 at 18.8 T, which is roughly a linear increase. Later, enhancement of ε_H = 65 at 9.4 T and ε_H = 75 at 18.8 T were reported for BDPA, this time by using a matrix consisting of 95% deuterated orthoterphenyl (OTP-$d_{95\%}$).[161] At an even higher field, 21.15 T, an enhancement of ε_H = 73 was reported using BDPA/ OTP-$d_{95\%}$ (this result is from Chapter 2).[181] It should be noted that the reported values come from experiments which were performed at moderate sample spinning rates, either 8[19, 161] or 12.5[181] kHz, using 3.2 mm rotors.
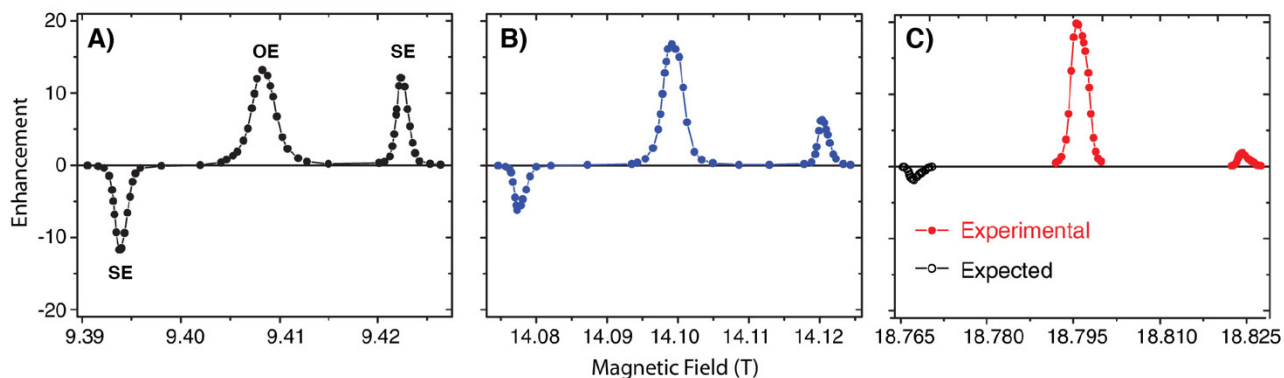
Figure 4-1. Field sweep profiles for the ^{1}H enhancement of BDPA dispersed in polystyrene at magnetic fields of around A) 9.4 T, B) 14.1 T and C) 18.8 T. The enhancement of the Overhauser effect scales linearly with B_0 while the solid effect, SE, scales as approximately B_0^{-2}. Figure reproduced from reference[19].

Another way to improve DNP at high field is to improve the efficiency of the CE by altering the design of the polarizing agent (see Section 1.2.2). Cross-Effect DNP has been extensively studied and many design parameters have been discovered,[58-60, 84, 94, 255-256] and theoretical models proposed,[67, 169, 257-263] allowing tailoring of the structure of CE polarizing agents in order to optimize their performance. Unfortunately, CE polarizing agents that perform very well at moderate magnetic fields and spinning frequencies (e.g. AMUPOL), scale unfavourably when going to higher magnetic fields.[59, 64, 264] AMUPol in an aqueous matrix, spinning at 8 kHz MAS, gives an enhancement of ε_H = 235 at 9.4 T, but only ε_H = 30 at 18.8 T.[59, 265]

Capitalizing on the work of Hu et al.,[67] Mathies et al. introduced the concept of mixed biradicals in 2015 in which a TEMPO-like moiety was tethered to a trityl radical.[66] In particular the performance of the resulting TEMTriPol-1 scaled favourably with the magnetic field between 5 T and 14.1 T, yielding a ^{1}H enhancement of 60 at 5 T, 87 at 14.1 T, and 65 at 18.8 T, which was attributed to the strength of the exchange interaction between the trityl radical and the nitroxide.[66] Merging this finding with the previous concept of decorated binitroxides to provide longer electron relaxation times, Wisser et al. proposed a series of mixed BDPA-nitroxide biradicals and evaluated their performance at both high field (up to 21.15 T) and fast MAS (up to 40 kHz using a 1.3 mm rotor). In particular, the radical HyTEK-2 yields ^{1}H enhancements of up to 185 at 18.8 T and 40 kHz MAS in a 1.3 mm rotor which was, so far, the highest DNP enhancement reported at high magnetic field and fast MAS.[64]

4.1.2 Higher MAS frequencies

Increasing the MAS frequency improves spectral resolution and extends coherence lifetimes in solid-state NMR spectra, which has been a driving force for the development of MAS probes with increasingly small rotor diameter, capable of progressively faster spinning. Currently, 0.5 mm diameter rotors can spin up to 150 kHz at room temperature.[248, 266-267] In general, with increase in spin rate comes a decrease in sample volume, as the rotor used has a smaller diameter. This dilution in sample volume might seem to be a limitation, but it is partially counterbalanced by the fact that the sensitivity of a NMR coil scales with the inverse of the coil diameter.[268]

Most of the state-of-the-art MAS DNP has been developed using rotors with a diameter of 3.2 mm, which can spin up to maximum 15 kHz at 100 K. In a sample of proline with TOTAPOL as the polarizing agent, ε was found to first increase with spin rate and reaches a maximum around 3 kHz, but then decreases as seen in Figure 4-2. This decrease is attributed to the rise in sample temperature (around 10 K) when increasing the MAS rate from static to 12 kHz, and is expected to diminish significantly if the temperature is carefully controlled.[42, 58] In recent years, along with the development of DNP instrumentation for stronger magnetic fields[251, 269], achievable maximum spin rates in DNP have been increasing.

DNP at up to 40 kHz MAS with 1.3 mm rotors was first reported in 2016.[175, 265] It was shown that on a sample of proline with AMUPol as the polarizing agent, the CE DNP enhancement stayed relatively constant around $\varepsilon = 60$ when the spin rate was increased from 15-40 kHz. With increased spin rate, the T_B increases and the contribution factor (the fraction of nuclei contributing to the NMR signal) decreases. Regardless, the overall sensitivity enhancements are still high. Additionally, as mentioned before, another advantage of faster MAS rates is the increase in transverse coherence lifetimes, which facilitates the use of CPMG acquisition for further sensitivity enhancements.[265]

The rotor diameter itself also has an effect on DNP enhancements. At the same MAS rate and temperature, the DNP enhancement factor measured on a sample of AMUPol dissolved in a mixture of glycerol and water, was reported to give an enhancement around two times higher in a 1.3 mm rotor than the same sample in 3.2 mm rotor This is ascribed mostly to more efficient microwave penetration in the smaller rotor. It should also be noted that the waveguide coupling has been improved in 1.3 mm probes, compared to 3.2 mm DNP probes.[47, 49]

The Overhauser effect mechanism for polarization transfer has been shown to yield higher enhancements with increased spin rate.[19, 175] A sample of BDPA dissolved in OTP was found to give an enhancement of over 100 at a MAS rate of 40 kHz, with the enhancement increasing as a function of MAS rate ($\varepsilon_H = 23$ at 0.5 kHz MAS). BDPA is a narrow line radical, it has a contribution factor of 1 in OTP and does not enhance relaxation much (see Section 1.2.3 for description of overall sensitivity). It does however have a relatively long polarization build-up time, which increases with increased MAS rate.[36] A method to overcome the sensitivity limitation imposed by the long T_B values was shown in Chapter 2.
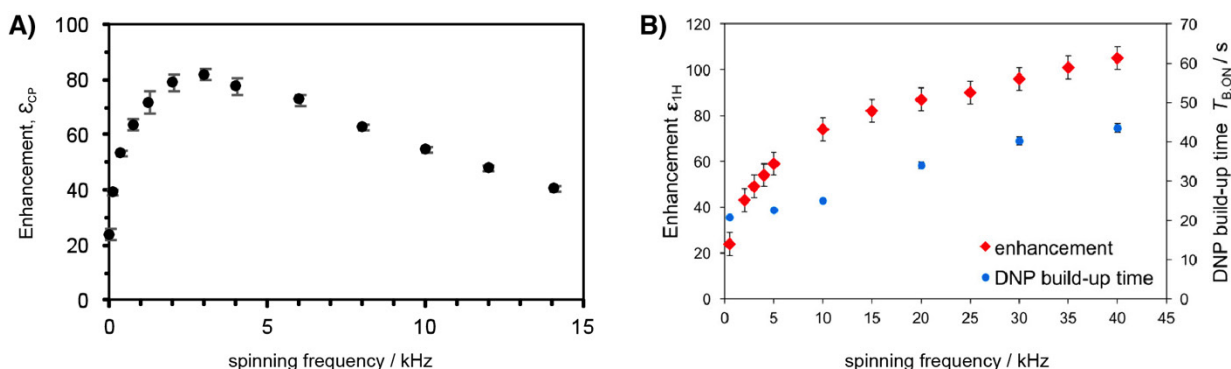
Figure 4-2. A) ^{1}H-^{13}C DNP signal enhancement as a function of MAS rate in a sample of proline dissolved in 10 mM solution of TOTAPOL in glycerol-d$_8$/D$_2$O/H$_2$O (60/30/10 volume ratio). The experiment was performed at 9.4 T and around 100 K, in a 3.2 mm rotor. Figure reproduced from reference[42]. B) ^{1}H enhancement as a function of MAS rate in a 60 mM solution of BDPA in 95% d-OTP/OTP at 18.8 T. Figure reproduced from reference[175].

Under certain conditions, CE enhancements can also increase as the sample spinning rate is increased.[64] This behaviour was not predicted by microscopic models,[68] but spin diffusion models (similar to the one introduced in Section 1.3.5) can be used to reproduce the behaviour.[175] This will be discussed further in Section 4.2.2.

Proton detection and suppression of solvent signals

Faster spinning frequencies open up the possibility of proton detection in DNP NMR. The high natural isotopic abundance and the high gyromagnetic ratio of protons make for attractive qualities for the NMR characterization of proton containing compounds, and proton correlation experiments are powerful tools for structural determination in many materials.[4] That said, proton homonuclear couplings are strong and ^{1}H line widths in solids spinning at <20 kHz are usually so broad that the spectra are not useful unless decoupling methods are used. Their superior sensitivity can however be utilized in spinning regimes of over 25 kHz, where the possibility of indirect

detection opens up.[270-271] Proton detection enhances the signal intensity of a lower-γ nucleus in heteronuclear NMR experiments by detecting on ^{1}H and observing the heteronuclei indirectly. Wang *et al.* showed this in combination with DNP in 1.3 mm rotors at spinning frequencies up to 40 kHz. As an example, ^{1}H detected ^{1}H-^{89}Y DNP HETCOR at 40 kHz MAS surpassed the sensitivity of DNP HETCOR recorded using 3.2 mm rotors at a lower spinning rate.[272]

At MAS rates of around 60 kHz or higher, the ^{1}H signals are narrow enough to represent an alternative to proton homonuclear decoupling.[273] However, since DNP samples contain somewhat large amounts of solvent/matrix, the solvent resonance can overlap with the peaks of interest and even mask them. This is also often true for ^{13}C DNP spectra, as both glycerol and many organic solvents have strong ^{13}C signals. Formulating the sample differently can in some cases work, for example by using ^{13}C depleted solvents or by selecting solvents that do not overlap with the material of interest, but this is not always practical and would be even more challenging for ^{1}H than ^{13}C. Solvent suppression methods represent a more general solution to the problem, and their development is important in the context of ^{1}H detected DNP NMR.

Among the methods introduced for solvent suppression in DNP at 9.4 T in a 3.2 mm rotor, one strategy is to make use of the fact that the transverse coherence lifetimes of the solvent spins are usually shorter than for example those of sites on the surface. Solvent signals can therefore be filtered out with a spin-echo prior to signal acquisition, or a proton spin lock before CP.[166] Another method for solvent suppression is to use deuterated solvents and ^{2}H-^{13}C dipolar recoupling sequences to selectively dephase the solvent ^{13}C resonances.[274] It is also possible to use highly concentrated radical solutions, which leads to strong paramagnetic relaxation and shortens the apparent relaxation times of the nuclear spins close to the radicals.[275]

4.1.3 Higher or lower temperatures

Although the experimental conditions presented in this chapter do not deviate far from 100 K, the following section nonetheless gives an overview of DNP at lower and higher temperatures.

DNP NMR at temperatures <100 K

Commercial MAS DNP systems spin the sample at around 100 K, but it is well known that lowering sample temperatures can be beneficial for DNP performance.[276] Considerable effort is currently being put into developing instrumentation for DNP at temperatures lower than 100 K, involving the use of cold He gas.[46, 277-278] MAS using helium gas for cooling and spinning was first introduced in the 1980's.[273, 279] At temperatures around 70 K, increase in Boltzmann polarization and reduction in thermal noise from RF circuitry, already provide a gain in sensitivity of around an order of magnitude. The expected gains can be reduced by instrumental factors as well as increase in relaxation times.[273]

Examples of DNP at <100 K can be seen in Figure 4-3, where DNP enhancement factor under MAS is plotted as a function of temperature. A sample of urea dissolved in a glass forming solution with AMUPol, was shown to give an enhancement of 290 at 110K, going up to over 600 at 55K. Low temperatures also slow down electron relaxation of nitroxides, lowering the microwave power requirements for optimal DNP performance (which could for example be important for pulsed techniques).[277] Figure 4-3B shows how, in a solution of triradical polarizing agent DOTOPA-Ethanol in a glassy matrix, the enhancement is much more strongly dependent on temperature than the build-up time, which leads to increase in overall sensitivity.[43]
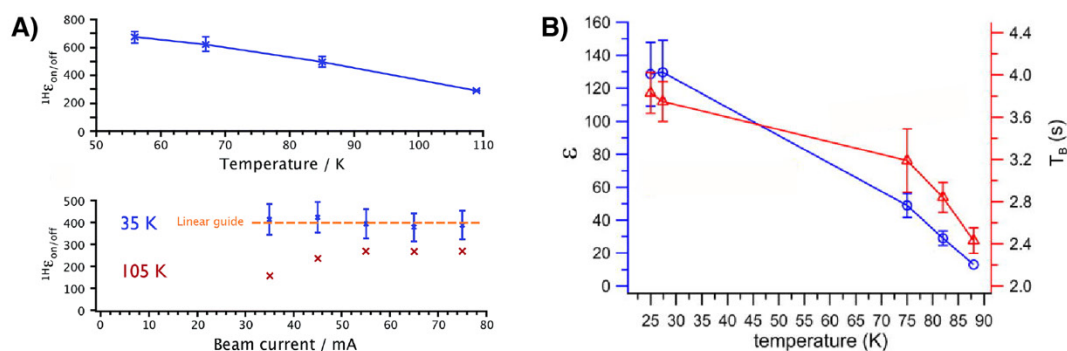
Figure 4-3. DNP enhancements as a function of temperatures <100 K, at 9.4 T. A) ^{1}H enhancement at 10 kHz MAS and T <110 K in a ^{13}C-urea solution containing 5 mM AMUPol, and the effect of the microwave beam current on ε in the same sample at 5 kHz MAS. B) ^{1}H-^{13}C CP enhancement at ~6.7 kHz MAS, on a 10 mM solution of DOTOPA-Ethanol in an aqueous glass forming matrix, and the change in build-up time as a function of temperature in the same sample. Figures reproduced from reference[277] and reference[43].

DNP NMR at temperatures >100 K

Contrary to going to lower temperatures, there is also interest in DNP at higher temperatures. It should be noted that DNP has been studied extensively at room temperature in specific systems such as diamond,[36] but the interest here is to create a glassy matrix that can be applied more generally to different compounds for DNP at >100 K. This is notably appealing for biological applications such as studies of dynamics in solid proteins, as protein spectral resolution gets significantly worse at around 100 K when side-chains freeze in a heterogeneous distribution of conformers.[110]

The ^{1}H DNP enhancement of TOTAPOL polarizing a biological sample was observed to drop from around 120 at 100 K to around 10 at 180 K, as can be seen in Figure 4-4.[280] A similar result was found for another CE biradical, TEKPol in TCE, where the enhancement went from 150 at 100 K to around 30 at 180 K.[58] In both cases the decrease in enhancement was thought to be mainly because of the glass-forming behaviour of the DNP matrix, at temperatures above the glass transition temperature, the electron relaxation rates of the radicals increase leading to lower enhancements.

Some early low field MAS DNP experiments were performed at room temperature.[36, 182] Notably, the first DNP experiments at 5 T were carried out at room temperature, using the monoradical polarizing agent BDPA in a matrix of polystyrene (ε ≈ 10 through SE).[39] Building on these findings, OTP was identified as a DNP matrix suitable for higher temperature experiments, as it has a relatively high glass transition temperature of 243 K. The matrix has been demonstrated to be compatible with different polarization transfer mechanisms (Figure 4-4C), leading to DNP enhancements of over 60 at 240 K. [161]
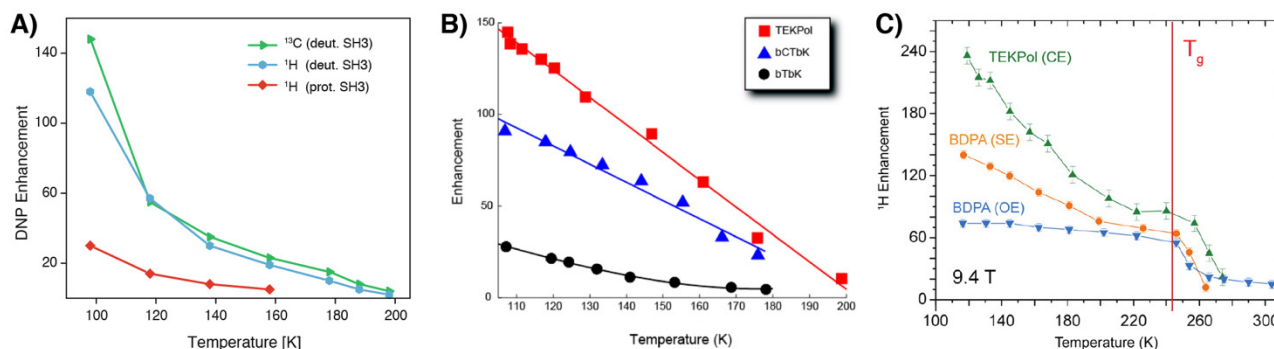

Figure 4-4. DNP enhancements as a function of temperatures >100 K, at 9.4 T. The samples are A) deuterated and protonated SH3 protein domains in a glycerol/water matrix with 20 mM TOTAPOL as the polarizing agent, B) 16 mM solutions of three different binitroxides in TCE, and C) 16 mM TEKPol and 32 mM BDPA in an 95% OTP-d$_{14}$. Reproduced from references [58, 161, 280] respectively.

4.2   DNP at 21.15 T and up to 65 kHz MAS

4.2.1   Introduction

Here we present the first DNP MAS experiments using a 0.7 mm MAS probe. This probe allows us to reach spinning frequencies of up to 65 kHz, with µw irradiation, at 100 K, and at a field of 21.15 T. We report the performance, at very fast MAS, of BDPA in 95% deuterated orthoterphenyl (OTP-d$_{95\%}$) and HyTEK2 in 1,1,2,2-tetrachloroethane (TCE). In both we find that enhancements continue to increase significantly with increasing spinning rates, and we obtain enhancement factors of up to 200 for HyTEK2. Beyond the good DNP performance, we also report the highest directly detected ^{1}H resolution in DNP MAS solid-state NMR spectra observed so far.

At 100 K the 0.7 mm rotors can stably spin at rates up to 65 kHz. Although 0.7 mm rotors can spin stably up to 120 kHz at room temperature, at 100 K fluid dynamics of the cold nitrogen gas limits the maximum rate. Notably, the density of N$_{2(g)}$ is about 3 times higher at 100 K as compared to 298 K and the speed of sound is a factor 2 slower.[277] (In principle this could be mitigated by, for example, spinning using helium gas, but this is technically not straightforward.) Spinning stability at 65 kHz and 100 K is usually very reliable and stable in the range of ±9 Hz (see Figure 4-5).
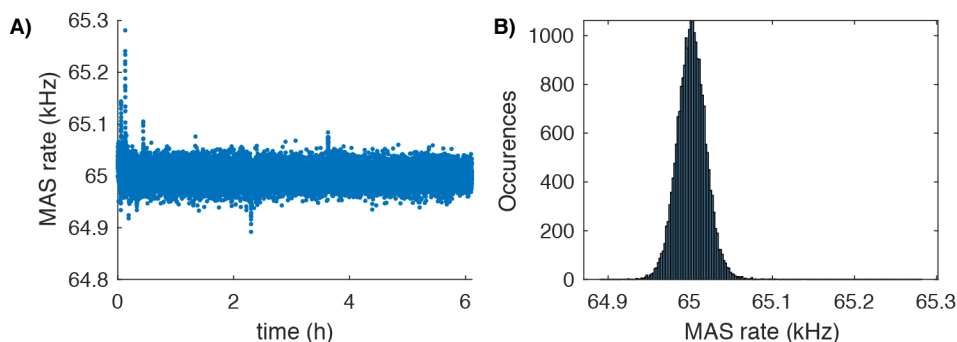
Figure 4-5. A) MAS rate measured every second during 6h with a sample spinning at 65 kHz, at ca. 100 K. In the first 20 min, we can observe some instabilities due to the temperature equilibrating. The spikes at 0.4 h and 3.6 h correspond to the operator turning the gyrotron from off to on; the spike at 2.3 h corresponds to the gyrotron being turned from on to off. The instability caused by the operation of the µwaves causes instabilities that are then regulated by the MAS regulation unit in few minutes. B) Histogram of the MAS rate measurements during the 6h. The standard deviation of the distribution is 18 Hz, giving a MAS rate of 65 kHz ± 9 Hz.

4.2.2   Results and discussion

For reasons stated in Sections 4.1.1 and 4.1.2, OE DNP with BDPA in OTP-d$_{95\%}$ appeared to be a system of choice to perform DNP measurements using very fast MAS in 0.7 mm rotors at 21.15 T. Figure 4-6 shows the ^{1}H DNP enhancement of a 60 mM solution of BDPA in OTP-d$_{95}$. The sample was prepared following the method of ref[161]. Following on from the observations made at up to 40 kHz, here we see that the ^{1}H enhancement continues to increase as the MAS frequency increases up to 65 kHz, reaching a maximum of ε_H = 106. Although Figure 4-6 reports a maximum enhancement of 106, we have been able to reach ε_H = 128 at 65 kHz MAS with a different sample. We attribute this difference to the quality of glass formation upon freezing the sample, which is a recurrent feature in many DNP matrices including OTP.[58, 87, 163, 281] At 65 kHz MAS we measured a build-up time $T_{B,on}$ = 58 s, and the enhancements were determined with a polarization (recycle) delay of 1.3 × $T_{B,on}$ = 75 s (red dots Figure 4-6). We also measured the ^{1}H enhancements with a polarization delay of 10 s and observed enhancements consistently lower than for the longer recycle delay (blue dots in Figure 4-6). This is a clear signature of ^{1}H-^{1}H spin diffusion relaying hyperpolarization among the ^{1}H nuclei in the OTP matrix.[107, 109] It is possible to rationalize this behaviour using the same source-sink spin diffusion model proposed in ref[175]. This model

hypothesizes that the detected DNP behaviour results from the flow of hyperpolarization from the BPDA/OTP-$d_{95\%}$ source matrix to dilute sinks (eg. paramagnetic impurities). Using this model, the enhancements with polarization delays of 10 s and 75 s were simulated across the whole range of spinning rates from 0 to 65 kHz. The simulated enhancements are reported in Figure 4-6 (solid lines) and fit very well to the experimental data. The details of the simulation model are given in Appendix VI. The spin diffusion model explains both why ε_H increases when the MAS rate increases at a constant polarizing delay, and also why for a given MAS rate ε_H increases when the polarization delay increases from 10 to 75 s. The results give additional very strong support to the original source-sink model.[175]

The temperature of the sample in the rotor was monitored at each MAS rate using the $T_1(^{79}\text{Br})$ of a KBr crystal added to the rotor.[282] The internal temperature under μw irradiation increases from 95 K at 10 kHz MAS to ~105 K at 65 kHz MAS, indicating that the frictional heating induced by MAS in the 0.7 mm DNP LTMAS probe is only around 10 K. The contribution factor has not been remeasured here as it was previously found to be 1 up to 40 kHz MAS.[175]
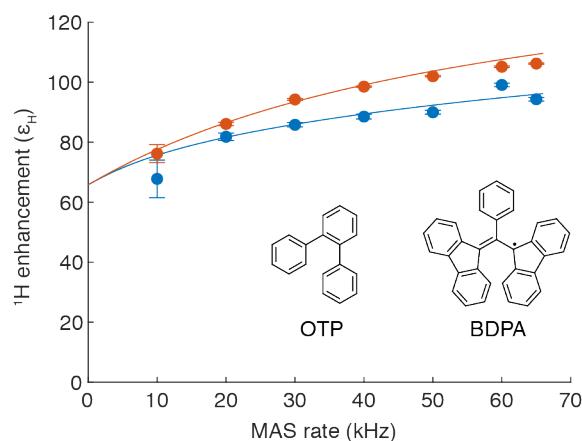
Figure 4-6. ^{1}H DNP enhancements measured for a 60 mM frozen solution of BDPA in OTP-$d_{95\%}$ at MAS rates up to 65 kHz. Measurements were made with polarization delays of 10 s (blue) and 75 s (orange) at each spinning frequency. The error bars are calculated from the estimated error based on the signal-to-noise ratio of the μwave ON and OFF spectra (see Appendix VI for details). The blue and orange lines correspond to the simulated DNP enhancements in both cases, based on the source-sink relayed DNP model (see Appendix VI for details regarding the simulations).[64] The OTP and BDPA structures are shown.

Although OE DNP using BDPA provides a large ^{1}H DNP enhancement, the long ^{1}H build-up time prevents it from being an efficient polarizing system. In some cases, flip-back,[181, 283] or frequency selective approaches[284] should be applicable. The rational design of radicals performing OE DNP is still very challenging, which slows down development of better OE DNP.[285] While there is large interest in OE DNP,[286] it does not appear to be the polarizing system of choice in these conditions.

As stated in Section 4.1.1, even though CE biradicals that perform well at moderate magnetic fields tend to give poor results at higher fields, rational design of cross-effect polarizing agents has resulted in high CE enhancements at $B_0 > 9.4$ T.[64, 66] Table 4-1 shows the performance of AMUPol at different magnetic fields and spinning frequencies, underlining the drop in enhancement with B_0, but also showing ε at different MAS rates.

Table 4-1. [1]H enhancement measured on 10 mM AMUPol in glycerol-d_8/D$_2$O/H$_2$O : 6/3/1 : v/v/v solution at different magnetic fields and using different rotor sizes available for DNP MAS experiments, from 3.2 mm to 0.7 mm. Data taken from literature are referenced with the corresponding publications. Data without references are new data measured in the present work, and experimental details are provided in Appendix VI. The ^{1}H enhancements are measured from the ^{13}C resonances from a [1]H-^{13}C CPMAS of ^{13}C-labelled proline dissolved in the polarizing solution.

Magnetic field	3.2 mm sapphire 8 kHz MAS	1.3 mm zirconia 10 kHz MAS	0.7 mm zirconia 10 kHz MAS	1.3 mm zirconia 40 kHz MAS	0.7 mm zirconia 60 kHz MAS
9.4 T	235[59]	265[264]	-	290[264]	-
18.8 T	30[265]	58[265]	-	56[265]	-
21.15 T	17[264]	-	46	-	42

The heterobiradical HyTEK-2 was found to give ^{1}H enhancements of up to 185 at 18.8 T and 40 kHz MAS in a 1.3 mm rotor. This was, at the time, the highest DNP enhancement reported at high magnetic field and fast MAS.[64] It was found to increase with spinning frequency and therefore seemed to be an ideal system for experiments at up to 65 kHz. Figure 4-7 plots the ^{1}H DNP enhancement and the ^{1}H DNP build-up time as function of the MAS rate obtained with a 32 mM HyTEK-2 solution in TCE. We measured ε_H = 147 at 10 kHz, which then increases almost linearly to ε_H = 200 at the maximum MAS rate of 65 kHz.

At the same magnetic field in a 3.2 mm rotor, enhancements of 64 at 10 kHz were previously reported. We attribute the improvement of the performance between 0.7 mm and 3.2 mm rotors at the same spinning speed to better penetration of the μwaves. An analogous difference was observed previously between 3.2 mm and 1.3 mm rotors at the same MAS rate.[64, 265] We also made the same observation with a 10 mM AMUPOL in glycerol-d_6/H$_2$O/D$_2$O : 6/3/1 v/v/v solution, as shown in Table 4-1.
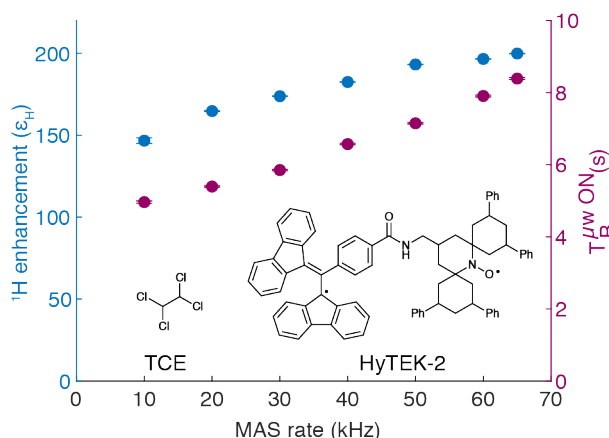
Figure 4-7. [1]H DNP enhancement (blue) and the 1H DNP build- up time in seconds (purple) for a 32 mM solution of HyTEK-2 in 1,1,2,2-tetrachloroethane (TCE) as function of the MAS rate. The error bars of the ^{1}H enhancement are estimated from the signal-to-noise ratio of the μwaves ON and OFF spectra, the error bar of the build up times are the error of the fit (see Appendix VI for details). HyTEK-2 and TCE molecules are represented on the figure.

As reported in ref[64], the combination of fast MAS and high magnetic field with the nitroxide-BDPA radical HyTEK-2 allows us to reach unprecedented DNP performance at this magnetic field; the increase with MAS rate is again attributed to decoupling of the polarizing bath from polarization sinks, as for the BPDA/OTP-$d_{95\%}$ example above. We note that prior to measurement, the sample was degassed of dissolved O$_2$ using freeze-thaw cycles in the probe.[160, 287] This is always necessary when using TCE as a DNP solvent, degassing here allows us to increase the ^{1}H DNP enhancement (measured at 20 kHz MAS) by 66 % after 4 freeze-thaw cycles. The temperature of the sample was monitored based on longitudinal relaxation rate T_1([79]Br) of a KBr crystal included in the sample[282] (see

Figure 4-8). Similarly, to what we observed above with BDPA/OTP-d$_{95\%}$, very fast MAS induces sample heating of only about 10 K, and here in addition μw irradiation induces another 10 K heating due to the use of TCE that absorbs some μw. The contribution factor has not been remeasured here, it was previously found to be constant at 0.71 between 5 to 40 kHz MAS,[64] and we believe this value can be extrapolated to 65 kHz MAS. All in all, our data demonstrate that the HyTEK-2 radical is a very efficient polarizing agent for very fast MAS DNP at high field. We were able to reach a ^{1}H DNP enhancement of 200, which is a new record for both a magnetic field of 21.15 T and the HyTEK2 polarizing agent.
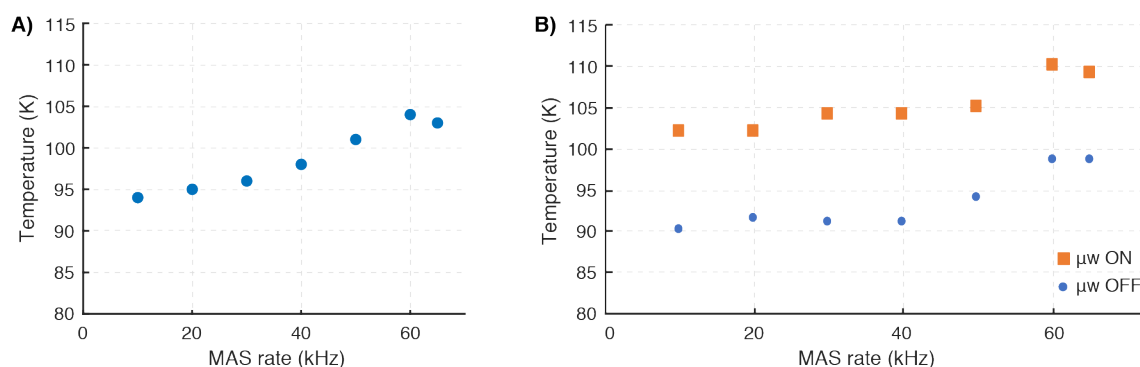
Figure 4-8. Measured temperatures as a function of MAS rate in a 0.7 mm rotor containing A) 60 mM BDPA in OTP-d$_{95\%}$ under μwave irradiation and B) 32 mM HyTEK2 in TCE with and without μw irradiation, at maximum cooling power from the LT cabinet. Temperatures are measured from the T_1(^{79}Br) of crystalline KBr included in the rotor.[282]

One of the most promising outcomes for NMR with fast MAS (60 kHz and higher) is the achievable ^{1}H resolution, which allows for example to record directly or indirectly ^{1}H NMR spectra without the use of sophisticated $^1$H homonuclear decoupling schemes.[288] In DNP MAS, reaching such regimes was not possible until now as the hardware was limited to up to 40 kHz. Here, as proof-of-concept, we present ^{1}H detected DNP MAS experiments at 65 kHz MAS on a micro-crystalline powder of U-^{13}C,^{15}N histidine hydrochloride impregnated with 32 mM HyTEK-2 in TCE, at 100 K. In the impregnation approach, the histidine does not dissolve in TCE and the hyperpolarization diffuses from the frozen HyTEK-2/TCE phase to the histidine crystal through spontaneous spin diffusion, as is now well established.[106-107] HyTEK-2/TCE was chosen as between the two DNP systems benchmarked here it provides the higher sensitivity gain (in terms of DNP enhancements and build-up times.) Figure 4-9A shows DNP enhanced ^{1}H spectra at different MAS rates. The strong TCE signal was partially suppressed using a spin echo of 3 ms prior to acquisition.[166] At 10 kHz MAS, this method of solvent suppression was not efficient enough, and the spectrum is actually dominated by the TCE signal. One can observe both the significant increase in sensitivity and spectral resolution as the spinning frequency is increased. In addition to the increase of the DNP enhancement with HyTEK-2 at higher MAS rates, these observations are related to the increase of the ^{1}H coherence lifetime, the decrease of the ^{1}H linewidth, and the reduction of the number of sidebands as the spin rate increases.[252, 288] The duration of the spin echo for solvent suppression was kept constant (at 3.0 ms) between the different MAS rates in order to compare the intensity between the spectra. The enhancement of the histidine signals in the 20 kHz spectrum is ε_H = 41 (note that the sample was not degassed). The slight asymmetry of the ^{1}H signals is attributed to shimming issues, probably due to the current probe design which includes an extension of the waveguide into the stator to improve overall performance.[47]

Figure 4-9B and C show the two-dimensional DNP enhanced ^{1}H detected ^{1}H-^{13}C and ^{1}H-^{15}N HETCOR spectra of impregnated U-^{13}C,^{15}N histidine at 62.5 kHz MAS. The HETCOR spectrum is fully resolved and allows all the resonances to be assigned.
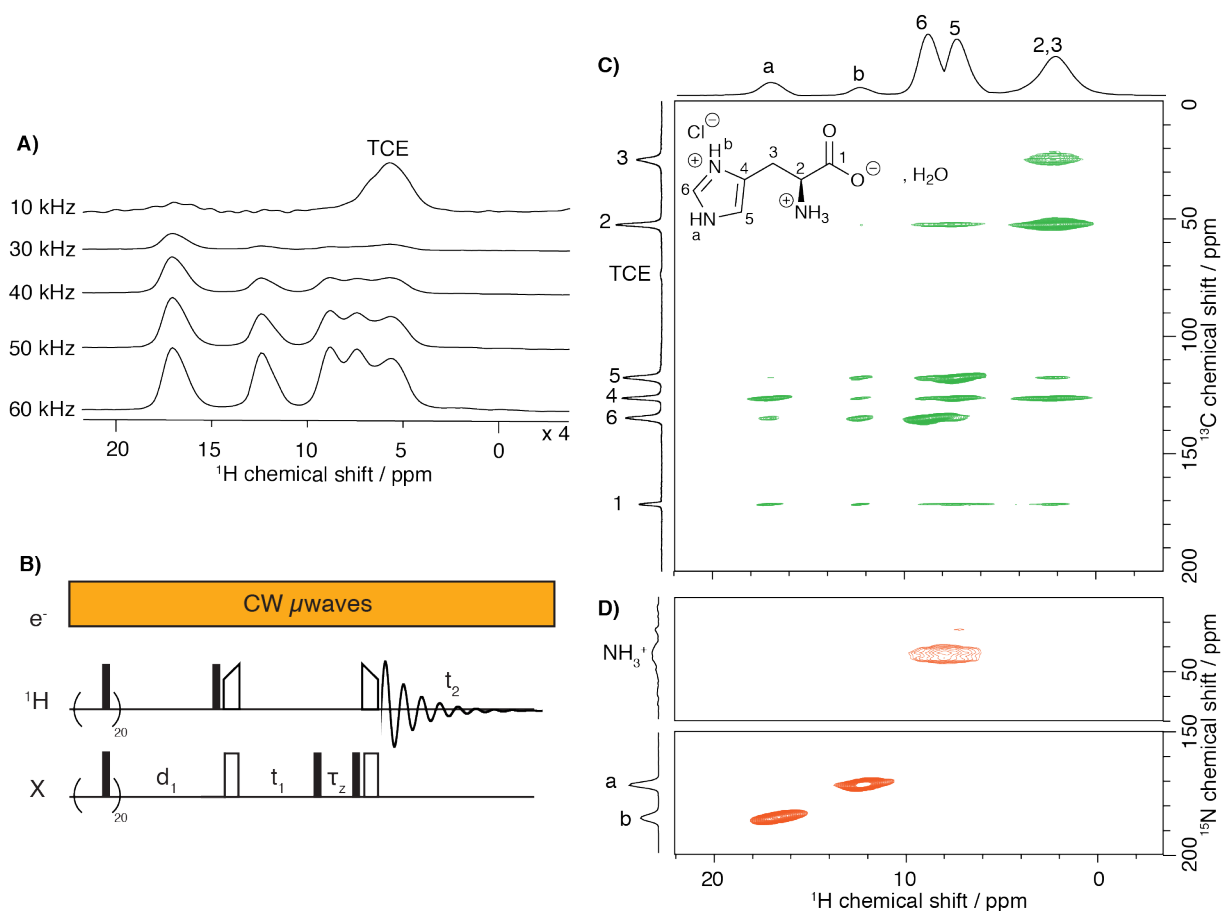
Figure 4-9. A) 900 MHz DNP enhanced ^{1}H spectra at different MAS rates between 10 to 60 kHz of U-^{13}C,^{15}N-histidine.HCl.H$_2$O impregnated with 32mM HyTEK2 in TCE. The spectra are all recorded with a 3 ms total spin echo prior to acquisition for solvent suppression.[166] Note that the spectrum at 10 kHz is dominated by the solvent signal. B) The ^{1}H-^{13}C ^{1}H-detected HETCOR pulse sequence. C) ^{1}H-^{13}C and D) ^{1}H-^{15}N ^{1}H-detected DNP HETCOR spectra of the same sample spinning at 62.5 kHz. For clarity, the signal-free region between 70 to 150 ppm of the ^{15}N dimension is not shown. H2/3 signals, clearly visible in B), are not visible in A) as they do not survive the spin echo used for solvent suppression. See Table 4-2 in Appendix VI for detailed acquisition parameters.

4.2.3   Conclusion

In conclusion, we have reported DNP MAS experiments using 0.7 mm rotors spinning at 65 kHz at a magnetic field of 21.15 T. The enhancements measured for the samples studied here increase with increasing MAS rates. This allows us to obtain the highest enhancements measured at this magnetic field so far. In particular, we found that HyTEK2 can yield a ^{1}H DNP enhancement of 200 at the maximum spinning frequency. We then showed how reaching these spin rates under DNP conditions opens up the possibility of using ^{1}H detected spectra more widely in MAS DNP, and as an example we obtained resolved DNP enhanced ^{1}H detected 1D and 2D spectra.

4.2.4 Appendix VI

Sample preparation

60 mM BPDA in 95% deuterated OTP. Orthoterphenyl (OTP) and α,γ-Bisdiphenylene-β-phenylallyl complex with benzene(1:1) (BDPA) were obtained from Sigma-Aldrich. 98% deuterated OTP (OTP-d$_{98\%}$) and deuterated chloroform were purchased from Cambridge Isotopes Laboratories. All chemicals were used as received with no further purification. The sample was prepared following the method described by Lelli *et al.*[161] Orthoterphenyl (OTP) and OTP-d$_{98\%}$ were mixed to afford a mixture with 95% deuterated OTP (OTP-d$_{95\%}$). The appropriate amount of BDPA was added to obtain a concentration of 60 mM of BDPA in OTP-d$_{95\%}$. The preparation was then dissolved in deuterated chloroform and the latter evaporated. The obtained powder was then transferred into a 0.7 mm zirconia rotor, and the latter closed with vespel drive and bottom caps. A few grains of crystalline KBr were added to the rotor before closing to allow sample temperature measurements. The rotor was then introduced into a capillary which was plunged into a water bath at 80°C for a few minutes in order to melt the preparation, and then quickly transferred to the precooled DNP probe to obtain a glassy frozen solution of 60 mM BDPA in OTP-d$_{95\%}$.[281]

32 mM HyTEK-2 in TCE. 1,1,2,2-tetrachloroethane was obtained from Sigma-Aldrich. The HyTEK-2 radical was prepared following the published procedure.[64] The radical was dissolved in the appropriate amount of TCE to give a 32 mM solution. The obtained solution was then transferred into a 0.7 mm zirconia rotor and the latter closed with vespel drive and bottom caps. A few grains of crystalline KBr were added to the rotor before closing to allow sample temperature measurements.

U-13C,15N histidine impregnated with 32 mM HyTEK-2 in TCE. Uniformly labelled histidine was acquired from Cambridge Isotope Laboratories. The crystalline powder was manually crushed using a mortar and pestle to reduce the size of the grains. The powder was then impregnated with a 32 mM solution of HyTEK-2 in TCE (roughly 1 μL of solution was used to impregnate 5 mg of powder).[101] The obtained powder was then transferred into a 0.7 mm zirconia rotor and the latter closed with vespel drive and bottom caps.

DNP enhanced solid-state NMR

Experiments were performed on a 900 MHz (21.15 T) Avance Neo Bruker solid-state NMR spectrometer. The spectrometer is equipped with a low temperature magic angle spinning, LTMAS, 0.7 mm triple resonance probe tuned to ^{1}H, ^{13}C, and ^{15}N. The probe is coupled with a Bruker gyrotron producing 593 GHz continuous wave (CW) microwaves (μw). As this NMR magnet does not a have a built-in sweep coil, the frequency of the gyrotron was tuned to match with the maximum DNP enhancement by modifying the gyrotron cavity temperature as described in reference[181]. The optimal cavity temperature was 34°C for OE DNP with BDPA (as reported in reference[181]) and at 28°C for CE DNP with HyTEK2 (as reported in reference[64]). For BDPA/OTP, the μwave power was optimized to obtain maximum enhancement on a sample spinning at 60 kHz and found at ca. 34 W at the probe base. For HyTEK2/TCE, the μwave power was optimized to obtain maximum enhancement on a sample spinning at 60 kHz and found at ca. 15 W at the probe base.

The ^{1}H enhancements were measured by taking the ratio between the integrated ^{1}H spectra recorded with and without μw irradiation. The ^{1}H spectra used to measure enhancements were obtained using an echo (π/2)-τ-(π)-τ sequence, with ^{1}H radiofrequency field amplitude set at 150 kHz and τ at 4 rotor periods at each MAS rate. The recycle delay between scans was 10 s and 75 s for measuring ^{1}H DNP enhancements on BDPA/OTP, set to 10 s to measure the ^{1}H DNP enhancements on HyTEK2/TCE, and set to 10 s on AMUPOL in glycerol-d6/H2O/D2O : 6/3/1 v/v/v solution. ^{1}H polarization was saturated using a train of 30 (π/2) pulses separated by 3 ms between each scan, preceding the recycle delay.

The ^{1}H build-up times were measured using a saturation-recovery sequence. A 4 rotor period spin echo was used before acquisition to remove probe background. At the beginning of each scan, ^{1}H polarization was saturated using a train of 30 (π/2) pulses separated by 3 ms, and preceding the variable recycle delay. The radiofrequency field amplitude for the ^{1}H pulses were set to 150 kHz.

Temperature measurements are based on the longitudinal relaxation time $T_1(^{79}\text{Br})$ of crystalline KBr included in the sample.[282] $T_1(^{79}\text{Br})$ was measured using a saturation-recovery sequence. ^{79}Br polarization was saturated using a train of 30 (π/2) pulses separated by 3 ms between each scan, and preceding the variable recycle delay.

The ^{1}H-^{13}C ^{1}H-detected HETCOR was recorded with the pulse sequence shown in Figure 4-9B, which was introduced by Zilm and co-workers.[289] The water suppression block was replaced by a z-filter.

Table 4-2. Experimental parameters used in the ^{1}H-detected HETCOR experiments.

	^{1}H-^{13}C ^{1}H-detected HETCOR	^{1}H-^{15}N ^{1}H-detected HETCOR
MAS rate	62.5 kHz	62.5 kHz
Number of saturation pulses	20	20
Delay between saturation pulses	3 ms	3 ms
Recycle delay (d$_1$)	1 s	1 s
RF field amplitude for ^{1}H pulses	160 kHz	160 kHz
RF field amplitude for ^{13}C pulses	45 kHz	50 kHz
^{1}H to X CP		
RF field amplitude ^{1}H	Ramp from 90 kHz to 100 kHz	Ramp from 90 kHz to 100 kHz
RF field amplitude X	Constant amplitude at 18 kHz	Constant amplitude at 45 kHz
Spin lock duration	2 ms	2 ms
X to ^{1}H CP		
RF field amplitude ^{1}H	Ramp from 100 kHz to 90 kHz	Ramp from 100 kHz to 90 kHz
RF field amplitude X	Constant amplitude at 18 kHz	Constant amplitude at 45 kHz
Spin lock duration	500 µs	500 µs
z-filter delay (τ_Z)	200 ms	200 ms
Acquisition in the indirect dimension (t$_1$)		
Total acquisition time	8.2 ms	8.2 ms
Dwell time	16 µs	32 µs
Number of transients recorded	1024	512
Acquisition in the direct dimension (t$_2$)		
Total acquisition time	5.6 ms	2.8 ms
Dwell time	5.5 µs	5.5 µs
Number of transients recorded	1024	512
Number of scans per increment	4	2
Acquisition mode	States-TPPI	States-TPPI

Estimation of errors

The errors ($\Delta\varepsilon$) on the ^{1}H DNP enhancement (ε) were evaluated using the following equation:

$$\Delta\varepsilon = \varepsilon\left(\frac{\Delta I_{\mu w\,ON}}{I_{\mu w\,ON}} + \frac{\Delta I_{\mu w\,OFF}}{I_{\mu w\,OFF}}\right)$$

(Eq. 4-1)

where $\Delta I_{\mu w\,ON}$ and $\Delta I_{\mu w\,OFF}$ are the error on the intensity of the ^{1}H signal, respectively with and without µw irradiation, estimated from the noise level.

The error on the build-up times are evaluated using the following procedure. A first fit is performed on the experimental data. Then a build-up curve is calculated from the fitted build-up time and a new list of points is created with addition of random noise (estimated from the s/n ratio measured on the NMR data). The new list is then fitted again. This process is repeated 100 times to obtain a distribution of fitted build-up times. The standard deviation of this distribution provides the error of the fit.

Time-dependent source-sink model with a numerical approach

The source-sink model used is the same as that used by Chaudhari *et al.*[175] The system is assumed to be composed by a uniform OTP matrix containing the dissolved BDPA polarizing agent (source), and a small concentration of relaxing particles that act as polarizing sink spots (sink). The source domain is characterized by a local equilibrium polarization (P$_0$) that is different with or without µw irradiation. For the sink domain, the local equilibrium polarization does not change with or without µw irradiation. This system is analyzed with both an analytical and a numerical approach, starting with the numerical.

Here, the system is assumed to be linear, the sink being located in the middle, as represented below:
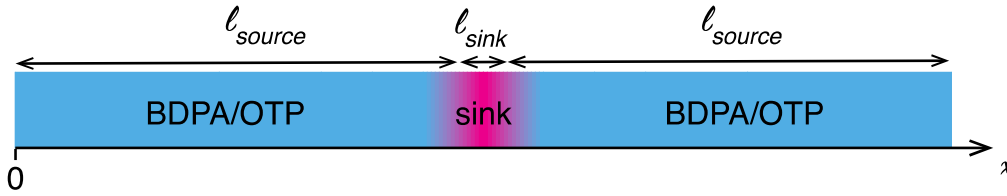
Matlab (R2020a) was used to solve the spin diffusion equation numerically and get the polarization $(x,t) \rightarrow P(x,t)$ in the system as function of space and time:

$$\frac{\partial P}{\partial t} = D(v_r)\frac{\partial^2 P}{\partial x^2} - \frac{P(x,t) - P^0(x)}{T_1(x)}$$

(Eq. 4-2)

where the T_1, P^0, D functions are defined as follow:

$$T_1(x) = \frac{T_1^{sink} - T_1^{source}}{2}\left[\tanh\bigl(p(x - l_{source})\bigr) - \tanh\left(p\bigl(x - (l_{sink} + l_{source})\bigr)\right)\right] + T_1^{source}$$

(Eq. 4-3)

$$P^0(x) = \begin{cases} \dfrac{1 - \varepsilon_0}{2}\left[\tanh\bigl(p(x - l_{source})\bigr) - \tanh\left(p\bigl(x - (l_{sink} + l_{source})\bigr)\right)\right] + \varepsilon_0 & \text{if µw ON} \\[2em] 1 & \text{if µw OFF} \end{cases}$$

(Eq. 4-4)

$$D(v_r) = \frac{D_0}{1 + 0.6v_r}$$

(Eq. 4-5)

where p represents the slope of the hyperbolic tangent used to link the two domains.

As saturation-recovery is used to perform the measurement, the initial condition is:

$$\forall x, \qquad P(x, t = 0) = 0$$

(Eq. 4-6)

For the boundary condition, it is assumed that no polarization can enter, and no polarization leave from the border of the system, thus:

$$\forall t, \qquad \vec{J_P}(x = 0, t) = \vec{J_P}(x = 2l_{\text{source}} + l_{\text{sink}}, t) = \vec{0}$$

(Eq. 4-7)

Which translates using Fick's first law:

$$\forall t, \qquad \frac{\partial P}{\partial x}(x = 0, t) = \frac{\partial P}{\partial x}(x = 2l_{\text{source}} + l_{\text{sink}}, t) = 0$$

(Eq. 4-8)

Note that as the BDPA radical is used here, and it operates with the Overhauser Effect, such that depolarization, quenching effects, or intrinsic MAS dependence of the DNP mechanism are considered negligible. In the simulation, we assume the signal arises only from the source (BDPA/OTP phase), thus the simulated time signal is obtained by integration:

$$S(t) = \int_0^{l_{\text{source}}} P(x, t)\, dx + \int_{l_{\text{source}} + l_{\text{sink}}}^{2l_{\text{source}} + l_{\text{sink}}} P(x, t)\, dx$$

(Eq. 4-9)

And the DNP enhancement as function of the time:

$$\varepsilon(t) = \frac{S_{\mu w\ \text{ON}}(t)}{S_{\mu w\ \text{OFF}}(t)}$$

(Eq. 4-10)

To produce the simulations shown in Figure 4-6, ^{1}H DNP enhancements were simulated for different MAS rates v_r and plot for $t = 10\ s$ and $t = 75\ s$. The parameters used in the simulation were:

$$
\begin{aligned}
T_B^{\text{source}} &= 57\ s \\
T_1^{\text{sink}} &= 1\ ms \\
\varepsilon_0 &= 180 \\
p &= 7000\ \mu m^{-1} \\
l_{\text{sink}} &= 1\ nm \\
l_{\text{source}} &= 32.2\ nm \\
D_0 &= 2.0 \times 10^{-4} \mu m^2 s^{-1}
\end{aligned}
$$

The size of the sink and source match the average distance expected for a 12 µM homogenous distribution of sinks in the BDPA/OTP source phase.

Chapter 5   Conclusions

5.1   Summary

In summary, this thesis has presented DNP approaches which can increase sensitivity in the NMR spectra of both organic and inorganic solids.

For organic solids, two very different methods were discussed. The first one involves the addition of a flip-back pulse in a MAS DNP experiment, which is simple in practice. The flip-back method allows for more rapid recycling of proton magnetization, and although its use is limited to certain heteronuclear decoupling schemes, it was demonstrated to provide additional sensitivity gains in relayed DNP of microcrystalline solids (on top of those already provided by DNP). Flip-back recovery is especially efficient for solids with long ^{1}H longitudinal relaxation rates, such as salicylic acid and histidine. The second approach discussed was to shift DNP to higher magnetic fields and higher spinning frequencies, which has been made possible by building on years of instrumental development in the field of NMR. The first DNP results at 21.1 T / 593 GHz are reported on a sample of BDPA in a partially deuterated OTP glass, a system which has slow ^{1}H longitudinal relaxation rates and benefits from the use of the flip-back method. The first DNP MAS experiments using 0.7 mm rotors spinning at frequencies up to 65 kHz at 21.1 T are also reported, with ^{1}H DNP enhancements increasing with increasing MAS frequency, reaching a maximum value of 200 for a sample of HyTEK-2 in TCE. The achievable spinning frequencies yield unprecedented ^{1}H resolution in MAS DNP and further motivate the use of ^{1}H detected spectra.

For inorganic solids, the possibility of making use of homonuclear spin diffusion between low-γ nuclei to transport hyperpolarization from the surface of a particle towards the bulk was presented. Spin diffusion between lower-γ nuclei is expected to be slow, but was confirmed to be present in various different compounds with long T_1 relaxation times, even at MAS rates of 12.5 kHz. This finding was used to develop a general strategy where surface-generated hyperpolarization is used to increase the sensitivity of bulk NMR signals in inorganic solids. A high level of polarization is maintained at the surface of the materials either by direct DNP, or by repetitive bursts of cross-polarization with a multiple contact CP sequence. These methods can increase the sensitivity in bulk spectra of inorganic compounds by orders of magnitude, and were shown to work for several different nuclei. The experimental optimization of the multiple contact CP method was described, and a variation where the rotation rate of the sample is modulated during the experiment was presented, combining more efficient spin diffusion at low MAS frequencies with the improved resolution at higher spinning frequencies. To gain further insight into the relay process, two-dimensional spin diffusion experiments were employed to study the transfer of surface-generated hyperpolarization towards the bulk of a material under MAS.

5.2 Outlook

High magnetic fields are beneficial for resolution in NMR spectra of quadrupolar nuclei (spin $I > \frac{1}{2}$). The challenges associated with solid-state NMR of quadrupolar nuclei have not been listed in this thesis, although NMR of two such isotopes was shown in Section 3.3 (^{6}Li and ^{7}Li have relatively small quadrupolar moments and were treated as spin-$\frac{1}{2}$ nuclei). Without going into detail, in addition to the issues faced by spin-$\frac{1}{2}$ nuclei, such as low gyromagnetic ratios and/or natural abundance, the NMR spectra of quadrupolar nuclei are dominated by quadrupolar interactions which lead to broadening and even lower sensitivity. These interactions are field dependant, and half-integer spin $I > \frac{1}{2}$ nuclei experience an even more dramatic effect than spin-$\frac{1}{2}$ nuclei when going to higher fields, with the resolution increasing proportional to $(B_0)^2$. This can be critical for nuclei with low sensitivity such as ^{17}O.[253, 290] DNP has already proven useful in NMR of quadrupoles at fields from 9.4 T to 18.8 T. For example, it has been shown to enable acquisition of natural abundance ^{17}O spectra,[171, 290] as well as surface spectra of ^{27}Al[291-292] and other even lower-γ nuclei[104, 293]. The field dependent improvement in spectral resolution makes high-field DNP an attractive option for NMR of quadrupolar nuclei,[1, 11, 294-295] and combination with fast MAS can open up the possibility of ^{1}H-detection to further increase sensitivity in spectra of materials which contain protons.[270-271]

In the future, the possibility of combining fast MAS with the multiple contact CP method for bulk hyperpolarization of inorganic materials can be envisaged. Preliminary experiments show that spin diffusion between ^{31}P atoms is present even at 60 kHz in a sample of microcrystalline $Sn_2P_2O_7$, as shown in Figure 5-1. The multiple contact CP method also seems promising, providing higher SNR than direct acquisition of the ^{31}P spectrum. (It should be noted that the spectra shown in Figure 5-1B are not sensitivity optimized, but were both acquired in the same amount of time.) In addition, pulse cooling is compatible with CPMG acquisition, as was demonstrated by the Rossini group for ^{31}P and ^{113}Cd spectra of Cd_3P_2 and CdSe nanoparticles.[88] This could be particularly beneficial at fast MAS, due to the longer transverse coherence lifetimes which can result at higher spinning frequencies.[265]
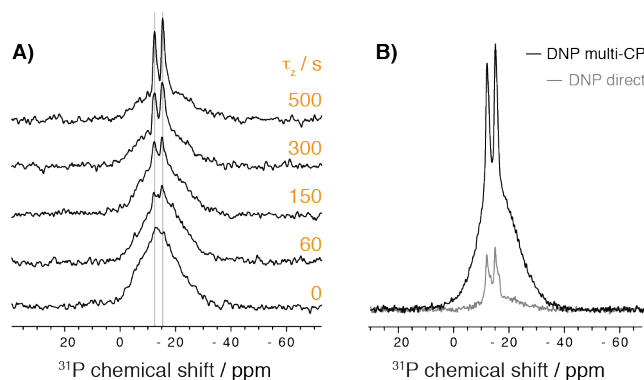
Figure 5-1. DNP enhanced ^{31}P spectra of powdered $Sn_2P_2O_7$ spinning at 60 kHz and 100 K, at a magnetic field of 21.1 T. The powder was impregnated with a 32 mM solution of HyTEK-2 in TCE. A) CP followed by a variable length z-filter, confirming ^{31}P spin diffusion at 60 kHz. B) Constant-time comparison of a DNP enhanced ^{31}P spectrum acquired with multiple contact CP (τ_z = 20 s and L = 15) and a direct DNP spectrum of ^{31}P (τ_{rd} = 300 s).

The new techniques described in this thesis can in principle be applied to a range of different organic and inorganic materials, and can be especially beneficial for increasing sensitivity in NMR spectra of compounds which have long T_1 relaxation times. In particular, the method presented for hyperpolarization of inorganic bulk increases the diversity of materials that can be studied with impregnation DNP.

References

1. MacKenzie, K. J. D.; Smith, M. E., *Multinuclear Solid-State NMR of Inorganic Materials*. Elsevier Science: Oxford, UK, 2002.
2. Tycko, R., Biomolecular Solid State NMR: Advances in Structural Methodology and Applications to Peptide and Protein Fibrils. *Annual Review of Physical Chemistry* **2001,** *52*, 575-606.
3. Hanna, J. V.; Smith, M. E., Recent Technique Developments and Applications of Solid State NMR in Characterising Inorganic Materials. *Solid State Nuclear Magnetic Resonance* **2010,** *38* (1), 1-18.
4. Brown, S. P., Applications of High-Resolution 1H Solid-State NMR. *Solid State Nuclear Magnetic Resonance* **2012,** *41*, 1-27.
5. Moran, R. F.; Dawson, D. M.; Ashbrook, S. E., Exploiting NMR Spectroscopy for the Study of Disorder in Solids. *International Reviews in Physical Chemistry* **2017,** *36* (1), 39-115.
6. Pecher, O.; Carretero-Gonzalez, J.; Griffith, K. J.; Grey, C. P., Materials' Methods: NMR in Battery Research. *Chemistry of Materials* **2017,** *29* (1), 213-242.
7. Abragam, A., *Principles of Nuclear Magnetism*. Clarendon Press: 1961.
8. Styles, P.; Soffe, N. F.; Scott, C. A.; Cragg, D. A.; Row, F.; White, D. J.; White, P. C. J., A High-Resolution NMR Probe in Which the Coil and Preamplifier Are Cooled with Liquid-Helium. *Journal of Magnetic Resonance* **1984,** *60* (3), 397-404.
9. Andrew, E. R.; Bradbury, A.; Eades, R. G., Nuclear Magnetic Resonance Spectra from a Crystal Rotated at High Speed. *Nature* **1958,** *182* (4650), 1659-1659.
10. Verardi, R.; Traaseth, N. J.; Masterson, L. R.; Vostrikov, V. V.; Veglia, G., Isotope Labeling for Solution and Solid-State NMR Spectroscopy of Membrane Proteins. *Advances in Experimental Medicine and Biology* **2012,** *992*, 35-62.
11. Ashbrook, S. E.; Smith, M. E., Solid State 17O NMR - an Introduction to the Background Principles and Applications to Inorganic Materials. *Chemical Society Reviews* **2006,** *35* (8), 718-735.
12. Bloch, F.; Hansen, W. W.; Packard, M., The Nuclear Induction Experiment. *Physical Review* **1946,** *70* (7-8), 474-485.
13. Levitt, M., *Spin Dynamics: Basics of Nuclear Magnetic Resonance*. John Wiley & Sons: Chichester, England, 2001.
14. Pines, A.; Gibby, M. G.; Waugh, J. S., Proton-Enhanced NMR of Dilute Spins in Solids. *The Journal of Chemical Physics* **1973,** *59* (2), 569-590.
15. Schaefer, J.; Stejskal, E. O., Carbon-13 Nuclear Magnetic Resonance of Polymers Spinning at the Magic Angle. *Journal of the American Chemical Society* **1976,** *98* (4), 1031-1032.
16. Hartmann, S. R.; Hahn, E. L., Nuclear Double Resonance in Rotating Frame. *Physical Review* **1962,** *128* (5), 2042-2053.
17. Overhauser, A. W., Polarization of Nuclei in Metals. *Physical Review* **1953,** *91* (2), 476-476.
18. Carver, T. R.; Slichter, C. P., Polarization of Nuclear Spins in Metals. *Physical Review* **1953,** *92* (1), 212-213.
19. Can, T. V.; Caporini, M. A.; Mentink-Vigier, F.; Corzilius, B.; Walish, J. J.; Rosay, M.; Maas, W. E.; Baldus, M.; Vega, S.; Swager, T. M.; Griffin, R. G., Overhauser Effects in Insulating Solids. *The Journal of Chemical Physics* **2014,** *141* (6), 064202.
20. Abragam, A., Overhauser Effect in Nonmetals. *Physical Review* **1955,** *98* (6), 1729-1735.
21. Schmugge, T. J.; Jeffries, C. D., High Dynamic Polarization of Protons. *Physical Review* **1965,** *138* (6a), 1785-1801.
22. Wind, R. A.; Li, L. Y.; Lock, H.; Maciel, G. E., Dynamic Nuclear Polarization in the Nuclear Rotating Frame. *Journal of Magnetic Resonance* **1988,** *79* (3), 577-582.
23. Hwang, C. F.; Hill, D. A., New Effect in Dynamic Polarization. *Physical Review Letters* **1967,** *18* (4), 110-112.
24. Hwang, C. F.; Hill, D. A., Phenomenological Model for the New Effect in Dynamic Polarization. *Physical Review Letters* **1967,** *19* (18), 1011-1014.
25. Hu, K.-N.; Debelouchina, G. T.; Smith, A. A.; Griffin, R. G., Quantum Mechanical Theory of Dynamic Nuclear Polarization in Solid Dielectrics. *The Journal of Chemical Physics* **2011,** *134* (12), 125105.
26. Hovav, Y.; Feintuch, A.; Vega, S., Theoretical Aspects of Dynamic Nuclear Polarization in the Solid State - the Cross Effect. *Journal of Magnetic Resonance* **2012,** *214*, 29-41.

27. Atsarkin, V. A.; Rodak, M. I., Temperature of Spin-Spin Interactions in Electron-Paramagnetic Resonance. *Soviet Physics Uspekhi* **1972,** *15*, 251.

28. Henstra, A.; Dirksen, P.; Schmidt, J.; Wenckebach, W. T., Nuclear Spin Orientation Via Electron Spin Locking (NOVEL). *Journal of Magnetic Resonance* **1988,** *77* (2), 389-393.

29. Ardenkjaer-Larsen, J. H.; Fridlund, B.; Gram, A.; Hansson, G.; Hansson, L.; Lerche, M. H.; Servin, R.; Thaning, M.; Golman, K., Increase in Signal-to-Noise Ratio of > 10,000 Times in Liquid-State NMR. *Proceedings of the National Academy of Sciences of the United States of America* **2003,** *100* (18), 10158-10163.

30. Natterer, J.; Bargon, J., Parahydrogen Induced Polarization. *Progress in Nuclear Magnetic Resonance Spectroscopy* **1997,** *31*, 293-315.

31. Ward, H. R.; Lawler, R. G., Nuclear Magnetic Resonance Emission and Enhanced Absorption in Rapid Organometallic Reactions. *Journal of the American Chemical Society* **1967,** *89* (21), 5518.

32. Bargon, J.; Fischer, H., Chemically Induced Dynamic Nuclear Polarization in Reactions with Certain Radicals. *Zeitschrift Fur Naturforschung Part a-Astrophysik Physik Und Physikalische Chemie* **1968,** *A 23* (12), 2109.

33. Myhre, P. C.; Webb, G. G.; Yannoni, C. S., Magic Angle Spinning Nuclear Magnetic Resonance near Liquid-Helium Temperatures. Variable-Temperature CPMAS Studies of C4h7+ to 5 K. *Journal of the American Chemical Society* **1990,** *112* (24), 8992-8994.

34. Hirsch, M. L.; Kalechofsky, N.; Belzer, A.; Rosay, M.; Kempf, J. G., Brute-Force Hyperpolarization for NMR and Mri. *Journal of the American Chemical Society* **2015,** *137* (26), 8428-8434.

35. Raftery, D.; MacNamara, E.; Fisher, G.; Rice, C. V.; Smith, J., Optical Pumping and Magic Angle Spinning: Sensitivity and Resolution Enhancement for Surface NMR Obtained with Laser-Polarized Xenon. *Journal of the American Chemical Society* **1997,** *119* (37), 8746-8747.

36. Wind, R. A.; Duijvestijn, M. J.; Vanderlugt, C.; Manenschijn, A.; Vriend, J., Applications of Dynamic Nuclear Polarization in C-13 NMR in Solids. *Progress in Nuclear Magnetic Resonance Spectroscopy* **1985,** *17*, 33-67.

37. Maresch, G. G.; Kendrick, R. D.; Yannoni, C. S.; Galvin, M. E., Dynamic Nuclear Polarization Via Confined Electrons in Bulk Solids. *Journal of Magnetic Resonance* **1989,** *82* (1), 41-50.

38. Afeworki, M.; Schaefer, J., Mechanism of DNP-Enhanced Polarization Transfer across the Interface of Polycarbonate Polystyrene Heterogeneous Blends. *Macromolecules* **1992,** *25* (16), 4092-4096.

39. Becerra, L. R.; Gerfen, G. J.; Temkin, R. J.; Singel, D. J.; Griffin, R. G., Dynamic Nuclear Polarization with a Cyclotron Resonance Maser at 5 T. *Physical Review Letters* **1993,** *71* (21), 3561-3564.

40. Becerra, L. R.; Gerfen, G. J.; Bellew, B. F.; Bryant, J. A.; Hall, D. A.; Inati, S. J.; Weber, R. T.; Un, S.; Prisner, T. F.; Mcdermott, A. E.; Fishbein, K. W.; Kreischer, K. E.; Temkin, R. J.; Singel, D. J.; Griffin, R. G., A Spectrometer for Dynamic Nuclear-Polarization and Electron Paramagnetic Resonance at High Frequencies. *Journal of Magnetic Resonance Series A* **1995,** *117* (1), 28-40.

41. Rosay, M.; Blank, M.; Engelke, F., Instrumentation for Solid-State Dynamic Nuclear Polarization with Magic Angle Spinning NMR. *Journal of Magnetic Resonance* **2016,** *264*, 88-98.

42. Rosay, M.; Tometich, L.; Pawsey, S.; Bader, R.; Schauwecker, R.; Blank, M.; Borchard, P. M.; Cauffman, S. R.; Felch, K. L.; Weber, R. T.; Temkin, R. J.; Griffin, R. G.; Maas, W. E., Solid-State Dynamic Nuclear Polarization at 263 GHz: Spectrometer Design and Experimental Results. *Physical Chemistry Chemical Physics* **2010,** *12* (22), 5850-5860.

43. Thurber, K.; Tycko, R., Low-Temperature Dynamic Nuclear Polarization with Helium-Cooled Samples and Nitrogen-Driven Magic-Angle Spinning. *Journal of Magnetic Resonance* **2016,** *264*, 99-106.

44. Berry, D.; Deng, H.; Dobbs, R.; Horoyski, P.; Hyttinen, M.; Kingsmill, A.; MacHattie, R.; Roitman, A.; Sokol, E.; Steer, B., Practical Aspects of EIK Technology. *Ieee Transactions on Electron Devices* **2014,** *61* (6), 1830-1835.

45. Itin, B.; Sergeyev, I., Strategies for Efficient Sample Preparation for Dynamic Nuclear Polarization Solid-State NMR of Biological Macromolecules. In *Protein NMR. Methods in Molecular Biology*, Ghose, R., Ed. Humana Press, New York: NY, 2018; Vol. 1688.

46. Tycko, R., NMR at Low and Ultralow Temperatures. *Acounts of Chemical Research* **2013,** *46* (9), 1923-1932.

47. Purea, A.; Reiter, C.; Dimitriadis, A. I.; de Rijk, E.; Aussenac, F.; Sergeyev, I.; Rosay, M.; Engelke, F., Improved Waveguide Coupling for 1.3 Mm MAS DNP Probes at 263 GHz. *Journal of Magnetic Resonance* **2019,** *302*, 43-49.

48. Thankamony, A. S. L.; Wittmann, J. J.; Kaushik, M.; Corzilius, B., Dynamic Nuclear Polarization for Sensitivity Enhancement in Modern Solid-State NMR. *Progress in Nuclear Magnetic Resonance Spectroscopy* **2017,** *102*, 120-195.

49. Nanni, E. A.; Barnes, A. B.; Matsuki, Y.; Woskov, P. P.; Corzilius, B.; Griffin, R. G.; Temkin, R. J., Microwave Field Distribution in a Magic Angle Spinning Dynamic Nuclear Polarization NMR Probe. *Journal of Magnetic Resonance* **2011,** *210* (1), 16-23.

50. Griffin, R. G.; Swager, T. M.; Temkin, R. J., High Frequency Dynamic Nuclear Polarization: New Directions for the 21st Century. *Journal of Magnetic Resonance* **2019,** *306*, 128-133.

51. Casano, G.; Karoui, H.; Ouari, O., Polarizing Agents: Evolution and Outlook in Free Radical Development for DNP. In *Handbook Ofhigh Field Dynamic Nuclear Polarization* Michaelis, V. K.; Griffin, R.; Corzilius, B.; Vega, S., Eds. John Wiley & Sons: 2020; pp 103-120.

52. Can, T. V.; Ni, Q. Z.; Griffin, R. G., Mechanisms of Dynamic Nuclear Polarization in Insulating Solids. *Journal of Magnetic Resonance* **2015,** *253*, 23-35.

53. Kundu, K.; Mentink-Vigier, F.; Feintuch, A.; Vega, S., DNP Mechanisms. In *Handbook of High Field Dynamic Nuclear Polarization*, Michaelis, V. K.; Griffin, R. G.; Corzilius, B.; Vega, S., Eds. John Wiley & Sons: 2020; pp 15-70.

54. Kaushik, M.; Bahrenberg, T.; Can, T. V.; Caporini, M. A.; Silvers, R.; Heiliger, J.; Smith, A. A.; Schwalbe, H.; Griffin, R. G.; Corzilius, B., Gd(III) and Mn(II) Complexes for Dynamic Nuclear Polarization: Small Molecular Chelate Polarizing Agents and Applications with Site-Directed Spin Labeling of Proteins. *Physical Chemistry Chemical Physics* **2016,** *18* (39), 27205-27218.

55. Stevanato, G.; Kubicki, D. J.; Menzildjian, G.; Chauvin, A. S.; Keller, K.; Yulikov, M.; Jeschke, G.; Mazzanti, M.; Emsley, L., A Factor Two Improvement in High-Field Dynamic Nuclear Polarization from Gd(III) Complexes by Design. *Journal of the American Chemical Society* **2019,** *141* (22), 8746-8751.

56. Baranov, P. G.; von Bardeleben, H. J.; Jelezko, F.; Wrachtrup, J., Fundamentals of Epr Related Methods. In *Magnetic Resonance of Semiconductors and Their Nanostructures*, Springer: Vienna, 2017; Vol. 253.

57. Song, C. S.; Hu, K. N.; Joo, C. G.; Swager, T. M.; Griffin, R. G., TOTAPOL: A Biradical Polarizing Agent for Dynamic Nuclear Polarization Experiments in Aqueous Media. *Journal of the American Chemical Society* **2006,** *128* (35), 11385-11390.

58. Zagdoun, A.; Casano, G.; Ouari, O.; Schwarzwalder, M.; Rossini, A. J.; Aussenac, F.; Yulikov, M.; Jeschke, G.; Coperet, C.; Lesage, A.; Tordo, P.; Emsley, L., Large Molecular Weight Nitroxide Biradicals Providing Efficient Dynamic Nuclear Polarization at Temperatures up to 200 K. *Journal of the American Chemical Society* **2013,** *135* (34), 12790-12797.

59. Sauvee, C.; Rosay, M.; Casano, G.; Aussenac, F.; Weber, R. T.; Ouari, O.; Tordo, P., Highly Efficient, Water-Soluble Polarizing Agents for Dynamic Nuclear Polarization at High Frequency. *Angewandte Chemie International Edition* **2013,** *52* (41), 10858-10861.

60. Matsuki, Y.; Maly, T.; Ouari, O.; Karoui, H.; Le Moigne, F.; Rizzato, E.; Lyubenova, S.; Herzfeld, J.; Prisner, T.; Tordo, P.; Griffin, R. G., Dynamic Nuclear Polarization with a Rigid Biradical. *Angewandte Chemie International Edition* **2009,** *48* (27), 4996-5000.

61. Perras, F. A.; Wang, L.-L.; Manzano, J. S.; Chaudhary, U.; Opembe, N. N.; Johnson, D. D.; Slowing, I. I.; Pruski, M., Optimal Sample Formulations for DNP SENS: The Importance of Radical-Surface Interactions. *Current Opinion in Colloid & Interface Science* **2018,** *33*, 9-18.

62. Stevanato, G.; Casano, G.; Kubicki, D.; Rao, Y.; Esteban Hofer, L.; Menzildjian, G.; Karoui, H.; Siri, D.; Cordova, M.; Yulikov, M.; Jeschke, G.; Lelli, M.; Lesage, A.; Ouari, O.; Emsley, L., Open and Closed Radicals: Local Geometry around Unpaired Electrons Governs Magic-Angle Spinning Dynamic Nuclear Polarization Performance. *Journal of the American Chemical Society* **2020,** *142* (39), 16587-16599.

63. Rossini, A. J., Materials Characterization by Dynamic Nuclear Polarization-Enhanced Solid-State NMR Spectroscopy. *Journal of Physical Chemistry Letters* **2018,** *9* (17), 5150-5159.

64. Wisser, D.; Karthikeyan, G.; Lund, A.; Casano, G.; Karoui, H.; Yulikov, M.; Menzildjian, G.; Pinon, A. C.; Purea, A.; Engelke, F.; Chaudhari, S. R.; Kubicki, D.; Rossini, A. J.; Moroz, I. B.; Gajan, D.; Coperet, C.; Jeschke, G.; Lelli, M.; Emsley, L.; Lesage, A.; Ouari, O., BDPA-Nitroxide Biradicals Tailored for Efficient Dynamic Nuclear Polarization Enhanced Solid-State NMR at Magnetic Fields up to 21.1 T. *Journal of the American Chemical Society* **2018,** *140* (41), 13340-13349.

65. Dane, E. L.; Maly, T.; Debelouchina, G. T.; Griffin, R. G.; Swager, T. M., Synthesis of a BDPA-TEMPO Biradical. *Organic Letters* **2009,** *11* (9), 1871-1874.

66. Mathies, G.; Caporini, M. A.; Michaelis, V. K.; Liu, Y. P.; Hu, K. N.; Mance, D.; Zweier, J. L.; Rosay, M.; Baldus, M.; Griffin, R. G., Efficient Dynamic Nuclear Polarization at 800 Mhz/527 GHz with Trityl-Nitroxide Biradicals. *Angewandte Chemie International Edition* **2015,** *54* (40), 11770-11774.

67. Hu, K. N.; Bajaj, V. S.; Rosay, M.; Griffin, R. G., High-Frequency Dynamic Nuclear Polarization Using Mixtures of TEMPO and Trityl Radicals. *Journal of Chemical Physics* **2007,** *126* (4).

68. Mentink-Vigier, F.; Akbey, U.; Oschkinat, H.; Vega, S.; Feintuch, A., Theoretical Aspects of Magic Angle Spinning - Dynamic Nuclear Polarization. *Journal of Magnetic Resonance* **2015,** *258*, 102-120.

69. Perras, F. A.; Raju, M.; Carnahan, S. L.; Akbarian, D.; van Duin, A. C. T.; Rossini, A. J.; Pruski, M., Full-Scale Ab Initio Simulation of Magic-Angle-Spinning Dynamic Nuclear Polarization. *Journal of Physical Chemistry Letters* **2020,** *11* (14), 5655-5660.

70. Li, Y. X.; Equbal, A.; Tagami, K.; Han, S., Electron Spin Density Matching for Cross-Effect Dynamic Nuclear Polarization. *Chemical Communications* **2019,** *55* (53), 7591-7594.

71. Corzilius, B.; Michaelis, V. K.; Penzel, S. A.; Ravera, E.; Smith, A. A.; Luchinat, C.; Griffin, R. G., Dynamic Nuclear Polarization of H-1, C-13, and Co-59 in a Tris(Ethylenediamine)Cobalt(III) Crystalline Lattice Doped with Cr(III). *Journal of the American Chemical Society* **2014,** *136* (33), 11716-11727.

72. Corzilius, B.; Smith, A. A.; Barnes, A. B.; Luchinat, C.; Bertini, I.; Griffin, R. G., High-Field Dynamic Nuclear Polarization with High-Spin Transition Metal Ions. *Journal of the American Chemical Society* **2011,** *133* (15), 5648-5651.

73. Chakrabarty, T.; Goldin, N.; Feintuch, A.; Houben, L.; Leskes, M., Paramagnetic Metal-Ion Dopants as Polarization Agents for Dynamic Nuclear Polarization NMR Spectroscopy in Inorganic Solids. *ChemPhysChem* **2018,** *19* (17), 2139-2142.

74. Wolf, T.; Kumar, S.; Singh, H.; Chakrabarty, T.; Aussenac, F.; Frenkel, A. I.; Major, D. T.; Leskes, M., Endogenous Dynamic Nuclear Polarization for Natural Abundance O-17 and Lithium NMR in the Bulk of Inorganic Solids. *Journal of the American Chemical Society* **2019,** *141* (1), 451-462.

75. Carnahan, S. L.; Venkatesh, A.; Perras, F. A.; Wishart, J. F.; Rossini, A. J., High-Field Magic Angle Spinning Dynamic Nuclear Polarization Using Radicals Created by Gamma-Irradiation. *Journal of Physical Chemistry Letters* **2019,** *10* (17), 4770-4776.

76. Katz, I.; Blank, A., Dynamic Nuclear Polarization in Solid Samples by Electrical-Discharge-Induced Radicals. *Journal of Magnetic Resonance* **2015,** *261*, 95-100.

77. Vitzthum, V.; Borcard, F.; Jannin, S.; Morin, M.; Mieville, P.; Caporini, M. A.; Sienkiewicz, A.; Gerber-Lemaire, S.; Bodenhausen, G., Fractional Spin-Labeling of Polymers for Enhancing NMR Sensitivity by Solvent-Free Dynamic Nuclear Polarization. *ChemPhysChem* **2011,** *12* (16), 2929-2932.

78. Thankamony, A. S. L.; Lafon, O.; Lu, X. Y.; Aussenac, F.; Rosay, M.; Trebosc, J.; Vezin, H.; Amoureux, J. P., Solvent-Free High-Field Dynamic Nuclear Polarization of Mesoporous Silica Functionalized with TEMPO. *Applied Magnetic Resonance* **2012,** *43* (1-2), 237-250.

79. Gajan, D.; Schwarzwalder, M.; Conley, M. P.; Gruning, W. R.; Rossini, A. J.; Zagdoun, A.; Lelli, M.; Yulikov, M.; Jeschke, G.; Sauvee, C.; Ouari, O.; Tordo, P.; Veyre, L.; Lesage, A.; Thieuleux, C.; Emsley, L.; Coperet, C., Solid-Phase Polarization Matrixes for Dynamic Nuclear Polarization from Homogeneously Distributed Radicals in Mesostructured Hybrid Silica Materials. *Journal of the American Chemical Society* **2013,** *135* (41), 15459-15466.

80. van der Cruijsen, E. A. W.; Koers, E. J.; Sauvee, C.; Hulse, R. E.; Weingarth, M.; Ouari, O.; Perozo, E.; Tordo, P.; Baldus, M., Biomolecular DNP-Supported NMR Spectroscopy Using Site-Directed Spin Labeling. *Chemistry - A European Journal* **2015,** *21* (37), 12971-12977.

81. Takahashi, H.; Lee, D.; Dubois, L.; Bardet, M.; Hediger, S.; De Paepe, G., Rapid Natural-Abundance 2d C-13-C-13 Correlation Spectroscopy Using Dynamic Nuclear Polarization Enhanced Solid-State NMR and Matrix-Free Sample Preparation. *Angewandte Chemie International Edition* **2012,** *51* (47), 11766-11769.

82. Fernandez-de-Alba, C.; Takahashi, H.; Richard, A.; Chenavier, Y.; Dubois, L.; Maurel, V.; Lee, D.; Hediger, S.; De Paepe, G., Matrix-Free DNP-Enhanced NMR Spectroscopy of Liposomes Using a Lipid-Anchored Biradical. *Chemistry - A European Journal* **2015,** *21* (12), 4512-4517.

83. Su, Y. C.; Andreas, L.; Griffin, R. G., Magic Angle Spinning NMR of Proteins: High-Frequency Dynamic Nuclear Polarization and H-1 Detection. *Annual Review of Biochemistry* **2015,** *84*, 465-497.

84. Zagdoun, A.; Rossini, A. J.; Gajan, D.; Bourdolle, A.; Ouari, O.; Rosay, M.; Maas, W. E.; Tordo, P.; Lelli, M.; Emsley, L.; Lesage, A.; Coperet, C., Non-Aqueous Solvents for DNP Surface Enhanced NMR Spectroscopy. *Chemical Communications* **2012,** *48* (5), 654-656.

85. Berruyer, P.; Emsley, L.; Lesage, A., DNP in Materials Science: Touching the Surface. In *The Handbook of High Field Dynamic Nuclear Polarization*, Michaelis, V. K.; Griffin, R. G.; Corzilius, B.; Vega, S., Eds. John Wiley & Sons: 2020; pp 337-352.

86. Piveteau, L.; Ong, T. C.; Rossini, A. J.; Emsley, L.; Coperet, C.; Kovalenko, M. V., Structure of Colloidal Quantum Dots from Dynamic Nuclear Polarization Surface Enhanced NMR Spectroscopy. *Journal of the American Chemical Society* **2015,** *137* (43), 13964-13971.

87. Viger-Gravel, J.; Berruyer, P.; Gajan, D.; Basset, J. M.; Lesage, A.; Tordo, P.; Ouari, O.; Emsley, L., Frozen Acrylamide Gels as Dynamic Nuclear Polarization Matrices. *Angewandte Chemie International Edition* **2017,** *56* (30), 8726-8730.

88. Hanrahan, M. P.; Chen, Y. H.; Blome-Fernandez, R.; Stein, J. L.; Pach, G. F.; Adamson, M. A. S.; Neale, N. R.; Cossairt, B. M.; Vela, J.; Rossini, A. J., Probing the Surface Structure of Semiconductor Nanoparticles by DNP SENS with Dielectric Support Materials. *Journal of the American Chemical Society* **2019,** *141* (39), 15532-15546.

89. Pump, E.; Viger-Gravel, J.; Abou-Hamad, E.; Samantaray, M. K.; Hamzaoui, B.; Gurinov, A.; Anjum, D. H.; Gajan, D.; Lesage, A.; Bendjeriou-Sedjerari, A.; Emsley, L.; Basset, J. M., Reactive Surface Organometallic Complexes

Observed Using Dynamic Nuclear Polarization Surface Enhanced NMR Spectroscopy. *Chemical Science* **2017,** *8* (1), 284-290.

90. Lelli, M.; Rossini, A. J.; Casano, G.; Ouari, O.; Tordo, P.; Lesage, A.; Emsley, L., Hydrophobic Radicals Embedded in Neutral Surfactants for Dynamic Nuclear Polarization of Aqueous Environments at 9.4 Tesla. *Chemical Communications* **2014,** *50* (71), 10198-10201.

91. Liao, W. C.; Ong, T. C.; Gajan, D.; Bernada, F.; Sauvee, C.; Yulikov, M.; Pucino, M.; Schowner, R.; Schwarzwalder, M.; Buchmeiser, M. R.; Jeschke, G.; Tordo, P.; Ouari, O.; Lesage, A.; Emsley, L.; Coperet, C., Dendritic Polarizing Agents for DNP SENS. *Chemical Science* **2017,** *8* (1), 416-422.

92. Rossini, A. J.; Zagdoun, A.; Lelli, M.; Gajan, D.; Rascón, F.; Rosay, M.; Maas, W. E.; Copéret, C.; Lesage, A.; Emsley, L., One Hundred Fold Overall Sensitivity Enhancements for Silicon-29 NMR Spectroscopy of Surfaces by Dynamic Nuclear Polarization with CPMG Acquisition. *Chemical Science* **2012,** *3* (1), 108-115.

93. Kobayashi, T.; Lafon, O.; Thankamony, A. S. L.; Slowing, I. I.; Kandel, K.; Carnevale, D.; Vitzthum, V.; Vezin, H.; Amoureux, J. P.; Bodenhausen, G.; Pruski, M., Analysis of Sensitivity Enhancement by Dynamic Nuclear Polarization in Solid-State NMR: A Case Study of Functionalized Mesoporous Materials. *Physical Chemistry Chemical Physics* **2013,** *15* (15), 5553-5562.

94. Zagdoun, A.; Casano, G.; Ouari, O.; Lapadula, G.; Rossini, A. J.; Lelli, M.; Baffert, M.; Gajan, D.; Veyre, L.; Maas, W. E.; Rosay, M.; Weber, R. T.; Thieuleux, C.; Coperet, C.; Lesage, A.; Tordo, P.; Emsley, L., A Slowly Relaxing Rigid Biradical for Efficient Dynamic Nuclear Polarization Surface-Enhanced NMR Spectroscopy: Expeditious Characterization of Functional Group Manipulation in Hybrid Materials. *Journal of the American Chemical Society* **2012,** *134* (4), 2284-2291.

95. Corzilius, B.; Andreas, L. B.; Smith, A. A.; Ni, Q. Z.; Griffin, R. G., Paramagnet Induced Signal Quenching in MAS-DNP Experiments in Frozen Homogeneous Solutions. *Journal of Magnetic Resonance* **2014,** *240*, 113-123.

96. Thurber, K. R.; Tycko, R., Perturbation of Nuclear Spin Polarizations in Solid State NMR of Nitroxide-Doped Samples by Magic-Angle Spinning without Microwaves. *Journal of Chemical Physics* **2014,** *140* (18).

97. Mentink-Vigier, F.; Paul, S.; Lee, D.; Feintuch, A.; Hediger, S.; Vega, S.; De Paepe, G., Nuclear Depolarization and Absolute Sensitivity in Magic-Angle Spinning Cross Effect Dynamic Nuclear Polarization. *Physical Chemistry Chemical Physics* **2015,** *17* (34), 21824-21836.

98. Mentink-Vigier, F.; Mathies, G.; Liu, Y. P.; Barra, A. L.; Caporini, M. A.; Lee, D.; Hediger, S.; Griffin, R. G.; De Paepe, G., Efficient Cross-Effect Dynamic Nuclear Polarization without Depolarization in High-Resolution MAS NMR. *Chemical Science* **2017,** *8* (12), 8150-8163.

99. Jaudzems, K.; Polenova, T.; Pintacuda, G.; Oschkinat, H.; Lesage, A., DNP NMR of Biomolecular Assemblies. *Journal of Structural Biology* **2019,** *206* (1), 90-98.

100. Ni, Q. Z.; Daviso, E.; Can, T. V.; Markhasin, E.; Jawla, S. K.; Swager, T. M.; Temkin, R. J.; Herzfeld, J.; Griffin, R. G., High Frequency Dynamic Nuclear Polarization. *Accounts of Chemical Research* **2013,** *46* (9), 1933-1941.

101. Lesage, A.; Lelli, M.; Gajan, D.; Caporini, M. A.; Vitzthum, V.; Miéville, P.; Alauzun, J.; Roussey, A.; Thieuleux, C.; Mehdi, A.; Bodenhausen, G.; Coperet, C.; Emsley, L., Surface Enhanced NMR Spectroscopy by Dynamic Nuclear Polarization. *Journal of the American Chemical Society* **2010,** *132* (44), 15459-15461.

102. Rossini, A. J.; Zagdoun, A.; Lelli, M.; Lesage, A.; Coperet, C.; Emsley, L., Dynamic Nuclear Polarization Surface Enhanced NMR Spectroscopy. *Accounts of Chemical Research* **2013,** *46* (9), 1942-1951.

103. Lelli, M.; Gajan, D.; Lesage, A.; Caporini, M. A.; Vitzthum, V.; Mieville, P.; Heroguel, F.; Rascon, F.; Roussey, A.; Thieuleux, C.; Boualleg, M.; Veyre, L.; Bodenhausen, G.; Coperet, C.; Emsley, L., Fast Characterization of Functionalized Silica Materials by Silicon-29 Surface-Enhanced NMR Spectroscopy Using Dynamic Nuclear Polarization. *Journal of the American Chemical Society* **2011,** *133* (7), 2104-2107.

104. Perras, F. A.; Kobayashi, T.; Pruski, M., Growing Signals from the Noise: Challengin Nuclei in Materials DNP. In *Handbook of High Field Dynamic Nuclear Polarization*, Michaelis, V. K.; Griffin, R. G.; Corzilius, B.; Vega, S., Eds. John Wiley & Sons: 2020.

105. Rossini, A. J.; Widdifield, C. M.; Zagdoun, A.; Lelli, M.; Schwarzwalder, M.; Coperet, C.; Lesage, A.; Emsley, L., Dynamic Nuclear Polarization Enhanced NMR Spectroscopy for Pharmaceutical Formulations. *Journal of the American Chemical Society* **2014,** *136* (6), 2324-2334.

106. Rossini, A. J.; Zagdoun, A.; Hegner, F.; Schwarzwälder, M.; Gajan, D.; Copéret, C.; Lesage, A.; Emsley, L., Dynamic Nuclear Polarization NMR Spectroscopy of Microcrystalline Solids. *Journal of the American Chemical Society* **2012,** *134* (40), 16899-16908.

107. Pinon, A. C.; Schlagnitweit, J.; Berruyer, P.; Rossini, A. J.; Lelli, M.; Socie, E.; Tang, M.; Pham, T.; Lesage, A.; Schantz, S.; Emsley, L., Measuring Nano- to Microstructures from Relayed Dynamic Nuclear Polarization NMR. *The Journal of Physical Chemistry C* **2017,** *121* (29), 15993-16005.

108. Zhao, L.; Pinon, A. C.; Emsley, L.; Rossini, A. J., DNP-Enhanced Solid-State NMR Spectroscopy of Active Pharmaceutical Ingredients. *Magnetic Resonance in Chemistry* **2018,** *56* (7), 583-609.

109. van der Wel, P. C. A.; Hu, K. N.; Lewandowski, J.; Griffin, R. G., Dynamic Nuclear Polarization of Amyloidogenic Peptide Nanocrystals: GNNQQNY, a Core Segment of the Yeast Prion Protein Sup35p. *Journal of the American Chemical Society* **2006,** *128* (33), 10840-10846.

110. Barnes, A. B.; Corzilius, B.; Mak-Jurkauskas, M. L.; Andreas, L. B.; Bajaj, V. S.; Matsuki, Y.; Belenky, M. L.; Lugtenburg, J.; Sirigiri, J. R.; Temkin, R. J.; Herzfeld, J.; Griffin, R. G., Resolution and Polarization Distribution in Cryogenic DNP/MAS Experiments. *Physical Chemistry Chemical Physics* **2010,** *12* (22), 5861-5867.

111. Ernst, M.; Meier, B., Spin Diffusion in Solids. In *Solid State NMR of Polymers*, Ando, I.; Asakura, T., Eds. Elsevier Science B.V.: 1998; Vol. 84, pp 83-121.

112. Emsley, L., Spin Diffusion for NMR Crystallography. In *Encyclopedia of Magnetic Resonance*, John Wiley & Sons: 2009.

113. Edzes, H. T.; Bernards, J. P. C., Two-Dimensional Exchange NMR in Static Powders: Interchain C-13 Spin Exchange in Crystalline Polyethylene. *Journal of the American Chemical Society* **1984,** *106* (5), 1515-1517.

114. Manolikas, T.; Herrmann, T.; Meier, B. H., Protein Structure Determination from C-13 Spin-Diffusion Solid-State NMR Spectroscopy. *Journal of the American Chemical Society* **2008,** *130* (12), 3959-3966.

115. Clauss, J.; Schmidt-Rohr, K.; Spiess, H. W., Determination of Domain Sizes in Heterogeneous Polymers by Solid-State NMR. *Acta Polymerica* **1993,** *44* (1), 1-17.

116. Caravatti, P.; Neuenschwander, P.; Ernst, R. R., Characterization of Heterogeneous Polymer Blends by 2-Dimensional Proton Spin Diffusion Spectroscopy. *Macromolecules* **1985,** *18* (1), 119-122.

117. Seidel, K.; Etzkorn, M.; Sonnenberg, L.; Griesinger, C.; Sebald, A.; Baldus, M., Studying Molecular 3D Structure and Dynamics by High-Resolution Solid-State NMR: Application to L-Tyrosine-Ethylester. *Journal of Physical Chemistry A* **2005,** *109* (11), 2436-2442.

118. Elena, B.; Pintacuda, G.; Mifsud, N.; Emsley, L., Molecular Structure Determination in Powders by NMR Crystallography from Proton Spin Diffusion. *Journal of the American Chemical Society* **2006,** *128* (29), 9555-9560.

119. Bloembergen, N., On the Interaction of Nuclear Spins in a Crystalline Lattice. *Physica XV* **1949,** *3-4*, 386-426.

120. Maricq, M. M.; Waugh, J. S., NMR in Rotating Solids. *Journal of Chemical Physics* **1979,** *70* (7), 3300-3316.

121. Suter, D.; Ernst, R. R., Spin Diffusion in Resolved Solid-State NMR Spectra. *Physical Review B* **1985,** *32* (9), 5608-5627.

122. Kubo, A.; McDowell, C. A., ^{31}p Spectral Spin Diffusion in Crystalline Solids. *Journal of Chemical Physics* **1988,** *89* (1), 63-70.

123. Haeberlen, U.; Waugh, J. S., Coherent Averaging Effects in Magnetic Resonance. *Physical Review* **1968,** *175* (2), 453-467.

124. Zhang, S. M.; Meier, B. H.; Ernst, R. R., Local Monitoring of Proton Spin Diffusion in Static and Rotating Samples Via Spy Detection. *Solid State Nuclear Magnetic Resonance* **1992,** *1* (6), 313-320.

125. Bockmann, A.; Ernst, M.; Meier, B. H., Spinning Proteins, the Faster, the Better? *Journal of Magnetic Resonance* **2015,** *253*, 71-79.

126. Blumberg, W. E., Nuclear Spin-Lattice Relaxation Caused by Paramagnetic Impurities. *Physical Review* **1960,** *119* (1), 79-84.

127. Khutsishvili, G. R., Spin Diffusion. *Soviet Physics Uspekhi* **1966,** *8* (5), 743.

128. Schmidt-Rohr, K.; Spiess, H. W., *Multidimensional Solid-State NMR and Polymers*. Academic Press: 1994.

129. Veshtort, M.; Griffin, R. G., Proton-Driven Spin Diffusion in Rotating Solids Via Reversible and Irreversible Quantum Dynamics. *Journal of Chemical Physics* **2011,** *135* (13), 134509.

130. Kubo, A.; McDowell, C. A., Spectral Spin Diffusion in Polycrystalline Solids under Magic-Angle Spinning. *Journal of the Chemical Society, Faraday Transactions 1: Physical Chemistry in Condensed Phases* **1988,** *84* (11), 3713-3730.

131. Reichert, D.; Bonagamba, T. J.; Schmidt-Rohr, K., Slow-Down of C-13 Spin Diffusion in Organic Solids by Fast MAS: A CODEX NMR Study. *Journal of Magnetic Resonance* **2001,** *151* (1), 129-135.

132. Wittmann, J. J.; Hendriks, L.; Meier, B. H.; Ernst, M., Controlling Spin Diffusion by Tailored Rf-Irradiation Schemes. *Chemical Physics Letters* **2014,** *608*, 60-67.

133. Halse, M. E.; Zagdoun, A.; Dumez, J. N.; Emsley, L., Macroscopic Nuclear Spin Diffusion Constants of Rotating Polycrystalline Solids from First-Principles Simulation. *Journal of Magnetic Resonance* **2015,** *254*, 48-55.

134. Vanderhart, D. L., Natural-Abundance C-13-C-13 Spin Exchange in Rigid Crystalline Organic Solids. *Journal of Magnetic Resonance* **1987,** *72* (1), 13-47.

135. Kessemeier, H.; Norberg, R. E., Pulsed Nuclear Magnetic Resonance in Rotating Solids. *Physical Review* **1967,** *155* (2), 321-337.

136. Colombo, M. G.; Meier, B. H.; Ernst, R. R., Rotor-Driven Spin Diffusion in Natural-Abundance 13c Spin Systems. *Chemical Physics Letters* **1988,** *146* (3), 189-196.

137. Andrew, E. R.; Bradbury, A.; Eades, R. G.; Wynn, V. T., Nuclear Cross-Relaxation Induced by Specimen Rotation. *Physics Letters* **1963,** *4* (2), 99-100.

138. Raleigh, D. P.; Levitt, M. H.; Griffin, R. G., Rotational Resonance in Solid State NMR. *Chemical Physics Letters* **1988,** *146* (1), 71-76.

139. Challoner, R.; Kummerlen, J.; McDowell, C. A., Spectral Spin Diffusion under *N = 0* Rotational Resonance. *Molecular Physics* **1994,** *83* (4), 687-700.

140. Roos, M.; Micke, P.; Saalwachter, K.; Hempel, G., Moderate MAS Enhances Local H-1 Spin Exchange and Spin Diffusion. *Journal of Magnetic Resonance* **2015,** *260*, 28-37.

141. Zhang, W.; Cory, D. G., First Direct Measurement of the Spin Diffusion Rate in a Homogenous Solid. *Physical Review Letters* **1998,** *80* (6), 1324-1327.

142. Robyr, P.; Meier, B. H.; Ernst, R. R., Radio-Frequency-Driven Nuclar Spin Diffusion in Solids. *Chemical Physics Letters* **1989,** *162* (6), 417-423.

143. Thurber, K. R.; Yau, W.-M.; Tycko, R., Low-Temperature Dynamic Nuclear Polarization at 9.4 T with a 30 mW Microwave Source. *Journal of Magnetic Resonance* **2010,** *204* (2), 303-313.

144. Leguennec, P.; Nechtschein, M.; Travers, J. P., Nonexponential NMR Relaxations in Heterogeneously Doped Solids. *Physical Review B* **1993,** *47* (5), 2893-2896.

145. Tegenfeldt, J.; Haeberlen, U., Cross Polarization in Solids with Flip-Back of I-Spin Magnetization. *Journal of Magnetic Resonance* **1979,** *36* (3), 453-457.

146. Boxhoorn, G.; Kortbeek, A. G. T. G.; Hays, G. R.; Alma, N. C. M., A High-Resolution Solid-State 29Si NMR Study of Zsm-5 Type Zeolites. *Zeolites* **1984,** *4* (1), 15-21.

147. Harbison, G. S.; Smith, S. O.; Pardoen, J. A.; Courtin, J. M. L.; Lugtenburg, J.; Herzfeld, J.; Mathies, R. A.; Griffin, R. G., Solid-State C-13 NMR Detection of a Perturbed 6-S-Trans Chromophore in Bacteriorhodopsin. *Biochemistry* **1985,** *24* (24), 6955-6962.

148. Sherwood, M. H.; Alderman, D. W.; Grant, D. M., Two-Dimensional Chemical-Shift Tensor Correlation Spectroscopy. Multiple-Axis Sample-Reorientation Mechanism. *Journal of Magnetic Resonance* **1989,** *84* (3), 466-489.

149. Hughes, C. D.; Sherwood, M. H.; Alderman, D. W.; Grant, D. M., Chemical-Shift-Chemical-Shift Correlation Spectroscopy in Powdered Solids. *Journal of Magnetic Resonance, Series A* **1993,** *102* (1), 58-72.

150. Bennett, A. E.; Rienstra, C. M.; Auger, M.; Lakshmi, K. V.; Griffin, R. G., Heteronuclear Decoupling in Rotating Solids. *The Journal of Chemical Physics* **1995,** *103* (16), 6951-6958.

151. Fung, B. M.; Khitrin, A. K.; Ermolaev, K., An Improved Broadband Decoupling Sequence for Liquid Crystals and Solids. *Journal of Magnetic Resonance* **2000,** *142* (1), 97-101.

152. De Paepe, G.; Elena, B.; Emsley, L., Characterization of Heteronuclear Decoupling through Proton Spin Dynamics in Solid-State Nuclear Magnetic Resonance Spectroscopy. *Journal of Chemical Physics* **2004,** *121* (7), 3165-3180.

153. Johnson, R. L.; Schmidt-Rohr, K., Quantitative Solid-State 13c NMR with Signal Enhancement by Multiple Cross Polarization. *Journal of Magnetic Resonance* **2014,** *239*, 44-49.

154. Lopez, J. J.; Kaiser, C.; Asami, S.; Glaubitz, C., Higher Sensitivity through Selective 13c Excitation in Solid-State NMR Spectroscopy. *Journal of the American Chemical Society* **2009,** *131* (44), 15970-15971.

155. Jannin, S.; Bornet, A.; Colombo, S.; Bodenhausen, G., Low-Temperature Cross Polarization in View of Enhancing Dissolution Dynamic Nuclear Polarization in NMR. *Chemical Physics Letters* **2011,** *517* (4), 234-236.

156. Grzesiek, S.; Bax, A., The Importance of Not Saturating Water in Protein NMR. Application to Sensitivity Enhancement and NOE Measurements. *Journal of the American Chemical Society* **1993,** *115* (26), 12593-12594.

157. Demers, J.-P.; Vijayan, V.; Lange, A., Recovery of Bulk Proton Magnetization and Sensitivity Enhancement in Ultrafast Magic-Angle Spinning Solid-State NMR. *The Journal of Physical Chemistry B* **2015,** *119* (7), 2908-2920.

158. Zhang, R.; Chen, Y.; Rodriguez-Hornedo, N.; Ramamoorthy, A., Enhancing NMR Sensitivity of Natural-Abundance Low-Γ Nuclei by Ultrafast Magic-Angle-Spinning Solid-State NMR Spectroscopy. *ChemPhysChem* **2016,** *17* (19), 2962-2966.

159. Hall, D. A.; Maus, D. C.; Gerfen, G. J.; Inati, S. J.; Becerra, L. R.; Dahlquist, F. W.; Griffin, R. G., Polarization-Enhanced NMR Spectroscopy of Biomolecules in Frozen Solution. *Science* **1997,** *276* (5314), 930--932.

160. Kubicki, D. J.; Rossini, A. J.; Purea, A.; Zagdoun, A.; Ouari, O.; Tordo, P.; Engelke, F.; Lesage, A.; Emsley, L., Amplifying Dynamic Nuclear Polarization of Frozen Solutions by Incorporating Dielectric Particles. *Journal of the American Chemical Society* **2014,** *136* (44), 15711-15718.

161. Lelli, M.; Chaudhari, S. R.; Gajan, D.; Casano, G.; Rossini, A. J.; Ouari, O.; Tordo, P.; Lesage, A.; Emsley, L., Solid-State Dynamic Nuclear Polarization at 9.4 and 18.8 T from 100 K to Room Temperature. *Journal of the American Chemical Society* **2015,** *137* (46), 14558-14561.

162. Detken, A.; Hardy, E. H.; Ernst, M.; Meier, B. H., Simple and Efficient Decoupling in Magic-Angle Spinning Solid-State NMR: The XiX Scheme. *Chemical Physics Letters* **2002,** *356* (3), 298-304.

163. Barnes, A. B.; De Paepe, G.; van der Wel, P. C. A.; Hu, K. N.; Joo, C. G.; Bajaj, V. S.; Mak-Jurkauskas, M. L.; Sirigiri, J. R.; Herzfeld, J.; Temkin, R. J.; Griffin, R. G., High-Field Dynamic Nuclear Polarization for Solid and Solution Biological NMR. *Applied Magnetic Resonance* **2008,** *34* (3-4), 237-263.

164. Debelouchina, G. T.; Bayro, M. J.; Wel, P. C. A. v. d.; Caporini, M. A.; Barnes, A. B.; Rosay, M.; Maas, W. E.; Griffin, R. G., Dynamic Nuclear Polarization-Enhanced Solid-State NMR Spectroscopy of GNNQQNY Nanocrystals and Amyloid Fibrils. *Physical Chemistry Chemical Physics* **2010,** *12* (22), 5911-5919.

165. Lewandowski, J. R.; Halse, M. E.; Blackledge, M.; Emsley, L., Direct Observation of Hierarchical Protein Dynamics. *Science* **2015,** *348* (6234), 578-581.

166. Yarava, J. R.; Chaudhari, S. R.; Rossini, A. J.; Lesage, A.; Emsley, L., Solvent Suppression in DNP Enhanced Solid State NMR. *Journal of Magnetic Resonance* **2017,** *277* (Supplement C), 149-153.

167. Pinon, A. C.; Rossini, A. J.; Widdifield, C. M.; Gajan, D.; Emsley, L., Polymorphs of Theophylline Characterized by DNP Enhanced Solid-State NMR. *Molecular Pharmaceutics* **2015,** *12* (11), 4146-4153.

168. Lesage, A.; Bardet, M.; Emsley, L., Through-Bond Carbon–Carbon Connectivities in Disordered Solids by NMR. *Journal of the American Chemical Society* **1999,** *121* (47), 10987-10993.

169. Maly, T.; Debelouchina, G. T.; Bajaj, V. S.; Hu, K. N.; Joo, C. G.; Mak-Jurkauskas, M. L.; Sirigiri, J. R.; van der Wel, P. C. A.; Herzfeld, J.; Temkin, R. J.; Griffin, R. G., Dynamic Nuclear Polarization at High Magnetic Fields. *Journal of Chemical Physics* **2008,** *128* (5).

170. Lafon, O.; Thankamony, A. S.; Rosay, M.; Aussenac, F.; Lu, X.; Trebosc, J.; Bout-Roumazeilles, V.; Vezin, H.; Amoureux, J. P., Indirect and Direct 29Si Dynamic Nuclear Polarization of Dispersed Nanoparticles. *Chemical Communications* **2013,** *49* (28), 2864-2866.

171. Blanc, F.; Sperrin, L.; Jefferson, D. A.; Pawsey, S.; Rosay, M.; Grey, C. P., Dynamic Nuclear Polarization Enhanced Natural Abundance 17O Spectroscopy. *Journal of the American Chemical Society* **2013,** *135* (8), 2975-2978.

172. Zhao, L.; Li, W.; Plog, A.; Xu, Y.; Buntkowsky, G.; Gutmann, T.; Zhang, K., Multi-Responsive Cellulose Nanocrystal-Rhodamine Conjugates: An Advanced Structure Study by Solid-State Dynamic Nuclear Polarization (DNP) NMR. *Physical Chemistry Chemical Physics* **2014,** *16* (47), 26322-26329.

173. Wolf, P.; Valla, M.; Rossini, A. J.; Comas-Vives, A.; Nunez-Zarur, F.; Malaman, B.; Lesage, A.; Emsley, L.; Coperet, C.; Hermans, I., NMR Signatures of the Active Sites in Sn-Beta Zeolite. *Angewandte Chemie International Edition* **2014,** *53* (38), 10179-10183.

174. Lee, D.; Monin, G.; Duong, N. T.; Lopez, I. Z.; Bardet, M.; Mareau, V.; Gonon, L.; De Paepe, G., Untangling the Condensation Network of Organosiloxanes on Nanoparticles Using 2d 29Si-29Si Solid-State NMR Enhanced by Dynamic Nuclear Polarization. *Journal of the American Chemical Society* **2014,** *136* (39), 13781-13788.

175. Chaudhari, S. R.; Wisser, D.; Pinon, A. C.; Berruyer, P.; Gajan, D.; Tordo, P.; Ouari, O.; Reiter, C.; Engelke, F.; Coperet, C.; Lelli, M.; Lesage, A.; Emsley, L., Dynamic Nuclear Polarization Efficiency Increased by Very Fast Magic Angle Spinning. *Journal of the American Chemical Society* **2017,** *139* (31), 10609-10612.

176. Perras, F. A.; Wang, Z.; Naik, P.; Slowing, II; Pruski, M., Natural Abundance O-17 DNP NMR Provides Precise O-H Distances and Insights into the Bronsted Acidity of Heterogeneous Catalysts. *Angewandte Chemie International Edition* **2017,** *56* (31), 9165-9169.

177. Rankin, A. G. M.; Webb, P. B.; Dawson, D. M.; Viger-Gravel, J.; Walder, B. J.; Emsley, L.; Ashbrook, S. E., Determining the Surface Structure of Silicated Alumina Catalysts Via Isotopic Enrichment and Dynamic Nuclear Polarization Surface-Enhanced NMR Spectroscopy. *Journal of Physical Chemistry C* **2017,** *121* (41), 22977-22984.

178. Protesescu, L.; Rossini, A. J.; Kriegner, D.; Valla, M.; de Kergommeaux, A.; Walter, M.; Kravchyk, K. V.; Nachtegaal, M.; Stangl, J.; Malaman, B.; Reiss, P.; Lesage, A.; Emsley, L.; Coperet, C.; Kovalenko, M. V., Unraveling the Core-Shell Structure of Ligand-Capped Sn/Snox Nanoparticles by Surface-Enhanced Nuclear Magnetic Resonance, Mossbauer, and X-Ray Absorption Spectroscopies. *Acs Nano* **2014,** *8* (3), 2639-2648.

179. Mollica, G.; Dekhil, M.; Ziarelli, F.; Thureau, P.; Viel, S., Quantitative Structural Constraints for Organic Powders at Natural Isotopic Abundance Using Dynamic Nuclear Polarization Solid-State NMR Spectroscopy. *Angewandte Chemie International Edition* **2015,** *54* (20), 6028-6031.

180. Marker, K.; Pingret, M.; Mouesca, J. M.; Gasparutto, D.; Hediger, S.; De Paepe, G., A New Tool for NMR Crystallography: Complete C-13/N-15 Assignment of Organic Molecules at Natural Isotopic Abundance Using DNP-Enhanced Solid-State NMR. *Journal of the American Chemical Society* **2015,** *137* (43), 13796-13799.

181. Bjorgvinsdottir, S.; Walder, B. J.; Pinon, A. C.; Yarava, J. R.; Emsley, L., DNP Enhanced NMR with Flip-Back Recovery. *Journal of Magnetic Resonance* **2018,** *288*, 69-75.

182. Duijvestijn, M. J.; Vanderlugt, C.; Smidt, J.; Wind, R. A.; Zilm, K. W.; Staplin, D. C., C-13 NMR Spectroscopy in Diamonds Using Dynamic Nuclear Polarization. *Chemical Physics Letters* **1983,** *102* (1), 25-28.

183. Hu, J. Z.; Solum, M. S.; Wind, R. A.; Nilsson, B. L.; Peterson, M. A.; Pugmire, R. J.; Grant, D. M., H-1 and N-15 Dynamic Nuclear Polarization Studies of Carbazole. *Journal of Physical Chemistry A* **2000,** *104* (19), 4413-4420.

184. Dementyev, A. E.; Cory, D. G.; Ramanathan, C., Dynamic Nuclear Polarization in Silicon Microparticles. *Physical Review Letters* **2008,** *100* (12), 127601.

185. Zagdoun, A.; Rossini, A. J.; Conley, M. P.; Gruning, W. R.; Schwarzwalder, M.; Lelli, M.; Franks, W. T.; Oschkinat, H.; Coperet, C.; Emsley, L.; Lesage, A., Improved Dynamic Nuclear Polarization Surface-Enhanced NMR Spectroscopy through Controlled Incorporation of Deuterated Functional Groups. *Angewandte Chemie International Edition* **2013,** *52* (4), 1222-1225.

186. Peersen, O. B.; Wu, X. L.; Kustanovich, I.; Smith, S. O., Variable-Amplitude Cross-Polarization MAS NMR. *Journal of Magnetic Resonance Series A* **1993,** *104* (3), 334-339.

187. Henrichs, P. M.; Cofield, M. L.; Young, R. H.; Hewitt, J. M., Nuclear Spin-Lattice Relaxation Via Paramagnetic Centers in Solids. C-13 NMR of Diamonds. *Journal of Magnetic Resonance* **1984,** *58* (1), 85-94.

188. Lafon, O.; Rosay, M.; Aussenac, F.; Lu, X.; Trebosc, J.; Cristini, O.; Kinowski, C.; Touati, N.; Vezin, H.; Amoureux, J. P., Beyond the Silica Surface by Direct Silicon-29 Dynamic Nuclear Polarization. *Angewandte Chemie International Edition* **2011,** *50* (36), 8367-8370.

189. Wenckebach, W. T., *Essentials of Dynamic Nuclear Polarization*. Spindrift Publications: 2016.

190. Clough, S.; Gray, K. W., Spin Diffusion and Nuclear Magnetic Resonance in Rotating Solids. *Proceedings of the Physical Society* **1962,** *80* (6), 1382.

191. Clough, S.; Gray, K. W., The Stochastic Theory of the Nuclear Magnetic Resonance Line in Rotating Solids. *Proceedings of the Physical Society* **1962,** *79* (3), 457.

192. Levitt, M. H.; Raleigh, D. P.; Creuzet, F.; Griffin, R. G., Theory and Simulations of Homonuclear Spin Pair Systems in Rotating Solids. *The Journal of Chemical Physics* **1990,** *92* (11), 6347-6364.

193. Chen, J. C.; Wu, X. P.; Shen, L.; Li, Y. H.; Wu, D.; Ding, W. P.; Gong, X. Q.; Lin, M.; Peng, L. M., Identification of Different Tin Species in SnO2 Nanosheets with Sn-119 Solid-State NMR Spectroscopy. *Chemical Physics Letters* **2016,** *643*, 126-130.

194. Ji, X.; Bornet, A.; Vuichoud, B.; Milani, J.; Gajan, D.; Rossini, A. J.; Emsley, L.; Bodenhausen, G.; Jannin, S., Transportable Hyperpolarized Metabolites. *Nature Communications* **2017,** *8*, 13975.

195. Ratcliffe, C. I.; Yu, K.; Ripmeester, J. A.; Badruz Zaman, M.; Badarau, C.; Singh, S., Solid State NMR Studies of Photoluminescent Cadmium Chalcogenide Nanoparticles. *Physical Chemistry Chemical Physics* **2006,** *8* (30), 3510-3519.

196. PhySy Ltd, *Rmn 1.1*. 2016.

197. Bjorgvinsdottir, S.; Walder, B. J.; Pinon, A. C.; Emsley, L., Bulk Nuclear Hyperpolarization of Inorganic Solids by Relay from the Surface. *Journal of the American Chemical Society* **2018,** *140* (25), 7946-7951.

198. Zhang, S. M.; Wu, X. L.; Mehring, M., Successive Polarization under Mismatched Hartmann-Hahn Condition. *Chemical Physics Letters* **1990,** *166* (1), 92-94.

199. Nevzorov, A. A., Ergodicity and Efficiency of Cross-Polarization in NMR of Static Solids. *Journal of Magnetic Resonance* **2011,** *209* (2), 161-166.

200. Raya, J.; Perrone, B.; Hirschinger, J., Chemical Shift Powder Spectra Enhanced by Multiple-Contact Cross-Polarization under Slow Magic-Angle Spinning. *Journal of Magnetic Resonance* **2013,** *227*, 93-102.

201. Rosay, M. Ph.D. Thesis. Massachusetts Institute of Technology, Cambridge, MA, 2001.

202. Akbey, U.; Altin, B.; Linden, A.; Ozcelik, S.; Gradzielski, M.; Oschkinat, H., Dynamic Nuclear Polarization of Spherical Nanoparticles. *Physical Chemistry Chemical Physics* **2013,** *15* (47), 20706-20716.

203. Sangodkar, R. P.; Smith, B. J.; Gajan, D.; Rossini, A. J.; Roberts, L. R.; Funkhouser, G. P.; Lesage, A.; Emsley, L.; Chmelka, B. F., Influences of Dilute Organic Adsorbates on the Hydration of Low-Surface-Area Silicates. *Journal of the American Chemical Society* **2015,** *137* (25), 8096-8112.

204. Kobayashi, T.; Perras, F. A.; Chaudhary, U.; Slowing, I. I.; Huang, W. Y.; Sadow, A. D.; Pruski, M., Improved Strategies for DNP-Enhanced 2d H-1-X Heteronuclear Correlation Spectroscopy of Surfaces. *Solid State Nuclear Magnetic Resonance* **2017,** *87*, 38-44.

205. Redfield, A. G., Nuclear Magnetic Resonance Saturation and Rotary Saturation in Solids. *Physical Review* **1955,** *98* (6), 1787-1809.

206. Look, D. C.; Lowe, I. J., Nuclear Magnetic Dipole-Dipole Relaxation Along Static and Rotating Magnetic Fields: Application to Gypsum. *Journal of Chemical Physics* **1966,** *44* (8), 2995-3000.

207. Levitt, M. H.; Freeman, R., NMR Population Inversion Using a Composite Pulse. *Journal of Magnetic Resonance* **1979,** *33* (2), 473-476.

208. Duan, P.; Schmidt-Rohr, K., Composite-Pulse and Partially Dipolar Dephased Multicp for Improved Quantitative Solid-State C-13 NMR. *Journal of Magnetic Resonance* **2017,** *285*, 68-78.

209. Levitt, M. H.; Suter, D.; Ernst, R. R., Spin Dynamics and Thermodynamics in Solid-State NMR Cross Polarization. *Journal of Chemical Physics* **1986,** *84* (8), 4243-4255.

210. Metz, G.; Ziliox, M.; Smith, S. O., Towards Quantitative CP-MAS NMR. *Solid State Nuclear Magnetic Resonance* **1996,** *7* (3), 155-160.

211. Kolbert, A. C.; Bielecki, A., Broadband Hartmann-Hahn Matching in Magic-Angle-Spinning NMR Via an Adiabatic Frequency Sweep. *Journal of Magnetic Resonance Series A* **1995,** *116* (1), 29-35.

212. Zeigler, R. C.; Wind, R. A.; Maciel, G. E., The Stop-and-Go Spinning Technique in MAS Experiments. *Journal of Magnetic Resonance* **1988,** *79* (2), 299-306.

213. Samoson, A.; Tuherm, T.; Past, J., Ramped-Speed Cross Polarization MAS NMR. *Journal of Magnetic Resonance* **2001,** *149* (2), 264-267.

214. Hirsh, D. A.; Rossini, A. J.; Emsley, L.; Schurko, R. W., Cl-35 Dynamic Nuclear Polarization Solid-State NMR of Active Pharmaceutical Ingredients. *Physical Chemistry Chemical Physics* **2016,** *18* (37), 25893-25904.

215. Tarascon, J. M.; Armand, M., Issues and Challenges Facing Rechargeable Lithium Batteries. *Nature* **2001,** *414* (6861), 359-367.

216. Zhu, G. N.; Wang, Y. G.; Xia, Y. Y., Ti-Based Compounds as Anode Materials for Li-Ion Batteries. *Energy & Environmental Science* **2012,** *5* (5), 6652-6667.

217. Reddy, M. V.; Rao, G. V. S.; Chowdari, B. V. R., Metal Oxides and Oxysalts as Anode Materials for Li Ion Batteries. *Chemical Reviews* **2013,** *113* (7), 5364-5457.

218. Grey, C. P.; Tarascon, J. M., Sustainability and in Situ Monitoring in Battery Development. *Nature Materials* **2017,** *16* (1), 45-56.

219. Jin, Y. T.; Kneusels, N. J. H.; Marbella, L. E.; Castillo-Martinez, E.; Magusin, P. C. M. M.; Weatherup, R. S.; Jonsson, E.; Liu, T.; Paul, S.; Grey, C. P., Understanding Fluoroethylene Carbonate and Vinylene Carbonate Based Electrolytes for Si Anodes in Lithium Ion Batteries with NMR Spectroscopy. *Journal of the American Chemical Society* **2018,** *140* (31), 9854-9867.

220. Leskes, M.; Kim, G.; Liu, T.; Michan, A. L.; Aussenac, F.; Dorffer, P.; Paul, S.; Grey, C. P., Surface-Sensitive NMR Detection of the Solid Electrolyte Interphase Layer on Reduced Graphene Oxide. *Journal of Physical Chemistry Letters* **2017,** *8* (5), 1078-1085.

221. Jin, Y. T.; Kneusels, N. J. H.; Magusin, P. C. M. M.; Kim, G.; Castillo-Martinez, E.; Marbella, L. E.; Kerber, R. N.; Howe, D. J.; Paul, S.; Liu, T.; Grey, C. P., Identifying the Structural Basis for the Increased Stability of the Solid Electrolyte Interphase Formed on Silicon with the Additive Fluoroethylene Carbonate. *Journal of the American Chemical Society* **2017,** *139* (42), 14992-15004.

222. Hope, M. A.; Rinkel, B. L. D.; Gunnarsdóttir, A. B.; Märker, K.; Menkin, S.; Paul, S.; Grey, C. P., Selective NMR Observation of the SEI–Metal Interface by Dynamic Nuclear Polarisation from Lithium Metal. *Nature Communications* **2020,** *11* (2224).

223. Sani, M. A.; Martin, P. A.; Yunis, R.; Chen, F. F.; Forsyth, M.; Deschamps, M.; O'Dell, L. A., Probing Ionic Liquid Electrolyte Structure Via the Glassy State by Dynamic Nuclear Polarization NMR Spectroscopy. *Journal of Physical Chemistry Letters* **2018,** *9* (5), 1007-1011.

224. Vijayakumar, M.; Kerisit, S.; Yang, Z. G.; Graff, G. L.; Liu, J.; Sears, J. A.; Burton, S. D.; Rosso, K. M.; Hu, J. Z., Combined Li-6,Li-7 NMR and Molecular Dynamics Study of Li Diffusion in Li2TiO3. *Journal of Physical Chemistry C* **2009,** *113* (46), 20108-20116.

225. Lee, D.; Hediger, S.; De Paepe, G., Is Solid-State NMR Enhanced by Dynamic Nuclear Polarization? *Solid State Nuclear Magnetic Resonance* **2015,** *66-67*, 6-20.

226. Bjorgvinsdottir, S.; Walder, B. J.; Matthey, N.; Emsley, L., Maximizing Nuclear Hyperpolarization in Pulse Cooling under MAS. *Journal of Magnetic Resonance* **2019,** *300*, 142-148.

227. Xu, G. J.; Han, P. X.; Dong, S. M.; Liu, H. S.; Cui, G. L.; Chen, L. Q., Li4Ti5O12-Based Energy Conversion and Storage Systems: Status and Prospects. *Coordination Chemistry Reviews* **2017,** *343*, 139-184.

228. Ruprecht, B.; Wilkening, M.; Uecker, R.; Heitjans, P., Extremely Slow Li Ion Dynamics in Monoclinic Li2TiO3 - Probing Macroscopic Jump Diffusion Via Li-7 NMR Stimulated Echoes. *Physical Chemistry Chemical Physics* **2012,** *14* (34), 11974-11980.

229. Schmidt, W.; Wilkening, M., Diffusion-Induced Li-7 NMR Spin-Lattice Relaxation of Fully Lithiated, Mixed-Conducting Li7ti5o12. *Solid State Ionics* **2016,** *287*, 77-82.

230. Dorrian, J. F.; Newnham, R. E., Refinement of the Structure of Li2TiO3. *Materials Research Bulletin* **1969,** *4* (3), 179-183.

231. Deschanvres, A.; Raveau, B.; Sekkal, Z., Synthesis and Crystallographic Study of New Solid Solution of Spinel Li1+XTi2-XO4 Less Than or Equal to X Less Than or Equal to O, 333. *Materials Research Bulletin* **1971,** *6* (8), 699-704.

232. Massiot, D.; Fayon, F.; Capron, M.; King, I.; Le Calve, S.; Alonso, B.; Durand, J. O.; Bujoli, B.; Gan, Z. H.; Hoatson, G., Modelling One- and Two-Dimensional Solid-State NMR Spectra. *Magnetic Resonance in Chemistry* **2002,** *40* (1), 70-76.

233. Chernaya, V. V.; Mitiaev, A. S.; Chizhov, P. S.; Dikarev, E. V.; Shpanchenko, R. V.; Antipov, E. V.; Korolenko, M. V.; Fabritchnyi, P. B., Synthesis and Investigation of Tin(II) Pyrophosphate Sn2p2o7. *Chemistry of Materials* **2005,** *17* (2), 284-290.

234. Amornsakchai, P.; Apperley, D. C.; Harris, R. K.; Hodgkinson, P.; Waterfield, P. C., Solid-State NMR Studies of Some Tin(II) Compounds. *Solid State Nuclear Magnetic Resonance* **2004,** *26* (3-4), 160-171.

235. Prisco, N. A.; Pinon, A. C.; Emsley, L.; Chmelka, B. F., Quantitative Scaling Analyses for Predictive Modelling of Polarization Transfer across Dissimilar Interfaces. *Submitted* **2020**.

236. Pinon, A. C.; Skantze, U.; Viger-Gravel, J.; Schantz, S.; Emsley, L., Core-Shell Structure of Organic Crystalline Nanoparticles Determined by Relayed Dynamic Nuclear Polarization NMR. *Journal of Physical Chemistry A* **2018,** *122* (44), 8802-8807.

237. Viger-Gravel, J.; Schantz, A.; Pinon, A. C.; Rossini, A. J.; Schantz, S.; Emsley, L., Structure of Lipid Nanoparticles Containing siRNA or mRNA by Dynamic Nuclear Polarization-Enhanced NMR Spectroscopy. *Journal of Physical Chemistry B* **2018,** *122* (7), 2073-2081.

238. Day, S. E.; Kettunen, M. I.; Gallagher, F. A.; Hu, D. E.; Lerche, M.; Wolber, J.; Golman, K.; Ardenkjaer-Larsen, J. H.; Brindle, K. M., Detecting Tumor Response to Treatment Using Hyperpolarized C-13 Magnetic Resonance Imaging and Spectroscopy. *Nature Medicine* **2007,** *13* (11), 1382-1387.

239. Kuchel, P. W.; Shishmarev, D., Dissolution Dynamic Nuclear Polarization NMR Studies of Enzyme Kinetics: Setting up Differential Equations for Fitting to Spectral Time Courses. *Journal of Magnetic Resonance Open* **2019,** *1*, 100001.

240. Jeener, J.; Meier, B. H.; Bachmann, P.; Ernst, R. R., Investigation of Exchange Processes by Two-Dimensional NMR Spectroscopy. *Journal of Chemical Physics* **1979,** *71* (11), 4546-4553.

241. Szeverenyi, N. M.; Sullivan, M. J.; Maciel, G. E., Observation of Spin Exchange by Two-Dimensional Fourier Transform C-13 Cross Polarization-Magic-Angle Spinning. *Journal of Magnetic Resonance* **1982,** *47* (3), 462-475.

242. Abel, E. W.; Coston, T. P. J.; Orrell, K. G.; Sik, V.; Stephenson, D., Two-Dimensional NMR Exchange Spectroscopy - Quantitative Treatment of Multisite Exchanging Systems. *Journal of Magnetic Resonance* **1986,** *70* (1), 34-53.

243. Haber, S.; Leskes, M., What Can We Learn from Solid State NMR on the Electrode-Electrolyte Interface? *Advanced Materials* **2018,** *30* (41).

244. Perrin, C. L.; Dwyer, T. J., Application of Two-Dimensional NMR to Kinetics of Chemical Exchange. *Chemical Reviews* **1990,** *90* (6), 935-967.

245. Caldarelli, S.; Emsley, L., Intrinsic Asymmetry in Multidimensional Solid-State NMR Correlation Spectra. *Journal of Magnetic Resonance* **1998,** *130* (2), 233-237.

246. Kock, M.; Griesinger, C., Fast NOESY Experiments - an Approach for Fast Structure Determination. *Angewandte Chemie International Edition* **1994,** *33* (3), 332-334.

247. Hayashi, S.; Hayamizu, K., High-Resolution Solid-State P-31 NMR of Alkali Phosphates. *Bulletin of the Chemical Society of Japan* **1989,** *62* (10), 3061-3068.

248. Agarwal, V.; Penzel, S.; Szekely, K.; Cadalbert, R.; Testori, E.; Oss, A.; Past, J.; Samoson, A.; Ernst, M.; Bockmann, A.; Meier, B. H., De Novo 3D Structure Determination from Sub-Milligram Protein Samples by Solid-State 100 Khz MAS NMR Spectroscopy. *Angewandte Chemie-International Edition* **2014,** *53* (45), 12253-12256.

249. Andreas, L. B.; Jaudzems, K.; Stanek, J.; Lalli, D.; Bertarello, A.; Le Marchand, T.; Paepe, D. C. D.; Kotelovica, S.; Akopjana, I.; Knott, B.; Wegner, S.; Engelke, F.; Lesage, A.; Emsley, L.; Tars, K.; Herrmann, T.; Pintacuda, G., Structure of Fully Protonated Proteins by Proton-Detected Magic-Angle Spinning NMR. *Proceedings of the National Academy of Sciences of the United States of America* **2016,** *113* (33), 9187-9192.

250. Struppe, J.; Quinn, C. M.; Sarkar, S.; Gronenborn, A. M.; Polenova, T., Ultrafast H-1 MAS NMR Crystallography for Natural Abundance Pharmaceutical Compounds. *Molecular Pharmaceutics* **2020,** *17* (2), 674-682.

251. Matsuki, Y.; Idehara, T.; Fukazawa, J.; Fujiwara, T., Advanced Instrumentation for DNP-Enhanced MAS NMR for Higher Magnetic Fields and Lower Temperatures. *Journal of Magnetic Resonance* **2016,** *264*, 107-115.

252. Zorin, V. E.; Brown, S. P.; Hodgkinson, P., Origins of Linewidth in H-1 Magic-Angle Spinning NMR. *Journal of Chemical Physics* **2006,** *125* (14).

253. Rankin, A. G. M.; Trebosc, J.; Pourpoint, F.; Amoureux, J. P.; Lafon, O., Recent Developments in MAS DNP-NMR of Materials. *Solid State Nuclear Magnetic Resonance* **2019,** *101*, 116-143.

254. Hoult, D. I.; Richards, R. E., The Signal-to-Noise Ratio of the Nuclear Magnetic Resonance Experiment. *Journal of Magnetic Resonance* **1976,** *24* (1), 71-85.

255. Hu, K. N.; Yu, H. H.; Swager, T. M.; Griffin, R. G., Dynamic Nuclear Polarization with Biradicals. *Journal of the American Chemical Society* **2004,** *126* (35), 10844-10845.

256. Kubicki, D. J.; Casano, G.; Schwarzwalder, M.; Abel, S.; Sauvee, C.; Ganesan, K.; Yulikov, M.; Rossini, A. J.; Jeschke, G.; Coperet, C.; Lesage, A.; Tordo, P.; Ouari, O.; Emsley, L., Rational Design of Dinitroxide Biradicals for Efficient Cross-Effect Dynamic Nuclear Polarization. *Chemical Science* **2016,** *7* (1), 550-558.

257. Kessenikh, A. V.; Lushchikov, V. I.; Manenkov, A. A.; Taran, Y. V., Proton Polarization in Irradiated Polyethylenes. *Soviet Physics - Solid State* **1963,** *5* (2), 321-329.

258. Thurber, K. R.; Tycko, R., Theory for Cross Effect Dynamic Nuclear Polarization under Magic-Angle Spinning in Solid State Nuclear Magnetic Resonance: The Importance of Level Crossings. *Journal of Chemical Physics* **2012,** *137* (8).

259. Mentink-Vigier, F.; Marin-Montesinos, I.; Jagtap, A. P.; Halbritter, T.; van Tol, J.; Hediger, S.; Lee, D.; Sigurdsson, S. T.; De Paepe, G., Computationally Assisted Design of Polarizing Agents for Dynamic Nuclear Polarization Enhanced NMR: The Asympol Family. *Journal of the American Chemical Society* **2018,** *140* (35), 11013-11019.

260. Mentink-Vigier, F.; Akbey, U.; Hovav, Y.; Vega, S.; Oschkinat, H.; Feintuch, A., Fast Passage Dynamic Nuclear Polarization on Rotating Solids. *Journal of Magnetic Resonance* **2012,** *224*, 13-21.

261. Corzilius, B., Theory of Solid Effect and Cross Effect Dynamic Nuclear Polarization with Half-Integer High-Spin Metal Polarizing Agents in Rotating Solids. *Physical Chemistry Chemical Physics* **2016,** *18* (39), 27190-27204.

262. Mance, D.; Gast, P.; Huber, M.; Baldus, M.; Ivanov, K. L., The Magnetic Field Dependence of Cross-Effect Dynamic Nuclear Polarization under Magic Angle Spinning. *Journal of Chemical Physics* **2015,** *142* (23).

263. Leavesley, A.; Jain, S.; Kamniker, I.; Zhang, H.; Rajca, S.; Rajca, A.; Han, S., Maximizing NMR Signal Per Unit Time by Facilitating the E-E-N Cross Effect DNP Rate. *Physical Chemistry Chemical Physics* **2018,** *20* (43), 27646-27657.

264. Lund, A.; Casano, G.; Menzildjian, G.; Kaushik, M.; Stevanato, G.; Yulikov, M.; Jabbour, R.; Wisser, D.; Renom-Carrasco, M.; Thieuleux, C.; Bernada, F.; Karoui, H.; Siri, D.; Rosay, M.; Sergeyev, I. V.; Gajan, D.; Lelli, M.; Emsley, L.; Ouari, O.; Lesage, A., Tinypols: A Family of Water-Soluble Binitroxides Tailored for Dynamic Nuclear Polarization Enhanced NMR Spectroscopy at 18.8 and 21.1 T. *Chemical Science* **2020,** *11* (10), 2810-2818.

265. Chaudhari, S. R.; Berruyer, P.; Gajan, D.; Reiter, C.; Engelke, F.; Silverio, D. L.; Coperet, C.; Lelli, M.; Lesage, A.; Emsley, L., Dynamic Nuclear Polarization at 40 Khz Magic Angle Spinning. *Physical Chemistry Chemical Physics* **2016,** *18* (15), 10616-10622.

266. Penzel, S.; Smith, A. A.; Agarwal, V.; Hunkeler, A.; Org, M. L.; Samoson, A.; Bockmann, A.; Ernst, M.; Meier, B. H., Protein Resonance Assignment at MAS Frequencies Approaching 100 Khz: A Quantitative Comparison of J-Coupling and Dipolar-Coupling-Based Transfer Methods. *Journal of Biomolecular NMR* **2015,** *63* (2), 165-186.

267. Schledorn, M.; Malar, A. A.; Torosyan, A.; Penzel, S.; Klose, D.; Oss, A.; Org, M. L.; Wang, S. S.; Lecoq, L.; Cadalbert, R.; Samoson, A.; Bockmann, A.; Meier, B. H., Protein NMR Spectroscopy at 150 Khz Magic-Angle Spinning Continues to Improve Resolution and Mass Sensitivity. *Chembiochem* **2020,** *21* (17), 2540-2548.

268. Peck, T. L.; Magin, R. L.; Lauterbur, P. C., Design and Analysis of Microcoils for NMR Microscopy. *Journal of Magnetic Resonance Series B* **1995,** *108* (2), 114-124.

269. Barnes, A. B.; Markhasin, E.; Daviso, E.; Michaelis, V. K.; Nanni, E. A.; Jawla, S. K.; Mena, E. L.; DeRocher, R.; Thakkar, A.; Woskov, P. P.; Herzfeld, J.; Temkin, R. J.; Griffin, R. G., Dynamic Nuclear Polarization at 700 Mhz/460 GHz. *Journal of Magnetic Resonance* **2012,** *224*, 1-7.

270. Ishii, Y.; Tycko, R., Sensitivity Enhancement in Solid State N-15 NMR by Indirect Detection with High-Speed Magic Angle Spinning. *Journal of Magnetic Resonance* **2000,** *142* (1), 199-204.

271. Venkatesh, A.; Ryan, M. J.; Biswas, A.; Boteju, K. C.; Sadow, A. D.; Rossini, A. J., Enhancing the Sensitivity of Solid-State NMR Experiments with Very Low Gyromagnetic Ratio Nuclei with Fast Magic Angle Spinning and Proton Detection. *Journal of Physical Chemistry A* **2018,** *122* (25), 5635-5643.

272. Wang, Z.; Hanrahan, M. P.; Kobayashi, T.; Perras, F. A.; Chen, Y.; Engelke, F.; Reiter, C.; Purea, A.; Rossini, A. J.; Pruski, M., Combining Fast Magic Angle Spinning Dynamic Nuclear Polarization with Indirect Detection to Further Enhance the Sensitivity of Solid-State NMR Spectroscopy. *Solid State Nuclear Magnetic Resonance* **2020,** *109*, 101685.

273. Samoson, A.; Tuherm, T.; Past, J.; Reinhold, A.; Anupold, T.; Heinmaa, I., New Horizons for Magic-Angle Spinning NMR. In *New Techniques in Solid-State Nmr*, Klinowski, J., Ed. Springer: Berlin, 2005; Vol. 246, pp 15-31.

274. Lee, D.; Chaudhari, S. R.; De Paepe, G., Solvent Signal Suppression for High-Resolution MAS-DNP. *Journal of Magnetic Resonance* **2017,** *278*, 60-66.

275. Thureau, P.; Juramy, M.; Ziarelli, F.; Viel, S.; Mollica, G., Brute-Force Solvent Suppression for DNP Studies of Powders at Natural Isotopic Abundance. *Solid State Nuclear Magnetic Resonance* **2019,** *99*, 15-19.

276. Hall, D. A.; Maus, D. C.; Gerfen, G. J.; Inati, S. J.; Becerra, L. R.; Dahlquist, F. W.; Griffin, R. G., Polarization-Enhanced NMR Spectroscopy of Biomolecules in Frozen Solution. *Science* **1997,** *276* (5314), 930-932.

277. Bouleau, E.; Saint-Bonnet, P.; Mentink-Vigier, F.; Takahashi, H.; Jacquot, J. F.; Bardet, M.; Aussenac, F.; Purea, A.; Engelke, F.; Hediger, S.; Lee, D.; De Paepe, G., Pushing NMR Sensitivity Limits Using Dynamic Nuclear Polarization with Closed-Loop Cryogenic Helium Sample Spinning. *Chemical Science* **2015,** *6* (12), 6806-6812.

278. Matsuki, Y.; Ueda, K.; Idehara, T.; Ikeda, R.; Ogawa, I.; Nakamura, S.; Toda, M.; Anai, T.; Fujiwara, T., Helium-Cooling and -Spinning Dynamic Nuclear Polarization for Sensitivity-Enhanced Solid-State NMR at 14 T and 30 K. *Journal of Magnetic Resonance* **2012,** *225*, 1-9.

279. Hackmann, A.; Seidel, H.; Kendrick, R. D.; Myhre, P. C.; Yannoni, C. S., Magic-Angle Spinning NMR at near-Liquid-Helium Temperatures. *Journal of Magnetic Resonance* **1988,** *79* (1), 148-153.

280. Akbey, U.; Linden, A. H.; Oschkinat, H., High-Temperature Dynamic Nuclear Polarization Enhanced Magic-Angle-Spinning NMR. *Applied Magnetic Resonance* **2012,** *43* (1-2), 81-90.

281. Ong, T. C.; Mak-Jurkauskas, M. L.; Walish, J. J.; Michaelis, V. K.; Corzilius, B.; Smith, A. A.; Clausen, A. M.; Cheetham, J. C.; Swager, T. M.; Griffin, R. G., Solvent-Free Dynamic Nuclear Polarization of Amorphous and Crystalline Ortho-Terphenyl. *Journal of Physical Chemistry B* **2013,** *117* (10), 3040-3046.

282. Thurber, K. R.; Tycko, R., Measurement of Sample Temperatures under Magic-Angle Spinning from the Chemical Shift and Spin-Lattice Relaxation Rate of Br-79 in Kbr Powder. *Journal of Magnetic Resonance* **2009,** *196* (1), 84-87.

283. Jayanthi, S.; Lupulescu, A., Sensitivity Enhancement in 2d Double Cross Polarization Experiments under Fast MAS by Recycling Unused Protons. *Solid State Nuclear Magnetic Resonance* **2020,** *107*, 101652.

284. Wijesekara, A. V.; Venkatesh, A.; Lampkin, B. J.; VanVeller, B.; Lubach, J. W.; Nagapudi, K.; Hung, I.; Gor'kov, P. L.; Gan, Z. H.; Rossini, A. J., Fast Acquisition of Proton-Detected HETCOR Solid-State NMR Spectra of Quadrupolar Nuclei and Rapid Measurement of NH Bond Lengths by Frequency Selective HMQC and RESPDOR Pulse Sequences. *Chemistry - A European Journal* **2020,** *26* (35), 7881-7888.

285. Pylaeva, S.; Ivanov, K. L.; Baldus, M.; Sebastiani, D.; Elgabarty, H., Molecular Mechanism of Overhauser Dynamic Nuclear Polarization in Insulating Solids. *Journal of Physical Chemistry Letters* **2017,** *8* (10), 2137-2142.

286. Orlando, T.; Dervisoglu, R.; Levien, M.; Tkach, I.; Prisner, T. F.; Andreas, L. B.; Denysenkov, V. P.; Bennati, M., Dynamic Nuclear Polarization of C-13 Nuclei in the Liquid State over a 10 Tesla Field Range. *Angewandte Chemie International Edition* **2019,** *58* (5), 1402-1406.

287. Le, D.; Ziarelli, F.; Phan, T. N. T.; Mollica, G.; Thureau, P.; Aussenac, F.; Ouari, O.; Gigmes, D.; Tordo, P.; Viel, S., Up to 100% Improvement in Dynamic Nuclear Polarization Solid-State NMR Sensitivity Enhancement of Polymers by Removing Oxygen. *Macromolecular Rapid Communications* **2015,** *36* (15), 1416-1421.

288. Hodgkinson, P., High-Resolution H-1 NMR Spectroscopy of Solids. *Annual Reports on NMRHigh-Resolution H-1 NMR Spectroscopy of Solids Spectroscopy* **2010,** *72*, 185-223.

289. Paulson, E. K.; Morcombe, C. R.; Gaponenko, V.; Dancheck, B.; Byrd, R. A.; Zilm, K. W., Sensitive High Resolution Inverse Detection NMR Spectroscopy of Proteins in the Solid State. *Journal of the American Chemical Society* **2003,** *125* (51), 15831-15836.

290. Brownbill, N. J.; Gajan, D.; Lesage, A.; Emsley, L.; Blanc, F., Oxygen-17 Dynamic Nuclear Polarisation Enhanced Solid-State NMR Spectroscopy at 18.8 T. *Chemical Communications* **2017,** *53* (17), 2563-2566.

291. Vitzthum, V.; Mieville, P.; Carnevale, D.; Caporini, M. A.; Gajan, D.; Coperet, C.; Lelli, M.; Zagdoun, A.; Rossini, A. J.; Lesage, A.; Emsley, L.; Bodenhausen, G., Dynamic Nuclear Polarization of Quadrupolar Nuclei Using Cross Polarization from Protons: Surface-Enhanced Aluminium-27 NMR. *Chemical Communications* **2012,** *48* (14), 1988-1990.

292. Lee, D.; Takahashi, H.; Thankamony, A. S. L.; Dacquin, J. P.; Bardet, M.; Lafon, O.; De Paepe, G., Enhanced Solid-State NMR Correlation Spectroscopy of Quadrupolar Nuclei Using Dynamic Nuclear Polarization. *Journal of the American Chemical Society* **2012,** *134* (45), 18491-18494.

293. Nagashima, H.; Trebosc, J.; Kon, Y.; Sato, K.; Lafon, O.; Amoureux, J. P., Observation of Low-Gamma Quadrupolar Nuclei by Surface-Enhanced NMR Spectroscopy. *Journal of the American Chemical Society* **2020,** *142* (24), 10659-10672.

294. Ashbrook, S. E.; Sneddon, S., New Methods and Applications in Solid-State NMR Spectroscopy of Quadrupolar Nuclei. *Journal of the American Chemical Society* **2014,** *136* (44), 15440-15456.

295. Kentgens, A. P. M., A Practical Guide to Solid-State NMR of Half-Integer Quadrupolar Nuclei with Some Applications to Disordered Systems. *Geoderma* **1997,** *80* (3-4), 271-306.

Acknowledgements

This thesis would not be complete without mentioning some of the incredible people who have helped and supported me along the way, both directly and indirectly.

First of all, I would like to thank Lyndon Emsley for giving me the opportunity to join his research group. The work presented in this thesis would not have been possible without his insight and guidance. His approach to science and emphasis on teamwork has created an environment where I have always felt encouraged and supported to improve, and it has also been fun. Although this is an understatement: Thank you, Lyndon.

I would also like to thank the experts who took the time to read my thesis and evaluate my work: Clare Grey, Björn Corzilius and Christophe Copéret, as well as jury president Majed Chergui.

Throughout my time at EPFL I have gotten the opportunity to work with some fantastic post-docs, who have always been happy to share their knowledge of any aspect of DNP or solid-state NMR with me. I would like to thank Brennan, Pinelopi, Pierrick, Michael, Gabriele, Claudia, Andrea, Jasmine and Subba for their invaluable contributions to my learning process and to the research work presented in this thesis. Special thanks to Brennan for teaching me how to run DNP NMR experiments, along with so many other things.

I am also grateful to all the other members of the Emsley group, past and present: Baptiste, Albert, Federico, Arthur, Dominik, Martins, Aditya, Manuel, Bruno, Yu, Anna, Nicolas and all of the other students. Thanks for the great discussions and collaborations, and for all of your help. I have really enjoyed my time at EPFL and it wouldn't have been the same without you.

The DNP meetings, with Anne Lesage, Olivier Ouari, Moreno Lelli and others, are also worth mentioning as they undoubtedly contributed to my learning. I would also like to thank Michel Bardet, Brad Chmelka and the other scientists that I have had the chance to meet and interact with during the course of my studies.

Additionally, I would like to thank Nadia Gauljaux for efficiently taking care of all of the administrative things. I have also really appreciated the work of the people who keep the spectrometers running and in the best shape possible: Aurélien, Anto, Emilie, Pascal and Vladan. I also wish to thank the people at Bruker who have made it possible for me to work with state-of-the-art equipment, especially Christian Reiter and Nicolas Mathieu, for all their help and remote troubleshooting.

To my family: Takk fyrir allt. Ég gæti ekki hugsað mér betra fólk en ykkur til að hafa í kringum mig.

Curriculum vitae

Snædís Björgvinsdóttir

snaedis.bjoergvinsdottir@epfl.ch / snaedis.bjorgvinsdottir@gmail.com

Current position

Since 2016 Ph.D. student. Laboratory of Magnetic Resonance.

Thesis director: Lyndon Emsley.

École polytechnique fédérale de Lausanne, EPFL.

Education

2016 M.Sc. in chemistry. *University of Iceland.*

Project advisor: Snorri Th. Sigurdsson.

2013 B.Sc. in chemistry. *University of Iceland.*

Publications

(2020) *Hyperpolarization transfer pathways in inorganic materials.* S. Björgvinsdóttir, P. Moutzouri, B.J. Walder, N. Matthey, L. Emsley, *J. Magn. Reson.* accepted (2020).

2020 *Dynamic nuclear polarisation enhancement of 200 at 21.15 T enabled by 65 kHz magic angle spinning.* P. Berruyer, S. Björgvinsdóttir, A. Bertarello, G. Stevanato, Y. Rao, G. Karthikeyan, G. Casano, O. Ouari, M. Lelli, C. Reiter, F. Engelke, L. Emsley, *J. Phys. Chem. Lett.* 11 (2020) 8386-8391.

2020 *Sensitivity Enhancements in Lithium Titanates by Incipient Wetness Impregnation DNP NMR.* S. Björgvinsdóttir, P. Moutzouri, P. Berruyer, M.A. Hope, L. Emsley, *J. Phys. Chem. C* 124, 30 (2020) 16524–16528.

2019 *Maximizing hyperpolarization in pulse cooling under MAS.* S. Björgvinsdóttir, B.J. Walder, N. Matthey, L. Emsley, *J. Magn. Reson.* 300 (2019) 142-148.

2018 *Bulk nuclear hyperpolarization of inorganic solids by relay from the surface.* S. Björgvinsdóttir, B.J. Walder, A.C. Pinon, L. Emsley, *J. Am. Chem. Soc.* 140 (2018) 7946-7951.

2018 *DNP enhanced NMR with flip-back recovery.* S. Björgvinsdóttir, B.J. Walder, A.C. Pinon, J.R. Yarava, L. Emsley, *J. Magn. Reson.* 288 (2018) 69-75.

2015 *Enabling electrochemical reduction of nitrogen to ammonia at ambient conditions through rational catalyst design.* Y. Abghoui, A. L. Garden, V.F. Hlynsson, S. Björgvinsdóttir, H. Ólafsdóttir, E. Skúlason, *Phys Chem Chem Phys.* 17 (2015) 4909-4918.

Teaching experience

2017-2019   *École polytechnique fédérale de Lausanne, EPFL*, teaching assistant

- Nuclear magnetic resonance
- General chemistry
- Structural analysis

2012-2015   *University of Iceland*, teaching assistant

- Organic chemistry
- Statistics
- General chemistry

Grants and awards

2020   Best poster presentation award in physical chemistry, SCS fall meeting, 25 August 2020.

2019   Student stipend to attend EUROISMAR, 25-30 August 2019.

2019   Student stipend to attend ENC, 7-12 April 2019.

2018   JMR-ISMAR young scientist award. HYP18. September 2018.

2017   Student stipend to attend the Alpine Conference, 10-14 September 2017.

2014   Short term scientific mission (STSM) funded by COST action TD1103, November 2014.

2012   Research grant from the Icelandic Student Innovation Fund. Project leader: Egill Skúlason.